3 Seismic structure of the lithosphere

"One cannot embrace the unembraceable."

Kozma Prutkov

This chapter provides a short review of seismic methods used in lithosphere studies and their major results. It starts with an overview of laboratory measurements of seismic properties, which provide the basis for seismic interpretations, followed by a brief summary of seismic methods. For an introduction to seismic methods the reader is referred to the monograph of Shearer (1999). The advanced theory of seismic methods can be found in Aki and Richards (1980), Nolet (1987, 2008), Iyer and Hirahara (1993). Discussion of the major results of seismic studies of the lithosphere is structured by methods (converted waves, controlled source, and teleseismic tomography), which provide 1D, 2D, and 3D images of the lithosphere.

3.1 Laboratory studies of seismic properties of rocks

3.1.1 Introduction: Major elastic and anelastic parameters

An isotropic seismic model is defined by three parameters: density ρ of the material through which the wave is propagating, and the Lamé parameters λ and μ (see details in Section 8.1.1). The velocities of compressional (or *P*) waves *Vp* and shear (or *S*) waves *Vs* in an isotropic homogeneous medium are:

$$V_P = \sqrt{\frac{K + 4/3\mu}{\rho}}, \qquad V_S = \sqrt{\frac{\mu}{\rho}}, \tag{3.1}$$

where K is the modulus of incompressibility (or the bulk modulus, see eq. 8.2) and μ (also denoted by G) is the shear modulus (a measure of material resistance to shearing). The bulk sound velocity is defined as:

$$V_B = \sqrt{\frac{K}{\rho}} = \sqrt{V_P^2 - 4/3V_S^2}. \tag{3.2}$$

For an isotropic material, stress-induced deformation of the material in the direction of one axis will produce material deformation in three dimensions along the other axes (Hooke's

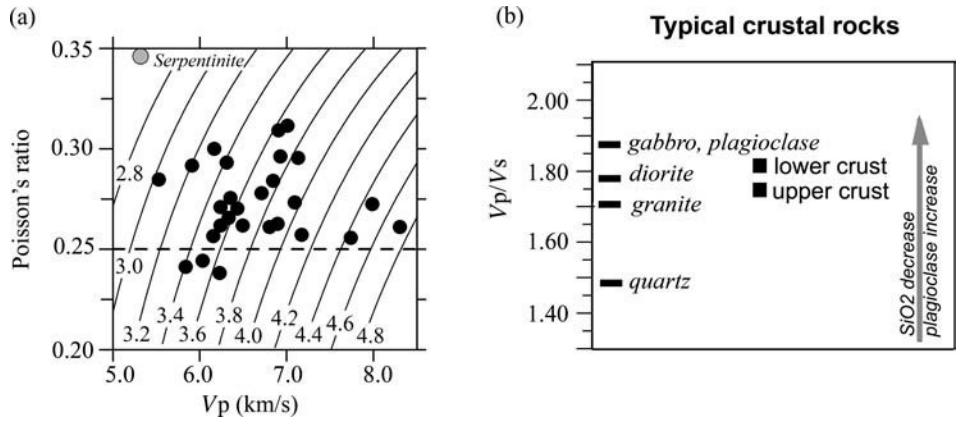

Fig. 3.1 (a) Relationship between *Vp* and Poisson's ratio based on laboratory measurements on crystalline (volcanic, igneous, and metamorphic) rocks (symbols – experimental data of Christensen, 1996). Thin dashed line corresponds to Poisson's ratio of 0.25 (*Vp/Vs* = 1.73). Thin lines – *Vs* (km/s) based on eq. 3.3. (b) *Vp/Vs* ratio for some crustal rocks.

law, eq. 8.1). The dimensionless Poisson's ratio v is the ratio of the relative transverse strain (normal to the applied load) to the relative axial strain (in the direction of the applied load); it quantifies the ratio of the lateral shortening to the longitudinal extension:

$$v = \frac{\lambda}{2(\lambda + \mu)} = 1 - \frac{V_P^2/2}{V_P^2 - V_S^2}. \tag{3.3}$$

The requirement for λ and μ to have positive values limits Poisson's ratio of a stable material to the range 0 to +0.5. (Some modern polymeric materials called auxetic may expand laterally when stretched and they have a negative Poisson's ratio (Lakes, 1987)). A perfectly incompressible material deformed elastically (e.g. liquids with $\mu = 0$) has a Poisson's ratio of exactly 0.5. For most crustal rocks, v varies between 0.25 and 0.30 (Fig. 3.1a). The mantle has $v \sim 0.25$ which is achieved when $\lambda = \mu$ (i.e. when $V_P = \sqrt{3} V_S$).

Since the Poisson's ratio concept is applicable only to an elastically deformed medium where Hooke's law is valid, the *Vp/Vs* ratio is widely used instead (Fig. 3.1b). The *Vp/Vs* ratio depends on many different factors such as composition, and there is no simple relation that exists between the *Vp/Vs* ratio and *Vp* or *Vs*, as indicated by studies of sedimentary (Castagna *et al.*, 1985; Mavko *et al.*, 1998) and igneous and metamorphic rocks (Christensen, 1996). Some other combinations of elastic moduli for isotropic materials that are in common use in seismology are:

$$\begin{aligned} K &= (V_P^2 - 4/3 V_S^2) \\ \lambda &= \rho(V_P^2 - 2V_S^2) \\ \mu &= \rho V_S^2. \end{aligned} \tag{3.4}$$

Anelasticity leads to attenuation of seismic energy. Seismic attenuation is described by the "quality factor" Q which quantifies the amount of energy ΔE lost per cycle:

$$\frac{2\pi}{Q} = -\frac{\Delta E}{E}, \tag{3.5}$$

where E is the peak energy. Commonly, the inverse parameter Q^{-1} (seismic attenuation) is used in seismology. This includes two parts, intrinsic attenuation Q_i^{-1} (which is a material property and quantifies local conversion of elastic energy to heat) and scattering attenuation Q_s^{-1}:

$$Q^{-1} = Q_i^{-1} + Q_s^{-1}. \tag{3.6}$$

Attenuation results in dispersion, i.e. frequency dependence of the moduli. For a change in period from 1 sec to 1000 sec, seismic velocities change by *c*. 1% for $Q_p \sim 200$ (typical for the upper mantle) and by *c*. 4% for $Q_p \sim 60$ (typical for the low-velocity zone, LVZ) (Masters and Shearer, 1995).

3.1.2 Effects of pressure and temperature

Seismic velocities

Under the physical conditions of the Earth's mantle, the elastic constants of rocks vary significantly. With increasing depth, temperature and pressure increase rapidly and reach *c*. 1400–1500 °C and *c*. 13.5 GPa at the top of the transition zone (at *c*. 410 km depth). While early experiments were made at ambient (standard pressure–temperature, STP) conditions (Birch, 1958), it was soon recognized that adequate comparison of observed seismic velocities with laboratory measurements on rock samples of different composition requires experiments at elevated (high) pressures and temperatures (Christensen, 1965; Kern, 1978). Experimental studies over the last half-century (with accuracy of individual measurements commonly better than 1%) have resulted in accumulation of an extensive database of seismic properties of rocks at crustal and upper mantle pressures and temperatures. Most of these measurements, in particular the early ones (Sato *et al*., 1989; Burlini and Kern, 1994), were made not at seismic, but at ultrasonic frequencies of 60–900 KHz (for comparison, the dominant period of the P-wave body waves is ~1 sec). As discussed later, laboratory experiments made at ultrasonic frequencies put certain limitations on the interpretation of seismic velocities in terms of temperature and composition, in particular at high temperatures (Fig. 3.2b).

The strong effect of temperature on elastic moduli (and hence on P- and S-wave velocities) has long been known from laboratory studies (e.g. Ide, 1937; Birch, 1943; Hughes and Cross, 1951; Christensen, 1965). Most measurements were made at temperatures lower than 600–700 °C (Kern, 1978; Christensen, 1979) and the amount of data for near-solidus temperatures ($T > 1000$ °C) remains very limited (Berckhemer *et al*., 1982; Murase and Kushiro, 1979; Murase and Fukuyama, 1980; Sato *et al*., 1989; Jackson, 1993). At low temperatures, the dependence of velocity on temperature is approximately linear (Sumino and Anderson, 1982):

$$\partial V_S/\partial T = -0.35 \text{ m/s/K}. \tag{3.7}$$

This relationship is based on laboratory experiments performed at high frequencies (~1 MHz, e.g. Kumazawa and Anderson, 1969) and accounts mostly for anharmonic effects

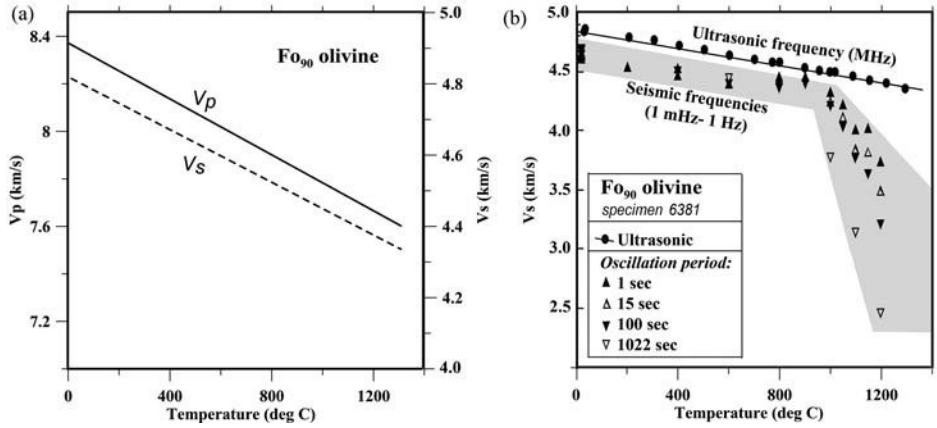

Fig. 3.2 Temperature-dependence of *Vp* (solid) and *Vs* (dashed) in fine-grained synthetic polycrystalline olivine samples (based on the results of Jackson *et al*., 2005). (a) Results obtained at ultrasonic frequencies of 20–50 MHz. (b) Comparison of the results obtained at ultrasonic frequencies (circles and solid line based on theoretical predictions) with those at seismic frequencies (gray shading and other symbols). Note different vertical scales of the two plots.

(Karato, 1993). The latter are the deviation of mineral lattice vibrations from harmonic oscillations and result in pressure- and temperature-dependence of elastic constants. With temperature increase, at low homologous (near-solidus) temperatures *Tm/T* (where *Tm* is the solidus temperature below which a rock is completely solid), the temperature effect on elastic moduli becomes strong. It leads to viscous behavior in the material, a sharp decrease in *Vp* and *Vs*, and a sharp increase in Poisson's ratio and *Vp/Vs*. Importantly, a significant (*c*. 3%) reduction of seismic velocities occurs before any melting in the system starts (Fig. 3.3).

Pressure and temperature have opposite effects on seismic velocities: while pressure increase causes an increase in both *Vp* and *Vs* velocities, an increase in temperature leads to a decrease in both of the seismic velocities (Fig. 3.4). At relatively low temperatures typical for a shallow lithosphere, when no melt is present, pressure and temperature effects on elastic moduli approximately compensate each other, so that Poisson's ratio remains approximately constant and depends mostly on the composition. This fact is widely used in seismology for mineralogical interpretations of Poisson's ratio variations in the lithosphere (in particular, in the crust).

Seismic attenuation, anelasticity, and effect of frequency

The effect of temperature on seismic attenuation is much stronger than on seismic velocities (Fig. 3.5). Experimental measurements of seismic attenuation in upper mantle rocks carried out over a wide range of pressures and temperatures at seismic (0.01–1 Hz) frequencies (Berckhemer *et al*., 1982; Jackson, 1993; Gribb and Cooper, 1998) show that at subsolidus temperatures the attenuation, Q^{-1}, in mantle rocks follows the Arrhenius law and exponentially increases with temperature T:

$$1/Q = A\tau^{\alpha} \exp\left(-\alpha E^{*}/RT\right), \tag{3.8}$$

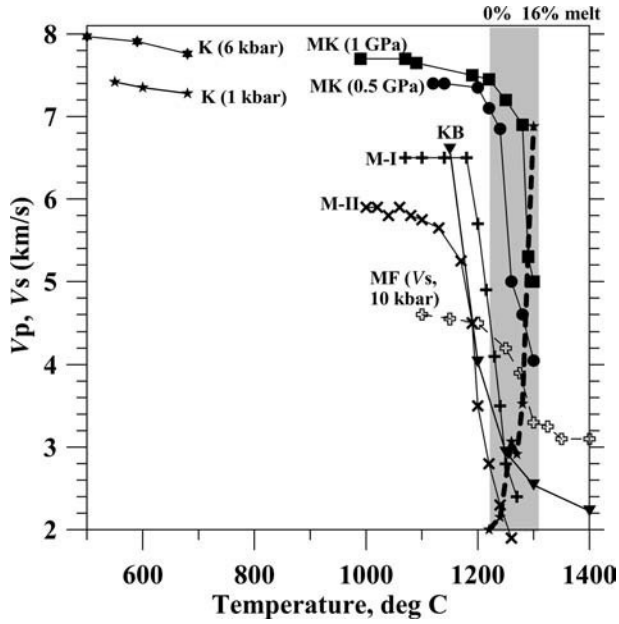

Fig. 3.3 Temperature-dependence of seismic velocities (based on Artemieva *et al*., 2004). Solid lines – *Vp*, dashed lines – *Vs*. Thick dashed line and shaded area: changes in melt volume (Murase and Fukuyama, 1980). Sources: K = Kern (1978), *Vp* in peridotite at 1 and 6 Kbar; MK = Murase and Kushiro (1979), *Vp* in peridotite at 0.5 and 1.0 GPa; KB = Kampfmann and Berckhemer (1985), *Vp* in dunite (at 0.1 Hz); MF = Murase and Fukuyama (1980), *Vs* in peridotite at 10 Kbar; M-I and M-II = Murase *et al*. (1977), *Vp* in two peridotite samples.

where E^* is the activation energy, R is the gas constant, τ is the oscillation period, A is a scaling constant (commonly assumed to be 0.148, Sobolev *et al*., 1996), and exponent α, determined from seismic studies and laboratory measurements on the upper mantle rocks, is almost temperature-independent and may range from 0.15 to 0.30 for different values of τ, T, and P (Jackson *et al*., 1992).

Laboratory measurements of seismic attenuation in dry peridotite at high temperatures $0.95 < T_m/T < 1.17$ (where T_m is solidus temperature) and at pressures of 200–730 MPa demonstrate a linear dependence of the P-wave quality factor Q_p on the homologous temperature T_m/T (Sato and Sacks, 1989; Sato *et al*., 1989). Laboratory results (performed at ultrasonic frequencies, 60–900 KHz) can be extrapolated to higher pressures through the pressure-dependent solidus temperature $T_m(P)$ (in Kelvin):

$$Q_p = Q_{pm}\exp[g(T_m(P)/T - a)], \tag{3.9}$$

where $Q_{pm} = 3.5 + P/0.073$ (here P is pressure in GPa), a and g are experimentally determined parameters (a is close to 1, while g is strongly T-dependent and increases from 6.75 to 13.3 with an increase in homologous temperature from 0.95 to 1.15).

Attenuation results in frequency-dependence of the elastic moduli which becomes particularly strong at near-solidus temperatures (Fig. 3.7). Jackson *et al*. (1992) measured seismic attenuation on dry dunite at seismic frequencies (0.01–1 Hz), at temperatures of 20°, 600°,

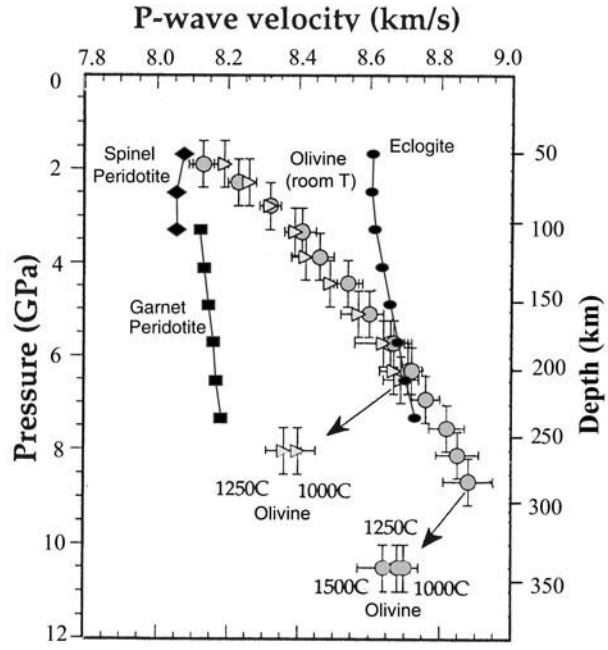

Fig. 3.4 Pressure-dependence of P-wave seismic velocity in mantle rocks. Gray symbols – San Carlos olivine at room temperature; the arrows show changes in velocity and pressure which result from heating (from Knoche *et al*., 1998). Black symbols – calculated compressional velocities for hypothetical mantle eclogite and fertile peridotite compositions at *in situ* mantle temperatures (James *et al*., 2004). Temperature is based on the cold Archean geotherm (Kaapvaal craton); pressure-to-depth conversion is calculated assuming densities of crust and mantle 2.7 and 3.3 g/cm^3, respectively.

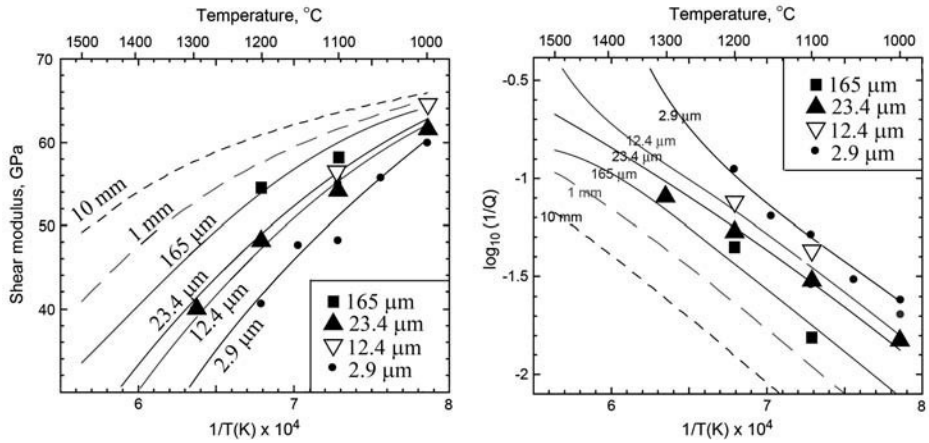

Fig. 3.5 Shear modulus μ and seismic attenuation as functions of temperature and grain size for a fixed oscillation period of 8.2 sec (after Faul and Jackson, 2005). Symbols show the experimental data, the lines are theoretical predictions.

800, and 1000 °C and at pressures up to 300 MPa. The experimental data allow for approximation of P-wave seismic attenuation as a function of temperature (T in °C) as:

$$1/Q_{p0} = \exp(0.00267^{*}T - 6.765), \tag{3.10}$$

where $1/Q_{p0}$ is the value of $1/Q_p$ at 1 s period (Figs. 3.6a and 3.8b). The value of Q_p depends strongly on oscillation period, τ, and between 600 and 1000 °C increases approximately exponentially with increasing temperature T and the Arrhenius law (3.8) takes the form:

$$1/Q_p = 1/Q_{p0}\tau^{\alpha}. \tag{3.8a}$$

At low frequencies (large oscillation period τ), attenuation is stronger and the shear modulus has smaller values than at high frequencies (Fig. 3.8).

With increasing temperature, anelasticity significantly affects seismic velocities, in particular for shear waves. In contrast to anharmonicity, anelasticity is accompanied by a loss of energy during wave propagation and thus anelastic effects are frequency-dependent. Their effect on seismic velocities becomes particularly important at high temperatures and low frequencies (at lower frequencies, seismic velocities are lower) and can be approximated as (Minster and Anderson 1981):

$$V_s(\text{anelastic}) = V_s(\text{elastic})[1 - C/Q(\tau, P, T)], \tag{3.11}$$

where $C = 2/\tan(\pi\alpha/2)$ and $1/Q(\tau, P, T)$ is given by Eq. (3.8). Note that extrapolation of relationship (3.8) to seismic frequencies may not be valid, as mechanisms of seismic attenuation other than the grain boundary process (assumed by Sato and Sacks, 1989) such as dislocation and micro-creep processes can be equally important at seismic conditions (Karato, 1998; Romanowicz and Durek, 2000). In the upper mantle, the correction for anelasticity approximately doubles the temperature derivatives (eq. 3.7) caused by anharmonicity alone (Karato, 1993). However, it is impossible to measure anelasticity effects at seismic frequencies in laboratory experiments based on wave propagation because wavelengths of seismic waves are significantly larger than sample size.

3.1.3 Effect of grain size variations

Experimental studies performed on various ultrabasic and basic rocks and on polycrystalline olivine aggregates have demonstrated that shear modulus and attenuation depend not only on oscillation period but also on grain size (Berckhemer *et al*., 1982; Kampfmann and Berckhemer, 1985). Recent experiments performed on melt-free polycrystalline aggregates of Fo90 olivine at fixed temperature and fixed frequency indicate that shear modulus increases and attenuation decreases with increase in grain size (Fig. 3.5). It is worth noting that the range of olivine grain sizes used in the experiments was significantly smaller than olivine grain size variations measured in upper mantle xenoliths from different continental locations (Fig. 3.9); a typical distribution of grain sizes in dunite samples that are widely used in laboratory studies is shown in Fig. 3.10.

Model calculations of grain size evolution in the oceanic upper mantle for a composite diffusion–dislocation creep rheology allow for estimation of grain size as a function of depth, seafloor age, and mantle water content (Behn *et al*., 2009), assuming that grain size

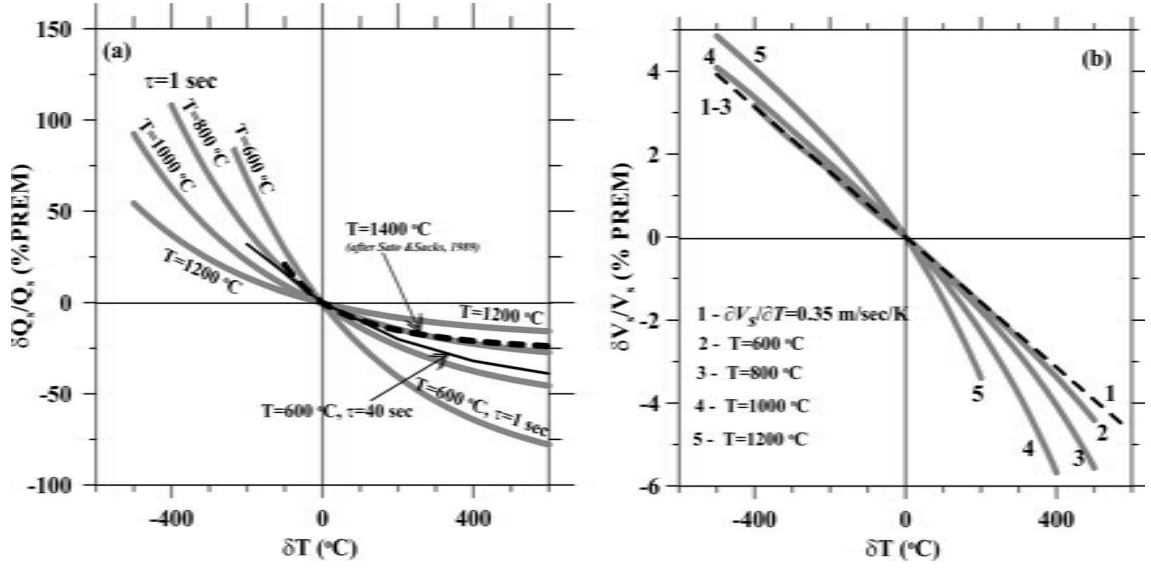

Fig. 3.6 Relative anomalies of Q_s (a) and V_s (b) with respect to PREM as a function of temperature anomalies calculated for upper mantle temperatures of 600, 800, 1000, 1200, and 1400 °C (after Artemieva *et al.*, 2004). (a) δQ_s anomalies calculated from the experimental data of Jackson *et al.* (1992), eqs. (3.10, 3.17), for $\tau = 1$ sec. For comparison, the results are also shown for $\tau = 40$ sec for $T = 600$ °C (thin black line). Dashed line – δQ_s calculated for high homologous mantle temperature T_m/T based on the experimental data of Sato and Sacks (1989), eq. (3.9). (b) δV_s anomalies caused by anelasticity (eqs. 3.8, 3.11), for $\tau = 40$ sec. For a comparison, dashed line: δV_s based on the linear relationship (3.7).

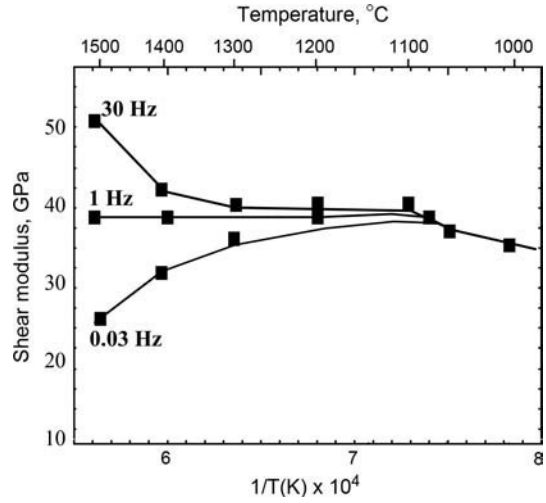

Fig. 3.7 Dispersion of the shear modulus of polycrystalline forsterite at high temperatures (after Berckhemer *et al.*, 1982).

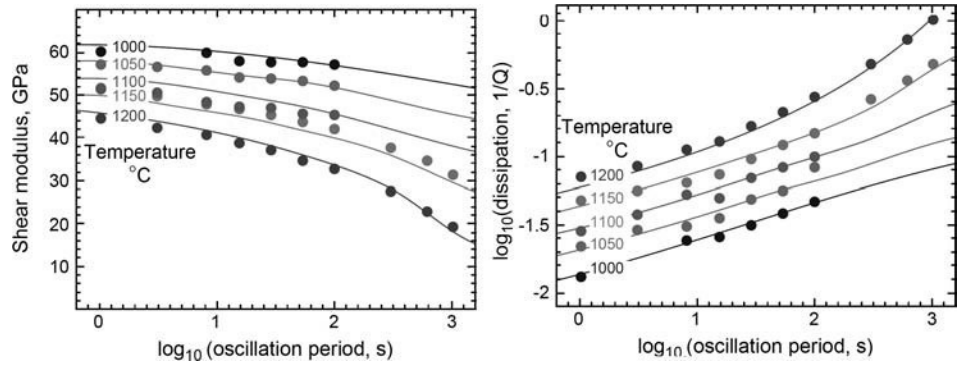

Fig. 3.8 Shear modulus μ and seismic attenuation as functions of temperature and period of oscillation for a sample with grain size 3 μm (from Faul and Jackson, 2005). The dots represent the experimental data, the lines are theoretical predictions.

evolution in the upper mantle is controlled by competition between dynamic recrystallization and grain growth (Austin and Evans, 2007). These theoretical calculations suggest that, in a 60-Ma-old oceanic mantle, grain size has a minimal value of ~10 mm at *c*. 130 km depth and increases to 20–30 mm above the transition zone in the case of a wet mantle (water content of 1000 ppm), but it is only ~5 to ~10 mm at depths between 150 and 400 km in the case of a dry mantle (water content 50 ppm).

The cratonic upper mantle, which is believed to be dry (Hirth *et al.*, 2000; for discussion of this hypothesis see Sections 6.3 and 8.1.3), has similar values of olivine grain size between 150 and 240 km depth as evidenced by mantle peridotite xenoliths from South Africa (Fig. 3.9a). Since neither abrupt changes in stress regime nor phase changes are expected at 140–150 km beneath the cratons, a pronounced drop in olivine grain size from

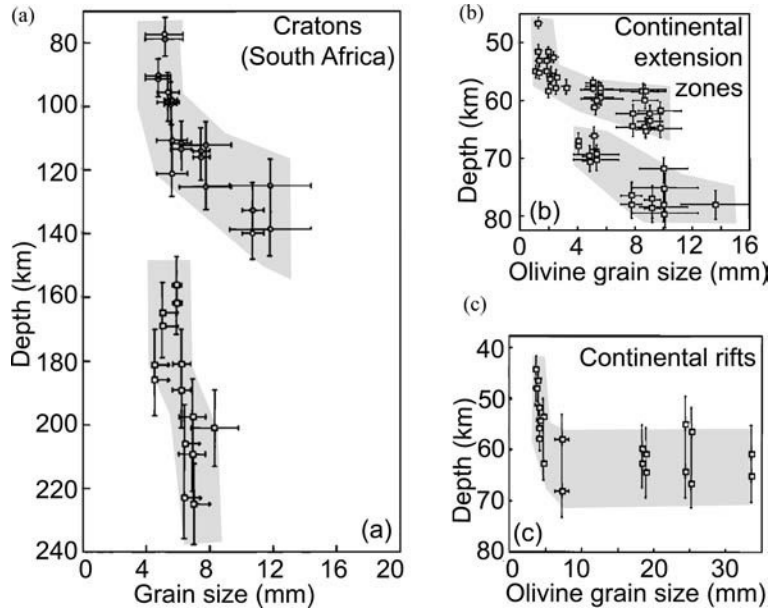

Fig. 3.9 Olivine grain-size distribution with depth for mantle peridotite xenoliths from (a) southern Africa kimberlites, (b) extensional Basin and Range Province, western USA, and (c) locations in France and Nevada typical of late stages of continental rifting (redrawn from Mercier, 1980).

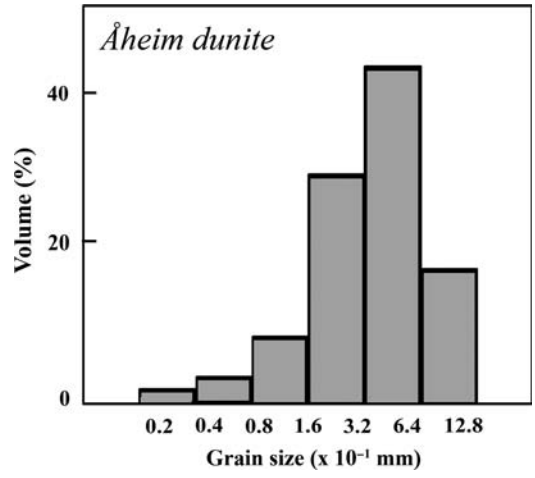

Fig. 3.10 Grain-size distribution in Åheim dunite samples that are widely used in laboratory studies (Berckhemer *et al*., 1982).

c. 12 mm at 120–140 km depth to 4–8 mm below 150 km in the cratonic mantle has been attributed to a dramatic (temperature-dependent) change in the dominant recrystallization mechanism from subgrain rotation at low temperatures to grain boundary migration at high temperatures (Poirier and Nicolas, 1975; Poirier and Guillope, 1979; Mercier, 1980).

Data on depth variation of grain size allow for calculation of variations in shear wave velocity and seismic quality factor with depth. The strong dependence of shear modulus and attenuation on grain size allows for interpretation of the low-velocity zone beneath the ocean basins by variations in grain size without requiring the presence of melts and fluids (Faul and Jackson, 2005). However, this explanation only holds for wet mantle, while grain size variations in a dry upper mantle are insufficient to explain the seismic LVZ in the absence of water and/or melt.

3.1.4 Effect of mineralogy

Laboratory measurements of seismic velocities in rocks form the basis for petrologic interpretations of the seismic velocity structure of the crust and the upper mantle. These data are summarized in a review by Christensen and Mooney (1995) who discuss the effects of mineralogy, chemistry, and metamorphic grade on compressional wave seismic velocities in the crust (Fig. 3.11) and on their temperature-dependence (Fig. 3.12). Unfortunately, similar analysis for *Vs* seismic velocities has received only limited attention.

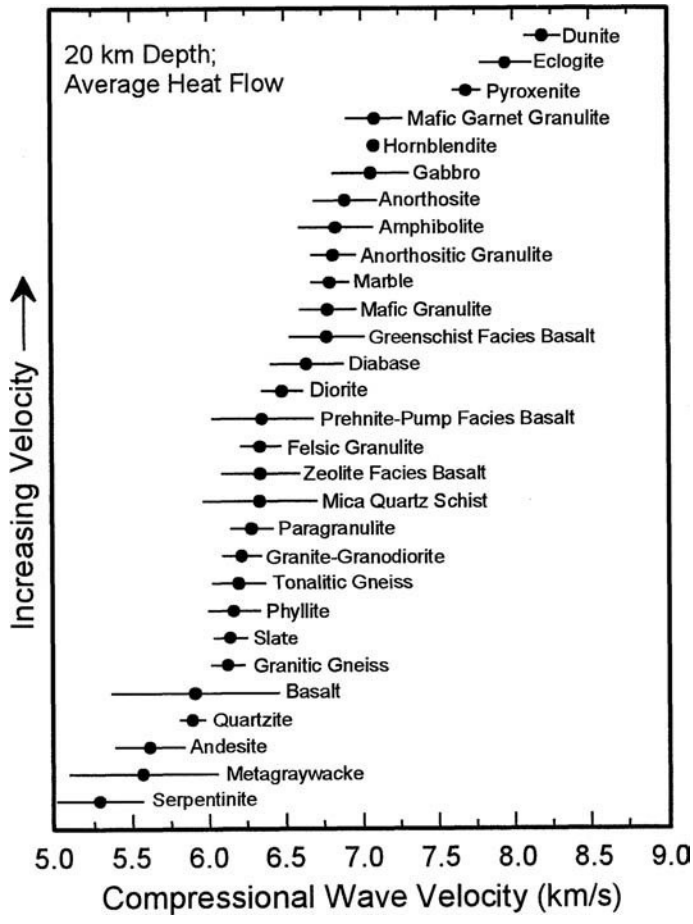

Fig. 3.11 Effect of composition of crustal and mantle rocks on P-wave velocity (from Christensen and Mooney, 1995).

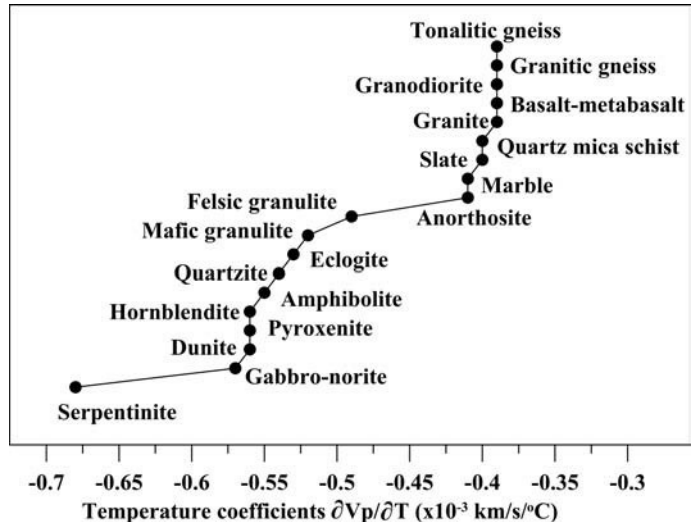

Fig. 3.12 Temperature coefficients for *Vp* seismic velocity in crystalline rocks (data of Christensen and Mooney, 1995).

An important conclusion of experimental seismic velocity measurements on crystalline rocks is the existence of a large variation in the range of elastic properties even for rocks with simple lithologies (such as granite and gabbro); for most crustal rocks velocity histograms have a normal distribution. Since variations in composition have different effects on shear and compressional wave velocities, the *Vp/Vs* ratio and Poisson's ratio provide better diagnostics of variations in the major element composition of crustal (in particular, lower crustal) and upper mantle rocks (e.g. Christensen and Fountain, 1975; Fig. 3.1). The effect of compositional variations in the upper mantle related to partial melting and melt extraction is discussed in Section 3.1.7.

3.1.5 Anisotropy

The lithosphere is heterogeneous. Wave propagation in heterogeneous media may result in seismic anisotropy, and seismic anisotropy is the rule rather than the exception (Montagner and Tanimoto, 1990; Maupin and Park, 2008). Heterogeneities that cause crustal and upper mantle seismic anisotropy can exist:

- *at the crystal scale*, caused by lattice-preferred orientation (LPO) due to alignment of anisotropic crystals such as olivine and orthopyroxene (Christensen and Lundquist, 1982; Nicolas and Christensen, 1987),
- *at the rock scale*, produced by rock fabric (Katayama *et al*., 2004),
- *at the crustal scale*, caused by rock foliation and layering (Crampin, 1977),
- *at the rock scale or crustal scale*, caused by stress-aligned microcracks and pores (which can be filled with fluids and melts) (Nur, 1971; Crampin, 1987),
- *at large scale in the mantle*, caused by a temperature difference between upgoing and downgoing flow in mantle convective cells (Montagner and Guillot, 2002).

Pores and microcracks

Aligned microcracks, as well as shear fabric, rock foliation, and layered bedding in sedimentary formations are the major causes of seismic velocity anisotropy in the Earth's crust. Microcracks and pore-spaces that exist in most rocks are often preferentially aligned by the stress-field acting on the rock mass. Such aligned microcracks caused by regional stress-induced deformation are widely observed in nature, for example in metamorphic complexes (Etheridge, 1983). Crustal anisotropy resulting from crack alignment has received particular attention, since it can be used to determine the state of stress in the crust (Crampin, 1981). Laboratory experiments and field observations indicate that most microfractures are extensional features oriented perpendicular to the direction of the current minimum compressional stress (e.g. Tapponnier and Brace, 1976; Kranz, 1983). Stress changes associated with earthquakes modify crack geometry and cause changes in shear wave splitting that can be used to predict earthquakes with the same signatures (Crampin, 1987). The stress- and pressure-dependence of macroscopic seismic properties of rocks is also of a great importance for oil recovery, geothermal energy, and the disposal of radioactive wastes.

Geochemical studies show that a large amount of fluids exist in crustal rocks (e.g. Fyfe *et al*., 1978) and greatly influence the macroscopic properties of rock masses. In crystalline rocks, fluids can exist in microinclusions (pores or partly healed microcracks). In the crust, the stress field and differential fluid pressure variations are necessarily dependent. The stress-induced variations of the internal crack geometry (due to opening, closure, subcritical and dynamic crack growth, and nucleations of cracks) promote changes in fluid pressure. The latter cause additional changes in macroscopic properties of fluid-saturated rock through their effects on both the elastic parameters and crack geometry. Furthermore, with changing pressure and temperature, pore fluids can change greatly their physical characteristics (density, conductivity, viscosity, acoustic velocities) which may result in a drastic change in the overall physical parameters of rock (Artemieva, 1996).

Pores and fluid-filled microcracks are essential only in the sedimentary and upper crustal rocks. It is widely accepted that fluid-filled cracks cannot exist deeper than 3 km because the confining pressure required to close elliptical cracks is proportional to the aspect ratio of the cracks and Young's modulus of the saturating fluid (e.g. Doyen, 1987). This means that for realistic values of crack aspect ratio and physical parameters of fluids, all cracks are expected to be closed at pressures ranging between 30–100 MPa. This conclusion is in agreement with *in situ* observations from the Kola Superdeep borehole which indicate that, due to the closure of microcracks under lithostatic pressure, their effect on seismic velocities becomes insignificant below *c*. 5 km depth (Kola Superdeep, 1984). In contrast, seismic studies suggest that fluid-filled microcracks are likely to exist in the continental crust down to a 10 to 20 km depth (Crampin, 1987). The existence of partially open cracks at these depths can be due to high pore pressures (Christensen, 1989) that can be produced by tectonic stress (subhorizontal tectonic compression, rapid tectonic loading due to sedimentation), chemical reactions (crack sealing by mineral deposition, metamorphic reactions involving pore-pressure buildup during dehydration), or phase changes in saturating fluid. According to numerical modeling of the closure of thermal microcracks (Zang, 1993), significant *in situ* porosity may be found at confining pressures up to 300 MPa (i.e. at a

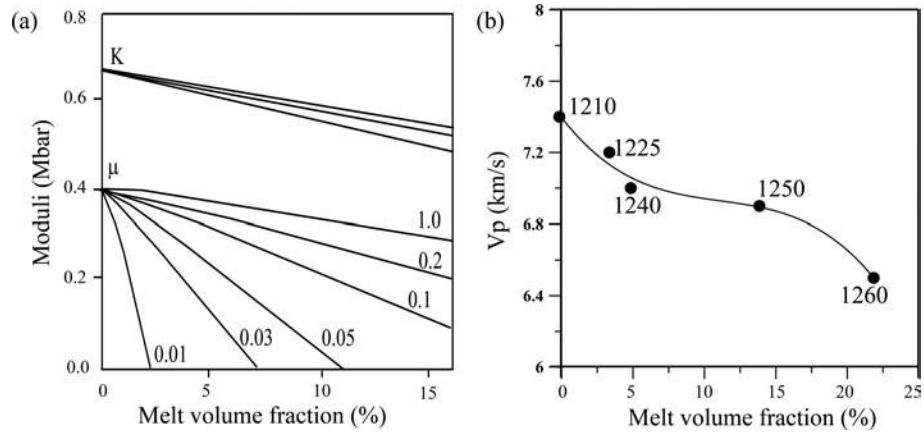

Fig. 3.13 (a) Elastic moduli for partially molten rock with ellipsoidal melt inclusions; numbers – aspect ratio of inclusions, i.e. the ratio of the short axis to the long axis (redrawn from Schmeling, 1985). (b) Changes in compressional velocity in spinel lherzolite (at 5 kbar) caused by changes in melt volume (based on laboratory data of Murase and Kushiro, 1979). Numbers – temperature in °C.

crustal depth of about 10 km), and the fraction of cracks that remain partially open under high pressures depends on the shape of the initial crack geometries that should be more realistic than elliptical.

Numerical modeling indicates that the amplitude of velocity reduction, as well as the amplitude of velocity anisotropy due to the presence of cracks in the upper crust or melt and fluid inclusions in the crustal and upper mantle rocks, depend critically on:

- the geometry of inclusions,
- the interconnectivity of the fluid phase (discussed in the next section).

For the same fluid (or melt) fraction, flattened elliptical inclusions with small aspect ratio (defined as the ratio between the short and the long axes) and thin films decrease shear modulus (and *Vs* seismic velocities) much more than inclusions with a more spherical geometry (Fig. 3.13a). Technical details on macroscopic elastic properties of cracked rocks can be found in numerous publications (e.g. Budiansky, 1965; Budiansky and O'Connell, 1976; Mavko, 1980; Schmeling, 1985a).

LPO anisotropy

The alignment of highly anisotropic olivine crystals (Fig. 3.14) by mantle flow and the associated deformation is believed to be the major cause of seismic anisotropy in the upper mantle (Babuska, 1984; Karato, 1992; Barruol and Kern, 1996; Ben Ismail and Mainprice, 1998). Two major deformation mechanisms play important roles under upper mantle conditions.

- *Dislocation creep* is caused by movement of crystalline dislocations within grains. It occurs at high stress, at large grain size, or at both, and leads to preferred orientation of

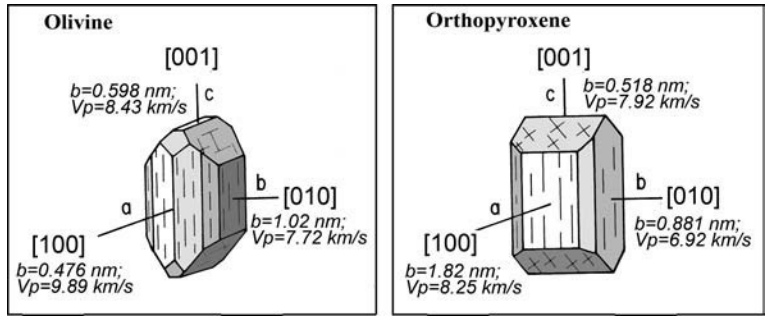

Fig. 3.14 Anisotropy of olivine and orthopyroxene crystals (based on Nicolas and Christensen, 1987). The length of the Burgers vector (b) and compressional wave velocity (V_p) are given for each slip direction. The favored slip direction is the one with the shortest Burgers vector.

minerals and to anisotropy. Additionally, dislocation-accommodated grain boundary sliding can play an important role in deformation, in particular of fine-grained samples (Hirth and Kohlstedt, 2003; Drury, 2005; Warren and Hirth, 2006).

- *Diffusion creep* is caused by solid-state diffusion between grain boundaries or across a crystal lattice, and occurs at relatively low stress, at small grain size, or at both. It does not lead to preferred orientation of minerals. It is commonly accepted that diffusion creep dominates in the upper mantle below a 250 km depth.

LPO (lattice preferred orientation) can develop not only by deformation due to dislocation slip, but by recrystallization as well. However, the former mechanism is dominant. Deformation by dislocation slip is simple shear and it is defined by the slip direction and the slip plane. The following notation (a three-value Miller index notation) is used in crystallography:

- planes are denoted by three indices in round brackets and each index denotes a plane orthogonal to a direction in the lattice; for example (100) refers to a plane normal to the *a*-direction; curly brackets like {100} denote the set of all planes that are equivalent by symmetry of the lattice (as in a cubic crystal);
- rectangular brackets denote directions in a crystal and the numbers are the smallest integers that correspond to the direction cosines; for example [100] is the direction parallel to the *a*-direction; triangular brackets as in <100> are used for equivalent directions.

The slip direction is characterized by the Burgers vector which specifies the magnitude and the direction of the lattice distortion in dislocations in a crystal lattice. The slip direction with the shortest Burgers vector is favored because of the lower strain energy associated with formation or motion of lattice dislocations. It is commonly assumed that olivine deformation is characterized by a single slip. Since Burgers vector along [100] is the smallest, the [100] slip is expected to dominate in olivine. However, the difference in the lengths of [100] and [001] vectors is small (Fig. 3.14) and under favorable physical/chemical conditions the dominant slip direction can change (Karato *et al.*, 2008). A significant LPO in olivine may develop in ~30 Ma at a typical geological strain rate of 10^{-15}/s (this value of strain rate corresponds to stress $\sigma = 10$ MPa and mantle viscosity $\eta = 10^{22}$ Pa s, eq. 8.11).

Experimental studies on the relationship between LPO and deformation in different minerals, including olivine, began in the 1970s (Carter and AveLallemant, 1970, Nicolas *et al*., 1973). Until the last decade, all interpretations of seismic anisotropy had been based on these and similar laboratory results, many performed at upper mantle P–T conditions (e.g. Karato and Rubie, 1997; Cordier and Rubie, 2001). Studies of mantle xenoliths from kimberlites and Alpine massifs, as well as mantle rocks from ophiolites and oceanic islands demonstrate that the *a*-axis in olivine commonly orients parallel to the macroscopic flow direction, and the [100] slip has greatest influence on the seismic properties. Mainprice and Silver (1993) estimated that an upper mantle with 50% and 100% of olivine content can produce maximum anisotropies of 6% and 13.9% for P-waves and 7.1% and 9.5% for S-waves, respectively. These values are greater than the S-wave anisotropy of 3–7% reported for most types of mantle-derived xenoliths. However, mantle rocks such as peridotites are polymineralic, and deformation mechanisms can vary for different minerals. In particular, olivine and orthopyroxene have different slip systems (Fig. 3.14b), different elastic properties, and different strengths.

Laboratory measurements on mantle xenoliths demonstrate that at pressures up to 600 MPa and at temperatures up to *c*. 600 °C shear-wave anisotropy remains approximately the same, while higher pressures and temperatures affect anisotropy (Kern, 1993). A temperature of *c*. 900 °C is critical: it is difficult to reorient deformed olivine crystals below this temperature (Goetze and Kohlstedt, 1973). As a result, rocks deformed in a high temperature environment and then cooled below 900 °C will preserve a "frozen-in" anisotropy. Partial melts may cause grain size increase and thus increase anisotropy or extend the depth interval with dislocation creep (Nicolas, 1992).

To sum up, *the conventional point of view*, based on laboratory studies of deformation in olivine aggregates at upper mantle P–T conditions, is that:

- deformation of olivine in the upper mantle down to *c*. 250 km depth occurs essentially by dislocation creep;
- the dominant slip is [100];
- below a 250 km depth, diffusion creep becomes the dominant deformation mechanism, leading to a rapid decrease in anisotropy in the upper mantle.

Recent (post-2000) experimental studies of olivine deformation challenge this commonly accepted point of view, whereas the physical grounds for questioning the paradigm are based on the fact that several different LPOs can develop in olivine (reviewed by Katayama *et al*., 2004; Mizukami *et al*., 2004; Karato *et al*., 2008). Different LPOs are produced by different kinematic processes, each with its own rate, and the physico-chemical conditions of deformation determine these rates and the type of LPO that is formed in different tectonic settings (Fig. 3.15c). In particular, olivine fabrics are sensitive not only to stress and temperature, but also to water content (Katayama *et al*., 2004; Jung *et al*., 2006). Under saturated conditions mantle olivine can undergo water-induced fabric transitions, when the orientation of the *a*-axis may become perpendicular to the mantle flow (Jung and Karato, 2001; Mizukami *et al*., 2004). The results of some recent high-pressure, high-temperature simple-shear laboratory experiments on olivine aggregates indicate the following.

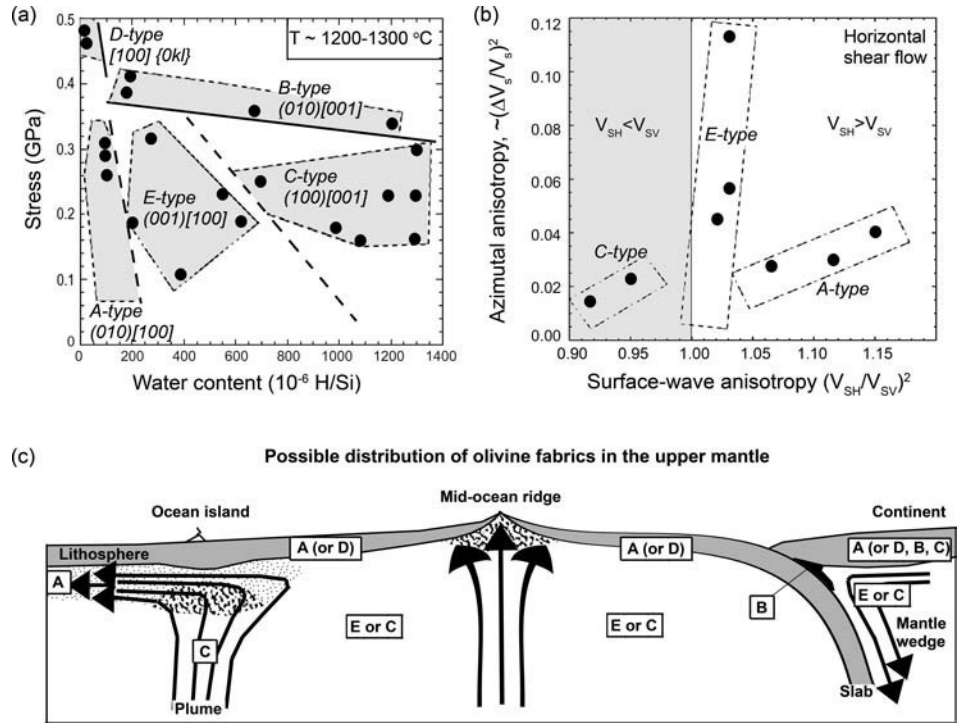

Fig. 3.15 (a) Deformation fabrics of olivine measured at high temperatures as a function of water content and stress. (b) The relation between the amplitudes of azimuthal and polarization anisotropy caused by horizontal shear flow for various types of olivine LPO. Symbols – laboratory data. (c) Diagram illustrating possible distribution of olivine fabrics (letters in boxes) in the upper mantle. (a – based on Katayama *et al*. 2004; b, c – based on Karato *et al*. 2008).

1) The olivine LPO at low pressure and high pressure is different, and the LPO may change with the pressure (depth) change (Couvy *et al*., 2004). The exact values of stress at which different types of olivine fabric are formed are unknown because measurements were taken in stress–relaxation tests (Karato *et al*., 2008). Similar conclusions were drawn by Mainprice *et al*. (2005) based on simple-shear laboratory experiments on olivine aggregates. They found that dislocation creep remains the dominant deformation mechanism at P–T conditions corresponding to *c*. 300 km depth, but with dominant activation of the [001] slip direction. These results were reported even for fine-grained, ~20–30 μm aggregates. A significant amount of water was detected in olivine samples in the experiments of both groups. Karato *et al*. (2008) classifies this as C-type olivine fabrics.
2) In the case of partial melting the olivine LPO is different from that in melt-free olivine (Holtzman *et al*., 2003). Deformation experiments on olivine + basaltic melt at $P = 0.3$ GPa and $T = 1250$ °C indicate that olivine fabric is the same as in a melt-free olivine (A-type fabric) when a small amount of water is present. Reduction of melt permeability leads to its localization in narrow bands, and olivine deformation localizes in the melt-rich bands so that its [100] axes orient normal to the macroscopic flow direction and [001] axes align along the shear direction (a fabric similar to the olivine B-type fabric).

These results have important implications for interpretations of seismic anisotropy. The vast majority of existing interpretations are based on the widely accepted notion that the A-type olivine fabric dominates in the upper mantle, so that the olivine [100] axes are oriented nearly parallel to the mantle flow direction, and the olivine (010) planes are nearly parallel to the flow plane. This results in anisotropic propagation of surface waves so that the direction of polarization of the faster shear wave tends to become parallel to the flow direction. In the case of horizontal mantle flow, the velocity of the horizontally polarized wave V_{SH} (see Fig. 3.28) is greater than the velocity of the vertically polarized wave V_{SV}, $V_{SH}/V_{SV} > 1$, while in the case of vertical mantle flow, $V_{SH}/V_{SV} < 1$. The A-fabric is expected to dominate under lithospheric conditions which are characterized by low water content and moderate stress and temperature (Karato *et al*., 2008). However, in case other olivine LPO fabrics can be formed under specific physico-chemical conditions, interpretations of seismic anisotropy can differ from the conventional. In particular, in the case of horizontal mantle flow, non-conventional $V_{SH}/V_{SV} < 1$ can be expected for C-type olivine fabrics (Fig. 3.15b).

Orthopyroxene which makes 20–30% of the upper mantle is also anisotropic (Fig. 3.14) and can also form LPO and contribute to seismic anisotropy (Skemer *et al*., 2006). The number of experimental studies of orthopyroxene deformation is limited. Because the length of the [001] Burgers vector in orthopyroxene is much shorter than those of other vectors, deformation occurs on the [001] slip system (Mercier, 1985). However, the contribution of orthopyroxene to seismic anisotropy is thought to be small compared to olivine (Christensen and Lundquist, 1982).

3.1.6 Melt and fluid inclusions

The amount of water stored in the mantle is assumed to be small; there is, however, a significant variation in the reported values (see discussion in Section 8.1.3). Bulk water content in the upper mantle is estimated to be *c*. 5–35 ppm in the oceanic lithosphere, 100–200 ppm in the MORB (mid-ocean ridge basalts) source, 200–500 ppm in the OIB (oceanic island basalts) source, and <200 ppm in the lower part of the upper mantle (Fig. 7.19). The continental lithospheric mantle of the Archean cratons, by comparison with "wet" oceanic lithosphere, is believed to be particularly "dry" (e.g. Hirth *et al*., 2000). However, a significant amount of water can be stored in the mantle in such "anhydrous" minerals as olivine, pyroxenes, and garnets (e.g. Bell and Rossman, 1992). The presence of even a small amount of water or fluid in crustal and mantle rocks significantly reduces seismic velocities: for example, a 0.3% increase in H_2O content causes a 1% decrease in P-wave velocity in partially serpentinized ultramafic rocks.

Another important aspect of the presence of fluids in the upper mantle is their effect on melting temperature of mantle peridotite (Thompson, 1992; Wyllie, 1995). In particular, the solidus of "wet" peridotite is significantly lowered at depths below *c*. 80 km (Fig. 3.16). This implies that at high temperatures, the presence of even small volumes of volatiles (water and carbon dioxide) in the upper mantle indirectly reduces seismic velocities by lowering mantle melting temperature.

Experimental studies of the properties of partially molten rocks demonstrate the strong role of the 3D geometry of a melt network and its interconnectivity on the seismic properties

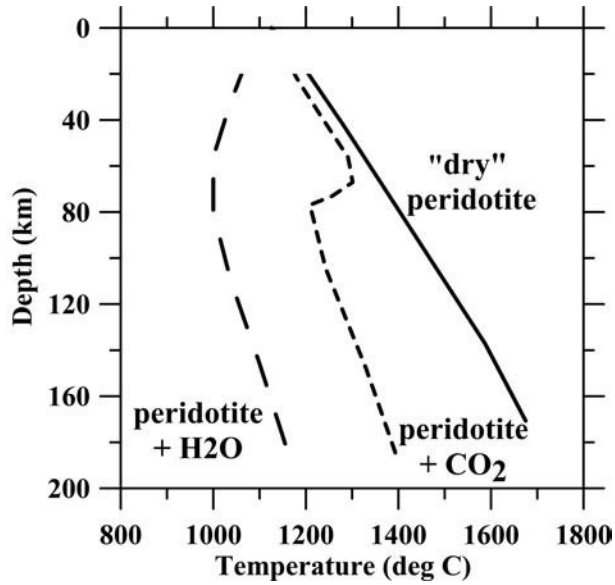

Fig. 3.16 P–T phase diagram for mantle peridotite with a major element composition similar to primitive mantle. Solid line – melting of a natural dry peridotite (Takahashi, 1986; Hirschmann, 2000). Dashed lines – melting of peridotite saturated with H_2O and CO_2 ($CO_2/(CO_2+H_2O)$) = 0.8 (compilation by Wyllie, 1995).

of crustal and mantle rocks. The interconnectivity of melt depends on the wetting (dihedral) angle between the solid and liquid phases (Fig. 7.15). Basaltic melt in the mantle (olivine-dominated) matrix is expected to have a wetting angle of 30–50° and to form a network of tubes along the grain boundaries (Fig. 7.14b). With such a geometry of melt distribution, partial melting should have a strong effect on the elastic properties of rocks; however the effect is significantly smaller than in the case of complete wetting which occurs when $\Theta = 0°$ (Stocker and Gordon, 1975). Recent results demonstrate that very small, unconnected grain boundary melt fractions can produce a significant shear wave velocity decrease such as observed in the LVZ (Faul and Jackson, 2007). Similarly, the presence of even a small amount of melt or fluids has a dramatic effect on seismic attenuation. However, the effect of melt or fluid inclusions on compressional wave velocities is small (Muellar and Massonne, 2001). In the case $\Theta > 60°$ (which may be typical of, at least, some upper mantle rocks), melt forms isolated pockets and its effect on the macroscopic rock properties depends on pocket geometry.

Up-to-date microstructural and experimental studies of melt distribution in mantle rocks, however, remain inconsistent. The reported grain-scale melt distributions include the following microstructures:

- melt concentration at two-grain boundaries at melt fractions above 0.05 (Hirth and Kohlstedt, 1995);
- melt concentration in a network of triple junction tubes with almost no melt along grain boundaries (for melt fraction *c*. 0.01) (Wark *et al*., 2003);

- domination of disc shaped inclusions or melt layers on two-grain boundaries with some melt distributed in a network of tubes along triple junctions (for melt fraction *c*. 0.1) (Faul, 19971; ten Grotenhuis *et al*., 2005);
- presence of transient melt features, corresponding to metastable structures in melt distribution, such as multigrain melt pools and melt lenses along grain boundaries (Walte *et al*., 2003).

An increase in melt content apparently changes the geometry of a melt network which has a dramatic effect on seismic velocities (e.g. Fig. 3.13) (Anderson and Sammis, 1970; Shankland *et al*., 1981). Based on this observation, seismic and electrical asthenospheres can be explained by the presence of partial melt in the mantle: while the observed anomaly in electrical conductivity requires the presence of several per cent of melt, the seismic velocity anomaly can be explained by a melt fraction of 0.1% in the case of very flattened melt inclusions (aspect ratio of 0.001) (Shankland *et al*., 1981). Such interpretations have recently been challenged by Karato and Jung (1998), who argue that

> the common belief that the seismic low velocity and high attenuation zone (the asthenosphere) is caused by the presence of a small amount of melt is not supported by recent mineral physics and seismological observations.

According to these authors, since water reduces seismic wave velocities, low percentage partial melting of the Earth's upper mantle will increase (not decrease, as common experience suggests) seismic wave velocities due to the removal of water from mantle olivine.

Figure 3.17 summarizes the effects of different parameters on variations of seismic velocities and attenuation.

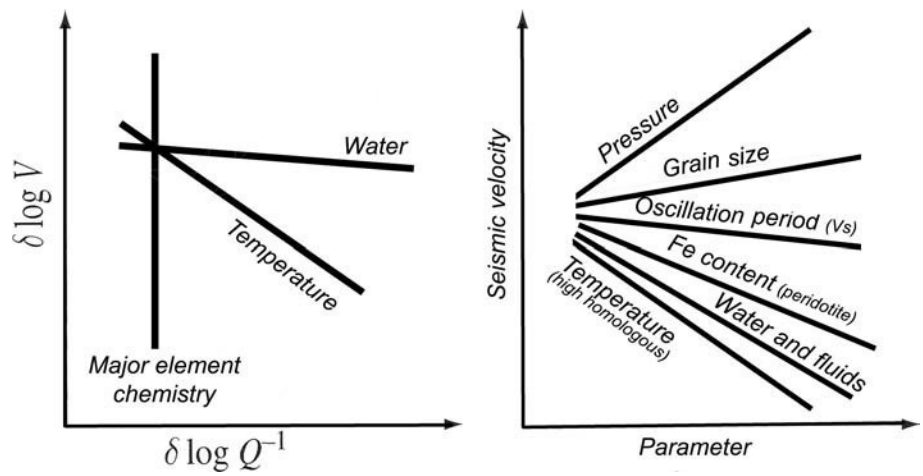

Fig. 3.17 Left: Relationship between attenuation and seismic velocity anomalies showing schematically the effects of water, temperature, and composition (redrawn from Karato, 2008; based on results of Shito and Shibutani, 2003). Right: Schematic diagram showing the effect of different parameters on seismic velocities.

3.1.7 Melt-depletion and mantle composition

Partial melting of the upper mantle and melt extraction cause its chemical differentiation with variations in major element chemistry that can be detected by seismological observations. Recent laboratory measurements combined with theoretical calculations for chemical and mineralogical compositions of natural peridotites indicate first-order differences between the composition of oceanic and continental lithospheric mantle (referred to as the oceanic and the continental trends). A detailed discussion of these differences is presented in Sections 6.1.2–6.1.4, while this section contains only general information useful in the interpretation of seismic velocity variations.

Oceanic melting trend

In the oceanic mantle, melting of mantle pyrolitic lherzolite produces the residual mantle rocks, such as lherzolite and harzburgite from mid-ocean ridges, that are formed after partial melts are derived from the uppermost mantle. The residue is depleted in (i.e. has a reduced concentration of) incompatible elements, such as SiO_2, Al_2O_3, CaO, with respect to compatible elements, such as MgO and Cr_2O_3. Atomic ratios Mg# = 100Mg/(Mg + Fe) of bulk rock and Cr# = 100 Cr/(Cr + Al) of spinel (since melting commonly occurs within the spinel stability field at P <2.5 GPa) are indicators of the degree of mantle melt-depletion: both Mg# and Cr# increase with an increase in the degree of partial melting and melt extraction (Fig. 3.18). With increasing degree of partial melting, the olivine [$(Fe_xMg_{1-x})_2SiO_4$] content increases from ~55 to ~85 vol%, while the composition of the residue changes from lherzolite towards harzburgite. Oceanic mantle may have little variation in Mg# with depth (Fig. 3.19), at least in part due to homogenizing effect of the convective mixing in the sublithospheric mantle.

Major characteristics of the oceanic trend are as follows (Matsukage *et al*., 2005).

- Compositional variations in peridotites are caused by one single melting event and a high Mg# corresponds to a low silica content.
- With Mg# increase, compressional and shear seismic velocities increase almost linearly, while density decreases.
- For P-wave velocity, the correlation of Vp with olivine content is significantly better than with Mg# (Fig. 3.20). However, the two parameters are not independent during partial melting in the shallow mantle, and seismic velocities in shallow oceanic peridotites are characterized by a single parameter such as Mg#.

Continental melting trend

In the subcontinental lithospheric mantle, melting may occur within both spinel and garnet stability fields. If melting occurs within the spinel stability field (as observed in many tectonically young provinces of the continents), chemical variations in spinel peridotites have trends similar to the oceanic settings. However, in cratonic settings, the composition of some

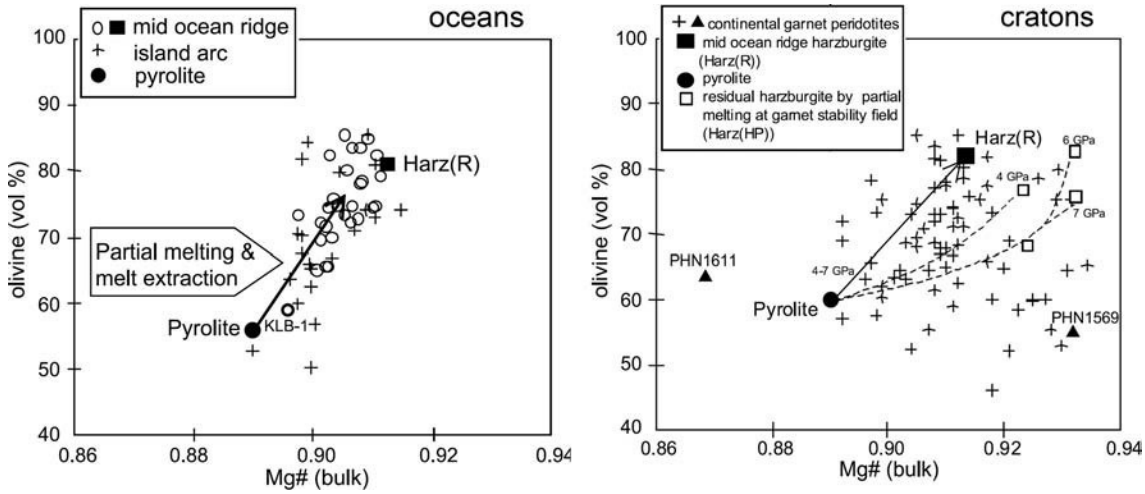

Fig. 3.18 Relationships between bulk Mg# = Mg/(Mg+Fe) atomic ratio and olivine content for mid-ocean ridge and island arc spinel peridotites (left) and for continental garnet peridotite xenoliths in kimberlite pipes (right) (from Matsukage *et al*., 2005). The solid squares (labeled Harz(R)) show one of the most depleted mid-ocean ridge (MOR) harzburgites. Thick vectors indicate the residual trend of partial melting and melt extraction at the spinel stability field (left) and to the garnet stability field for subducted MOR peridotites originally formed at the spinel stability field (right). Dashed lines (right) show the depletion trends of partial melting of mantle pyrolite and melt extraction at the garnet stability field at pressures of 4, 6, and 7 GPa. Two solid triangles (right) indicate seismological end-members of continental garnet peridotites (Jordan, 1979).

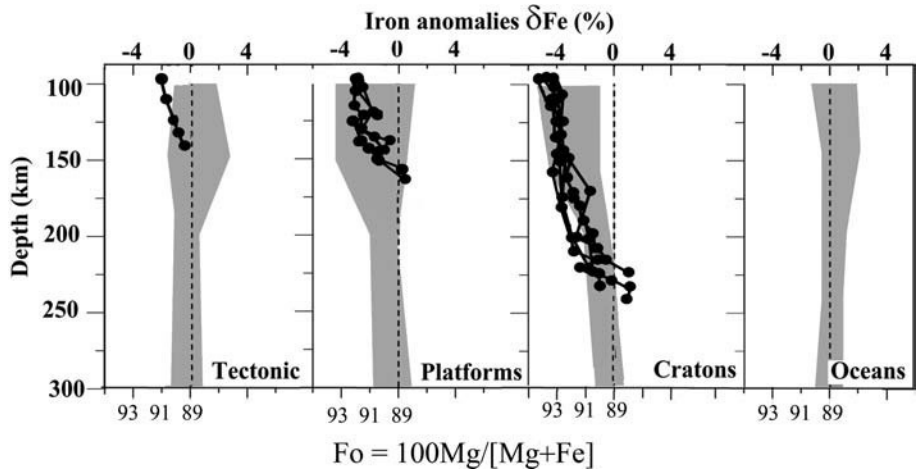

Fig. 3.19 Depth distribution of iron anomalies for several tectonic provinces delimited following the global tomography model 3SMAC (Nataf and Richard, 1996). Gray shading – iron anomalies calculated from a joint inversion of seismic tomographic model S16RLBM up to the spherical harmonic degree 16 (Woodhouse and Trampert, 1995) and the non-hydrostatic gravity anomalies derived from the geoid model EGM96 (Lemoine *et al*., 1998). (Source: Deschamps *et al*., 2002). Zero iron-anomaly corresponds to convective mantle with Fo = 89. Black lines – iron anomalies constrained by mantle peridotites (for details see Fig. 6.15).

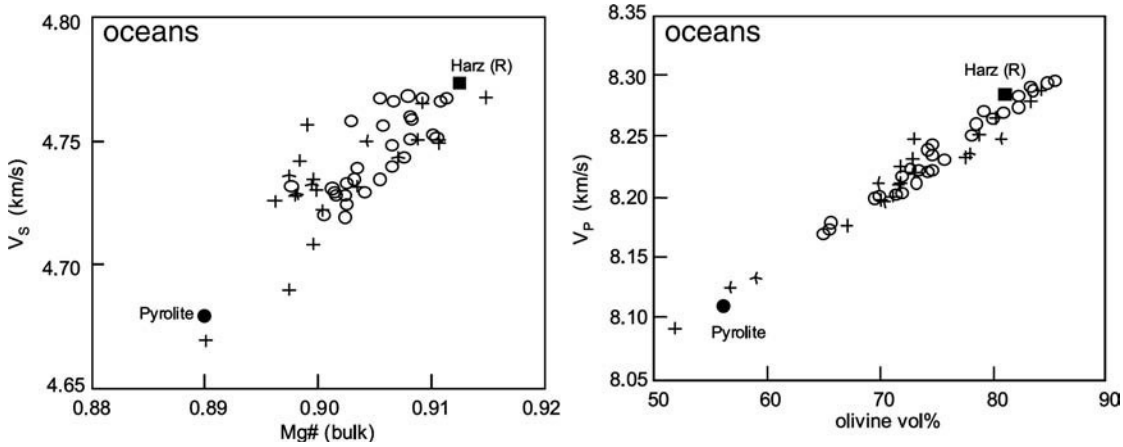

Fig. 3.20 Seismic velocities in mid-ocean ridge and island arc spinel peridotites at 1 GPa pressure as a function of bulk Mg/(Mg+Fe) atomic ratio and modal composition of olivine (from Matsukage *et al.*, 2005).

continental peridotites in the garnet stability field with very high bulk Mg# and high silica content cannot be explained by the partial melting of pyrolitic rocks alone and requires the presence (addition) of some orthopyroxene (Boyd, 1989; Walter, 1999). One proposed mechanism includes a two-stage process in which orthopyroxene can be formed at the expense of olivine by modal metasomatism in a reaction between melt-depleted peridotite and a silicic melt (Kelemen *et al.*, 1998). In the first stage, high Mg#, low modal orthopyroxene peridotites are created by large degrees of polybaric melting (at $P < 30$ kbar). At the second stage, interaction of these depleted residues with SiO_2-rich melts (generated mainly by partial melting of eclogitic basalt and sediment in a subduction zone) enriches them in orthopyroxene. As a result, the depletion trends for continental garnet peridotites differ significantly from the oceanic depletion trends produced by partial melting of pyrolite. In particular, no clear correlation between olivine fraction and Mg# exists for continental garnet peridotites (Fig. 3.18b).

Theoretical calculations of seismic velocities for natural peridotites and mineral assemblages typical of the continental lithospheric mantle indicate that shear-velocity is linearly correlated with Mg# and increases with iron-depletion (Fig. 3.21a; Fig. 6.12 and Section 6.1.4). This implies that, at the same temperatures, *V*s in the cratonic lithospheric mantle is faster down to *c*. 250–300 km depth than in lithospheric mantle of young continental and oceanic regions (Fig. 3.19). Unexpectedly, and in contrast to other continental locations, data for the Slave craton have been interpreted as showing no visible *V*s–Mg# correlation (Kopylova *et al.*, 2004). This conclusion is apparently biased by a very limited data set, since the Slave data clearly overlap with peridotite data from other locations (Fig. 3.21c). However, it cannot be excluded that the Slave trend is the true one due to a unique composition of its lithospheric mantle, while combining a large number of peridotite samples from diverse locations worldwide with a heterogeneous mantle composition (such as the dataset of Lee, 2003) obscures regional trends, which might also be present in datasets from individual cratons. This hypothesis is indirectly supported by the *V*p–Mg# trends for the Slave samples that are not evident in data from other continental locations (Fig. 3.21d).

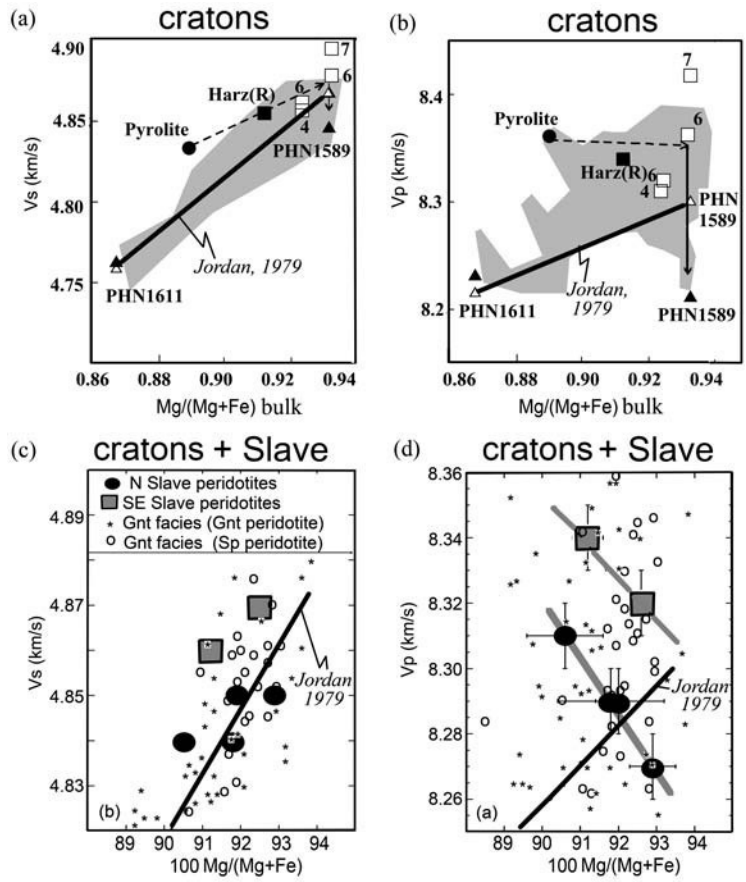

Fig. 3.21 Shear (a, c) and compressional (b, d) wave velocities in continental peridotites in garnet facies as a function of iron-depletion (expressed by Mg#). (a, b): Solid lines and open triangles – velocities calculated for two seismological end-members of garnet peridotites PHN1611 and PHN1589 (Jordan, 1979). Solid triangles – velocities calculated for residual harzburgites in garnet stability field at 1 atm and 300 K. Open squares and dashed arrows show the trends of the residue of partial melting at 4, 6, and 7 GPa. Thin arrows – the trends of orthopyroxene addition with constant bulk Mg# (Source: Matsukage *et al*., 2005). (c, d): Comparison of velocities calculated for 133 natural peridotites from several continental locations (Lee, 2003) (shown by gray shading in (a, b) and small symbols in (c, d)) with velocities calculated for peridotites from the Slave craton at ambient conditions (large symbols) (Kopylova *et al*., 2004). Gray lines – best fits for the Slave data; black lines as in (a, b). Gnt = garnet, Sp = spinel. Note different scales at (a, b) and (c, d).

For compressional wave velocity, the general *V*p–Mg# trend has the same sign as the *V*s–Mg# trend, but the correlation is poor due to a large scatter in values (Fig. 3.21b,d), and *V*p velocity correlates better with olivine content (Fig. 3.20b). As a result of the strong *V*s–Mg# and poor *V*p–Mg# correlation, the *Vp/Vs* ratio exhibits a strong negative correlation with Mg# (Fig. 3.22).

Data for the Slave craton apparently display a clear trend of *V*p decrease with an increase in iron-depletion, probably due to orthopyroxene enrichment (Kopylova *et al*., 2004) given

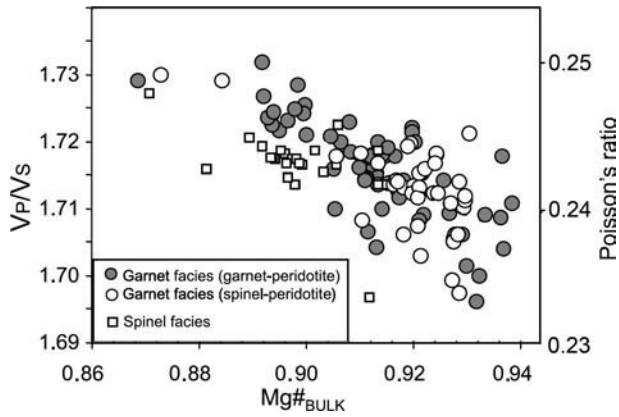

Fig. 3.22 The ratio *V*p/*V*s at room pressure–temperature conditions versus Mg# in mantle peridotites (based on Lee, 2003).

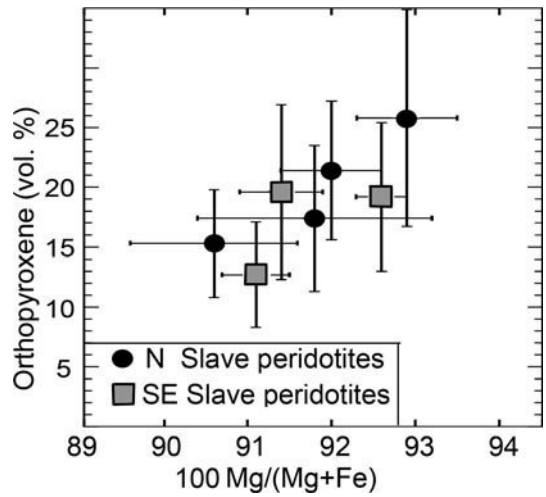

Fig. 3.23 Orthopyroxene enrichment in the Slave peridotites accompanies an increase in 100 Mg/(Mg+Fe) (based on Kopylova *et al.*, 2004). The plot shows data averaged by rock type for 40 individual samples.

that orthopyroxene content in peridotites from the Slave mantle correlates with iron-depletion (Fig. 3.23), while orthopyroxene addition at constant bulk Mg# significantly reduces *V*p wave speed (Fig. 3.21b). Note, however, that as for shear-velocity data, the strong negative *V*p–Mg# correlation reported for the Slave cratonic mantle may be an artifact of a small data set (40 individual samples).

In summary, the continental trend has the following characteristics (Matsukage *et al.*, 2005):

- The chemical composition of continental peridotites is controlled by at least two processes: partial melting and the addition of Si-rich materials (Matsukage *et al.*, 2005). Both of these processes change Mg# and Opx#, but in different ways. For this reason, seismic

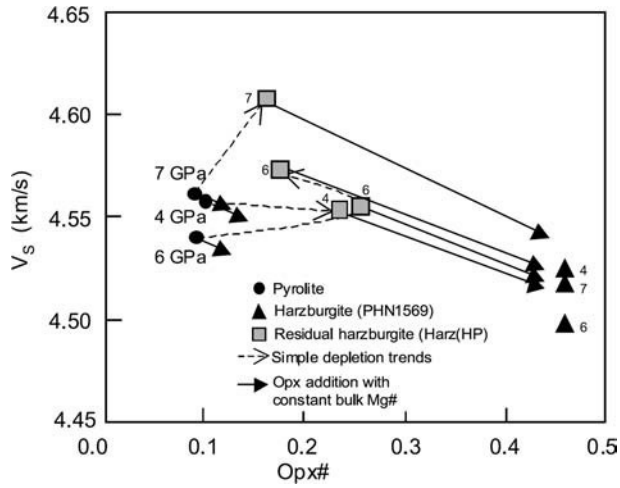

Fig. 3.24 Relationship between *Vs* seismic velocity and modal composition of orthopyroxene in pyrolite, in residual harzburgites in garnet stability field (Harz(HP)), and in continental garnet harzburgite with high orthopyroxene content (PHN1569) at pressures between 4 and 7 GPa. The dashed arrows show the trends of the residue of partial melting at 4, 6, and 7 GPa. The solid arrows show the trends of orthopyroxene addition with constant bulk Mg# (from Matsukage *et al*., 2005).

velocities in deep continental peridotites are characterized by two parameters, Mg# and Opx# (volume fraction of orthopyroxene). The values of Mg# and Opx# in the continental mantle range from 0.89 to 0.94 and from 0.06 to 0.45, respectively.

- Seismic velocities in the garnet stability field (>70 km depth) increase with iron-depletion (i.e. with increasing Mg#) but decrease with increasing orthopyroxene content (Fig. 3.24). For the same Mg#, an increase in Opx# by 0.1 causes *c*. 0.5% decrease in *V*s. A similar decrease in *V*s can be produced by a decrease in Mg# by 0.01.
- In shallow upper mantle (70 to 190 km depth, or at pressures between 3 and 6 GPa) the effect of Mg# variations (due to depletion caused by partial melting and melt extraction) can be relatively small, so that variations in orthopyroxene content can become the major cause of velocity differences between pyrolite and continental harzburgite (Fig. 3.21) and may produce maximum $\delta \ln V$s and $\delta \ln V$p of –1.8% and –2.3% respectively (Matsukage *et al*., 2005).
- Below a 190 km depth, the effect of iron-depletion on seismic velocities becomes particularly important and may produce maximum $\delta \ln V$s and $\delta \ln V$p of +1.1% and +1.0% respectively. Since seismic velocities in orthopyroxene increase rapidly with increasing pressure, the effects of iron-depletion and orthopyroxene-addition on seismic velocities can compensate each other with increasing depth.

3.1.8 Density–velocity relationship

In the strict sense, density is not a seismic parameter, but density and elastic moduli define seismic velocities (eq. 3.1). Birch's law (Birch, 1961) suggests a unique relationship

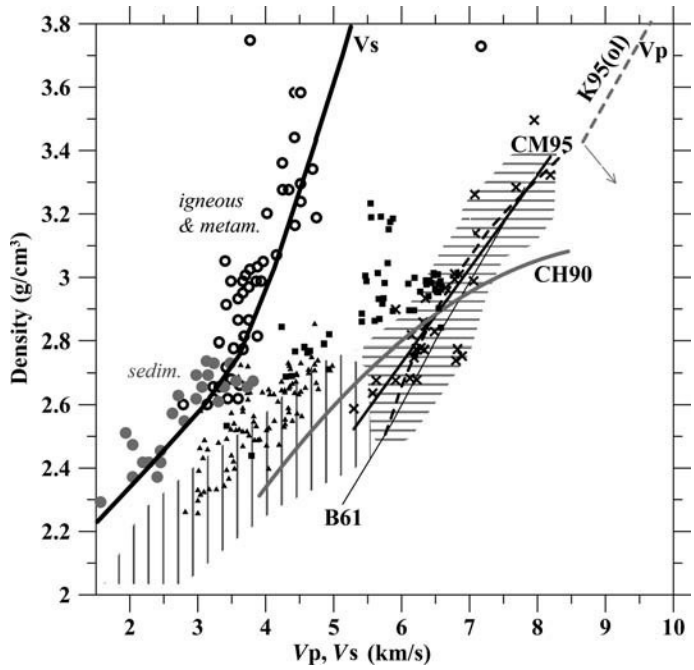

Fig. 3.25 Compressional and shear-wave velocity–density relationships for crustal and upper mantle rocks. *Vs* data: open black circles – data for igneous and metamorphic rocks; gray circles – data for sedimentary rocks. *Vp* data: thin black line (labeled B61) – Birch's relationship (Eq. 3.12) (after Birch, 1961). Hatching – laboratory measurements of P-wave velocity and density in sedimentary (vertical stripping) and metamorphic and igneous rocks (horizontal stripping) typical for the oceanic crust and upper mantle (after Ludwig *et al.*, 1970). Thick gray line (labeled CH90) – V_p–density relationship commonly used for the oceanic crust (after Carlson and Herrick, 1990). Data from the Mid-Atlantic Ridge: serpentinites (triangles) and gabbros (squares) (after Kelemen *et al.*, 2004). Crosses – experimental data (measured at pressure corresponding to a depth of 20 km and temperature of 309 °C) on average velocity versus average density for different rock types typical of the continental crust and mantle. Thick black line and dashed black line (both labeled CM95) – best linear fit to all data shown by crosses and best non-linear fit for mantle rocks only, respectively (after Christensen and Mooney, 1995). Gray dashed line labeled K95(ol) – calculated relationship for forsterite (mantle olivine) (after Karki *et al.*, 1995); thin arrow indicates the trend in velocity and density change in highly depleted cratonic mantle.

between compressional velocity V_p and density ρ for materials (isotropic polycrystals) with the same mean atomic weight M:

$$V_p = c_1(M) + c_2\rho. \tag{3.12}$$

According to Birch, this relationship should be valid for velocity and density changes of any origin (i.e. caused by variations in temperature, pressure, or composition). Theoretical calculations indicate that although Birch's law provides a good approximation, it is not always valid: the violation is strongest for silicates and oxides, and several mantle minerals show a non-linear dependence of velocity on density (Karki *et al.*, 1995).

Despite these limitations, empirical relationships between compressional wave velocity V_p and density ρ, based on laboratory measurements and theoretical analyses, have been widely applied in seismology for more than 50 years (Nafe and Drake, 1957; Gardner *et al*., 1974; Anderson and Bass, 1984). Correlation between compressional velocity and density is, in particular, important because it allows for gravity modeling constrained by seismic refraction data. However, even for rocks of similar composition, a wide range of densities (commonly with a scatter of up to 500 kg/cm^3 for crustal rocks) is possible for the same compressional wave velocities (Fig. 3.25). As a result of this scatter, any conversion of seismic velocities into densities, such as widely applied in gravity modeling, inevitably results in a significant uncertainty in gravity calculations, a fact almost never analyzed in the corresponding studies (an analysis of the problem can be found in Barton, 1986). In the worst case scenario, variations in observed gravity anomalies can be smaller than the uncertainty associated with the permissible range of densities as constrained by seismic data (Fig. 3.26), making gravity results meaningless.

Comparison of observed density-to-velocity heterogeneity ratios (i.e. the ratios of relative density variations to relative velocity variations):

$$R_{\rho/p} = \partial \ln \rho / \partial \ln V_p; \quad R_{\rho/s} = \zeta = \partial \ln \rho / \partial \ln V_s \tag{3.13}$$

with mineral physics predictions and laboratory measurements allows for speculation on the origin (e.g. thermal versus compositional) of seismic wave velocities and density variations. For example, $\zeta > 0$ for purely thermal anomalies because both density and seismic velocity increase (decrease) with temperature increase (decrease). Negative or low values of ζ cannot be explained by temperature variations alone and require the presence of compositional variations, e.g. in iron content (Fig. 3.19; Fig. 3.109). For the upper mantle, experimentally determined values of ζ are based on density and velocity measurements in olivine, and thus they refer to pure thermal effects, since elastic properties of other upper mantle minerals are not well documented. For olivine, which is the dominant mineral in the mantle, $\zeta = 0.35 - 0.45$, depending on mantle temperature (Isaac *et al*., 1989). Anelasticity reduces ζ in the upper mantle to values between *c*. 0.1 and 0.2–0.3 (Karato, 1993), and in general agreement between ζ experimentally determined for olivine and ζ theoretically predicted for the upper mantle from geophysical data is poor (Deschamps *et al*., 2001). Since elastic moduli depend on pressure, the density-to-velocity heterogeneity ratio can also be pressure-dependent.

3.2 Summary of seismic methods

3.2.1 Types of seismic waves

The main wave types traveling in solids and employed in seismic studies of the lithosphere are body waves (compressional P-waves, and shear S-waves) that travel through the volume of a solid material, and surface waves (Rayleigh and Love waves) that travel along free surfaces (interfaces). Surface waves propagate more slowly than body waves: in general, the velocities of Love and Rayleigh waves are *c*. 0.9 and 0.7 of the shear-wave velocity,

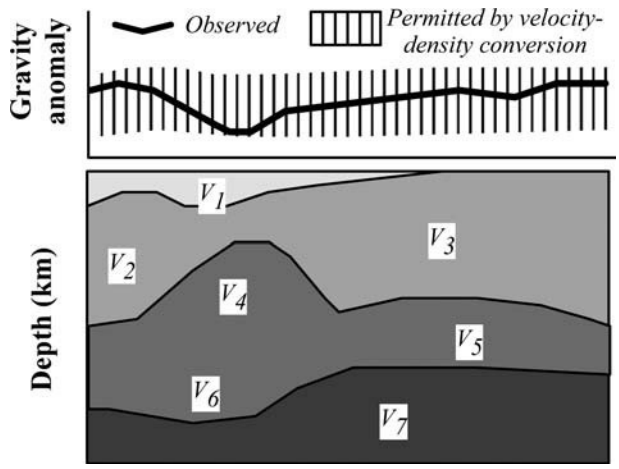

Fig. 3.26 Schematic illustration of the effect of a wide range of densities possible for rocks with the same seismic velocities on gravity modeling. In some cases, all variations of observed gravity anomalies along a seismic profile can be within the limits permitted by velocity–density conversion (calculated for the upper and lower bounds of permitted densities, Fig. 3.25). In such a case, a gravity model becomes meaningless.

respectively. However, the velocities of surface waves depend on the frequency of the propagating wave, and therefore on their depth of penetration (see below).

While Rayleigh waves exist near any free surface, Love waves require a velocity increase with depth. In Rayleigh waves particle motion is rotational (both horizontal and vertical components are present), while in Love waves particles have only transverse (horizontal) motion parallel to the surface but perpendicular to the direction of propagation (Fig. 3.27). Love waves propagate by multiple reflections as horizontally polarized S-waves in a lower-velocity near-surface layer (a waveguide), and are always dispersive (i.e. depend on wave frequency). Transverse waves are characterized by polarization, i.e. the orientation of the oscillations in the plane perpendicular to the direction of wave propagation. S-waves polarized in the horizontal plane are termed SH-waves and those polarized in the vertical plane are termed SV-waves (Fig. 3.28). In an anisotropic medium, transverse waves exhibit birefringence (shear-wave splitting).

3.2.2 Theoretical limits on seismic wave resolution

Seismic methods are classified into two broad categories: based on refracted (transmitted) and on reflected (scattered) waves. The former are used, for example, in seismic refraction profiling, travel time tomography, and surface wave dispersion analysis, while the latter are used in seismic reflection profiling. In practice, the resolution of seismic methods depends on data quality, which is commonly assumed to depend on the signal-to-noise ratio (i.e. the amplitude of the signal relative to noise). In general, it is accepted that the resolution increases when more seismic data are available.

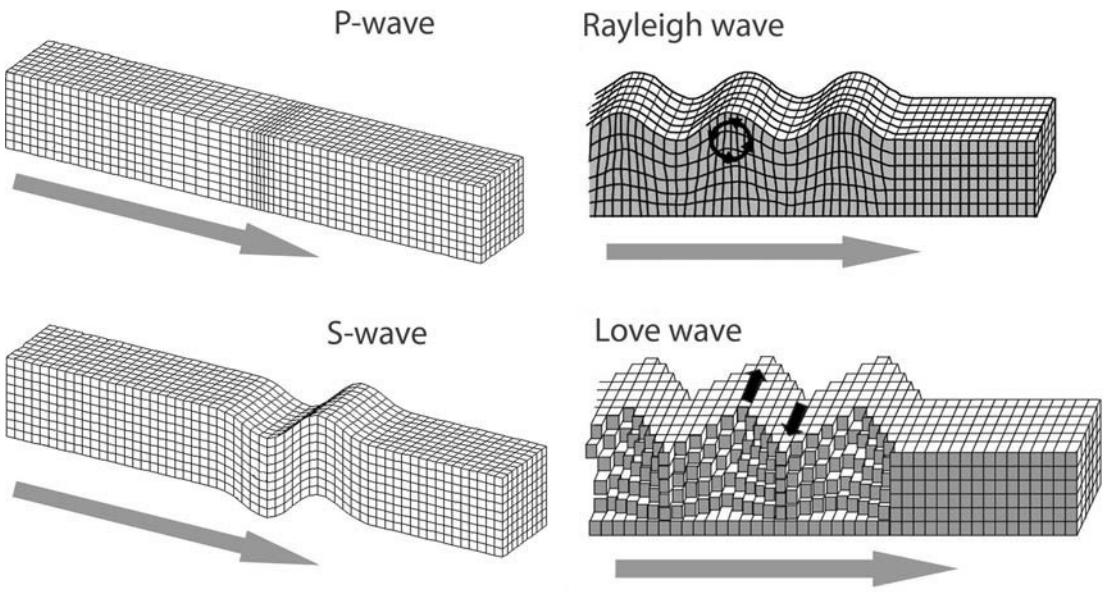

Fig. 3.27 Schematic illustration of types of seismic waves (after Bolt, 1976).

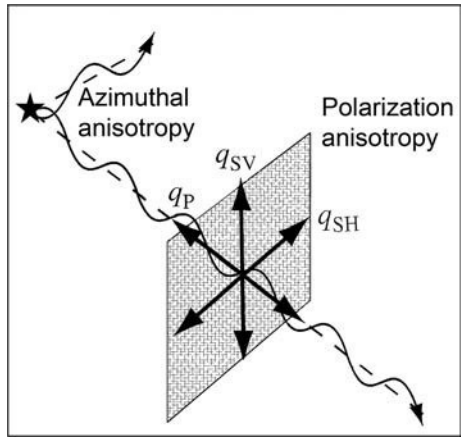

Fig. 3.28 Sketch illustrating two types of seismic anisotropy. Azimuthal anisotropy is the variation of seismic wave speed with the direction of wave propagation. Polarization anisotropy of surface waves is the variation of seismic wave speed with the orientation of oscillations in the plane perpendicular to the direction of wave propagation. A quasi-P wave (q_p) is polarized in the direction parallel to wave propagation, quasi-SH-waves are polarized horizontally, while quasi-SV-waves are polarized vertically. See also Fig. 3.112.

The theoretical limit on the resolution of seismic methods based on transmitted waves is determined by the Fresnel zone, which defines the volume in the radiation pattern along the raypath between the source and the receiver. Its diameter d is approximated as:

$$d = \sqrt{\lambda L/2} = \sqrt{VL/2f}, \tag{3.14}$$

where L is the total length of the path traveled by the wave, λ is the dominant wavelength, V is the velocity, and f is the dominant frequency (e.g. Bostock, 1999). This means that small details in the lithospheric structure are best resolved by high frequency waves. For example, for crustal seismology with typical frequencies of 5–20 Hz the absolute accuracy of depth determination (by refracted Pn waves) is not better than *c.* 1–2 km for the Moho depth.

For reflected waves, the lateral resolution at the discontinuity depends on the size of the Fresnel zone for the incident wave, while scattered waves are sensitive mainly to the structures of length scale comparable to the wavelength of the incident wave. For example, in a medium with vertical velocity gradient, waves with near-vertical incidence will produce reflected waves that will sample the zone with a width less than $\lambda/4$ (Richards, 1972).

Surface waves, since they are confined to the surface, decay more slowly with distance than body waves, which travel in three dimensions. The amplitude of surface waves decays as $1/\sqrt{L}$, where L is the distance the wave propagated from the source (e.g. earthquake), and it decreases exponentially with the depth. Dispersion is an important property of surface waves: lower frequency waves propagate faster and arrive ahead of higher frequency waves due to their deeper penetration into the Earth (because wave speed generally increases with increasing depth). For dispersed waves, the group velocity (i.e. the velocity with which the energy is propagated) is different from the phase velocity (i.e. the velocity with which the troughs and peaks propagate at a given frequency along the surface). Long-period seismology is an important practical application of the fact that waves with lower frequencies (longer wavelengths) penetrate to a greater depth. Seismic instruments used in such studies operate in the frequency range 0.05 to 0.01 Hz (period 20–100 s) which in the upper mantle corresponds to $\lambda \sim 160$–800 km and 90–500 km, for P- and S-waves correspondingly.

3.2.3 Methods of seismic data interpretation

One-dimensional techniques

The following discussion concentrates primarily on the methods used for studies of seismic structure of the subcrustal lithosphere. One-dimensional (1D) techniques used in seismic data interpretation assume a laterally uniform velocity structure. They are easy in use, efficient and fast in calculation. They include forward travel time and amplitude modeling, the Herglotz–Wiechert–Bateman inversion, and the τ_p inversion. As a result of one-dimensional velocity inversion, a 1D "average" velocity model can be constrained for a region from all available seismic data. The major limitation of these methods is that they often do not detect low-velocity zones (LVZ); if such zones are present in the real Earth, layers below LVZ will appear to be at shallower depths.

Ray theory

Ray theory (analogous to optical ray theory) is the primary method for the calculation of travel times in a velocity model: at each point the slope of a travel time curve determines a seismic velocity. The major limitations of ray theory are:

- usually it fails in predicting non-geometrical effects such as diffraction;
- it is a high-frequency approximation of the solution to the wave equation, which may be invalid at low frequencies (i.e. long periods);
- it may be invalid in structures with steep velocity gradients, where triplications in the travel time curve occur (caustics). The latter problem can be avoided by analyzing the delay time (τ_p) curve instead of the travel time curve, since the delay time curve is free of triplications and is single-valued;
- it fails to determine the velocity structure within a low velocity zone in the lithosphere: the LVZ refracts (or bends) the rays, so that no rays turn within the LVZ and a shadow zone is produced on the travel time or delay time curves.

The Herglotz–Wiechert–Bateman inversion

The Herglotz–Wiechert–Bateman (HWB) inversion method, invented about a century ago, is based on the assumption that the travel time curves are continuous and allows for calculation of a 1D velocity–depth model from a travel time curve. This model can be further modified and adjusted by iterative forward modeling to improve the overall travel time fit. In practice, travel time observations are scattered, and the HWB method is often used to find the best-fit travel time curve for the data. Since at each point the slope of the travel time curve defines a seismic velocity, seismic data are commonly inverted for a layered model with a small number of homogeneous layers. If only the first-arrival times are used, the solution is non-unique. A large number of possible models can effectively be discriminated if travel times of the secondary branches are available. The HWB method fails in the case of a LVZ since the solution becomes non-unique and both the velocity structure within the LVZ and the thickness of the LVZ cannot be uniquely determined (some limits can still be placed on the maximum thickness of the LVZ).

Non-uniqueness of 1D velocity inversions

The problem of non-uniqueness of seismic velocity inversions can be addressed by using regularization methods, which allow for finding the model in which a particular model parameter is maximized. Typical examples of regularization methods in seismology include finding solutions with smooth velocity–depth distribution (controlled by the first and the second velocity–depth derivatives). Since regularization tends to "smear" velocity anomalies to produce smooth models, "non-smooth" seismic structures constrained by such a model are considered to be real. If the fine-scale velocity structure cannot be reliably determined due to large scatter in travel time data, the upper and lower bounds on seismic velocity can be determined. Velocity bounds, in their turn, determine the bounds on the permitted depths thus permitting a large range of possible velocity–depth models (Fig. 3.29).

The velocity models based on travel time inversions are typically used only as a starting point for other seismic interpretations. More sophisticated applications of ray theory use data on amplitudes and phases. In particular, seismic amplitudes are very sensitive to velocity gradients and discontinuities. After the best fitting velocity–depth profile is obtained from

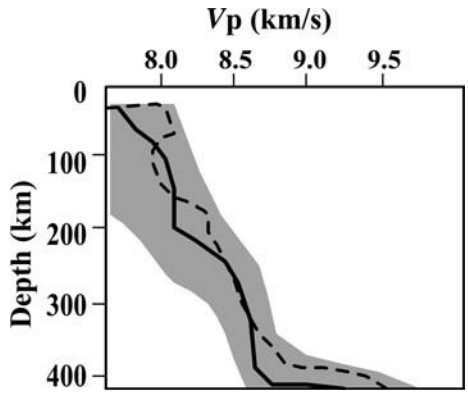

Fig. 3.29 The upper and lower bounds on *V*p seismic velocity in the upper mantle calculated by τ_p travel time method for earthquake data (based on Bessonova *et al.*, 1976). Gray shading – velocity–depth bounds for 98% confidence level; solid and dashed lines – possible velocity–depth profiles.

travel times, velocity–depth models can be refined by trial-and-error amplitude fitting by calculating synthetic seismograms (i.e. the seismic response of a medium to seismic wave propagation which, ideally, should be calculated for the same frequency band as the observed seismograms and should include converted and multiple phases). An important part of amplitude and phase analysis is accounting for geometrical spreading effects such as reflection and transmission at discontinuities and intrinsic attenuation (high frequencies are more attenuated than low frequencies).

1D reference models of the Earth

Large-scale 1D reference models of the Earth were developed several decades ago and are widely used in seismology. The PREM (preliminary reference Earth model) (Dziewonski and Anderson, 1981) is the global spherically symmetric reference model which is based on a large set of different observations and provides P- and S-velocities, density, and attenuation as functions of depth. The velocity structure of the upper mantle in the PREM model is dominated by the oceanic mantle, given that more than 70% of the Earth is covered by the oceans. In particular, in the depth range between 80 km and 220 km, the model includes the low-velocity zone (LVZ); at the same depths the model is transversely isotropic (with a vertical axis of symmetry) with the SH wave slightly faster than the SV wave. The depth range between 220 km and 400 km is characterized by high velocity gradients (Fig. 3.30). The presence of the LVZ in shallow mantle (80–220 km depth) is typical for the oceanic upper mantle, but is not widely observed in the continental regions (see Section 3.3.2). As a result, continent-scale seismic models which use the PREM as the reference model may have an artifact velocity perturbation at 220 km depth, which can be interpreted erroneously as the base of the seismic lithosphere (see Section 3.6.1).

In general, the PREM model should be used with caution as a reference model for regions dominated by the continental lithosphere. The *iaspei* (or *iasp91*) and *ak135* reference models

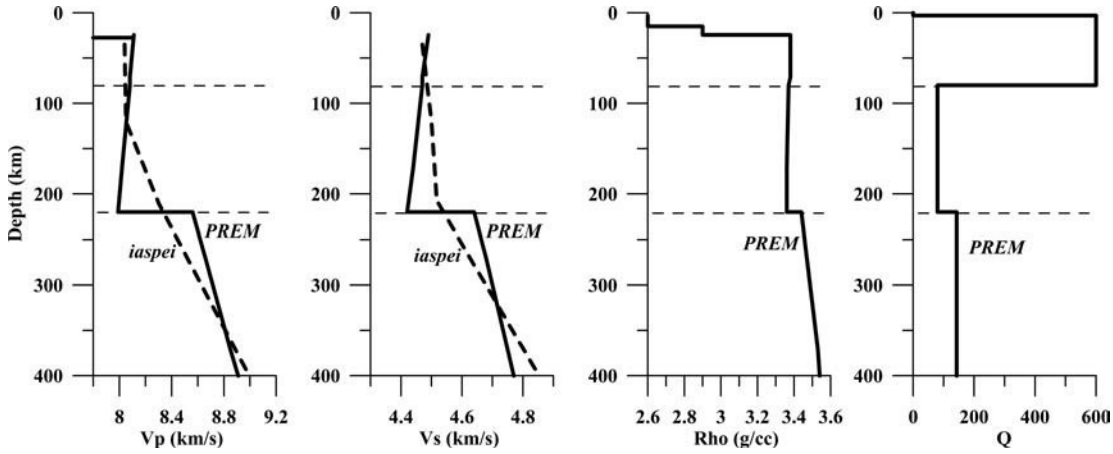

Fig. 3.30 Velocity, density, and Q structure of the upper mantle according to 1D reference models of the Earth based on the PREM (solid lines) and the *iaspei* (dashed lines) models (Dziewonski and Anderson, 1981; Kennett and Engdahl, 1991).

(Kennett and Engdahl, 1991; Kennett *et al*., 1995) are widely used as reference models for the continental mantle since they do not include the low-velocity zone at depths between 80 km and 220 km (Fig. 3.30). However, it is desirable for different reference models to be used for different tectonic structures (Kennett, 2006).

Two-dimensional techniques

One-dimensional models assume a laterally homogeneous lithosphere structure and may provide misleading results in regions with significant lateral heterogeneity, such as produced by dipping layers, igneous intrusions, and faults. However, 1D models can serve as starting models for 2D seismic modeling.

Two-dimensional (2D) interpretations are based on seismic data from linear arrays and are widely used in wide-angle and refraction seismology. The first step is to calculate the travel times in the velocity model. This is commonly achieved:

1) by determining the average 1D model by assuming that the ray paths from source to receiver are along a series of nearly horizontal refractors with constant velocity and thus the method assumes lateral velocity homogeneity and the absence of velocity gradients within the refractors,
2) by calculating travel times along (infinite-frequency) rays in a medium with arbitrary vertical and lateral variations of velocity and inclining discontinuities.

In the next step, forward modeling of travel times is followed by calculation of synthetic seismograms, which are then compared to the observed data. The misfit between synthetic and observed data is used in an iterative procedure where adjustments to the velocity model lead to adjustments of the travel time model.

Three-dimensional techniques

Preamble

Seismic tomography represents a three-dimensional (3D) seismic technique. In regions with dense seismic data coverage, 1D "average" velocity models (see above) can be used as regional "reference" models. In large-scale (e.g. global) tomography studies, global reference models, such as the PREM model, are used. For all available data, the travel time predicted from the reference model is subtracted from the observed travel time and a 3D model of residual travel times is computed. If the average of residual travel times is non-zero, the reference model requires modification. The model of residual travel times is next inverted into velocity perturbations relative to the reference model used in the inversion, and thus a tomographic model is constrained in an iterative procedure. Many tomographic models do not proceed beyond this point and the final model is presented as relative velocity perturbations with respect to the reference model, rather than in absolute velocities. This may lead to significant misinterpretations of tomographic models (e.g. Fig. 3.85a,b; see Section 3.6 for a detailed discussion).

Regularization methods and damping

Models of three-dimensional velocity perturbations are parameterized either by continuous functions (commonly by spherical harmonics laterally and by polynomials vertically) or by dividing the model into blocks. In the latter case, the model is typically undefined in many blocks that are undersampled by seismic rays and regularization methods are used. The most common of these is the damped mean squares regularization in which the weighting parameter controls the difference between the misfit to the data and the variance of the model. This method minimizes the size of the model and permits rough models with large velocity perturbations. Solutions with small-scale velocity anomalies (compared to the size of the blocks) should be treated with caution. Further, if a strong contrast in the real seismic structure occurs such as at the ocean-shield transition, damping will not match either real structure, but will result in underestimation of the true velocity variations (Kennett, 2006).

The roughness of the model (i.e. the absence of strong contrasts in adjacent blocks) is controlled by introducing the average of the adjacent blocks (using the Laplacian operator). In such regularization (minimum roughness inversion), the weighting parameter controls the difference between the misfit to the data and the model roughness. The disadvantage of this approach is that blocks with no rays are interpolated between adjacent cells or extrapolated at the edges of the grid. As a result, cells with little data but with large-amplitude perturbations should be treated with caution.

Another complication arises from the fact that in teleseismic tomography seismic sources (earthquakes) are unevenly distributed and there can be directions with both very high and very low densities of seismic rays. Such problems cannot be "healed" by regularization methods, and the final inversion models may contain linear velocity perturbations along the most densely sampled rays.

Resolution tests and sensitivity analysis

In the case of small-scale regional tomography studies, when the number of parameters (blocks) is small, the reliability of the estimated model can be assessed by computing the full resolution matrix which contains complete information on the model. Mathematical analysis of teleseismic inversion methods examines the effects of errors in reference models and in the source parameters of the seismic events on the final model (Aki *et al*., 1977). Resolution matrices for teleseismic inversion indicate the parts of the block model where the number of rays is insufficient for reliable constraints of velocity anomalies.

In large-scale models with a very large number of unknowns, exact solutions are not possible, a formal resolution cannot be computed, and different tests are used. Sensitivity tests (e.g., Spakman and Nolet, 1988; van der Hilst and Engdahl, 1991; van der Hilst *et al*., 1993) have become a standard way of assessing model resolution as they allow for relatively prompt computation of the results, even for a model with a large number of parameters, and for a comprehensive, visual inspection of spatial resolution of the model. The resolution is tested by the ability of the inversion scheme to retrieve a known input model for the same ray coverage as the one used for real data inversion. In a smearing test (which can be performed both for lateral and vertical resolution of the inversion scheme), synthetic travel times are computed for a model of velocity perturbations (such as an isolated velocity anomaly) for the same ray paths and with the same theoretical apparatus and simplifications as in the actual inversion of the real data. The synthetic data are then inverted to check how well the anomaly is recovered (both in size and amplitude) (see also Section 3.6). Another popular method is the checkerboard test (Lévêque *et al*., 1993), in which, instead of an isolated anomaly, a model with a regular pattern of heterogeneities (velocity anomalies) of alternating sign (commonly with a ±2–5% amplitude perturbation) separated by an equal number of zero amplitude anomaly nodes is superimposed on the ambient velocity model (Fig. 3.31). Since seismic data are always noisy, in some checkerboard tests Gaussian random noise is added to the data (Piromallo and Morelli, 2003).

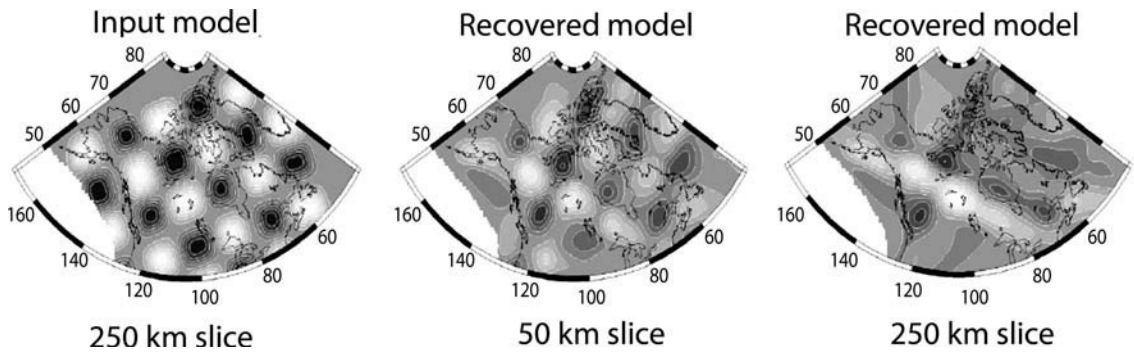

Fig. 3.31 Checkerboard resolution test for S-wave tomography of the Canadian Shield with velocity perturbations in the input model in the upper 500 km (after Frederiksen *et al*., 2001). The amplitude of velocity perturbations at 250 km depth is ±550 m/s. Both the resolution of the shape of heterogeneities and the amplitude of S-velocity perturbations decrease with depth: the amplitude of velocity perturbations is *c*. ±350 m/s at 50 km depth and *c*. ±200 m/s at 250 km depth.

A few words of caution should be stated about sensitivity tests (Lévêque *et al*., 1993; Shearer, 1999):

- the tests cannot check the uniqueness of the solution;
- they do not test the effect of errors in the theory because they are computed with the same theoretical model, assumptions, and simplifications that are used for the actual inversion;
- they are parameter-specific, i.e. in the case of an incorrect choice of parameters, the real Earth structure can be significantly different from the inverse "solution" even though sensitivity analysis will not necessarily reflect this;
- they only provide qualitative estimates of accuracy and resolution, but not necessarily a measure of the model true resolution as they only show a limited representation of the resolution matrix;
- they assume noise-free data and velocity perturbations with uniform amplitude thus effectively only controlling the higher amplitude anomalies;
- they check model resolution only for specific shapes of heterogeneities (e.g., as in checkerboard tests) that are very different from the real Earth structure.

Earthquake location problem

Seismology can be divided into two main categories by the sources of seismic waves: *passive-source seismology* which uses natural sources such as earthquakes, and *controlled-source seismology* in which the sources are man-made and which include primarily chemical explosions and seismic vibrators on land and airguns in marine seismic surveys. While the exact time and position of the seismic sources are known with high accuracy in controlled-source seismology, this is not the case for natural sources, where both the earthquake time and position are to be determined.

Major sources of error for earthquake location are assumptions of point source and lateral homogeneity of the medium. A common problem is mislocation of earthquakes that have occurred on a fault with different velocity structure on both sides of the fault. The problem of event location is relatively easily solved for 1D velocity models; however since travel times depend non-linearly on the earthquake location parameters, the location of seismic events for more sophisticated models remains a subject of seismic research. In particular, if earthquakes are located using a 1D reference model, their location can change in a 3D velocity model. In such cases, joint hypocenter and velocity inversions are used to simultaneously solve the problem for the velocity structure and the event locations.

3.3 Major seismic discontinuities in the lithosphere

3.3.1 The crust

Knowledge of the crustal structure is vital for the Earth sciences. On one side, the crust, which makes the upper (and thus best studied) part of the lithosphere, preserves a memory of

tectonic evolution and planetary differentiation. On the other side, it is an "obstacle" in geophysical studies of the lithospheric and deep mantle: the crustal effect should be taken into account ("subtracted" from the mantle signal) in various types of geophysical studies such as seismic tomography, gravity, and thermal modeling. Detailed overviews of crustal structure can be found in Tanimoto (1995), Christensen and Mooney (1995), Mooney *et al*. (2002); an overview of crustal composition is presented by Rudnick and Fountain (1995), Rudnick and Gao (2003). These publications form the basis for the following brief summary of the crustal velocity structure. Crustal reflectivity and reflection Moho are discussed in Section 3.5.1.

Continental crust

Crustal layers

Four layers are traditionally recognized within the continental crust (Fig. 3.32). The top, sedimentary, layer is commonly defined by $Vp < 5.6$ km; however this boundary velocity can vary significantly between different regions depending on the composition and velocity structure of the consolidated sediments, and its regional value is constrained by drilling data from boreholes reaching the basement. The next three layers form the crystalline crust (the

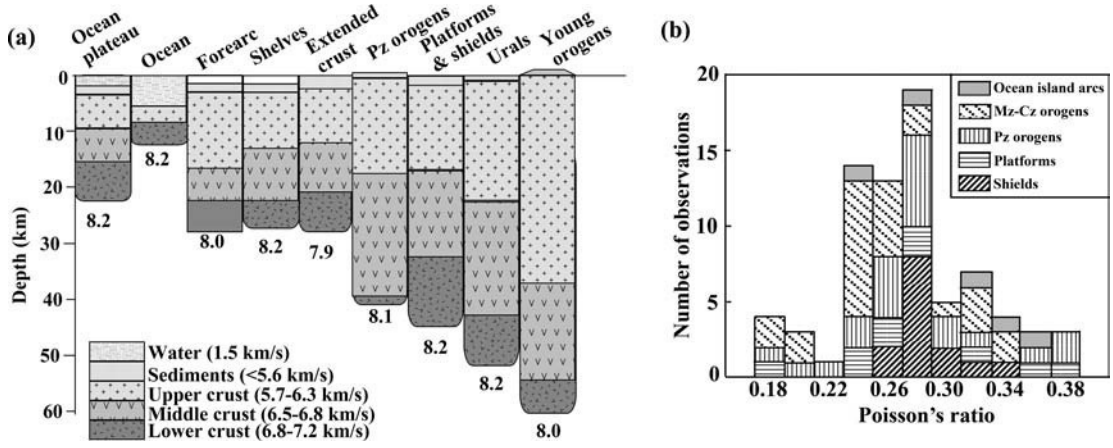

Fig. 3.32 (a) Structure of the primary types of continental and oceanic crust. The Paleozoic Urals orogen is shown separately because, in contrast to other Paleozoic orogens, it has a preserved thick crustal root. The upper crust is typically made of granitic–gneissic rocks with $5.7 < Vp < 6.4$ km/s; middle and lower crust with $6.4 < Vp < 6.8$ km/s and $6.8 < Vp < 7.2$ km/s, respectively, are composed of amphibolitic–granulitic–dioritic rocks; the lowermost crust with $7.2 < Vp < 7.8$ km/s is composed of mafic–granulitic rocks, while the upper mantle with $Vp > 7.6$–7.8 km/s has ultramafic composition. The Conrad discontinuity marks the transition between the upper and the middle-lower crust, while the Moho marks the boundary between the crust and the upper mantle. (b) Global variation of Poisson's ratio (after Zandt and Ammon, 1995). Note that regional crustal structure may differ significantly from any generalization (e.g. compare with Fig. 3.37).

basement). The upper crust with typical *V*p velocities of *c*. 5.7–6.3 km/s has a felsic (granites and low-grade gneisses) composition; the middle crust has typical *V*p velocities of 6.5–6.8 km/s and is composed of rocks of intermediate composition; the lower crust with typical *V*p velocities of 6.8–7.2 km/s has a mafic (basaltic) composition. Sometimes the transition between the upper and the middle crust is diffuse and they are considered together. In some continental settings, a layer with very high P-wave velocity of 7.2–7.6 km/s is observed in the lowermost crust.

Poisson's ratio depends on rock composition and increases with decreasing silica content (Fig. 3.1b). For this reason, Poisson's ratio usually increases with depth and is typically < 0.26 in felsic rocks, 0.26–0.28 in intermediate rocks, and > 0.28 in mafic rocks. Poisson's ratio in the continental crust varies from 0.18 to 0.38 with an average value of *c*. 0.24–0.28 (Fig. 3.32b). Typical average crustal values are 0.29 ± 0.02 in shields, 0.27 ± 0.03 in platforms and Paleozoic orogenic belts, 0.25 ± 0.04 in young (Meso-Cenozoic) orogens, and 0.31 ± 0.05 in island arcs (Zandt and Ammon, 1995).

An example of the proportions of major rock units along the 3000 km long European Geotraverse which crosses the European continent from the Baltic Shield to the Mediterranean sea is presented in Fig. 3.33. This is based on seismic refraction data along the profile combined with mapping, petrological studies, and the computed abundance of major elements and thirty-two minor and trace elements. The composition of the lower crust is derived from worldwide data on felsic granulite terranes and mafic xenoliths. The crust along the profile ranges in age from Archean to Cenozoic (Fig. 3.34), and its thickness varies by more than 20 km. Because of the strong heterogeneity of the crustal structure, the average values along the Geotraverse should be treated with caution since they may not necessarily be typical of any particular crustal structure in Europe. The results indicate that the volume proportions of the upper crust to felsic lower crust to mafic lowermost crust are about 1:0.6:0.4 (in this balance, sedimentary rocks which make ~7 % of the total crustal volume are included in the upper crust) (Wedepohl, 1995).

The Conrad discontinuity is observed regionally in specific continental settings as a sharp increase in seismic velocities at a depth of 15 to 20 km. It is considered to mark the transition

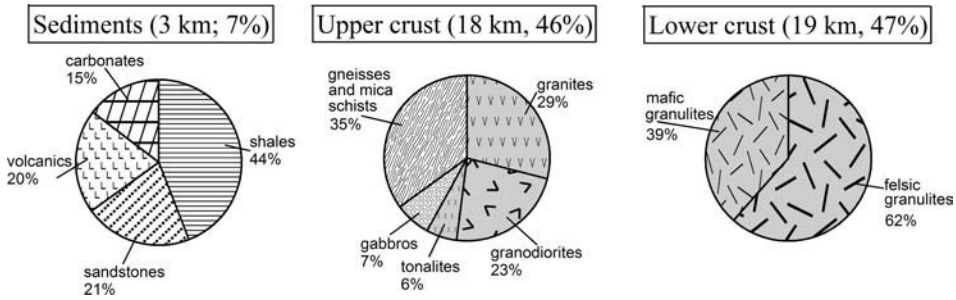

Fig. 3.33 Structure of the continental crust derived from the 3000 km long European Geotraverse (see Fig. 3.61 for location) generalized on the basis of mapping, petrological studies, and chemical balances (based on results of Wedepohl, 1995). Average crustal thickness along the profile is 40 km and it comprises 62% of Archean–Proterozoic crust (45.5 km thick) and 38% Proterozoic–Phanerozoic crust (30 km thick).

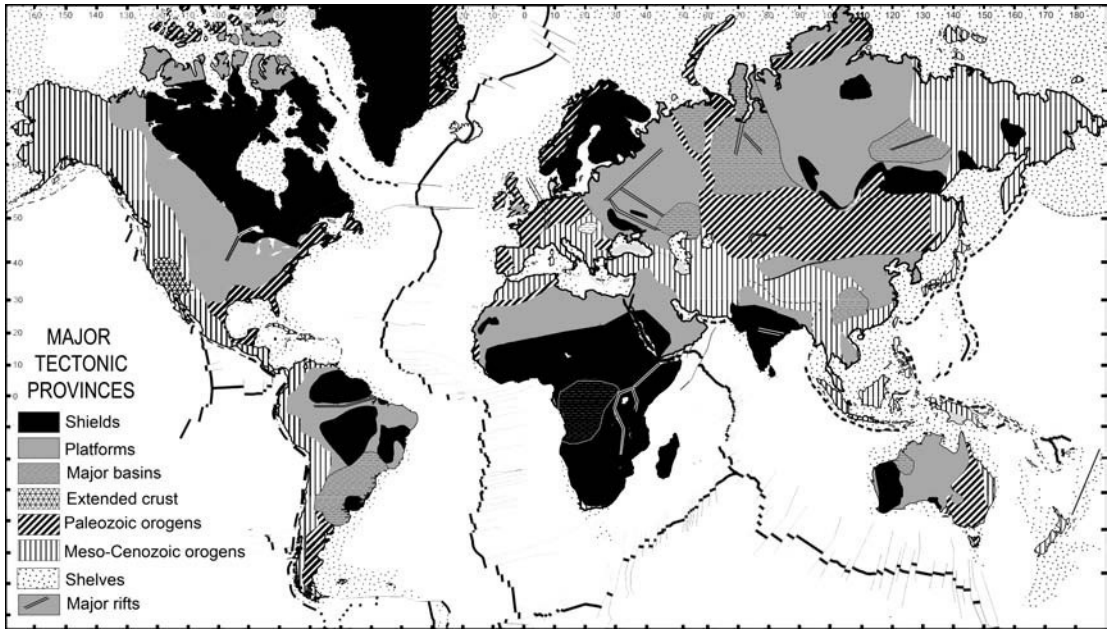

Fig. 3.34 Major tectonic provinces of the continents.

between the upper and the lower continental crust. Its origin remains unclear, although for several decades it has been interpreted as a compositional boundary between the sialic and the mafic crust.

The Moho and crustal thickness

The lowest P-wave velocity expected in the uppermost mantle is 7.6 km/s with the more common value of 7.8 km/s. Thus, conventionally a layer with $V\mathrm{p} > 7.6$–7.8 km/s is considered to be the mantle. The Mohorovičić discontinuity (commonly referred to as Moho or M-discontinuity) that marks the transition from the crust to the upper mantle was identified under the European continent from the analysis of P-waves in 1909 by Andrija Mohorovičić (1857–1936), a Croatian meteorologist and seismologist. The Moho is commonly interpreted as a compositional boundary, the origin of which is directly related to planetary differentiation. However, in some tectonic settings (e.g. in the rift zones) its formal seismological definition by P-wave velocity higher than 7.6 km/s leads to a situation where a part of a very high velocity lowermost crust can be formally interpreted as the mantle, or vice versa, when a part of a very low velocity uppermost mantle can be formally interpreted as the lower crust. The presence of a mixture of lower crustal and upper mantle material apparently observed in some tectonic provinces further complicates seismological constraints on the crustal thickness. In some tectonic settings, such as collisional (paleo)orogens with (paleo) subducting slabs, the double Moho is reported (e.g. Pechmann *et al*., 1984; Ponziani *et al*., 1995; Hansen and Dueker, 2009).

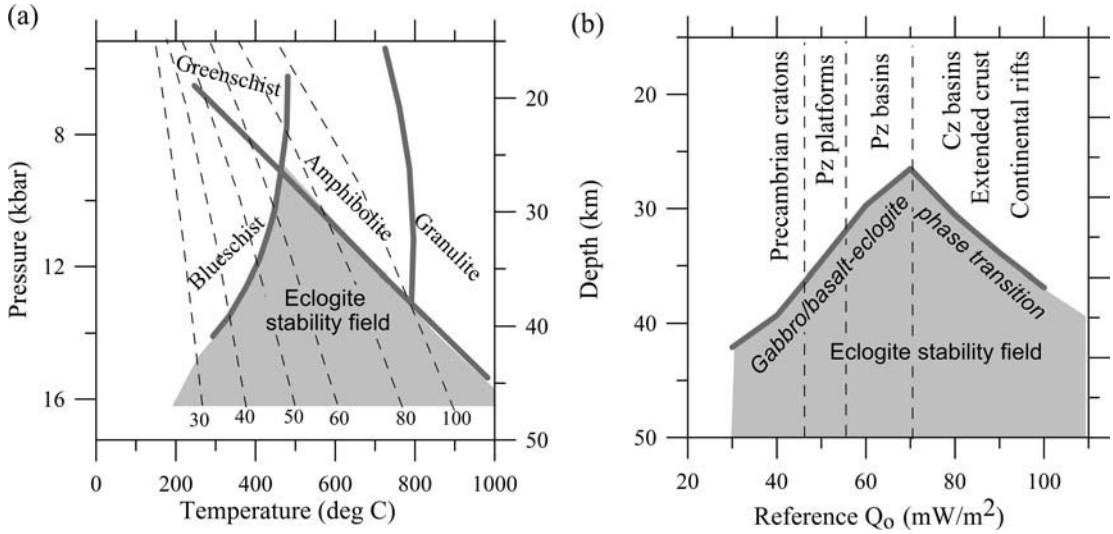

Fig. 3.35 Gabbro/basalt – eclogite phase transition in crustal rocks. Gray shading – eclogite stability field. Pressure–depth conversion is made assuming crustal density of 2.90 g/cm^3. (a) Phase diagram (after Spear, 1993). Thin dashed lines – typical continental reference geotherms (Pollack and Chapman, 1977); numbers – surface heat flow in mW/m^2. (b) Depth to gabbro/basalt–eclogite phase transition (thick gray line) in different continental settings plotted versus continental reference geotherms labeled in heat flow values (Pollack and Chapman, 1977). Note that for the same lithospheric geotherms, measured surface heat flow values can significantly differ from the "reference" value, in particular due to large lateral variations in crustal heat production. To simplify interpretations, tectonic provinces are marked on the top based on the typical heat flow values observed there.

Gabbro/basalt–eclogite phase transition, which in a typical continental crust occurs at *c*. 40–50 km depth, is thought to control the maximal average thickness of the continental crust. Since the rate of gabbro/basalt–eclogite transformation is very slow and strongly temperature-dependent, all laboratory experiments have been made at $T > 800$–1000 °C and extrapolated to the lower temperatures (e.g. Ito and Kennedy, 1971). Importantly, the actual P–T stability field of the system at low temperatures is unknown (Fig. 3.35). At high crustal temperatures, typical for Phanerozoic regions, gabbro/basalt–eclogite phase transition requires time in the order of a million years (Artyushkov, 1993); the question of whether gabbro can remain metastable for a billion years remains unclear. Deep crustal roots extending down into the eclogite stability field (Mengel and Kern, 1992) are only known (a) in cold intracratonic environments (such as at the Archean–Svecofennian suture in the Baltic Shield) since the rate of metamorphic reactions depends strongly on temperature, and lower crustal mafic rocks can apparently remain metastable over a geologically long time, and (b) in young orogens such as the Alps as long as gabbro/basalt–eclogite phase transition is still in process.

The global average for thickness of the continental crust is *c*. 39–42 km; however large variations in crustal thickness (from less than 30 km to ~60 km) are observed between

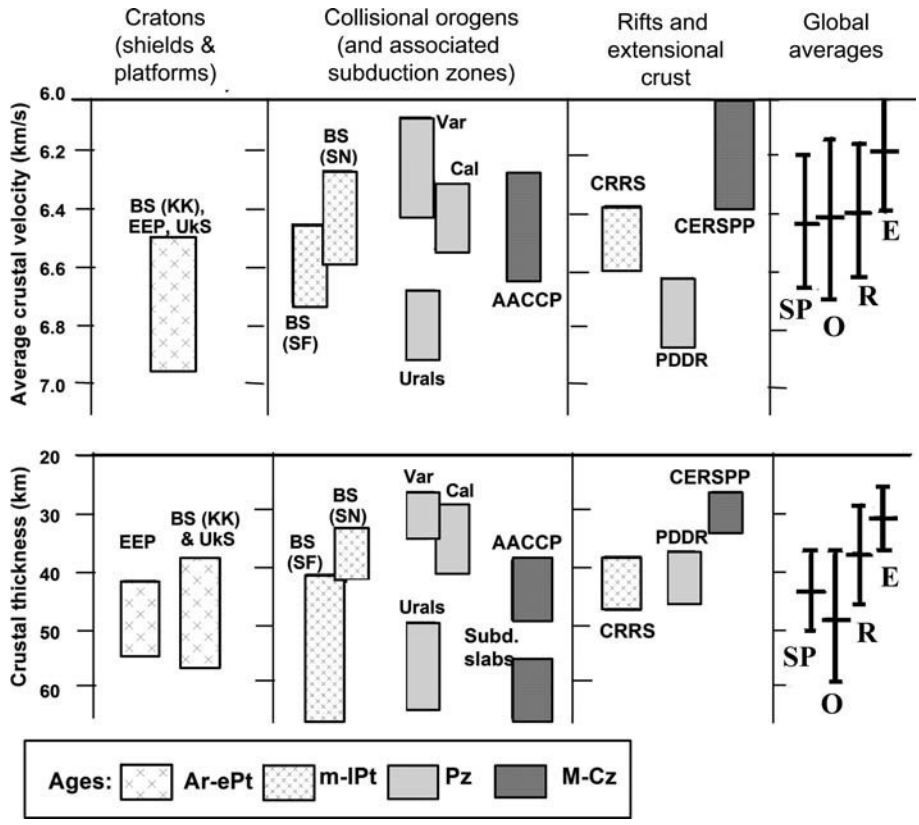

Fig. 3.36 Statistical properties of the on-shore European lithosphere for different tectonic structures (based on Artemieva *et al*., 2006): top – average basement velocity; bottom – crustal thickness. Different shadings refer to tectono-thermal ages of different tectonic provinces. Abbreviations for tectonic provinces: *Archean–Paleoproterozoic (Ar-ePt)*: BS = Baltic Shield, KK = Kola-Karelia, EEP = East European (Russian) Platform, UkS = Ukrainian Shield; *Mesoproterozoic and Neoproterozoic (m-lPt)*: SF = SvecoFennian and SN = SvecoNorwegian provinces of the Baltic Shield, CRRS = Central Russia Rift System; *Paleozoic (Pz)*: Cal = Caledonides, Var = Variscides, Urals, PDDR = Pripyat–Dnieper–Donets Rift; *Meso-Cenozoic (M-Cz)*: AACCP = Alps–Andes–Carpathians–Caucasus–Pyrenees, CERSPP = Central European Rift System–Pannonian Basin–Po Basin. The last column – global statistical averages with standard deviations (Christensen and Mooney, 1995): SP – for shields and platforms, O – for orogens, R – for rifts, E – for extended crust.

continental structures of different ages and different tectonic evolution, and even within similar tectonic structures with similar ages (Figs. 3.36, 3.37). Additional complications arise due to a highly non-uniform coverage of the continents by seismic studies; large regions (most of Africa, large parts of South America, Greenland, and Antarctica) have no or very limited seismic data (Fig. 3.38). The "white spots" can be filled using statistical values based on the typical seismic structure of the crust of different ages and in different tectonic settings. This approach has been used to construct the global crustal

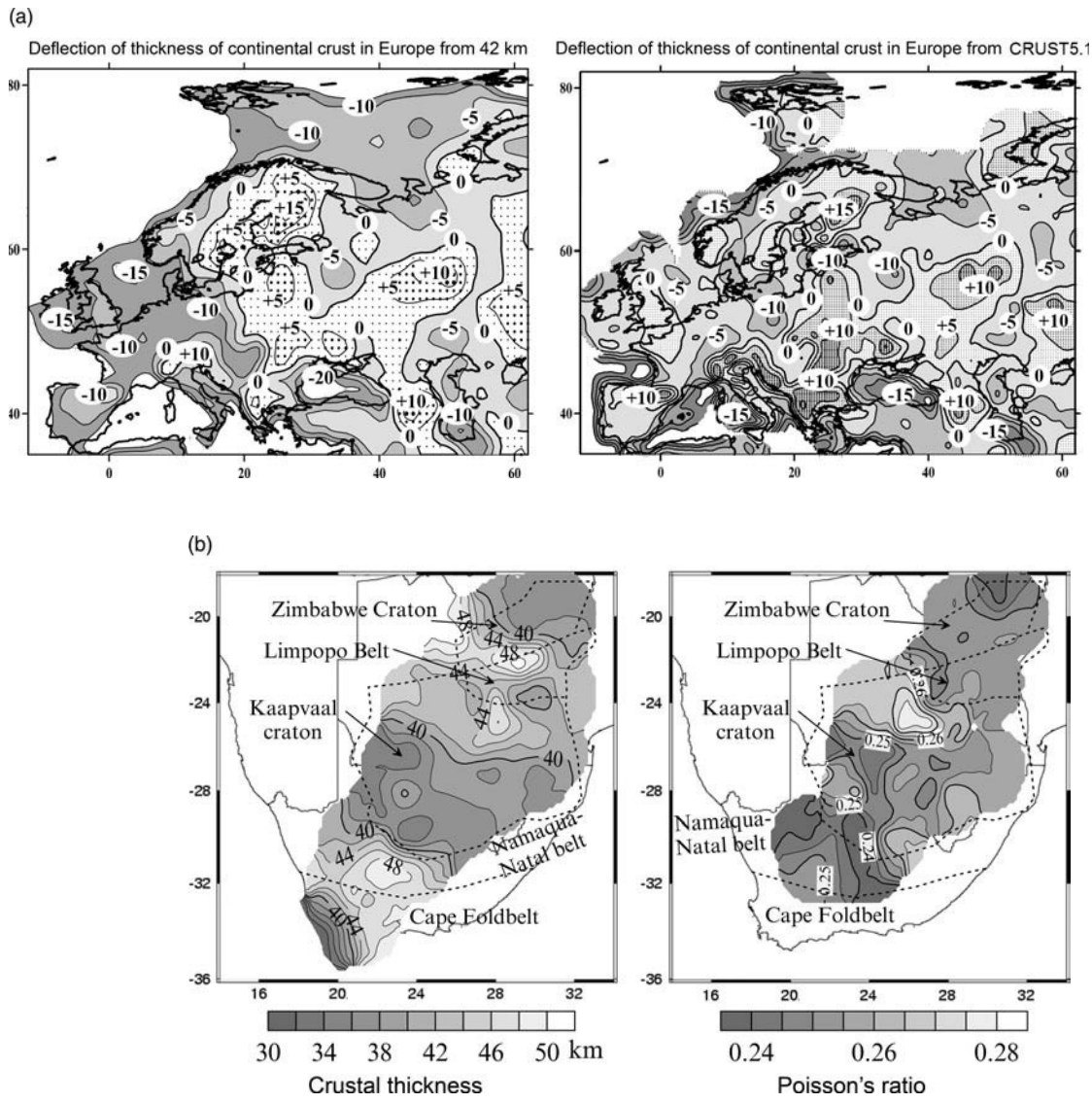

Fig. 3.37 Deflection of the actual crustal thickness in continental Europe (including shelves) from the global average for the continental crust (left) and global crustal model CRUST5.1 (right). Crustal thickness in Europe is smoothed with a low-pass filter for the seismic data compilation of Artemieva, 2007; Artemieva and Thybo, 2008, 2011. (b) Variations in crustal thickness and Poisson's ratio beneath South Africa based on receiver function analysis from 78 stations. Dashed lines – boundaries of major tectonic provinces (based on the results of Nair *et al*., 2006).

models CRUST 5.1 and CRUST 2.0 (Figs. 3.38, 3.39). However, any such generalization should be treated with caution because statistical crustal models, although useful in regions with no data, can be misleading and erroneous for individual tectonic structures. Thanks to an extremely high coverage by high quality seismic data (Fig. 3.38), Europe is

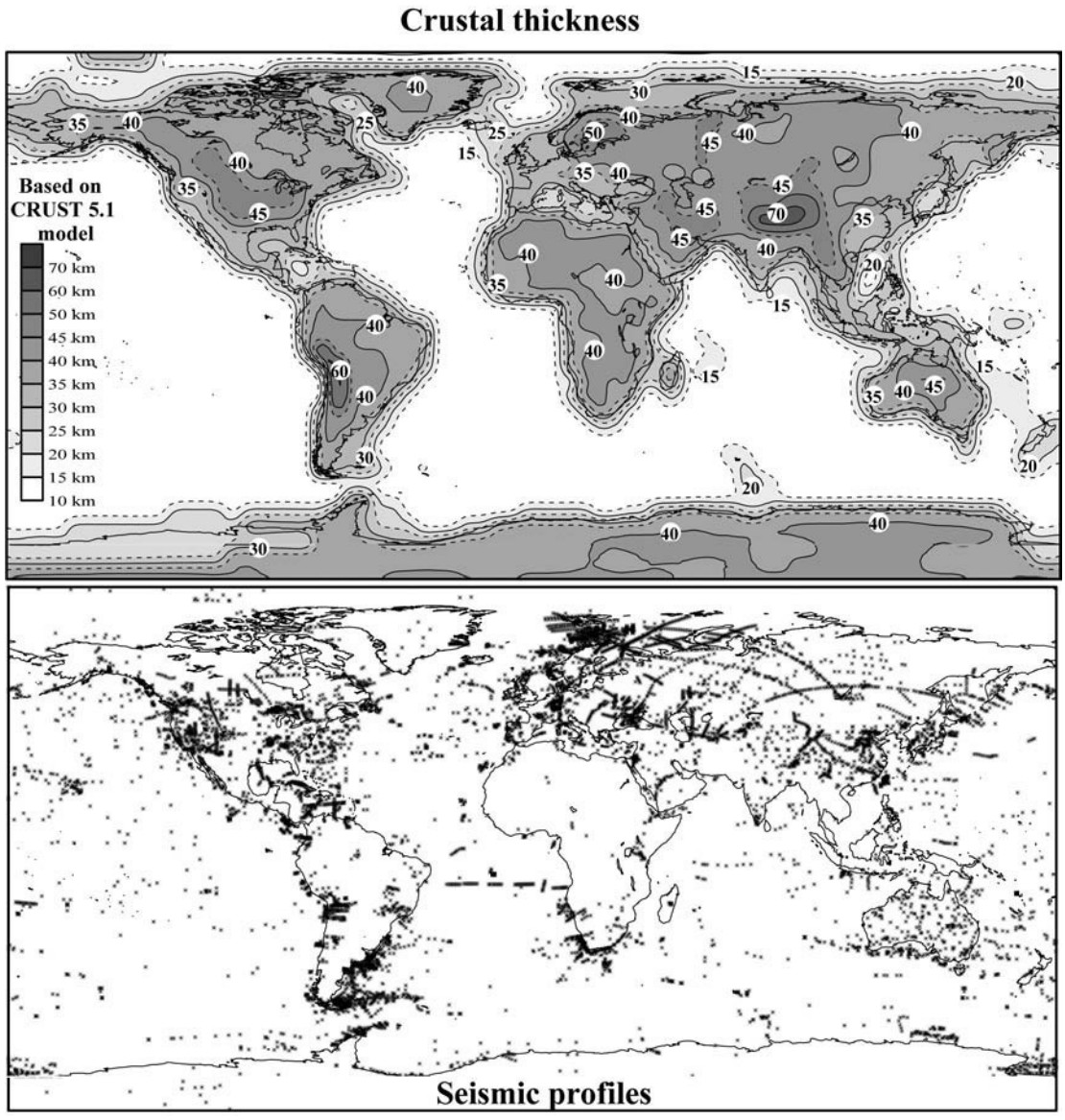

Fig. 3.38 Thickness on the crust (Source: CRUST 5.1 model, Mooney *et al.*, 1998). Because of a large averaging window on a regular (5° × 5°) grid, the individual structures are poorly resolved and the map provides a very generalized pattern similar to low-pass filtering. Bottom map shows coverage by seismic profiles in 2005.

the best region to compare statistical models for the continents with actual seismic crustal structure (Figs. 3.36, 3.37a). A comparison shows that very few of the tectonic structures in Europe have crustal thickness, thickness of sediments, or average crustal velocities that correspond to the global statistical averages for similar tectonic provinces of the world.

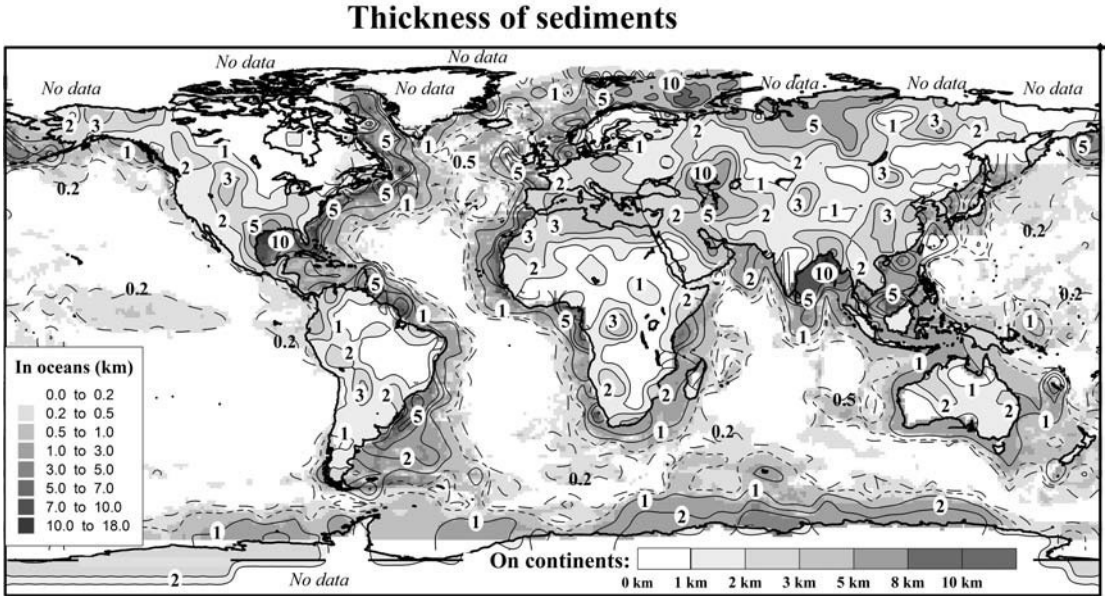

Fig. 3.39 Thickness of sediments in the continental regions (based on the CRUST 5.1 model, Mooney *et al.*, 1998) and in the oceans (based on a 5′ global compilation (Divins, 2008)). Continental shelves are excluded except for the Barents sea where high quality seismic data are available. Because of a large averaging window on a regular ($5° \times 5°$) grid, the individual structures are poorly resolved and the map provides a very generalized pattern similar to low-pass filtering.

Similar discrepancies should be expected for all other continents, reflecting the long, complicated, and commonly asynchronous history of evolution of individual tectonic provinces worldwide. The discrepancy between actual seismic interpretations and the statistical model, which for crustal thickness reaches ±(5–10 km) almost everywhere, stems from two major reasons:

- the existing statistical models are constrained by seismic reflection and refraction data that were available by 1995–1998 (CRUST 2.0 was additionally constrained by detailed borehole data on the thickness of the sedimentary cover); some of the regional interpretations used in statistical models were based not only on seismic data but on potential field data as well; in some regions recent seismic studies considerably revised old interpretations;
- CRUST 5.1 and CRUST 2.0 are constrained on $5° \times 5°$ and $2° \times 2°$ grids, respectively; as a result many short-wavelength variations in crustal structure, in particular in regions with complicated tectonics and highly heterogeneous crust, have been averaged (compare Figs. 3.39 and 3.40).

General trends in variations of crustal structure of the continents with age are exemplified by high-resolution seismic data from Europe (Fig. 3.41). The European continent provides

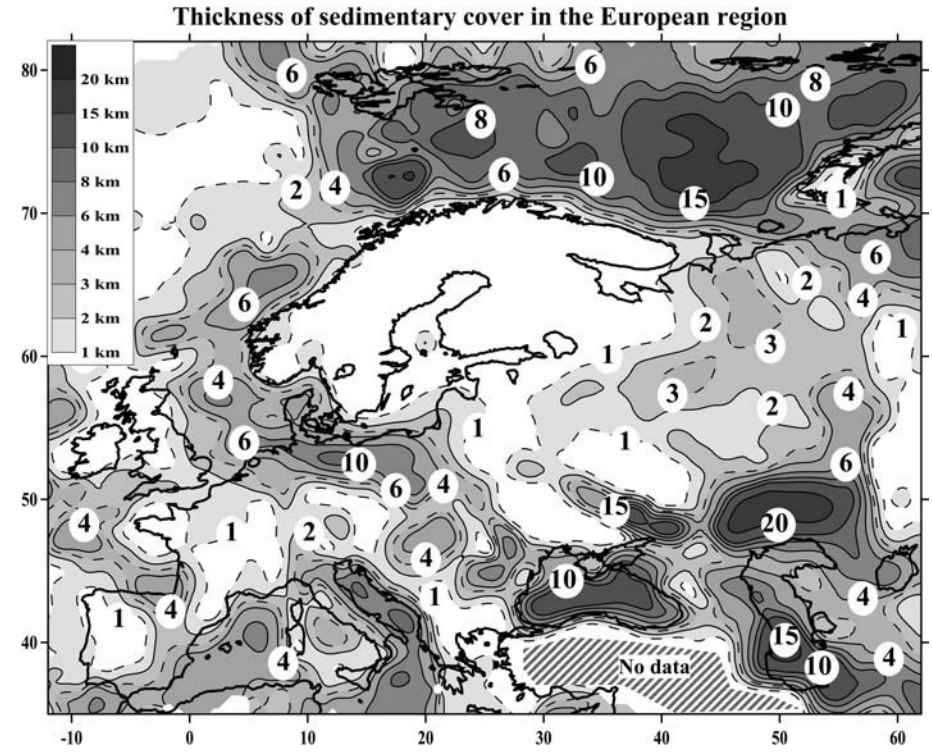

Fig. 3.40 Thickness of sediments in the European region constrained by the EXXON map (1985) complemented by numerous publications based on high-resolution regional seismic surveys and drilling (compilation of Artemieva and Thybo, 2011). The interpolation used to constrain the map filters out small-scale anomalies and thus the map show the minimum estimate of sedimentary thickness.

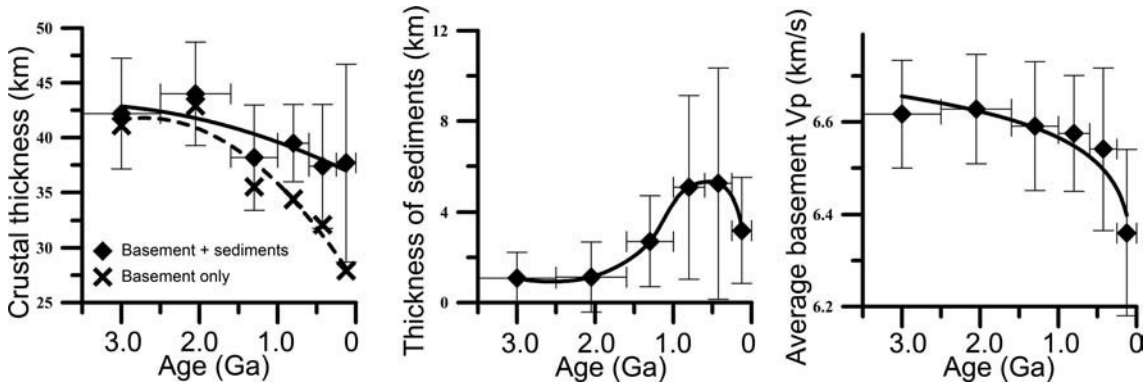

Fig. 3.41 Statistical properties of the continental crust in Europe averaged for six time intervals: Archean, Paleoproterozoic, Mesoproterozoic, Neoproterozoic, Paleozoic, and Meso-Cenozoic (after Artemieva, 2007). Horizontal bars – the time span used for averaging; vertical bars – standard deviation of the parameters.

a good test site owing to the diversity of its tectonic structures that cover *c*. 3 Ga of the continental evolution (Figs. 3.36, 3.60). The depth to the Moho generally increases with age; the pattern is even more pronounced for age variations of the thickness of the crystalline basement. This trend is, however, weak for the Precambrian crust, and although the Paleoproterozoic crust appears to have a slightly greater thickness than the Archean crust, the difference between them is within the typical uncertainty of seismic models. Furthermore, the basement age in most of the East European craton is Archean–Paleoproterozoic and the subdivision between the two ages is not straightforward, in particular, in the sediment-covered platform area. Typically, the thickness of sediments decreases with tectono-thermal age and is the largest in Paleozoic–Mesozoic basins (Fig. 3.40). A pronounced difference in average crustal velocity (the global average for the continental crust is 6.45 km/s) between the continental structures of different ages is the result of significant variations in thickness of crustal layers and average composition of the crust (Fig. 3.41).

Principal types of the continental crust

Stable parts of the continents

Cratons (from the Greek word meaning "strength") are tectonically stable parts of the continents that were formed in the Precambrian (>560 Ma) (Fig. 3.34; 2.16). Cratons with exposed Precambrian crystalline igneous and high-grade metamorphic rocks form Precambrian shields, the term introduced by German geologists in 1901. Platforms also form stable parts of the continents. Since the age of the platforms can be both Precambrian and Phanerozoic (most common Paleozoic), many of the platforms (in particular in Eurasia) were formed within the cratons and have remained their integral parts. For this reason, a subdivision of stable continents into terranes of Precambrian age, on one side, and platforms (with no age being specified), on the other side, while justified in some regional studies, is meaningless when employed in global crustal models. Contrary to shields, platforms are covered by a significant sequence of sedimentary rocks (commonly exceeding 2–3 km); in some basins the thickness of sediments can exceed 10 km (e.g. in the Peri-Caspian depression within the East European craton it exceeds 25 km, Fig. 3.39).

The crust in shields and platforms typically exceeds 40 km in thickness and commonly has a relatively thick lower crust (Fig. 3.32; Fig. 3.38), which results in a high average P-wave velocity in the crust (6.49 km/s for the shields). Poor coverage of stable continents by seismic data in the early 1990s, when data from cratonic South Africa and Australia dominated the global data set for the Archean terranes, led to the conclusion that the Archean crust is typically *c*. 35 km thick and thus is significantly thinner than the Paleoproterozoic crust that is typically *c*. 45 km thick (Durrheim and Mooney, 1991). New high-quality seismic data reported from different cratonic regions of the world do not support this conclusion (e.g. Fig. 3.37b). Since cratons preserve some of the oldest crust on the planet that has undergone a long tectonic evolution, the crustal structure of stable continents is highly heterogeneous both regarding thickness and the velocity structure. For example, within the Archean Kaapvaal craton, the crustal thickness is highly non-uniform over short distances with local variations between 50 km and 34 km (Nguuri *et al*., 2001). A belt of thick crust of thickness of 51–53 km (locally reaching 60 km depth) has been reported for the

Archean Dharwar craton in India (Gupta *et al*., 2003). Crustal thickness of 50 km and more is common in the Archean–Paleoproterozoic provinces of the East European Platform and the Ukrainian Shield (Trofimov, 2006; EUROBRIDGE, 2001). Values of *c*. 55 km (locally exceeding 60 km) are determined in the Baltic Shield (south-central Finland) at a paleo-collision zone between the Archean and Paleoproterozoic terranes (Hyvonen *et al*., 2007). On the other hand, the Archean cratons of western Australia apparently have a relatively thin (less than 40 km) crust, while crustal thickness in the Proterozoic Central Australia locally exceeds 50–55 km (Clitheroe *et al*., 2000).

Active parts of the continents

Young collisional orogens typically have thick crustal roots, although large variations in crustal structure exist between different Cenozoic orogens. The largest thickness of continental crust has been reported for the Andes and the Himalayas–Tibet region, where crustal roots extend down to *c*. 70 km. In other orogens crustal thickness commonly does not exceed 50–60 km. For example, in the Alps, crustal roots reach 50–55 km only in the western and central parts of the orogen and do not exceed 42–45 km in its eastern part (Grad *et al*., 2009; Schreiber *et al*., 2010). Seismic data on the crustal structure of other Cenozoic collisional orogens of Europe still remain limited; in particular little is known about the seismic structure of the crust beneath the Caucasus. Among Paleozoic orogens (the Appalachians, the Caledonides of Norway and Greenland, the Variscides, and the Urals), the Ural mountains are unique: this orogen which remained tectonically undisturbed within the continental interior since its formation has preserved thick crustal root that is *c*. 50 km deep and reaches 65 km in the central part and in the Polar Urals (Carbonell *et al*., 1996; Avtoneyev *et al*., 1992). In other Paleozoic orogens the crustal roots have been lost and crustal thickness is *c*. 40 km or less (Fig. 3.32).

The best known continental region of extended crust is the Cenozoic Basin and Range Province in western USA. The extended crust is typically only 30 km thick, and the lower crust is almost always missing. As a consequence, the Moho is marked by a sharp jump in seismic velocities. Crustal structure similar to the Basin and Range Province is observed in the Variscan belt of Europe, a 3000 km long Paleozoic orogen which extends from the North Sea to Iberia (Figs. 3.59, 3.60). Wide-spread anatectic granites indicate intensive melting of thickened continental crust at the late stages of the Variscan orogeny. Late Paleozoic large-scale normal faulting, crustal extension with possible rifting and delamination of the lower crust produced the modern crustal structure with a flat Moho at *c*. 30 km depth, analogous to the modern Basin and Range Province (Menard and Molnar, 1988). The Conrad discontinuity is often observed in the extended crust of the Variscides.

Various seismic studies indicate significant crustal thinning beneath some continental rift zones. For example, beneath the Kenya Rift the crust is thinned to *c*. 30 km and is underlain by a low-velocity mantle (with *Pn* velocity of 7.6 km/s). Supported by seismic studies in the East African Rift Zone, "classical" models for rifted terranes always have a thin crust. However, recent seismic studies indicate that continental rift zones can have normal continental crust with no crustal thinning. A seismic velocity model across the Baikal Rift Zone shows a gently deepening Moho from the Siberian Platform (41 km depth) into the Sayan–Baikal Fold Belt (46 km depth) with no Moho uplift beneath the rift axis (Thybo and Nielsen, 2009). Similarly, seismic reflection/refraction studies across the largest

in Europe (*c*. 2000 km long, up to 170 km wide, and 22 km deep) Paleozoic intracratonic Dnieper–Donets rift (Ukraine) indicate that the crust is *c*. 40–42 km thick, and the rift basin is underlain by a high density and high velocity zone at middle to lower crustal levels (Lyngsie *et al*., 2007). Only a weak crustal thinning is observed beneath the Paleozoic Oslo graben, where the crust is *c*. 34–35 km thick as compared to 38–40 km in the adjacent regions (Stratford *et al*., 2009).

The continental shelves are the off-shore continuation of the closest onshore crustal terranes with a tendency towards some crustal thinning below the shelves. Many of the shelves, in particular in the Arctic, are the continuation of the cratonic crust and have crustal thickness of *c*. 30 km. Along the Arctic shelves (e.g. in the Barents Sea), where the crust has been subject neither to the effects of oceanic break-up nor to intensive rifting episodes with related crustal thinning as in the North Sea, the crust is 30–35 km thick. In island arcs (e.g. Japan) the crustal thickness is about 20–30 km and has a pronounced 3D structure. A low velocity mantle with *Pn* velocity of 7.5–7.8 km/s suggests high mantle temperatures.

Oceanic crust

General patterns

Compared to the continental crust, the oldest oceanic crust is Jurassic (~180 Ma). Classically the oceanic crust is divided into three layers (Fig. 3.32). Layer 1 is the sedimentary layer with a highly variable thickness. Layer 2 has P-wave velocities of 4.5–5.6 km/s, is *c*. 1.5–2.0 km thick, and is made of extrusive volcanic rocks (pillow basalts at shallow depths which grade downwards into sheeted dikes). Layer 3 (typical thickness 4.5–5.0 km) with P-wave velocities of 6.5–7.0 km/s has gabbro composition similar to the composition of ophiolite complexes. The top of Layer 3 is transitional with interfingering of sheeted dikes into the lower part of Layer 2. Further down, the upper part of Layer 3 consists of isotropic gabbro, underlain by layered gabbro and harzburgite. In mid-ocean ridges, where the new oceanic crust is formed, the base of the crust also marks the base of the lithosphere. The thickness of the oceanic crust (commonly defined as the thickness of Layers 2 and 3) is fairly uniform globally (5.6–7.1 km according to different authors) and does not show any age dependence (Tanimoto, 1995).

Anomalous oceanic crust

Some oceanic regions have crustal thickness significantly thicker than global observations. These regions are of a particular interest because, as a rule, bathymetry there does not follow the square root dependence on ocean floor age (see Chapter 4). This fact, together with the presence of anomalously thick oceanic crust, is attributed to mantle thermal anomalies with a high degree of melt generation. In ocean plateaux, crustal thickness reaches 20 km (and may be as thick as 35 km beneath the Ontong–Java plateau); the origin of this thick crust is commonly ascribed to a large amount of melt generated by a mantle plume. However, the seismic structure of many other ocean plateaux is still poorly known and some of them (such as the Falkland Plateau, Lord Howe Rise, the Kerguelen Ridge, the Seychelles Ridge, and

the Arctic Ridge) may contain fragments of the continental crust (Mooney *et al*., 1998 and references therein).

A thick (15–25 km) crust beneath several aseismic ocean ridges such as the Walvis and the Ninety-East Ridge in the Indian Ocean (Detrick and Watts, 1979) has been also explained by the presence of large volumes of melt associated with mantle upwellings (e.g. White *et al*., 1992). Similarly, anomalously thick oceanic crust (30–35 km) underlies the Faeroe–Iceland–Greenland ridge that extends from Greenland to the British Isles across the Mid-Atlantic Ridge (Bott and Gunnarsson, 1980; White *et al*., 2008). The presence of a thick oceanic crust can be interpreted in favor of the presence of a mantle plume with anomalously high melting temperature at Iceland, while the east–west symmetric crustal structure of the Faeroe–Iceland–Greenland ridge around Iceland is used as an argument against the plume origin of Iceland unless the plume location has been semi-stationary with respect to the plate boundary (Lundin and Dore, 2005).

Crustal thickness in Iceland is a topic of hot debate: two competing models, "thin crust" and "thick crust", have been proposed for Iceland (see review by Foulger *et al*., 2005). Numerous seismic studies indicate that the oceanic Layer 3 (down to a depth of 10–20 km) has *V*p velocity of 6.5–7.0 km/s. Below this depth, in Layer 4 (which may extend down to 60 km depth), the P-wave velocity gradually increases to 7.0–7.6 km/s. The principal difference between the two crustal models is the petrologic interpretation of Layer 4: in the "thin crust" model it is interpreted as anomalous peridotite mantle with *c*. 2% of melt, while in the "thick crust" model the same layer is interpreted as gabbroic "lower crust" with lenses of melt.

It should be noted that some oceanic regions have anomalously thin crust. They include regions with slow spreading rates (< 2 cm/y), non-volcanic rifted margins that have earlier undergone extreme extension, and fracture zones where Layer 3 is very thin or absent.

3.3.2 Seismic discontinuities in the upper mantle

LVZ, G-discontinuity and the base of seismic lithosphere

Seismic lithosphere (or the *lid*) is defined as the seismic high-velocity region on the top of the mantle. It generally overlies a low-velocity zone (LVZ) that was first recognized by Beno Gutenberg (1959). Thus, the top of the LVZ defines the bottom of the lid (Anderson, 1995). Since the LVZ is located between the thermal boundary layer (above) and the nearly adiabatic mantle (below), in the oceans the top of the LVZ and the top of the asthenosphere (a layer with lowered viscosity) are equivalent and are marked by the seismically sharp, Gutenberg (G-), discontinuity that is characterized by an abrupt seismic velocity decrease of roughly 9% (Bagley and Revenaugh, 2008).

Starting from the early works, a decrease in seismic velocities in the LVZ was attributed solely to partial melting (e.g. Lambert and Wyllie, 1970). The mechanism behind this melting is still the subject of discussion; volatile enrichment of the mantle is a possible cause. Alternatively, a sharp decrease of water solubility in mantle minerals at the depths that correspond to the LVZ may cause excess water to form a hydrous silicate melt (Fig. 3.42) (Mierdel *et al*., 2007). If the LVZ below the seismic lithosphere results from

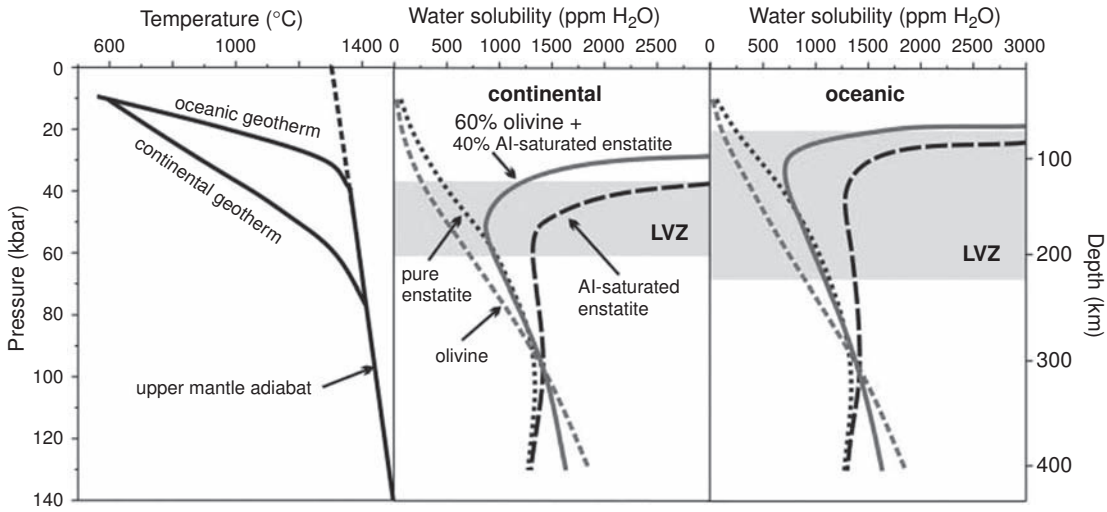

Fig. 3.42 Water solubility (in ppm by weight) in upper-mantle minerals as a function of depth for continental shield (middle panel) and oceanic mantle (right panel) calculated for typical oceanic and shield geotherms (left) (from Mierdel *et al*., 2007). While water solubility sharply decreases with pressure (depth) in aluminous orthopyroxene (long dashes), it continuously increases with depth in olivine (short dashes). The low velocity zone (LVZ) coincides with the depth where the water solubility in mantle minerals is at a minimum. Gray shading – typical position of the LVZ below continental shields and oceans. Compare with Figs. 7.17 and 7.18.

partial melt, the lithospheric base should be a rheological boundary and it may be marked by a change in mantle anisotropy pattern from frozen-in anisotropy in the lithosphere to anisotropy in the asthenosphere due to mantle flow.

Recent studies favor explanations other than partial melting, such as high-temperature relaxation (Anderson, 1980), a contrast in volatile content from water-depleted lithosphere to water-rich asthenosphere (Karato and Jung, 1998), and grain size variations without requiring the presence of melts (Faul and Jackson, 2007). These mechanisms suggest that the base of a seismic lithosphere should be a diffuse boundary which extends over a certain depth interval. Seismic studies in the western and central Pacific based on multiple ScS reverberations put an upper limit of 30 km on the transition interval where most of the velocity decrease from the lid to the LVZ takes place (Bagley and Revenaugh, 2008), while a recent study based on converted P-to-S and S-to-P waves suggests that the velocity drop at the discontinuity occurs over depths of 11 km or less (Rychert and Shearer, 2007). The width of this transitional interval is more easily explained by the termination of the zone of partial melting rather than by a change in grain size. Furthermore, grain size variations with depth are insufficient to explain the seismic LVZ in the absence of water and/or melt and can only be applied to wet mantle.

The low-velocity zone, as its name indicates, is associated with negative velocity gradient: velocity in the upper mantle across the upper boundary of the LVZ decreases with increasing

depth. Negative velocity gradients are a common feature in the upper mantle (e.g. Thybo, 2006; Fig. 3.70), in regions where a velocity increase due to compression becomes less than a velocity decrease due to heating (Anderson *et al*., 1968). In particular, synthetic computation of the isotropic elastic wave velocities in a pyrolitic mantle indicates that a solid-state low-velocity zone can provide a satisfactory quantitative explanation of a drop in seismic velocities at 100–200 km depth in a 100 Ma Pacific Ocean (Stixrude and Lithgow-Bertelloni, 2005). These results imply that *not every seismic LVZ in the mantle should be interpreted as the lithospheric base*. In tomography studies, the base of the seismic lithosphere is closely linked to the top of a LVZ and in practice it is commonly defined either as the zone of high velocity gradient in the upper mantle or as the bottom of the layer with positive velocity anomalies, which should correspond to a transition from the high-velocity lithosphere to the LVZ. However, seismic tomography and seismic refraction models will not necessarily indicate the same depth to the lithospheric base.

Lehmann (L-) discontinuity

The Lehmann (or L-) discontinuity at a depth of *c*. 220 km associated with a *c*. 2% velocity increase is named after its discoverer, the Danish female seismologist Inge Lehmann (1888–1993). According to Francis Birch,

> Lehmann discontinuity was discovered through exacting scrutiny of seismic records by a master of a black art for which no amount of computerization is likely to be a complete substitute.

It was first observed in seismic refraction studies of earthquake data below Europe and in GNOME nuclear explosion data below the North American craton (Lehmann, 1959, 1961, 1962) (although the existence of a seismic discontinuity at around 200–220 km depth had been predicted much earlier by a Russian geophysicist Prince Golitzyn (Galitzin, 1917)).

For several years the Lehmann discontinuity was considered to be a global boundary at ~220 km depth (now extended to a depth range of 160–280 km) interpreted as the base of the low-velocity zone (Thybo and Perchuc, 1997a). Isotropic models of the Earth require the presence of a low-velocity zone in the upper mantle with a 5–10% shear-velocity decrease, implying significant melting of the upper mantle at this depth. Introduction of transverse isotropy can significantly reduce the magnitude of the velocity drop at the discontinuity. The PREM model (which includes transverse isotropy in the depth range between 24.4 km and 220 km), includes the 220 km depth as the first order discontinuity (Fig. 3.30). As a result, tomographic inversions in which PREM is used as a reference model tend to locate a velocity minimum at a 220 km depth (Su *et al*., 1994). Since the velocity jump associated with the L-discontinuity is small (<5% in PREM), the uncertainties in travel time measurements are significantly larger than the uncertainties associated with the 410 km and 660 km discontinuities.

Global- or continent-scale seismic studies from the 1990s based on stacking of SH-components of surface waves showed little evidence for the L-discontinuity, suggesting that if it is a global feature, it should be extremely variable in depth. In fact, the depth to the

L-discontinuity is apparently correlated with tectonic setting, being shallow in tectonically active regions and deep in stable cratons (Revenaugh and Jordan, 1991). A recent targeted survey for the presence of the L-discontinuity based on long-period SS precursors indicated that it is a local feature with lateral velocity variations, regionally present under the continents and island arc regions (Vidale and Benz, 1992; Deuss and Woodhouse, 2004). Under the continental areas it is observed twice as often as under oceans, with the most robust observations under Eurasia and Africa (Fig. 3.43). The L-discontinuity is also detected under South America; weak L-reflections are detected under western Australia with no evidence for the L-discontinuity under eastern Australia. There is little evidence for the L-reflection under North America (e.g. Gu *et al*., 2001). Furthermore, arrivals from the L-discontinuity differ significantly in phase and in amplitude from predicted arrivals and cannot be explained by a simple horizontal boundary associated with an increase in seismic velocity.

Interpretations of the nature of the Lehmann discontinuity indicate that its origin can be closely related to the lithospheric structure. For stable continental regions some interpretations of the origin of the L-discontinuity are closely related to the concept of the seismic lithosphere (the *lid*). Lehmann discontinuity is interpreted as:

- the base of the petrologically distinct chemical boundary layer under the continental cratons (Jordan, 1975a, 1978),
- the base of the zone of partial melting (Vidale and Benz, 1992) within a stable continental lithosphere (Lambert and Wyllie, 1970; Hales, 1991; Thybo and Perchuc, 1997a),
- the depth at which the grain size changes from millimeter scale in the shallow mantle to centimeter scale in the lower part of the upper mantle above the transition zone (Faul and Jackson, 2005),
- the depth where an abrupt change in upper mantle seismic anisotropy occurs (Montagner and Anderson, 1989; Gaherty and Jordan, 1995) (Fig. 3.44); this change may be caused by the change in the preferred orientation of olivine due to a change in deformation mechanism from dislocation creep in the shallow mantle (favorable for creating anisotropic structures) to diffusion creep in the deeper mantle (favorable for isotropic structures) (Karato, 1992).

The latter interpretation is a subject for debate. Deuss and Woodhouse (2004) have measured the seismological Clapeyron slopes by correlating discontinuity depths with local velocity perturbations from a tomographic model. Assuming that velocity perturbations are solely due to temperature variations, they found that (except for the Middle East region) the Lehmann discontinuity is globally characterized by a negative Clapeyron slope (Fig. 3.43c). These authors argue that since all known phase transitions in the upper mantle above the transition zone have positive Clapeyron slopes, the only hypothesis that can explain a negative Clapeyron slope is the transition from dislocation to diffusion creep. A positive Clapeyron slope that they observed in the Middle East could be attributed to a phase transition from coesite to stishovite. In contrast to these interpretations, an anisotropic origin of the Lehmann discontinuity has been recently questioned by seismic interpretations for North America (Vinnik *et al*., 2005), the continent with little evidence for the L- reflection (Gu *et al*., 2001; Deuss and Woodhouse, 2004).

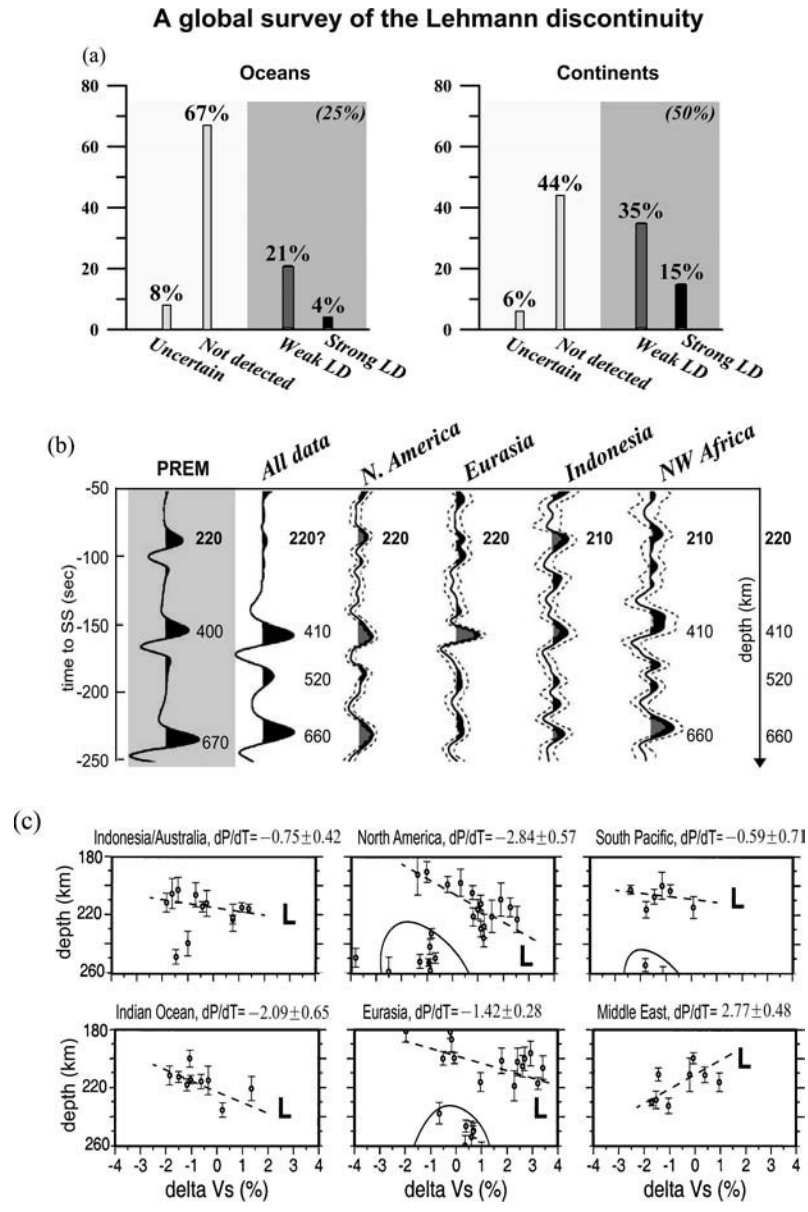

Fig. 3.43 A global survey of the Lehmann discontinuity (a – after Gu *et al.*, 2001; b, c – after Deuss and Woodhouse, 2004). In the oceans, 75% of regions show no evidence for the L-discontinuity near the 220 km depth. (b) Stacking results for synthetic seismograms (PREM) and real seismic data (SS-precursor data set). The dashed lines show the 95% confidence levels for the regional stacks. The gray areas represent robust reflections with the lower confidence level above zero. (c) Depth of robust reflections versus velocity perturbations at the same depth. Dashed lines are approximations of Clapeyron slopes dP/dT for 180–240 km depth (the Lehmann discontinuity); clusters of reflections at 240–340 km depth are not a part of the L-populations. The values of dP/dT are in MPa/K; for West Africa (not shown) dP/dT = -1.33 ± 0.93 MPa/K.

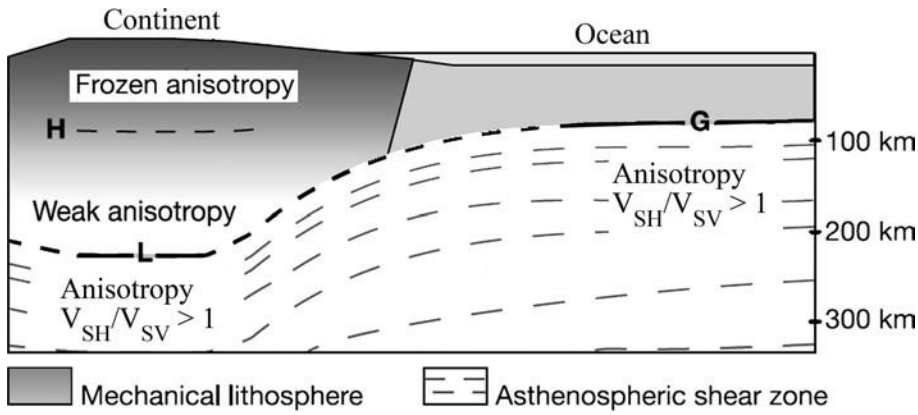

Fig. 3.44 Sketch illustrating an interpretation of the Lehmann (L) and Gutenberg (G) discontinuities in relation to seismic anisotropy; also shown is the Hales discontinuity (H) (from Gung *et al.*, 2003). Compare with Fig. 3.15 and 3.117.

3.4 Receiver function (converted waves) studies

3.4.1 The method

P- and S-converted waves

An incident seismic P-wave on an interface (crustal or mantle boundary with contrast seismic properties) continues as a direct (but deflected) P-wave and generates a converted S-wave (Figs. 3.45, 3.46). Similarly, an incident S-wave produces a converted P-wave. In the ideal situation of an isotropic horizontal-layered structure, P-to-S conversion results in SV phases so that all of the converted energy should be observed on the radial component and none on the transverse component, while the vertical component will be dominated by the high-amplitude initial P-wave (Vinnik, 1977). However, in teleseismic data P-to-SH conversions are commonly observed (Levin and Park, 1998).

The direct wave and a converted wave arrive at a receiver with a time difference t that depends on the depth H to the seismic interface, the velocities of the P- and S-wave in the layer above the interface, and the incidence angle of the impinging wave (i.e. the ray parameter = the slope of the travel time curve). In particular, for a P-to-S converted wave, the time separation between P_{direct} and Ps arrival is:

$$t = H\left(\sqrt{1/V_s^2 - p^2} - \sqrt{1/V_p^2 - p^2}\right), \tag{3.15}$$

where p is the ray parameter of the incident P-wave and Vs and Vp are average velocities in the layer between the velocity boundary and the receiver (Zhu and Kanamori, 2000).

If the velocity structure beneath the receiver is known, the converted phases may provide valuable information on the depth to seismic interfaces beneath the receiver. In

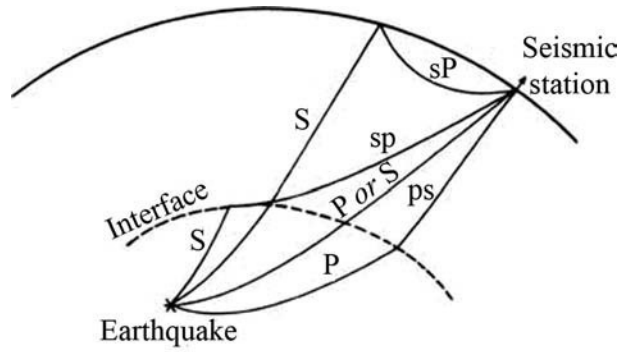

Fig. 3.45 Predicted ray paths for converted waves (from Sacks and Snoke, 1977).

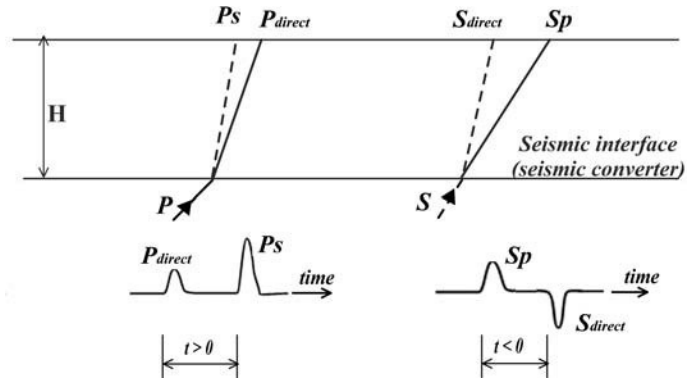

Fig. 3.46 Examples of P- and S-converted waves.

the real Earth, the incident wave produces not a single converted wave, but also multiples (Fig. 3.47). As for the primary P-to-S converted wave, their arrival times depend on the depth to the velocity contrast, the ray parameter of the incident P-waves, and the velocity structure of the layer between the seismic converter and the free surface. Since both the depth to the converter and the velocity structure above and below it are unknown, the ambiguity associated with the depth–velocity trade-off may be reduced by using the later arriving phases.

"Receiver functions"

To isolate the Earth structure near the receiver location, all other effects on the waveforms (such as distant structural variations and source effects) should be removed from the raw teleseismic data (Vinnik, 1977). "Receiver functions" are time-series that are computed from three-component seismograms after the response from the source and the vertically varying velocity structure beneath the receiver is isolated from the lateral heterogeneities.

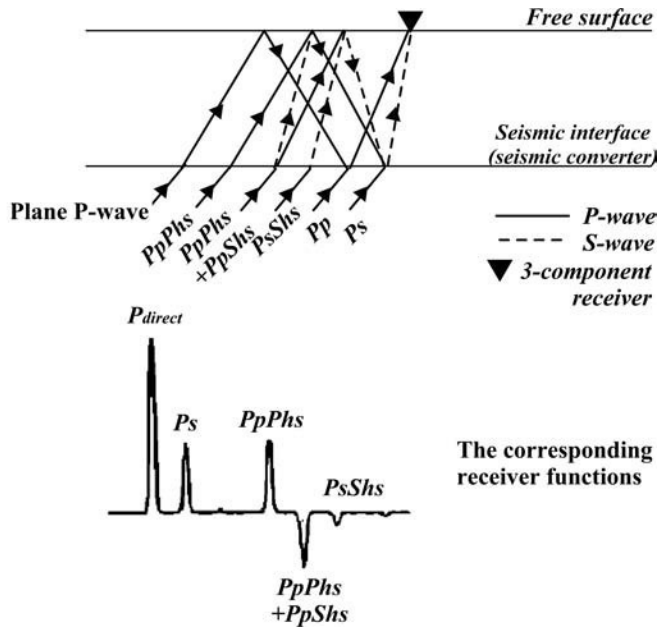

Fig. 3.47 A schematic ray diagram (upper) for major P-to-S converted phases and the corresponding receiver functions (lower) (redrawn after Ammon *et al*., 1990). The following convention is used in denoting the seismic phases: except for the first arrivals, lowercase letters refer to the upgoing phases and uppercase letters to the downgoing phases; *h* denotes reflection from the interface.

This is done by deconvolution of the vertical component (which contains primarily compressional motion) from the horizontal components of ground (shear) motion after the recordings are rotated to a coordinate system defined by the ray direction before deconvolution. To isolate the source effect, a special technique that takes advantage of the redundant source information in three-component seismograms has been proposed (Vinnik, 1977; Langston, 1979); to isolate the structure response an inversion method of Ammon *et al*. (1990) is commonly applied. The resultant time-series are dominated by the effects of the local structure beneath the receiver. This method, known as the Receiver Function (RF) technique, is effectively a 1D seismic method: it provides a point measurement to the depth of the seismic converter because typically the conversion point is laterally close to the station (approximately 1/3 of the depth to the interface and often within 10 km for crustal studies) so that lateral velocity variations can be ignored.

The amplitudes of the converted waves are small (for example, the amplitudes of the phases converted from discontinuities in the mantle are a few percent in amplitude of the parent wave), and special signal processing procedures are required to extract them from noise. A combined analysis of recordings (stacking) of seismic waves arriving from the same source region and recorded at the same seismograph station is commonly used to improve the signal-to-noise ratio of weak secondary signals used in the receiver function approach. Assuming a similar level of noise in individual receiver functions (individual

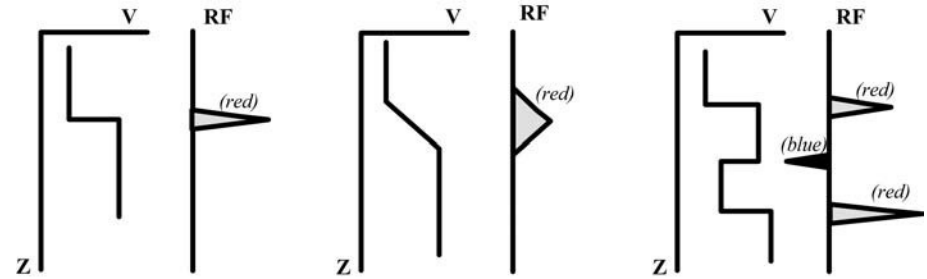

Fig. 3.48 Sketch illustrating receiver functions that correspond to three simplified velocity structures. Positive arrivals correspond to positive velocity contrast (conventionally shown in red); negative arrivals indicate the top of the low velocity zone (conventionally shown in blue).

waveforms radiated from different earthquakes), an improvement in the signal/noise ratio in the stack is proportional to the square root of the number of recordings. The amplitudes of the arrivals in RF depend on the incidence angle of the impinging wave and on the velocity contrast across the seismic converter. The latter property makes teleseismic RF (in which the arriving wave can be considered as a plane wave) a powerful tool for identifying the depth to major seismic interfaces in the lithosphere (primarily, depth to the Moho) and in the mantle (depth to the transition zone). To simplify visualization of RF interpretations, the positive polarity of the converted phase (which corresponds to a converter with a velocity increase with depth) is commonly shown in red and negative polarity (which corresponds to the top of a low velocity layer), in blue (Fig. 3.48).

Limitations of the RF method

The depth–velocity trade-off

RF inversions are non-unique and are primarily sensitive to the depth–velocity product (eq. 3.15) (Ammon *et al*., 1990). Thus, to determine the depth to a seismic converter, *a-priori* information from other seismic experiments is necessary to reduce the velocity–depth ambiguity. A comparison of travel times in a seismic experiment with travel times for standard reference models may help to exclude extreme models and limit the range of possible solutions.

An algorithm of stacking multiple converted phases (Zhu and Kanamori, 2000) is now in standard use to overcome the trade-off between the velocity structure and the depth to seismic converters. For these phases, the amplitudes of RF at all possible arrival times are summed for different thicknesses H of the layer (e.g. the crust) and different $k = V\mathrm{p}/V\mathrm{s}$. This procedure effectively transforms RF from the time domain into the depth (k–H) domain without the need to pick the arrival times of these phases. It provides the best estimations for both the depth to the converter and the $V\mathrm{p}/V\mathrm{s}$ ratio (Fig. 3.49). An *average* crustal model can be obtained by stacking RF from different distances and different directions.

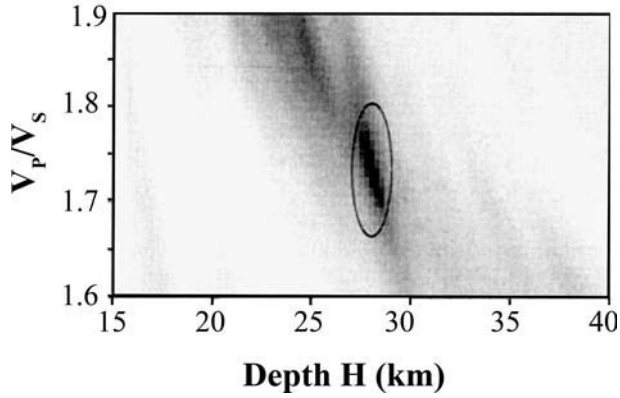

Fig. 3.49 Stacked receiver functions in the *V*p/*V*s – *H* domain used to determine the crustal thickness, *H*, beneath the PAS station in Southern California. The best estimate is 28 km with a *V*p/*V*s = 1.73; the ellipse shows the 1σ uncertainty (Zhu and Kanamori, 2000).

Moho and intracrustal discontinuities

Since the amplitudes of the arrivals in a RF depend on the velocity contrast at the seismic converter, a boundary with the largest velocity contrast will produce the strongest converted waves. Therefore, in crustal studies the largest contrast need not necessarily be at the base of the crust but may be at an intracrustal boundary. For example, in the case of a high-velocity lowermost crust with *V*p ~ 7.5 km/s, the velocity contrast at the Moho may be only *c*. 0.5 km/s, while the velocity contrast between the middle and the lowermost crust may be as large as 1.0 km/s. In such a case, the RF method will likely image the depth to the sharp intracrustal interface but not to the Moho. This may be the case in Greenland where conflicting depths to the Moho have been derived by RF, while refraction results agree with the deepest determination of the crust–mantle transition (Dahl-Jensen *et al*., 2003; Kumar *et al*., 2007). A similar example comes from Iceland, where the seismic signal from the Moho boundary varies from undetectable, to gradient zones and discrete discontinuities (Schlindwein, 2006). The complicated character of the signal is caused by the velocity structure of the crust, with the layer of rapid velocity increase at 8–14 km depth overlying the layer with almost constant velocities, which is masking seismic phases from the Moho.

Mantle discontinuities and the S-receiver functions

The RF method based on P-to-S converted waves has a disadvantage in studies of mantle seismic interfaces located at a depth of *c*. 70–200 km since in P receiver functions (PRF), the converted P phases from discontinuities in the mantle arrive in the time interval dominated by multiple reflections and scattering from crustal discontinuities (not necessarily from the Moho, but from the strongest crustal reflectors) (Fig. 3.50). To overcome this problem, the RF technique based on the S-to-P conversions has been proposed,

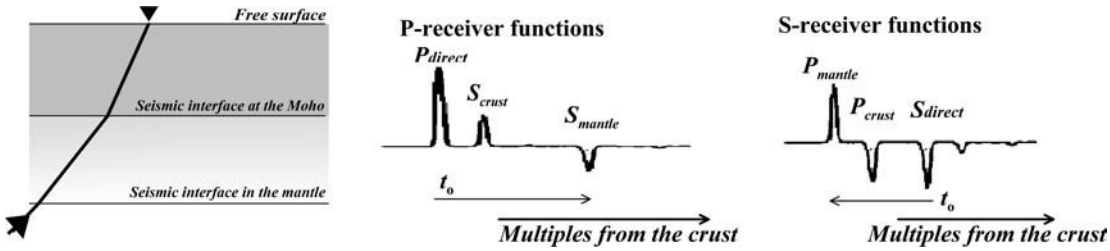

Fig. 3.50 A schematic diagram of P- and S-receiver functions for a seismic converter at 70–200 km depth in the mantle. In P-receiver functions phases from the mantle converter arrive within the crustal multiples and may not easily be identified. In contrast, in S-receiver functions it is the direct S-wave that arrives within the crustal multiples (due to high amplitude it can always be identified), while phases from the mantle converter arrive earlier and can also be easily identified.

in particular to study the depth to the lithosphere base (Farra and Vinnik, 2000). The S-receiver function technique (SRF) is based on the analysis of S-to-P converted phases (*Sp*) at seismic discontinuities in the upper mantle beneath stations. P-waves converted from a mantle velocity contrast arrive at the station much earlier than the direct S-waves, while all the multiple crustal reverberations arrive later than the S arrival (Fig. 3.50). Since high-amplitude direct S-waves can usually be easily identified even when they arrive within the crustal multiples, the S-receiver function analysis has advantages in studies of mantle discontinuities. Moreover, gradational boundaries in the mantle with a thickness of *c*. 30 km may be transparent at short periods (2–5 s) in PRF, but may be detectable at longer periods (10–15 s) in SRF.

A detailed discussion of the advantages and limitations of the S-receiver function technique is presented by Farra and Vinnik (2000) and is summarized here in brief:

- the time advance of the converted phase *Sp* relative to the direct S-wave depends on the depth of the discontinuity;
- the amplitude of *Sp* phase is nearly proportional to the *V*s velocity contrast at the discontinuity;
- the approximate position of the region sampled by the converted phase is at a roughly similar distance from the seismic station as the depth of the discontinuity;
- the greatest depth sampled by the SRF depends on epicentral distance;
- the method allows for detection of converted phases from the 410 km discontinuity implying that the SRF method is sensitive to detection of a *V*s velocity contrast of *c*. 0.2 km/s at a depth of about 400 km.

The apparent velocity of the *Sp* phase converted from a deep discontinuity may differ from the apparent velocity of the parent phase. For example, for the *Sp* phase from the 410 km discontinuity, the difference between the slowness of the *Sp* phase and its parent seismic phase (differential slowness) is around 0.6 s/deg for a standard Earth model. Because of noise or lateral heterogeneity of the Earth's structure, the observed slowness (the slowness of

the trace with maximum amplitude of signal) may deviate from the theoretical predictions and for the phase converted at a dipping interface differential slowness may diverge from the standard value by about 0.2 s/deg for a tilt of 1 deg.

3.4.2 Examples of PRF and SRF studies of the crust and the upper mantle

Thickness of Precambrian crust in Greenland

Over the past two decades, receiver function analysis has become a routine technique for estimating the depth to the Moho. The method has been successfully used, in particular, in imaging the crust–mantle transition in complex tectonic settings such as subduction zones (e.g. Bostock *et al*., 2002; Li *et al*., 2003b).

One of the most spectacular examples is the RF application to the GLATIS (Greenland Lithosphere Analysed Teleseismically on the Ice Sheet) seismic data acquired in the interior parts of Greenland where the crustal thickness was previously completely unknown (Fig. 3.51) (Kumar *et al*., 2007; Dahl-Jensen *et al*., 2003). In spite of the excellent data quality, RF interpretations for four out of 16 temporally deployed broadband stations were complicated by strong converted phases generated at the base of the ice sheet (more than 3 km thick in some places). Since RF analysis is based on the assumption that the observed

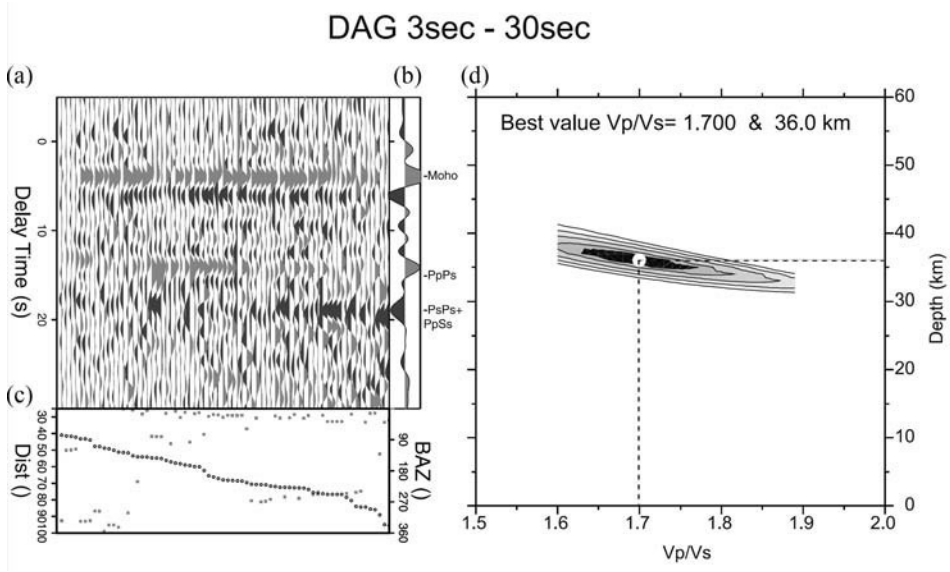

Fig. 3.51 Individual receiver functions (RFs) from all events used at the permanent seismic station DAG on the coast of northern East Greenland (a), the sum of the normal move-out-corrected individual RFs (a positive *P*s has a peak to the right) (b), the distance in degrees (black symbols) and azimuth in degrees (gray symbols) for each event (c), and a plot of stack energy for various V_P/V_S ratios and the depth to Moho. V_P is assumed to be 6.5 km/s (from Dahl-Jensen *et al*., 2003).

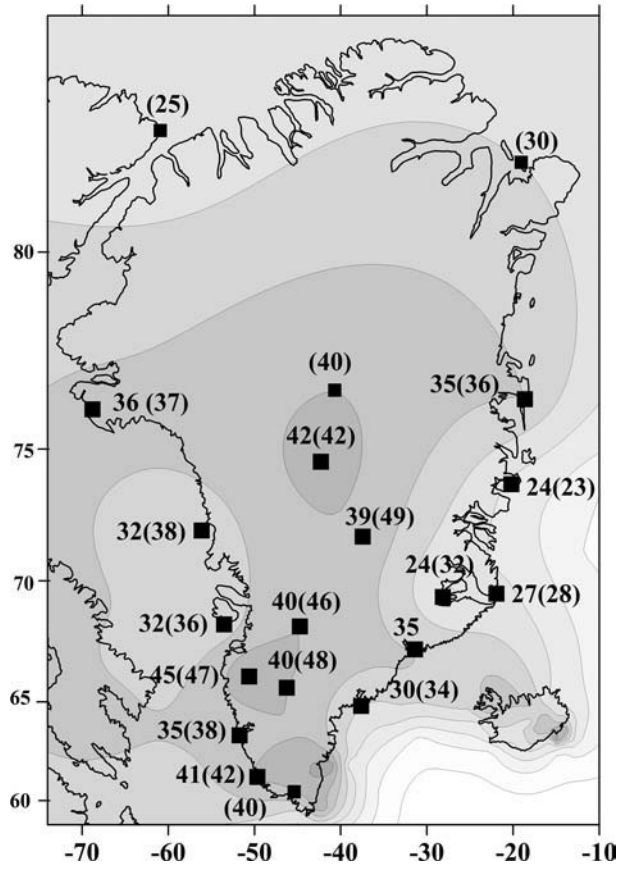

Fig. 3.52 Crustal thickness in Greenland (in km) based on receiver function analysis. Numbers – interpretations of Kumar *et al*. (2007) (no brackets) and Dahl-Jensen *et al*. (2003) (brackets). Seismic stations are shown as boxes.

wavefield is acquired at the free surface of an elastic half-space, seismic data collected on ice and on the ocean bottom have an added complication for RF interpretations as the time series constrained by standard methods may contain scattered energy from the ice or water column.

Receiver function studies in Greenland revealed significant lateral variations in the depth to the Moho. While the extended crust along the coast of East Greenland is less than 30 km thick, the Proterozoic part of central Greenland (north of the Archean core) has the largest values with an average depth to Moho close to 48 km (Fig. 3.52). Further to the north the Proterozoic crust is thinner, 37–42 km; similar values (around 40 km) were determined for the Archean crust in southern Greenland. Variations of 6–8 km in the thickness of the Proterozoic crust in Greenland may reflect the tectonic boundary between two ancient terranes (Dahl-Jensen *et al*., 2003). However, later studies based on RF analysis of the same GLATIS data indicate significantly smaller values of crustal thickness in the Proterozoic terranes, 39–42 km, with little lateral variations in central

Greenland (Kumar *et al*., 2007). A systematic difference in the values reported in the two studies for stations in central Greenland may suggest that the later study (with a systematically smaller crustal thickness) mapped, rather than the Moho, the top of the high-velocity lowermost crust, which is known to be present in regions with magmatic underplating in the crust. Alternatively, the difference between the two studies may be associated with strong converted phases from the ice column, since the largest discrepancy between the results is observed at the stations in inner Greenland where the ice thickness exceeds 2 km.

Lithosphere thickness in the collisional orogens of Central Asia

S-receiver functions (SRF) are a useful tool in mapping mantle discontinuities in the depth range obscured by crustal multiples present in P-receiver functions (PRF), such as the base of the lithosphere. Spectacular images of the upper mantle structure in Tibet, the Himalayas, and Central Asia constrained by RF for individual stations along a seismic profile provide 2D constraints on the dynamics of lithospheric plates in the zone of the largest present continent–continent collision and seismic images of Eurasian plate subduction (Kind *et al*., 2002).

In the Tien Shan, RF studies of the lithosphere structure, initiated almost two decades ago (Kosarev *et al*., 1993), clearly show converted phases from two interfaces: the upper with a positive velocity contrast is interpreted as the Moho. Different RF studies have revealed strong lateral variations in the crustal thickness of the Tien Shan and the Tarim Basin, with values ranging from 45 km to 65 km. The crustal thickness increases southwards to 80 km in northwest Tibet and exhibits a *c*. 20 km step in Moho depth across the Altyn Tagh Fault (Wittlinger *et al*., 2004).

The lower interface has a negative velocity contrast and is interpreted as the top of a layer with reduced seismic velocities. Although this interface may not necessarily be the lithosphere–asthenosphere boundary (LAB), in most studies it is hypothesized to be the lithospheric base. Under this assumption, lithosphere thickness variations in the Tien Shan region as determined from S-receiver functions are moderate, 90 km to 110 km (Oreshin *et al*., 2002). A later study, based on the same approach (Kumar *et al*., 2005), however, reported significant variations in the lithosphere thickness of the region: arrival times for converted waves range from *c*. –10 sec to *c*. –30 sec, which for the *iasp91* model results in depths ranging from 90 km to almost 300 km (Fig. 3.53). The depth of the mantle interface with a negative velocity contrast is in fairly good agreement with a lower resolution, surface wave tomography image of the region, which shows a high velocity body at 80–180 km depth in the south (presumably the Indian plate) and a southwards dipping low-velocity body in the north, that was interpreted as evidence for subsidence of the rigid Tarim Basin block of the Asian lithosphere under the Pamir and Karakoram ranges (Kumar *et al*., 2005). However, such an interpretation requires further support on the depth of the lithosphere–asthenosphere boundary since mantle discontinuity with a negative velocity contrast may not necessarily be the base of the lithosphere but, for example, a compositional intralithospheric boundary.

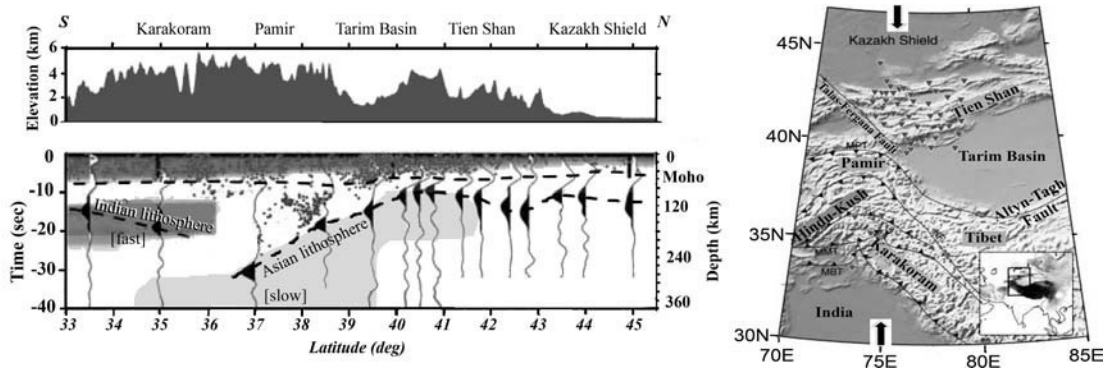

Fig. 3.53 Seismic section across the India–Asia collision zone (along 75 deg longitude) from S-receiver function analysis. Top panel – the topography along the profile. Bottom panel – depth to the Moho and to the upper mantle discontinuity with a negative velocity contrast. Zero time corresponds to the arrival time of the direct S-phase. Negative time-scale indicates times in front of the S arrival. Due to moveout correction the time axis is valid for a slowness of 6.4 s/deg. Gray shadings show velocity anomalies in the crust and the upper mantle based on surface wave tomography (dark shading – fast velocities, light shading – slow velocities). Dots are the earthquake hypocenters within a 100 km wide zone along the line. Right panel: location map with shaded topography (redrawn from Kumar *et al*., 2005).

Compositional boundary within the cratonic lithospheric mantle?

The presence of a prominent interface with a 4.5% reduction in seismic velocity in a 10 km thick layer at approximately 150 km depth has been identified beneath the Kalahari craton by S-receiver functions (Savage and Silver, 2008). Since xenolith data as well as numerous seismic investigations based on various techniques consistently place the lithospheric base beneath the Kalahari craton at greater depth, 200–220 km, the converter at 150 km depth represents an intralithospheric boundary. This boundary crosses several Archean sutures and is unlikely to be related to the Archean tectonics. The base to the boundary corresponds approximately to the depth where olivine grain size decreases (Fig. 3.10a). A decrease in grain size should reduce seismic velocities (Figs. 3.6a, 3.14); however the effect is probably too weak to explain the seismic structure of the Kaapvaal mantle. Spatial correlation of the strongest velocity anomaly with intense Karoo volcanism suggests that the seismic discontinuity is a compositional boundary that marks the transition from a depleted (high-velocity) cratonic lithospheric mantle to the lower part of the lithosphere that experienced the influence of basaltic melts and metasomatic fluids, which have refertilized the cratonic lithosphere.

Similar conclusions based on buoyancy analysis have been made for the southern parts of the Archean–Paleoproterozoic East European (Russian) Platform that have been subsiding since the Paleozoic (Artemieva, 2003). Voluminous basaltic magmatism associated with the Devonian (possibly, plume-related) rifting in the Peri-Caspian Basin and in the Sarmatia subcraton (where it has led to formation of the huge, more than 20 km deep, Dnieper–Donets rift) could have refertilized the lower part of the cratonic lithosphere and therefore increased

its density and created negative compositional buoyancy. The boundary between a highly depleted upper layer (with high seismic velocities) and a more fertile lower layer (with lower velocities) in the cratonic lithospheric mantle can produce a seismic discontinuity with negative velocity contrast similar to the one detected by SRF beneath the Kalahari craton (Savage and Silver, 2008).

Similarly, the presence of a seismic discontinuity with negative velocity contrast has been observed in other stable continental regions and can be a global feature for the Precambrian lithosphere; the depth to the top of this discontinuity varies from 80–100 km to *c*. 120–130 km (Thybo and Perchuc 1997a). A layer with reduced (*c*. 0 +1% as compared to the global continental model *iasp91*) seismic velocity has been identified within the high-velocity (*c*. +1 +3% as compared to the *iasp91* model) Proterozoic lithospheric mantle of the Baltic Shield along the FENNOLORA profile (Perchuc and Thybo, 1996), within the Archean Karelian mantle (Bruneton *et al*., 2004), within the Precambrian lithospheric mantle of the northeastern East European Platform along the long-range profile Quartz (Ryberg *et al*., 1996), within the lithospheric mantle of the West Siberian Basin and the Siberian craton (Nielsen *et al*., 1999), within the Precambrian lithospheric mantle of the central US (Rodgers and Bhattacharyya, 2001), the Canadian Shield (LeFevre and Helmberger, 1989), and Greenland (Darbyshire, 2005). In some regions (the Baltic Shield, North America) the observed reduction in S-velocity may be stronger than the reduction in P-velocity. Possible explanations for a layer with reduced seismic velocity within a high-velocity lithospheric mantle of a cratonic root include the presence of fluids, small pockets of partial melts (or temperature close to the solidus), metasomatism, or compositional variations.

Mantle transition zone and thermal state of the upper mantle

The mantle transition zone is bounded by two principal discontinuities at approximately 410 and 660 km depths. Seismological observations and data from experimental mineralogy indicate that although both the 410 and 660 km discontinuities are sharp, they may spread over a depth interval of *c*. 4–10 km. For example, transformation of α-olivine to β-phase takes place over a pressure interval of *c*. 0.25 GPa where both phases coexist. This would result in a transitional discontinuity at 410 km depth spread over *c*. 7 km. The presence of even a small amount of water in the mantle stabilizes the β-phase over a wider range of pressure and temperature and further broadens the transition interval (Wood, 1995). Recent experimental high-pressure, high-temperature mineralogical studies indicate that water in the mantle has a significant effect on the topography of seismic discontinuities in the transition zone, in particular along the active margins. There is significant depression of the 660 km seismic discontinuity and an upward shift of the 410 km seismic discontinuity by 1–2 GPa which may be associated not only with cold subduction but also with wet subduction (Litasov *et al*., 2005).

The RF technique allows for high-resolution determination of the transition zone thickness near a station (Fig. 3.54) (Vinnik, 1977). The P-to-S converted waves from the 410 and 660 km discontinuities travel practically identical paths through the upper mantle

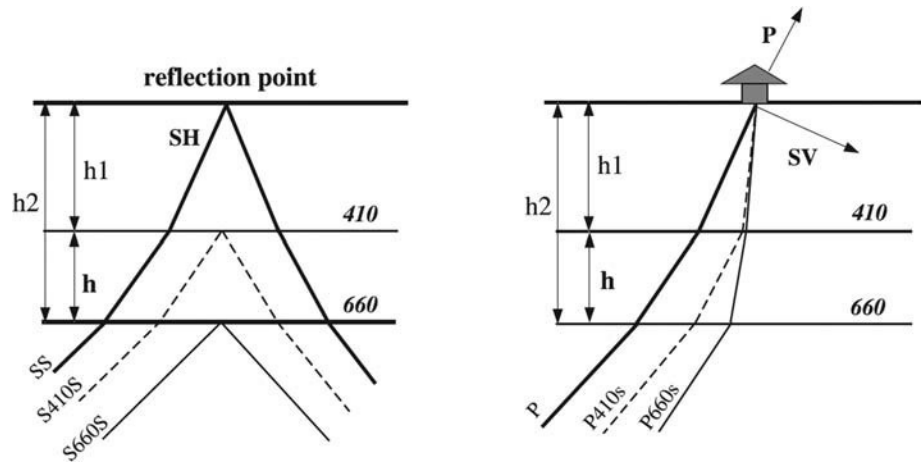

Fig. 3.54 Two approaches for calculation of the transition zone (TZ) thickness (from Gu and Dziewonski, 2002). Left: TZ thickness (*h*) is calculated from direct measurements of *S410S-S660S*, which is approximately twice the travel time of a near-vertical shear wave through the TZ. A schematic ray diagram shows SS and its precursors. Right: TZ thickness (*h*) is calculated from the differential times of *(P660s-P)-(P410s-P)* assuming that the ray parameter and both the P and the S velocities are known. A schematic ray diagram shows *P*ds phases (d denotes a TZ discontinuity).

above the 410 km phase boundary. Thus, the difference in their conversion times, $\Delta t = t_{660} - t_{410}$, characterizes the transition zone alone. The uncertainty in Δt estimates is typically less than 2 s (Gu and Dziewonski, 2002). The presence of velocity structure within the transition zone itself can produce another, up to 2 s, uncertainty in interpretations, but can successfully be overcome by computing the travel time residuals from two-way S travel time for a shear-wave that travels through the transition zone under each location (cap) (Fig. 3.55). Another complication in interpretations of the transition zone thickness arises from the fact that RF treats the arriving wave as a plane wave. Compared to a spherical wave, the plane wave approximation will lead to an overestimation of the time delay anomaly (up to 1.2 sec for an epicentral distance of 30–35°) and the transition zone thickness anomaly (up to 11 km for an epicentral distance of 30°) (Lawrence and Shearer, 2006). Due to velocity–depth trade-off in the RF analysis, larger Δt differences may indicate either greater thickness of the transition zone or lower seismic velocities above it. For the *iasp91* model, a change of 1 s in Δt corresponds approximately to a 10 km change in transition zone thickness.

An important property of the mantle transition zone is that its thickness provides important independent constraints on the thermal state of the overlying mantle. A decrease in mantle temperature causes elevation of the exothermic 410 km phase boundary (α-olivine → β-olivine phase transition) but depression of the endothermic 660 km phase boundary (γ-olivine → perovskite + magnesiowüstite phase transition) (see Fig. 9.12). An increase in mantle temperature has opposite effects on both of the discontinuities. Thus, the depths to the discontinuities are anticorrelated which results in a

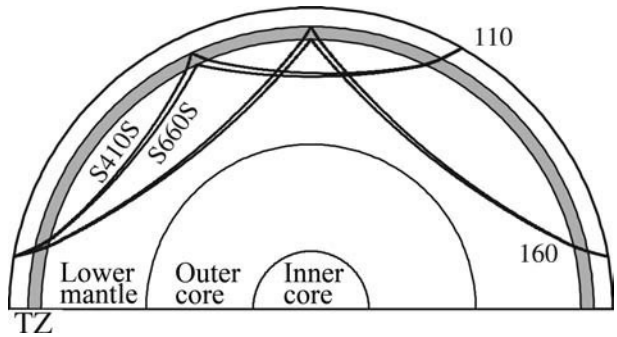

Fig. 3.55 A schematic diagram showing underside reflections *S410S* and *S660S* from the 410 km and 660 km discontinuities at distances of 110° and 160° (Gu and Dziewonski, 2002). The travel times *S410S-S660S* are primarily sensitive to transition zone (TZ) thickness near the reflection points.

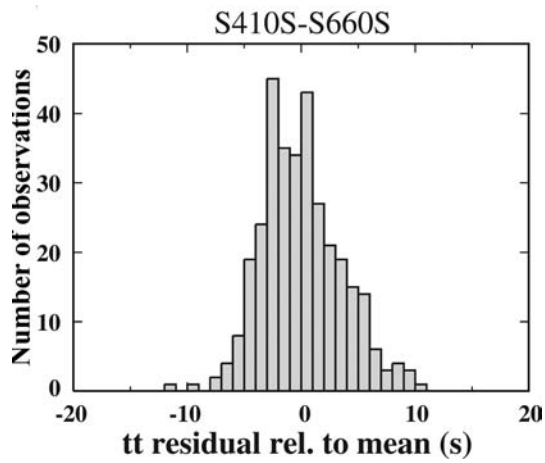

Fig. 3.56 Travel time residuals of the S410S-S660S measurements show an almost normal distribution with significant variations from the mean value of 242 ± 2 km (from Gu and Dziewonski, 2002).

decreased thickness of transition zone in regions with high mantle temperatures and increased thickness in regions where the ambient mantle is colder than average. The temperature effect on the conversion times difference Δt is commonly assumed to be $\partial(\Delta t)/\partial T = +0.009$ s/K. This means that a temperature variation in the mantle of *c*. 110 K will produce a Δt of *c*. 1 sec.

Global analyses of the travel time residuals of the S410S-S660S measurements show an almost normal distribution of transition zone thickness with a mean value of 242 ± 2 km and with significant (±10 km) deviations from it (Fig. 3.56) (e.g. Flanagan and Shearer, 1998). Globally, the thickness of the mantle transition zone is correlated with surface tectonics and shows a significant difference between the oceanic and the continental mantle (Figs. 3.57, 3.58). Different interpretations are consistent in showing

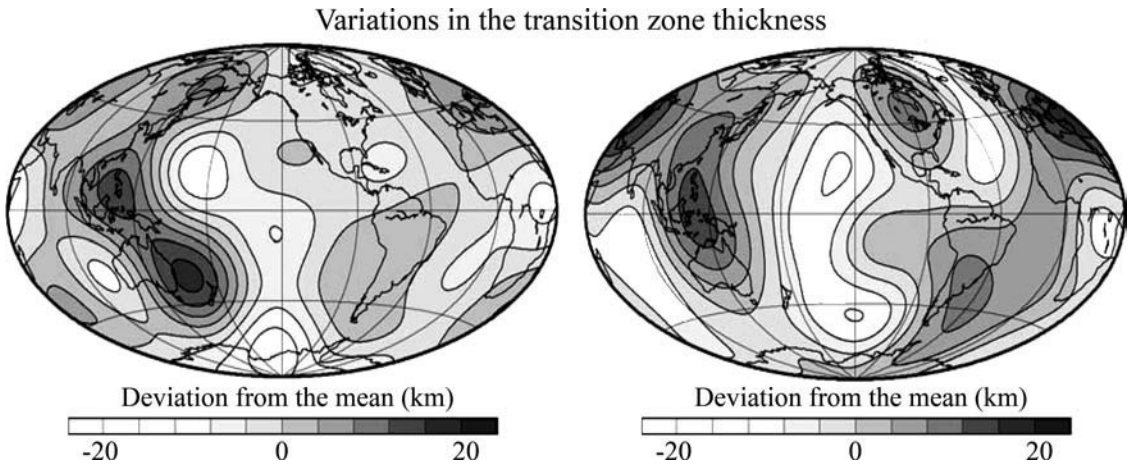

Fig. 3.57 Global variations in the transition zone thickness (left: interpretations of Flanagan and Shearer, 1998; right: interpretations of Gu and Dziewonski, 2002). Maps were filtered with a low-pass filter up to degree-6 spherical harmonics (from Gu and Dziewonski, 2002).

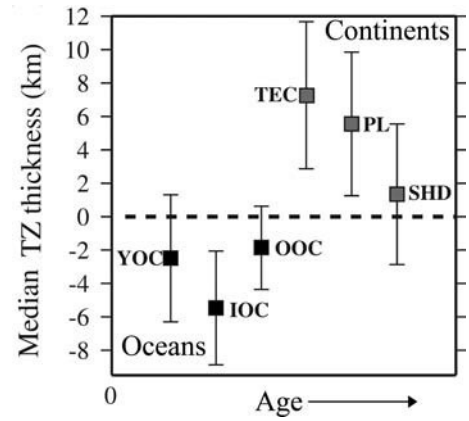

Fig. 3.58 Global variations in the transition zone thickness averaged for six tectonic provinces: YOC = young ocean; IOC = intermediate-age ocean; OOC = old ocean; TEC = tectonically active parts of the continents; PL = stable platforms; SHD = shields (from Gu and Dziewonski, 2002). The age-scale is non-linear.

significantly reduced thickness of the transition zone in oceanic regions, with the strongest anomaly in the Pacific Ocean. In continental regions the thickness of the transition zone is increased and the strongest anomaly is in Indochina. The thickness of the transition zone does not correlate with crustal age either in the oceans or on the continents (Fig. 3.58). The largest increase in transition zone thickness is observed in tectonically young continental structures and is apparently caused by cold subducting slabs in their mantle.

3.5 Controlled source methods: reflection/refraction studies of the upper mantle

3.5.1 Seismic reflection studies

The method and its resolution

Preamble

Application of the reflection method to geology was patented in 1916 in Germany by Ludger Mintrop and was first applied to hydrocarbon exploration in Oklahoma in 1920–1921. Since the mid 1970s the method has been widely used for crustal studies on the continents (e.g. profiles of COCORP in the USA, LITHOPROBE in Canada, ACORP in Australia, DEKORP in Germany, BIRPS in the U.K., ECORS in France, URSEIS in the Urals, FIRE in Finland, BABEL and MONA LISA profiles in the North and Baltic Sea) and, in particular, in the hydrocarbon exploration industry (for details see summary by Barazangi and Brown, 1986). Detailed reviews of reflection seismology can be found in Claerbout (1985) and Sheriff and Geldart (1982).

Seismic reflection data are typically recorded with dense regular shot and receiver spacing (commonly 50–500 m and 25–100 m, respectively) and to short offsets (<10 km). Controlled-source reflection seismology is based on the analysis of travel time (rather than amplitude) of seismic waves transmitted from the surface and reflected back to the surface from interfaces between geological layers with a contrast in the acoustic impedance (the product of seismic velocity and density). The amplitude of the reflected signal depends on the strength of the contrast in velocity or density. Such interfaces with a short wavelength change in elastic properties or density are loosely termed seismic discontinuities. Reflection seismology provides images of seismic discontinuities in the crust and the mantle and thus provides images of the structural geometry of the lithosphere, often with greater lateral and vertical resolution than refraction seismology.

Interpretation of seismic reflection data is based on application of:

(1) stacking of records to improve signal-to-noise ratio (stacking techniques use the normal moveout (NMO) correction for hyperbolic curvature of reflection travel times followed by the common midpoint (CMP) stacking),
(2) migration to compensate for energy scattering from dipping layers (effective for a dip less than 30°) and from lateral heterogeneities by summing along possible sources of scattered energy, and
(3) time shifts (static corrections) to compensate for variations in elevation and near-surface geology for on-shore profiles.

Resolution of reflection methods

The relative vertical resolution of seismic reflection studies is proportional to the wavelength of the seismic signal (Widess, 1982), i.e.

$$\delta \sim 0.25 V_p / f, \tag{3.16}$$

where Vp is P-wave velocity (in km/s) and f is frequency (in Hz). This yields a vertical resolution of *c*. 60 m for $f = 25$ Hz in a continental crust with average velocity of *c*. 6.0 km/s. In the upper mantle, reflected P-waves are dominated by frequencies of *c*. 20 Hz which correspond to wavelengths of *c*. 400 m (Bostock, 1999). The resolution increases with frequency increase and in upper crustal studies may reach 10–20 m for high-frequency signals. The horizontal resolution of seismic reflection studies is poorer. It depends on the size of the Fresnel zone (see eq. 3.14) and decreases with depth. This means that reflectivity gaps with lateral dimensions less than *c*. 3 km cannot be resolved using reflection data.

The depth measure used in seismic reflection is in two-way travel time (TWT) for the vertical travel path below the shot point, and knowledge of the average velocity structure is required to convert it to depth. Typically, reflection data cannot provide background velocities. Thus, most seismic reflection profiles are plotted as time sections rather than depth sections, and reflection surveys are often complemented by refraction experiments, where errors in the calculated depth can be 5–6%. In cases where external velocity data are unavailable, velocity structure is estimated directly from reflection data.

Origin of crustal and mantle reflectivity

Crustal reflectivity

Seismic reflectors are caused by contrasts in seismic velocity and/or density. However, globally, lower crustal reflectivity does not correlate with any intracrustal velocity boundaries but is rather controlled by crustal viscosity (Mooney and Brocher, 1987). Several mechanisms (reviewed by Mooney and Meissner, 1992) have been proposed to explain crustal reflectivity, and one or more of these mechanisms can be responsible for seismic reflectivity in different tectonic settings:

- lithologic and metamorphic layering (i.e. presence of mylonite zones)
- compositional layering (e.g. due to igneous intrusives into the crust)
- layered crustal porosity and the presence of pore fluids (probably applicable only for the upper crust)
- lenses of partial melt
- reflections from fault zones
- mineral alignment caused by ductile flow
- velocity anisotropy introduced by the preferred orientation of olivine crystals.

Reflection Moho

As suggested by refraction seismic surveys, the Moho is usually a compositional boundary which marks the transition from the crust to the upper mantle. By comparison with refraction data in coincident reflection/refraction seismic experiments, the "reflection Moho" is commonly assigned to the base of a package of nearly continuous reflectors at

TWT 8–12 sec which is underlain by a nearly transparent zone with no (or very few) seismic reflectors. The mantle below the "reflection Moho" generally does not reflect seismic waves at near-vertical incidence with frequencies >5–8 Hz (except at local structures such as shear zones). This implies that the "reflection Moho" corresponds to an intralithospheric boundary with an abrupt change in the scale of scattering heterogeneities: lower crustal heterogeneities have much smaller dimensions than upper mantle heterogeneities (Fuchs and Wenzel, 1997).

There are no *a-priori* reasons to assume that the bottom of the lower crustal reflectivity package (which is a structural characteristic) should correlate with the depth with a sharp increase in seismic velocity (associated with a compositional boundary). The origin of the general agreement between the reflection and the refraction Moho as observed in many continental studies is the subject of some debate. It is proposed that the Moho is a compositional boundary formed during chemical differentiation within the lithosphere; the aspect ratios of velocity heterogeneities and density of their distribution may be directly linked to the process of lithosphere differentiation and to magmatic processes. Alternatively or additionally, relative motion between the crust and the mantle at detachment zones facilitates differential deformation between the crust and the mantle.

Seismic discontinuities in the upper mantle

Global seismic reflection observations indicate that the upper mantle is homogeneous at seismic reflection wavelength. However, some isolated mantle reflectors have been identified at depths of 70–100 km and more, for example in long-range PNE (Peaceful Nuclear Explosions) profiles recorded in the USSR between the 1970s and 1990s (see next section). By analogy with strong reflectivity of the lower crust, which is believed to be caused by ductile flow, transparency (weak reflectivity) of the subcrustal lithosphere may be controlled by mantle rheology. Thus, if reflectivity of the upper mantle is essentially controlled by its ability to form laminations and anisotropy through shear flow, the reflectivity pattern can be a measure of upper mantle (lithospheric) rheology. Rheological discontinuities within the lithosphere imaged by reflection seismology may also reflect changes in deformation mechanisms (Karato and Wu, 1993). The base of the lithosphere is generally accepted to be a rheological boundary separating rigid lithospheric plate from less viscous convective mantle, and thus it manifests itself as a seismic discontinuity. Deeper in the mantle, phase changes in the minerals, in particular in olivine, caused by pressure and temperature increase with depth, are responsible for seismic discontinuities at 410, 520, and 660 km depths.

Seismic reflection expression of tectonic styles

Most reflection profiles are limited to the crustal depths and only a few reach to 80–100 km depths. Since reflection seismology is a big topic, and in particular for crustal studies, the focus here will be solely on reflection expression of different tectonic styles with emphasis on reflection studies of the subcrustal lithosphere.

Extended continental crust

Reflectivity patterns observed in the lithosphere are well correlated with distinct tectonic settings. One of the most interesting results of seismic reflection surveys comes from reflection transects through regions with extended continental crust and passive margins. These regions have a highly reflective lower crust which is in sharp contrast with the almost transparent upper mantle and nearly flat reflection Moho (Fig. 3.59). Such a pattern is observed in the Cenozoic Basin and Range Province in western USA and the Paleozoic Variscides of western Europe which, despite the differences in ages of the crustal extensions, have similar crustal reflectivity: in both regions the reflection Moho is at a *c*. 30 km depth and ignores the diversity of tectonic regimes and structures at the surface (e.g. Allmendinger *et al*., 1986; Meissner, 1999). The crust of the *c*. 3000 km long Variscan belt of Europe (Figs. 3.60; 3.61), which was formed by multiple Paleozoic terrane and continent–ocean collisional events, contains the Variscan collisional and subduction structures but has a nearly uniform crustal thickness. Flat Moho both in the Basin and Range Province and in the European Variscides is usually ascribed to extensional processes that have removed crustal roots below the pre-existing orogens (lower crustal eclogitization and delamination is an alternative explanation). For example, in western USA, crustal extension along a *c*. 323 km long profile varies from 300% in the western part of the profile to 15% in its central and eastern parts (Gans, 1987).

The lower crustal reflectivity in regions with extended crust is caused by compositional, metamorphic, and mineralogical layering (Mooney and Meissner, 1992). Its origin is attributed to mafic intrusions and ductile flow in the lower crust which make the reflectors

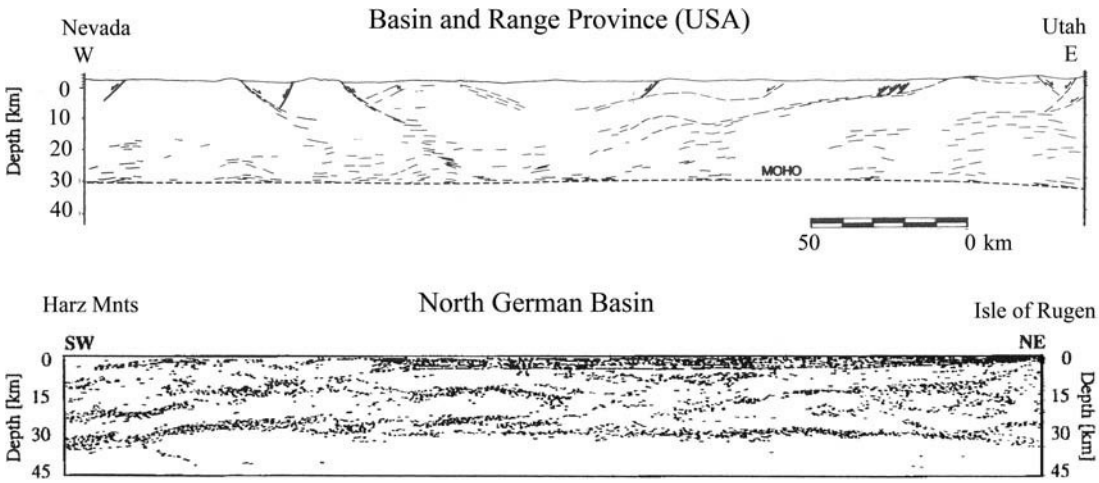

Fig. 3.59 Two reflection profiles through continental regions with extended crust. Upper: through the Basin and Range Province, western USA, along the COCORP 40° N seismic reflection transect (after Klemperer *et al*., 1986). Lower: through the European Variscides (North German Basin) along the DEKORP profile (from Meissner, 1999). Note flat Moho and poor upper mantle reflectivity along both profiles.

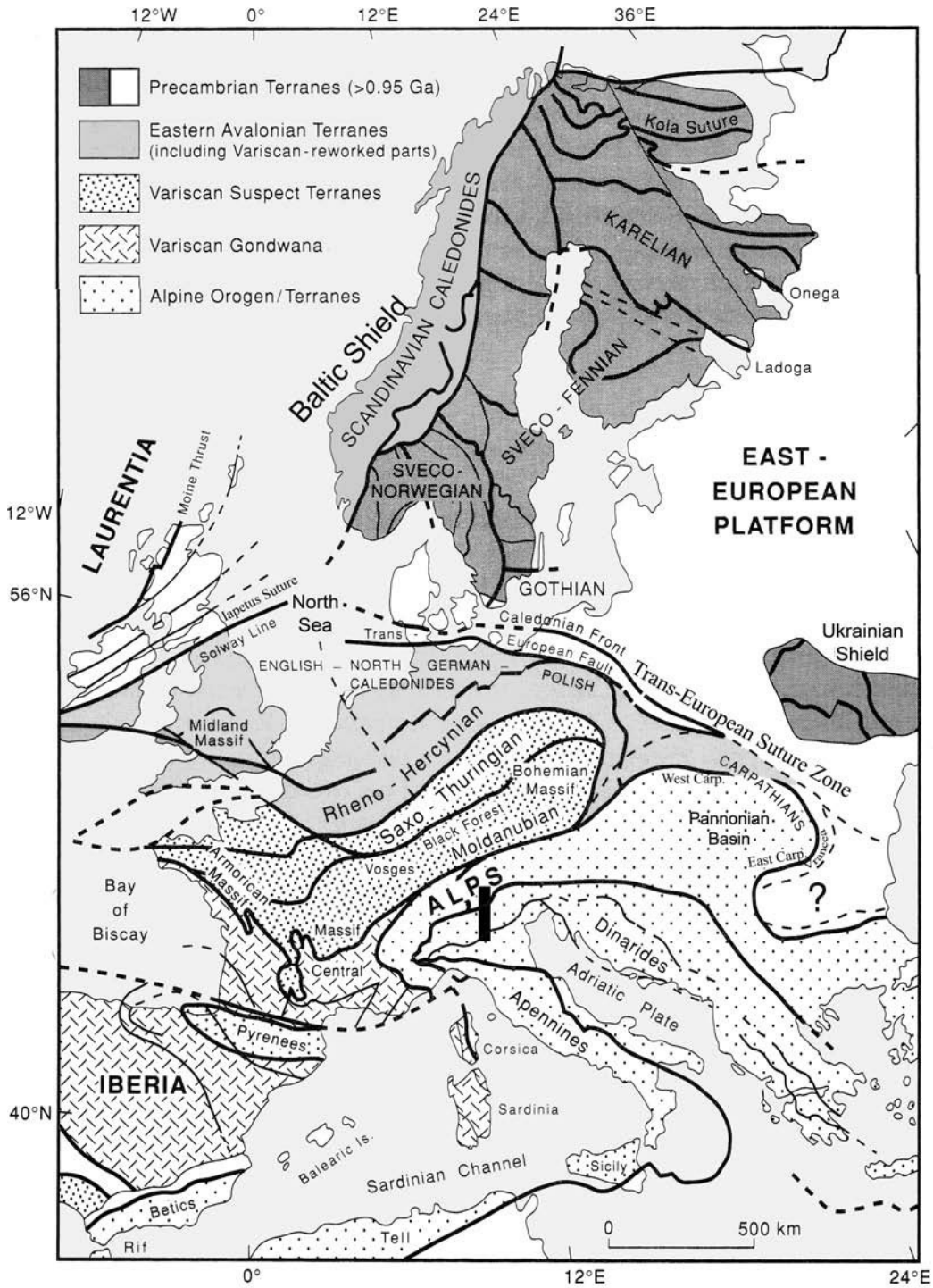

Fig. 3.60 Major tectonic units of western and northern Europe (after Berthelsen, 1992). Bold line – a part of the European Geotraverse (EGT) profile through the eastern Swiss Alps.

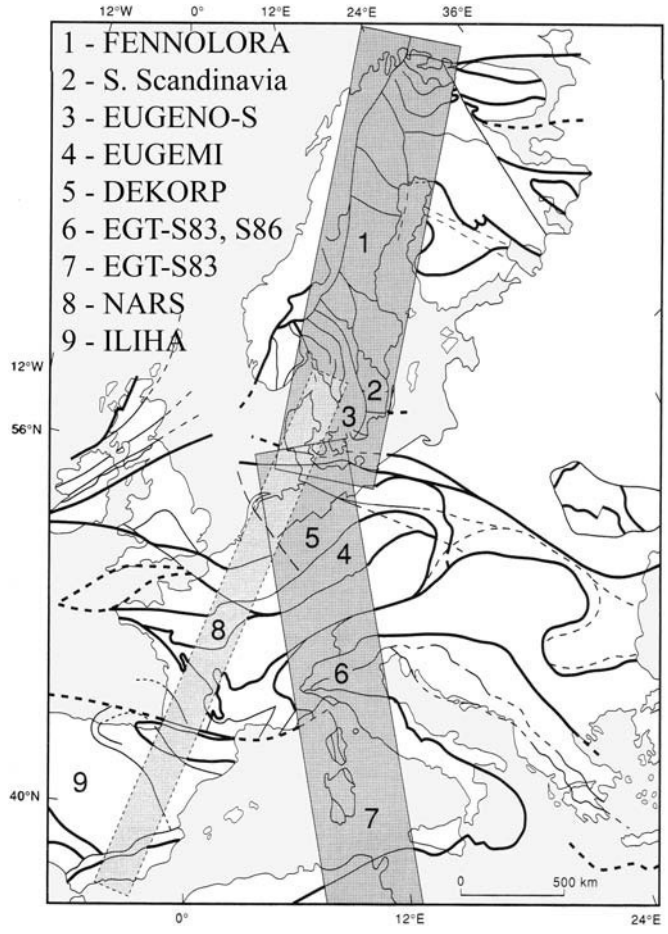

Fig. 3.61 European Geotraverse (EGT) seismic experiments in western Europe (from Blundell *et al.*, 1992). Numbers correspond to the individual projects within the joint program. Solid and dashed lines – boundaries of major tectonic structures.

near-horizontal. Upper mantle reflectors, both dipping and flat, that are observed in some reflection profiles in western Europe (e.g. between England and France) are probably related to Paleozoic tectonics (see below).

Collisional orogens and modern subduction zones

Seismic reflection studies provide images of modern subduction zones in the regions of continent–continent and continent–ocean collisional zones. Spectacular images of mantle reflectivity obtained for the Alps (e.g. Pfiffner *et al*., 1988), the Andes (ANCORP Working Group, 1999), and Tibet (Zhao and Nelson, 1993) provide the basis for geodynamic models of evolution for these regions.

The Alpine deformation zone is formed by convergence of the Eurasian and African plates, which began at *c*. 120 Ma and resulted in plate collision and subduction at *c*. 65 Ma

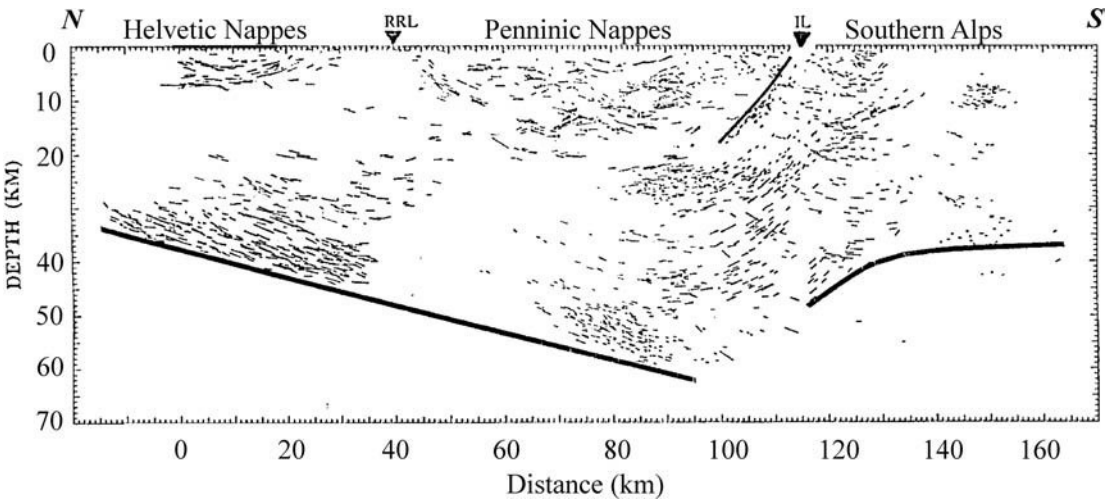

Fig. 3.62 Interpretation of migrated near-vertical reflection and wide-angle reflection and refraction data along the EGT profile through the eastern Swiss Alps (based on Kissling, 1993). Solid line – Moho (based mainly on wide-angle seismic data); thin solid line – Insubric Line (IL). For the location of the profile see Fig. 3.60 (black box) and Fig. 4.40a.

and uplift of the Alpine orogenic belt starting from *c*. 23 Ma. This convergence continues with a velocity of *c*. 9 mm/year. As a result, a highly complex and heterogeneous structure of the crust and upper mantle of the region has formed. High-resolution regional tomography models (although controversial, Lippitsch *et al*. 2003; Brückl *et al*., 2010) indicate the presence of several subduction zones: beneath the western and central Alps a lithospheric plate (presumably continental European lower lithosphere) is steeply subducting south-eastwards, while in the eastern Alps the second plate (interpreted as the continental Adriatic lower lithosphere) may be subducting northeastward (possibly, almost vertically) beneath the European plate. In the subduction zone beneath the central Alps, the lower crust is characterized by strong dipping reflections continuing down to *c*. 60 km depth (Fig. 3.62); the deepest part of these reflectors is interpreted as the crustal root formed during the collision.

The ANCORP seismic experiment across the Central Andean forearc shows spectacular images of the Nazca plate subducting beneath the Andes (Fig. 3.63). Strong mantle reflectors observed in this and similar seismic profiles (e.g. across the Vancouver island in Canada) are interpreted as images of subducting oceanic slabs with strong reflectivity variations, possibly related to different rheology.

Mantle reflectors and paleosubduction zones

Some of the first detected mantle reflectors were observed in the North Sea in the Scottish Caledonides (the so-called W-reflectors, Fig. 3.64) (Smythe *et al*., 1982). Originally they were interpreted as rift-related extensional shearing in the mantle. Later detailed waveform modeling indicated that they are produced by 6–8 km thick layers of high P-velocity

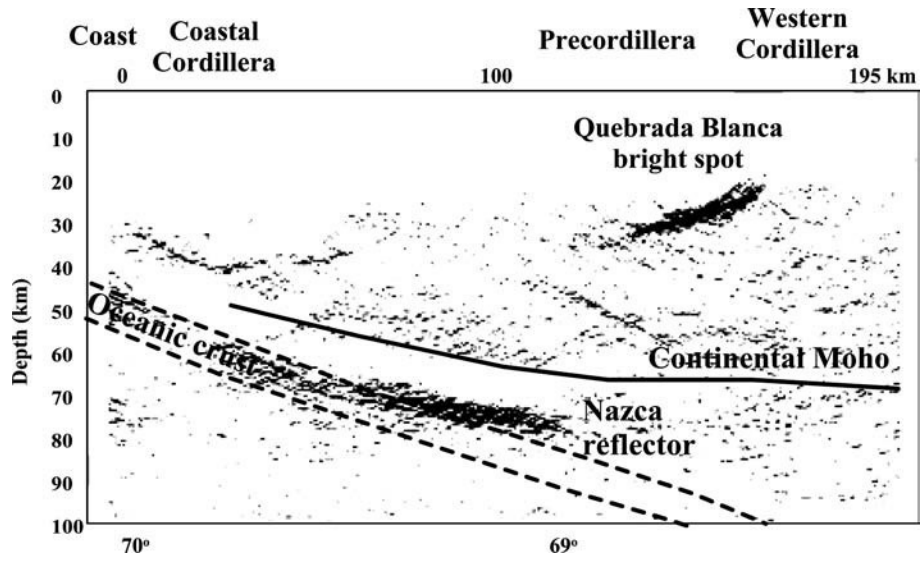

Fig. 3.63 Seismic reflection image of the Central Andean forearc and subduction zone from the ANCORP experiment (based on ANCORP WG, 1999). One of two strongest reflectors, the Nazca reflector, is interpreted as an image of the subducting oceanic crust.

(>8.4 km/s) and high density (>3.5 g/cc) and thus are likely to be remnants of fossil (Precambrian) subduction thrust faults. Consequent seismic reflection profiles in several parts of the Baltic region provided images of distinct mantle reflectors in the North and Baltic Seas (BABEL Working Group, 1990; 1993; MONA LISA Working Group, 1997). Similarity in the geometry of these reflectors with the reflectivity patterns observed in modern subduction zones and collisional sutures allows for their interpretation as traces of the ancient subduction of former oceanic crust. Their ages are constrained by those of known major tectonic events in the region (such as Paleoproterozoic plate convergence, subduction, and terrane accretion) and vary from *c*. 1.9 Ga for the northern part of the Bothnian Gulf to 1.6–1.4 Ga for the reflectors at the southern, Proterozoic, margins of the Baltic Shield, to *c*. 440 Ma for the reflector in the North Sea. The latter was probably formed during orogenic events related to the collision of Baltica, Laurentia, and Avalonia, closure of the Iapetus Ocean and Tornquist Sea, and subsequent amalgamation of a series of terranes at the edge of the East European craton.

Evidence for Paleozoic tectonic events has been found in seismic reflection studies in the Ural mountains. Mantle reflectors imaged at *c*. 175 km depth beneath the western margin of the Urals (Knapp *et al*., 1996) were interpreted as evidence for Paleozoic continent–ocean collision, followed by westward subduction and accretion of oceanic terranes along the eastern margin of the orogen. Alternatively, these reflections may mark the transition from lithosphere to ductile asthenosphere.

Images of dipping mantle reflectors have been produced in LITHOPROBE reflection profiles in the Canadian Shield in the Slave craton and in the Superior province (e.g., Calvert *et al*., 1995; Cook *et al*., 1999). Mantle reflectors extending from the lower crust down to

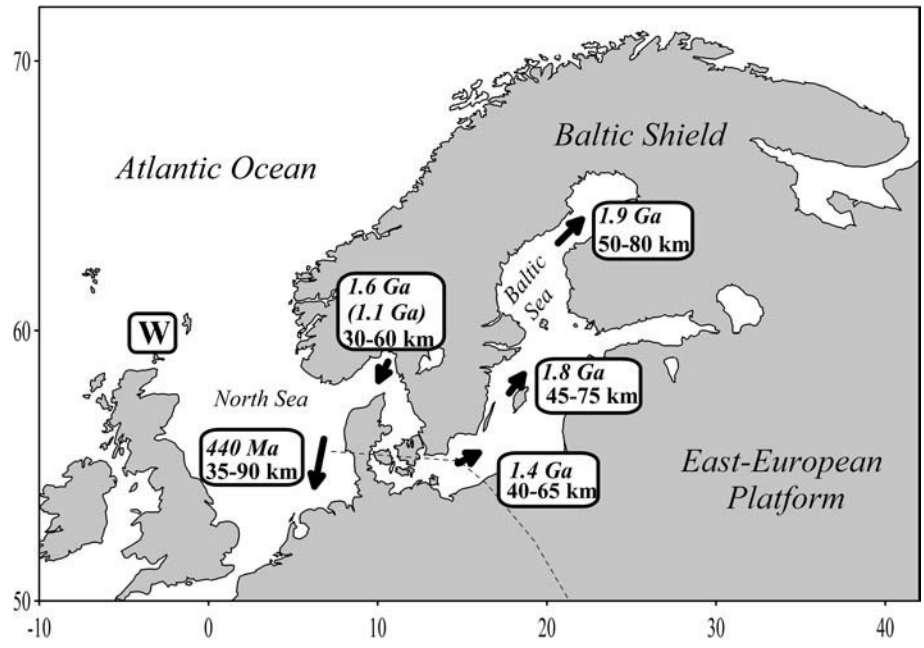

Fig. 3.64 Observations of subcrustal distinct dipping seismic reflectivity in the Baltic Shield (based on Balling, 2000). Arrows show dip direction and depth range of subcrustal reflectivity. These dipping seismic reflectors are interpreted as images of relict subduction zones and collisional sutures. Their ages range from *c*. 1.9 Ga for the northernmost reflector in the Bothnian Gulf to *c*. 440 Ma for the reflector in the southern part, in the North Sea, at the edge of the East European craton. W = W-reflectors of Smythe *et al*. (1982).

c. 100 km depth in the mantle were interpreted as Proterozoic subduction thrust below a 1.86–1.9 Ga volcanic arc at the western margin of the Slave craton. The most striking example of mantle reflectivity was imaged along LITHOPROBE Line 48 across the Archean Abitibi belt and the Paleoproterozoic Opatica plutonic belt in the Canadian Shield (Fig. 3.65). Dipping reflectors extending 30 km into the mantle were interpreted as images of a 2.69 Ga subduction thrust. These results provide strong evidence that some form of plate tectonics could have already been operating in the Archean.

Dipping tectonic boundaries in the lithosphere

Seismic reflection studies, in particular LITHOPROBE experiments in different parts of the Canadian Shield, provide evidence on the geometry of tectonic boundaries within the lithosphere. These results indicate that the boundaries between adjacent terranes are not necessarily vertical. A set of seismic transects across the Grenville Front, which separates the Archean lithosphere to the west from the Mesoproterozoic lithosphere to the east, clearly demonstrates that the deep expression of the edge of the Archean North American craton does not match its surface manifestation (Fig. 3.66). In particular, the Archean cratonic

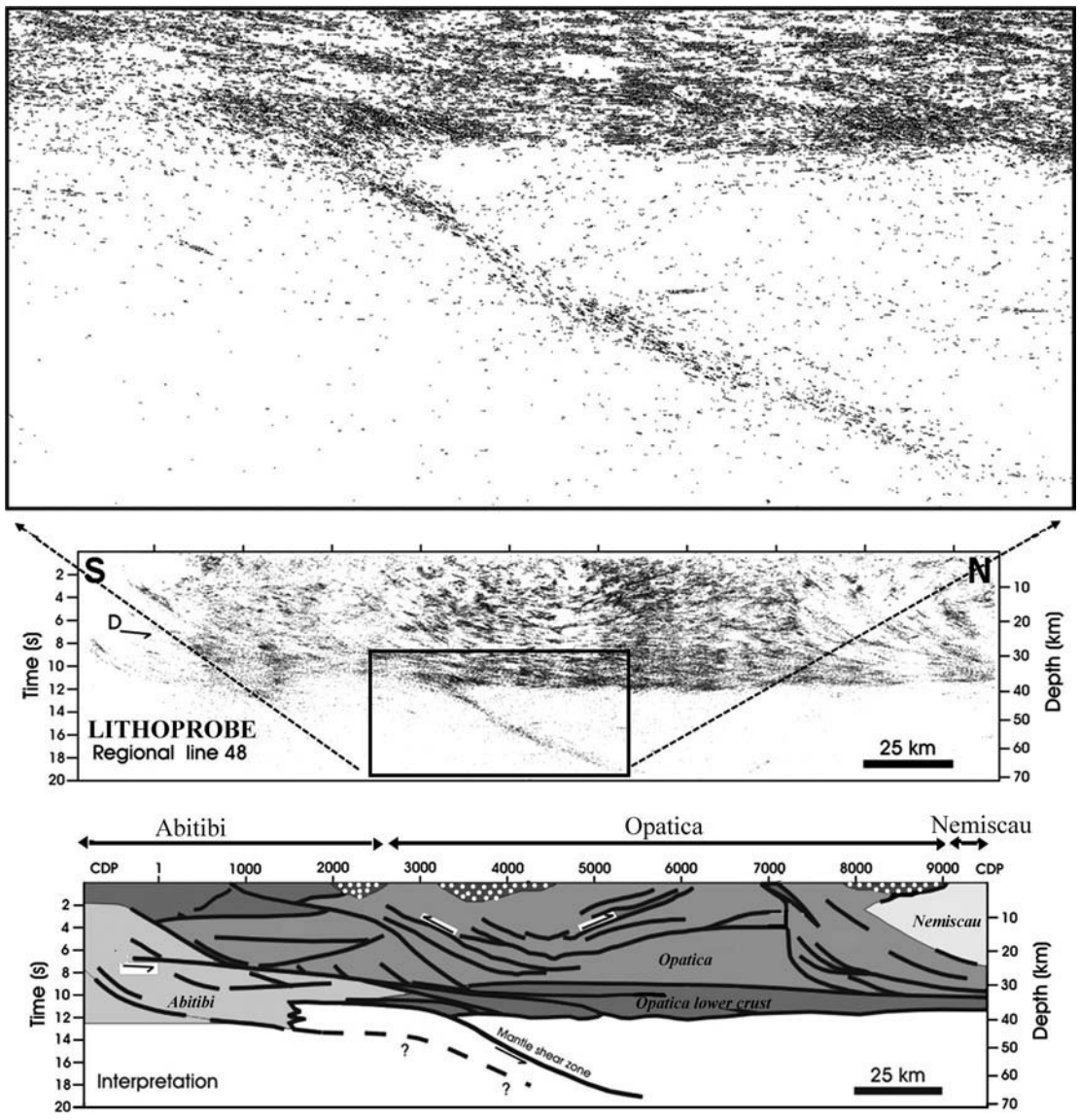

Fig. 3.65 Seismic reflection images (middle panel) from LITHOPROBE Line 48 in Quebec–Southern Ontario from the northern Abitibi belt to the Opatica plutonic belt (for location see Fig. 3.66). Upper part – zoomed central section of the reflection profile which shows a remarkable image of the fossil (*c*. 2.69 Ga) subduction zone and/or crustal delamination. Lower panel – tectonic interpretation based on geological, geochemical, and geophysical data (after Ludden and Hynes, 2000; www.lithoprobe.ca).

lithosphere of the eastern Canadian Shield underlies the Mesoproterozoic crust of the Grenville province over lateral distances of *c*. 200 km (Fig. 3.67). This implies that, within a few hundred kilometers of major tectonic boundaries, the age of the upper crust and the underlying lower crust and the upper mantle can differ dramatically.

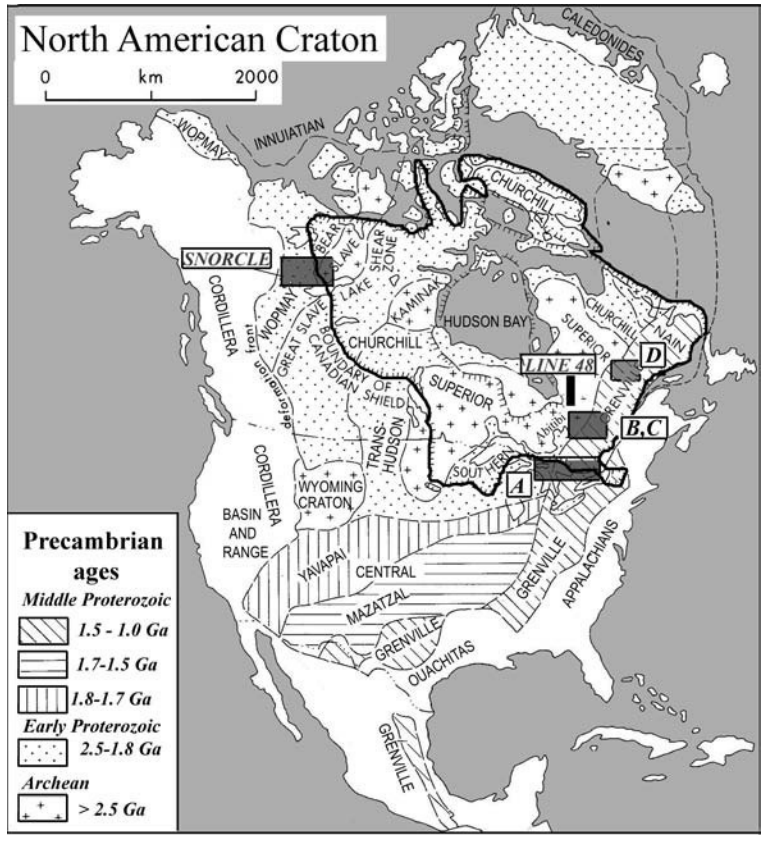

Fig. 3.66 Main geologic divisions of the North American craton and Greenland (after Goodwin, 1996 and Hoffman, 1989). Gray shadings show locations of the LITHOPROBE transects discussed in the text.

3.5.2 Seismic refraction and wide-angle reflection

The method

Seismic refraction studies are significantly younger than seismic reflection studies. The first cited paper on the application of this method to geology was only published in 1951, although the first refraction studies were initiated before the second world war. Since then, deep seismic sounding (DSS) profiles have provided important information on the velocity structure of the crust and the mantle. Compared to reflection seismology, a typical DSS profile is acquired on a linear array with long shot-to-receiver offsets (up to 500 km to allow for significant wave penetration below the crust), larger receiver spacing (typically 1–5 km, although some recent surveys deploy seismometers with smaller spacing), and larger shot spacing (20–100 km). Seismic waves are typically recorded at frequencies of 1–50 Hz which corresponds to wavelengths of 160 m–8 km for P-waves in

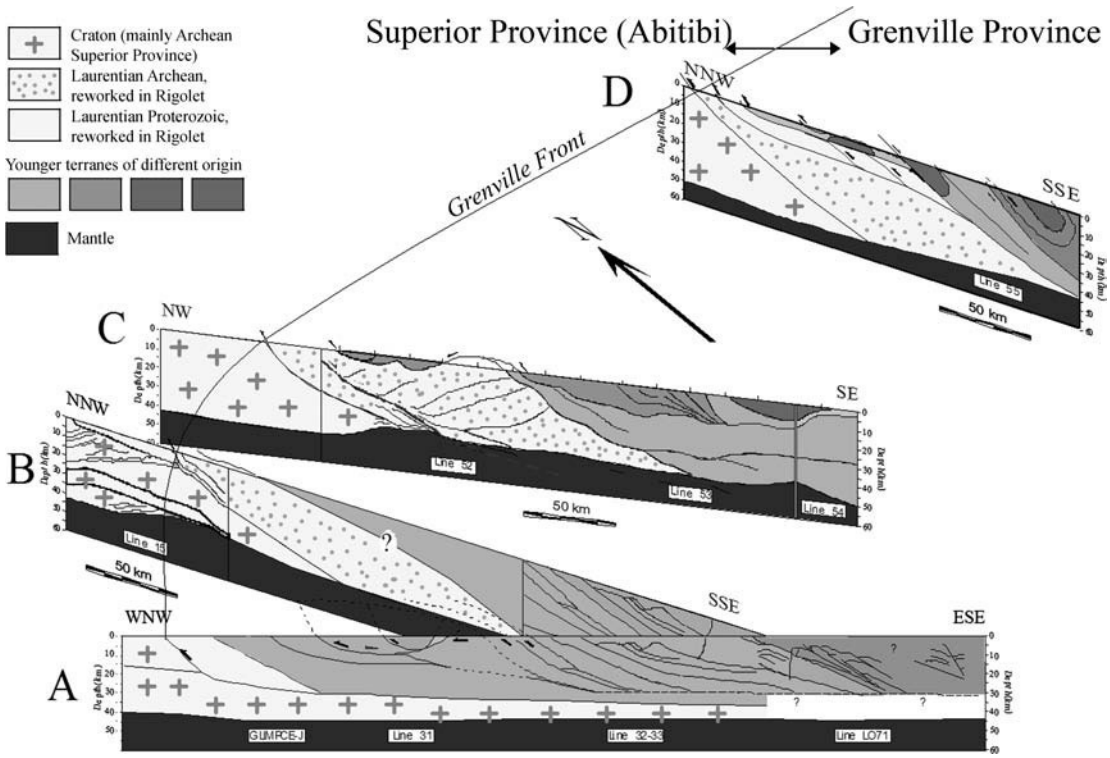

Fig. 3.67 Four composite sections of the Abitibi province and the Grenville province based on LITHOPROBE near-vertical-incidence seismic reflection profiles (based on Ludden and Hynes, 2000). For locations of the profiles see map in Fig. 3.66 (Boxes A, B, C, D). Note that the Archean terranes of the Canadian Shield underlay the Mesoproterozoic crust of the Grenville province.

the mantle. Thus, commonly, direct comparison of reflection data with refraction/wide-angle reflection is not possible due to dissimilar coverage by the two methods. The evolution of modern digital instruments and the availability of large pools of instruments have allowed seismologists to almost bridge the gap between the two techniques, although not yet fully.

Refraction profiles are usually reversed by positioning sources along the whole array (or at least at both ends) to allow for distinguishing lateral variations in the crust and mantle. It is common practice to combine refraction surveys with wide-angle reflection, since the latter provides important information on the structure of seismic discontinuities. The resolution of the refraction method is *c*. 5–10% for deeper crustal velocities and crustal thickness, and *c*. 3–5% for upper mantle velocities.

The number of seismic refraction profiles worldwide, including on-shore and marine seismic experiments, is enormous and they cannot be adequately covered in any review. Here the results of the method are illustrated by two unique seismic experiments:

(1) from the long-range profiles recorded between the 1960s and 1990s across Eurasia (northeastern Europe and Siberia) using nuclear explosions as the source, which allowed for determination of mantle structure down to *c*. 700 km depth and
(2) from one of the earliest (late 1960s) long-range refraction profiles in central North America (the Early Rise experiment) which provided important information on the structure of major seismic discontinuities in the upper mantle.

Heterogeneous upper mantle of Eurasia

Preamble

Impressive images of upper mantle seismic structure down to a depth of *c*. 700 km have been produced in unique and unprecedented seismic refraction and wide-angle reflection studies in Russia based on the PNE (Peaceful Nuclear Explosions) data acquired mostly in the 1980s (Fig. 3.68). These explosions were comparable in magnitude to 5–6 earthquakes and were complemented by chemical explosions. The profiles are 3000–4000 km long and reversed seismic data were recorded with 3-component seismographs located at *c*. 10 km intervals.

Interpretations of data along CRATON, QUARTZ, METEORITE, and RIFT (and partly HORIZONT) long-range seismic profiles allow the determination of seismic structure of the lithosphere and upper mantle in the Siberian Platform, West Siberian Basin, and the north-

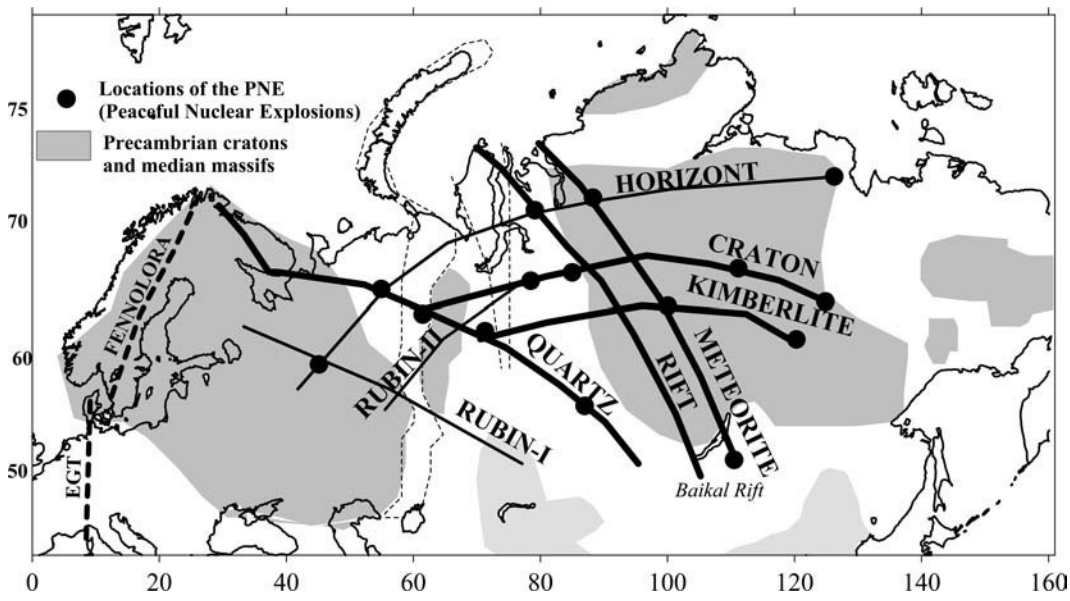

Fig. 3.68 Locations of the unique long-range PNE (Peaceful Nuclear Explosions) seismic profiles recorded in the USSR in the 1960s–1990s. Black circles – locations of nuclear explosions with energy release comparable to Mb = 5.0–6.0 earthquakes. Thin lines indicate profiles for which interpretations are limited or non-available. Also shown are the EGT (European Geotraverse) and the FENNOLORA seismic profiles. See Fig. 3.69 for the tectonic map.

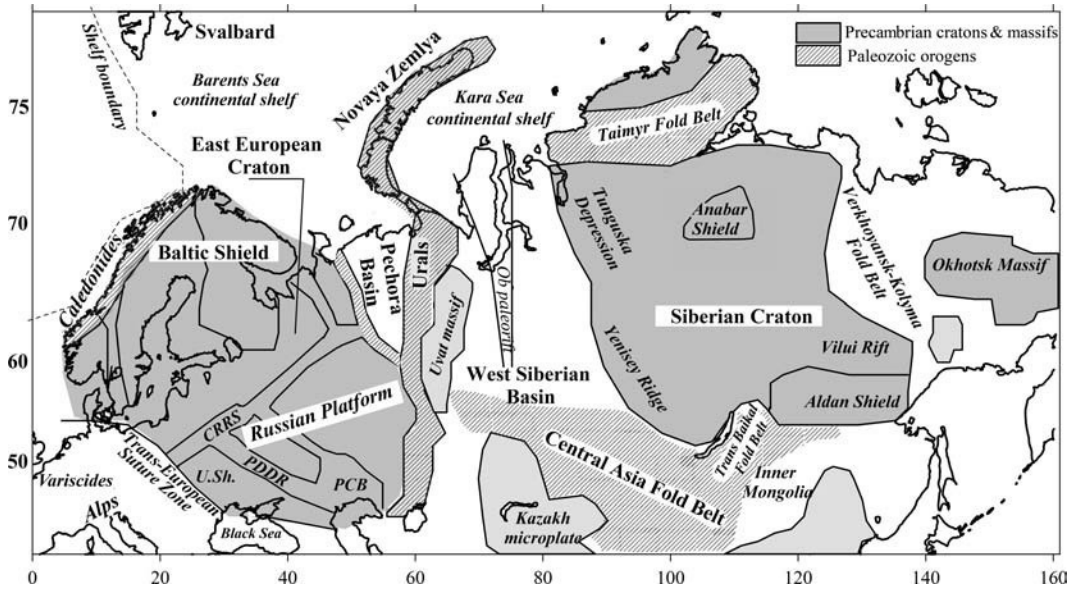

Fig. 3.69 Simplified tectonic map of the Precambrian Europe and Siberia. Dark shading shows major Precambrian structures (the East European craton, the Siberian craton and several median massifs). Dashed line – western margin of the Arctic Shelf. Abbreviations: CRRS = Central Russia Rift System; PCB = Peri-Caspian Basin; PDDD = Pripyat–Dnieper–Donets depression (rift); U.Sh. = Ukrainian Shield.

eastern parts of the East European (Russian) Platform and the Baltic Shield (Fig. 3.69). Early interpretations (Egorkin *et al*., 1987; Burmakov *et al*., 1987 and summaries in Fuchs, 1997; Mechie *et al*., 1997) were followed by modeling based on modern seismic processing (e.g. Priestly *et al*., 1994; Ryberg *et al*., 1996; Mechie *et al*., 1997; Morozova *et al*., 1999). The major results of the studies show the following.

LVZs

The upper mantle of the Siberian craton, the East European Platform, and the West Siberian basin is strongly heterogeneous and incorporates a series of thin (30–50 km thick) alternating high-velocity and low-velocity layers from the Moho down to a depth of *c*. 150–220 km with significant lateral variations of depth range and amplitude of velocity variation in the layers (Fuchs, 1997) (Figs. 3.70, 3.71). The physical nature of the observed multi-LVZs in the Eurasian mantle is speculative since velocity anomalies in the upper mantle do not correlate with gravity anomalies. A simple explanation would be a solid-state low-velocity zone at depths where a velocity increase due to compression becomes less than a velocity decrease due to heating (Anderson *et al*., 1968), an explanation that seems speculative for a cold cratonic mantle. However, the depths to the LVZs in the upper mantle of Eurasia are broadly consistent with global observations of a reduced velocity zone in the continental upper mantle, with the top at a *c*. 100 km depth, underlying a generally stratified uppermost mantle (Thybo and Perchuc, 1997a; Rodgers and Bhattacharyya, 2001). Importantly,

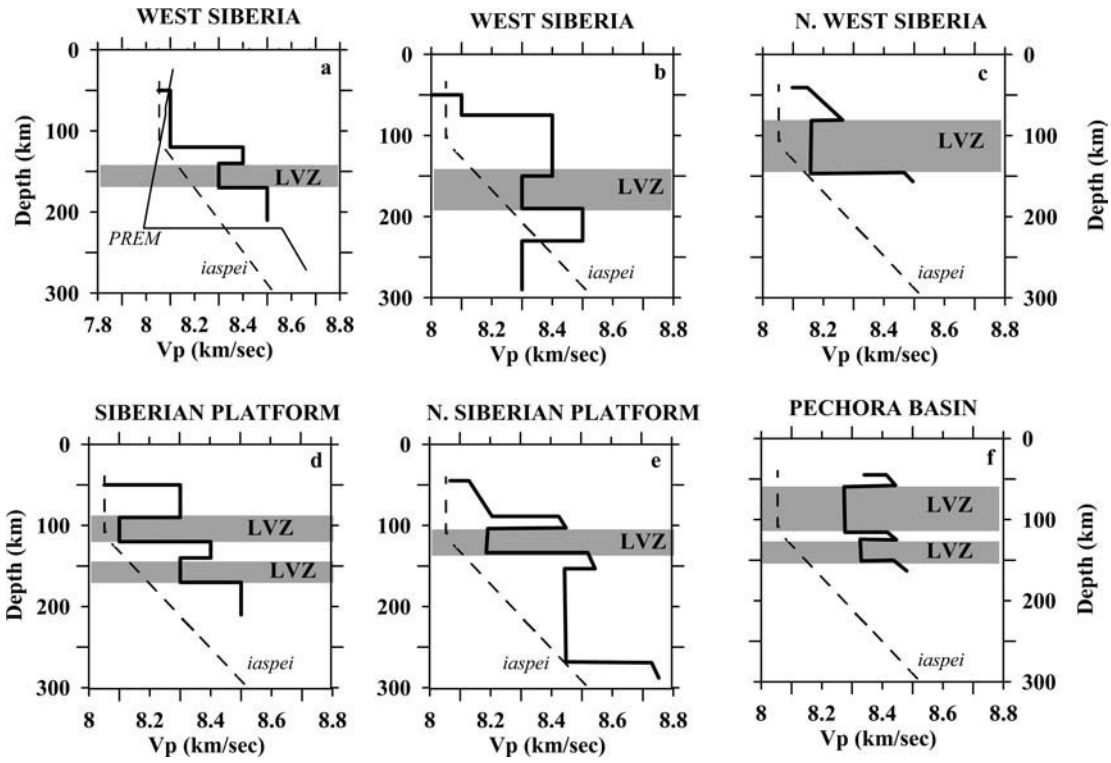

Fig. 3.70 1D velocity variations in the upper mantle of tectonic structures of Eurasia derived from 2D models based on long-range PNE profiles. (a) bold line – West Siberian Basin (WSB), profile CRATON (after Egorkin *et al*., 1987), thin solid line – PREM model, thin dashed line – *iaspei* model; (b) WSB, profile QUARTZ (after Morozova *et al*., 1999); (c) Ob paleorift, northern WSB, profile HORIZONT (after Burmakov *et al*., 1987); (d) Tunguska Depression of the Siberian platform, profile CRATON (after Egorkin *et al*., 1987); (e) northern Siberian Platform, profile HORIZONT (after Burmakov *et al*., 1987). Note that seismic velocities in the LVZs are higher than in the global continental model *iaspei*.

seismic velocities in the LVZs are higher than the global continental average, similar to seismic observations in other Precambrian regions (see Section 3.4.2).

Morozova *et al*. (1999) interpreted a LVZ (with $Vp = 8.3$ km/s) at the QUARTZ profile in the depth range of *c*. 140 to 180 km beneath the West Siberian basin as being associated with partial melting and considered its top as the lithospheric base and its base as the Lehmann discontinuity. Similar interpretations of LVZs as the lithosphere–asthenosphere boundary were proposed for the RIFT profile (e.g. Priestly *et al*., 1994). However, some authors (e.g. Mechie *et al*., 1997) include upper mantle LVZ at depths of *c*. 130–160 km only for the QUARTZ and RUBIN-1 profiles, but not for other PNE profiles (CRATON, METEORITE, KIMBERLITE, RIFT), where interpretations allow for models without LVZ down to the 410 km discontinuity. Furthermore, since seismic data permit the existence of several LVZs in the upper 80–220 km of the mantle, it is unclear the top of which of the multi-LVZs should be interpreted as the lithospheric base if the formal definition of the seismic lid is

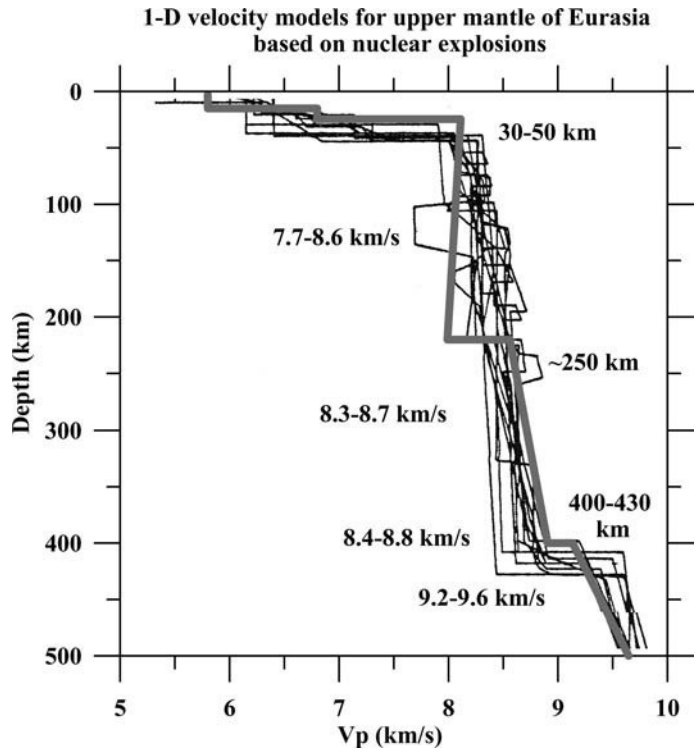

Fig. 3.71 1D velocity variations in the upper mantle of Eurasia based on long-range PNE profiles (based on Fuchs, 1997). Gray line – PREM model.

used for the lithosphere. It is more likely that the low-velocity zones are intralithospheric features which do not correspond to the lithospheric base. The presence of LVZs at a similar depth beneath all tectonic settings in Eurasia ranging from the Archean–Paleoproterozoic Siberian craton to Paleozoic rifts and basins (Fig. 3.70) suggests that they can be caused by changes in mantle mineralogy or olivine grain size with depth (compare with Fig. 3.9a).

The PNE seismic refraction and wide-angle reflection studies also detected the presence of seismic discontinuities at nominal 410 km, 520 km, and 660 km depth beneath Eurasia (Fig. 3.71). Along the QUARTZ profile, the 410 km discontinuity shallows northwards to *c*. 400 km depth beneath the Kola province of the Baltic Shield, while beneath the Altay mountains it is at 430 km depth (Morozova *et al*., 1999).

Teleseismic Pn

Observation of seismic *Pn* and *Sn* phases with velocities of >8.0 and 4.7 km/s, respectively, are common in most tectonic settings and, together with seismic reflections from the Moho, are used for the determination of crustal thickness. They are interpreted as subhorizontally refracted phases (possibly also multiply reflected and scattered) which have been turning at the top of the mantle due to a positive vertical velocity gradient. Alternatively, existence of a

sub-Moho waveguide has been proposed to explain *Pn* as waves reflected back towards the surface by scattering in a highly heterogeneous mantle (at a scale below the wavelength) (Fuchs, 1983). Such a waveguide can be generated by random successions of interchanging high- and low-velocity layers. Alternative explanations for the origin of *Pn* and *Sn* phases form the basis of recent debate when seismic data from the Soviet seismological program based on "Peaceful Nuclear Explosions" became available to several research groups in the west (Fuchs, 1997).

An intriguing feature observed in the PNE seismic data is the behaviour of a teleseismic *Pn* phase, a strong seismic phase with a long coda, that travels over unusually long (teleseismic) distances of >3000 km with a group velocity of 8.0–8.1 km/s (Ryberg *et al*., 1995). This phase, which is a secondary arrival observed behind the first arrivals and is relatively strong in the high-frequency band (>10 Hz), was termed a "high-frequency, teleseismic *Pn* phase". Modeling based on calculation of synthetic seismograms shows that the high-frequency component of this wave can be explained by forward and backward scattering in a laterally heterogeneous waveguide (with elongated anisotropic inhomogeneities with ±4% velocity fluctuations) between the Moho and a boundary at *c*. 100 km depth (Tittgemeyer *et al*., 1996) (Fig. 3.72).

Alternatively, the observed amplitudes of the teleseismic *Pn* phase can be explained by a "whispering gallery" where phases travelling in the upper mantle experience multiple reflections from the Moho (Morozov and Smithson, 2000). Scattering of "whispering gallery phases" from heterogeneities in the lower crust could explain the coda characteristics of the phase (Nielsen *et al*., 2003). Furthermore, the teleseismic *Pn* phase has also been observed at low frequencies, but with different coda characteristics in different frequency bands (Nielsen and Thybo, 2003). While the mantle scattering model (Ryberg *et al*., 1995) can only explain the high frequency part of the teleseismic *Pn* phase, and cannot explain the presence of the first arrivals (*Pn* phases), the "whispering gallery phase" can better explain all observations of the teleseismic *Pn* phase for realistic reflectivity properties of the lower crust, and it explains the observations of the first arrivals for a positive vertical velocity gradient in the upper mantle.

Seismic discontinuities in the upper mantle beneath North America

The Early Rise experiment was carried out in central North America in the mid 1960s (Iyer *et al*., 1969). An underwater shot point with chemical explosives was located in Lake Superior; a series of linear arrays of seismometers at *c*. 30 km spacing radiated from the shot point over 2000–3000 km (Fig. 3.73). The disadvantage of the geometry of the project, as compared to the Soviet PNE profiles, was the absence of reversed and overlapping profiles, which are crucial for interpretation of heterogeneous mantle structure. In spite of these limitations, the project provided important pioneering data on seismic discontinuities in the upper mantle of North America.

Travel time interpretations along different profiles show the presence of seismic discontinuities at depths of 80–90 km and at *c*. 125 km depth (Green and Hales, 1968; Lewis and Meyer, 1968). Hales (1969) proposed that these boundaries have a common origin for all profiles and are caused by the spinel–garnet phase transition. Another boundary (the so-called 8° discontinuity) was identified at *c*. 700–900 km offsets (Fig. 3.74) and was

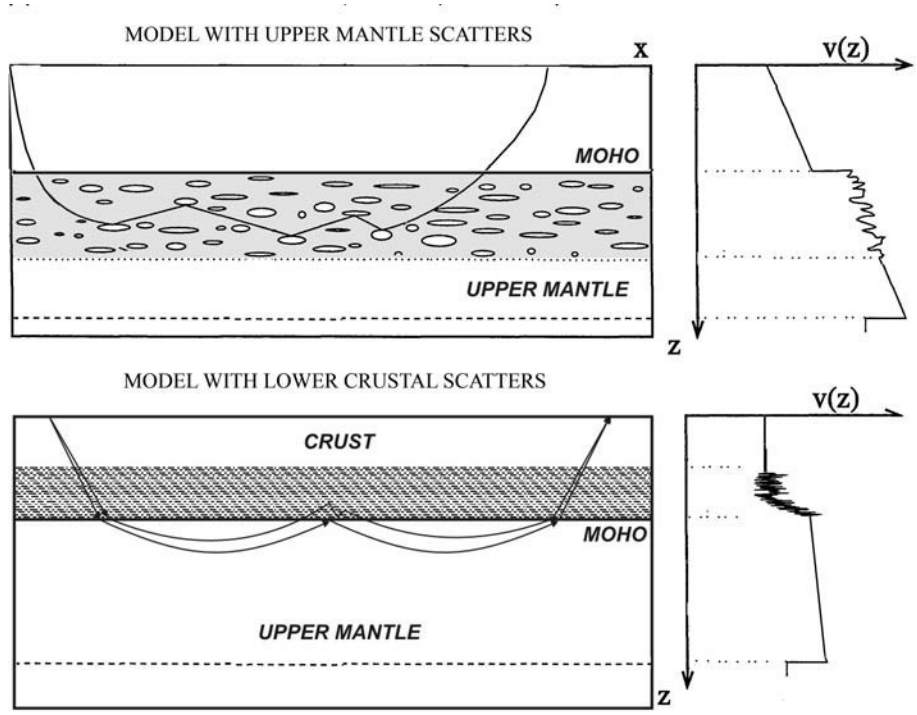

Fig. 3.72 Alternative velocity models for the origin of teleseismic *Pn* waves observed at the long-range PNE seismic profiles in Eurasia. One-dimensional velocity profiles (right) are extracted from the 2D velocity models for a 2000 km long QUARTZ profile. Upper: a sub-Moho waveguide model with transparent crust and Gaussian velocity fluctuations in the upper mantle which are generated by scatterers with anisotropic structure; their horizontal and vertical correlation lengths are 20 and 0.5 km, respectively (based on Ryberg *et al*., 1995). Lower: a "whispering gallery" model with lower crustal velocity fluctuations (at 15 to 40 km depth) with horizontal and vertical dimensions of 2.4 and 0.6 km, respectively (redrawn from Nielsen and Thybo, 2003).

interpreted as the top of the low-velocity zone beginning at near a depth of *c*. 100 km (Thybo and Perchuc, 1997a,b). The refracted branch from the 410 km discontinuity was identified on several profiles.

Reinterpretations of travel time data from the Early Rise profiles provided new information on the seismic and thermal structure of the upper mantle of North America. While all profiles show similar seismic structure for offsets less than 800 km, at greater offsets there is a significant difference between profiles 1 and 2 located entirely within the Canadian Shield and other profiles, in particular profiles 6, 8, and 9 trending west and southwest (Fig. 3.74). This difference can be explained in terms of cold-to-hot transition in the upper mantle, which corresponds to the transition from the cold cratonic lithosphere of the Canadian Shield to the hot upper mantle of Phanerozoic regions, in particular in western USA (Thybo *et al*., 2000). This transition in the mantle determined from the refraction data is in striking agreement with the margin of the North American craton as determined from surface wave tomography (Fig. 3.73). It also corresponds to the transition from almost aseismic to seismic regions.

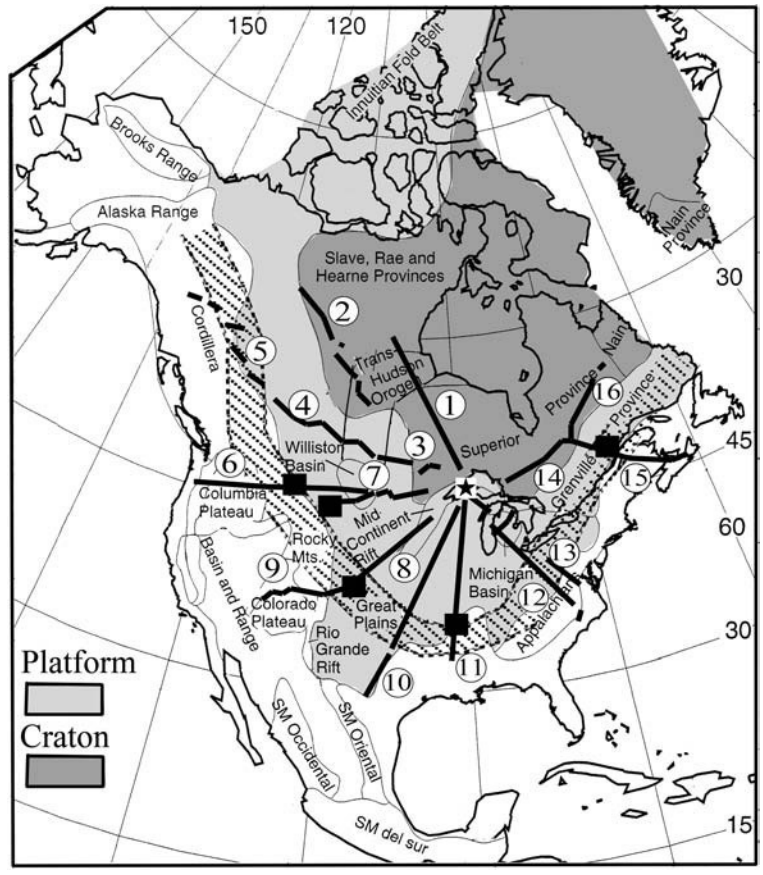

Fig. 3.73 Location map for the Early Rise long-range seismic profiles (numbered 1 to 16) radiating from the shot point in lake Superior (shown by a star). The transition from cold-to-hot regions is marked by black boxes (based on Thybo and Perchuc, 1997b); hatching – boundary of the North American craton as identified from surface wave tomography (van der Lee and Nolet, 1997).

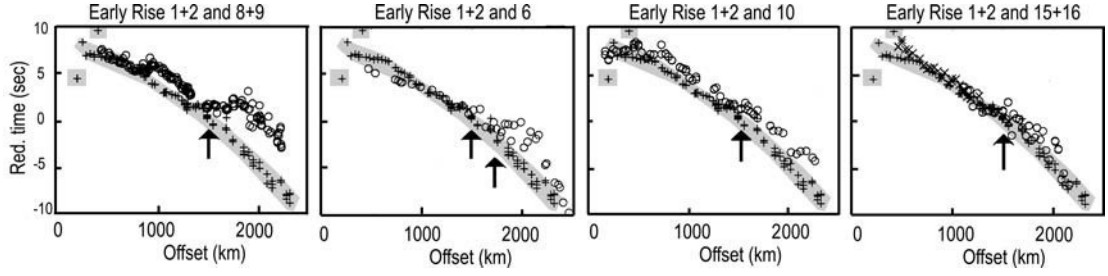

Fig. 3.74 Travel time plots of first arrivals for the Early Rise profiles (based on Thybo and Perchuc, 1997b). Numbers refer to profile numbers (for locations see Fig. 3.73). Profiles 1–2 which traverse only the cold cratonic lithosphere of the Canadian Shield are shown on each plot by crosses. Travel times for other profiles are shown by circles. The characteristic delays at *c*. 1300–1600 km offsets (arrows) are interpreted as the transition from cold-to-hot regions.

3.6 Teleseismic seismology

Teleseismic seismology uses large earthquakes (typically with magnitude greater than 4.5) as seismic sources. Broad-band waveforms from these earthquakes (teleseisms) recorded at global seismic observatories include waves radiating at different angles from the hypocenters, typically providing seismic data with good ray path coverage and in a wide frequency band. This section discusses teleseismic elastic tomography based on body-waves and surface-waves and anelastic tomography with the goal of recognizing the robust features common to different tomographic models. To facilitate a comparison of results from different research groups, a brief summary of the methods and their resolution is provided prior to discussion of global and regional seismic tomography results. Selected technical details related to tomographic inversion have been discussed earlier in this chapter (Section 3.2).

In the ocean of publications on methodological aspects of teleseismic seismology and the results of tomographic modeling, even a simple listing of the research groups and major large-scale and regional-scale tomographic models is not possible. The author apologizes to those researchers whose studies are not mentioned here. Overviews of elastic seismic tomography methods can be found in Romanowicz (1991), Iyer and Hirahara (1993), Nolet *et al*. (1994), Masters and Shearer (1995), Ritzwoller and Lavely (1995), Bijwaard *et al*. (1998), Dahlen and Tromp (1998), Boschi and Ekström (2002), Vasco *et al*. (2003), Ritsema *et al*. (2004), Kennett (2006), Nolet (2008). Some useful reference information can be found at: http://cfauvcs5.harvard.edu/lana/rem/index.htm, where several widely used global elastic tomography models are compared. Anelastic tomography is reviewed by Mitchell (1995), Bhattacharyya *et al*. (1996), Romanowicz and Durek (2000), while Jackson (2000) provides an overview of recent progress in laboratory measurements of seismic wave dispersion and attenuation.

3.6.1 Elastic tomography: methods and uncertainties

This section aims to provide some basic information on the advantages and limitations of body-wave and surface-wave tomography models. Shear-wave velocities in the upper mantle can be constrained with surface-wave phase- and group-velocities, body-wave travel times, and free-oscillation spectra, while P-wave velocity structure is constrained by much fewer data types. This section focuses primarily on surface-wave and body-wave tomography, and models constrained by free oscillations are omitted from the discussion. Because of differences in mantle sampling by the various body-wave and surface-wave types (see also Section 3.2), resolution of the deep structure can vary significantly between tomographic models constrained by different data, so that their comparison is, in general, like comparing apples and pears. In addition, long-period seismic waves have limited sensitivity to P-velocity structure.

A significant diversity exists even between tomography models based on the same seismic data, further influenced by model parameterization and the regularization used in

the inversion to stabilize the inverse problem (in particular, in poorly constrained regions). As discussed in Section 3.2.3, when damping is used, cells with small-scale velocity perturbations should be treated with caution. Roughness control (i.e. the absence of strong contrasts in adjacent blocks) results in models with significant but smoothly varying heterogeneity, and cells with few data but with large-amplitude perturbations should be treated with caution. Furthermore, regularization can dominate an inversion result in poorly resolved cells (Vasco *et al*., 2003). If different tomography models use the same type of regularization for poorly resolved regions, a strong correlation between model results does not exclude the possibility of other patterns of heterogeneity (in shape and amplitude) that are consistent with observations.

With these words of caution in mind, a comparison of large-scale tomographic models allows for recognition of robust, model- and inversion-independent, features of the upper mantle. In comparing different models, it is important to recognize reliably determined features which supply important information on the physical properties and structure of the upper mantle. Due to the limitations of the approach, only well-resolved structures should be compared between different tomography models.

Body-wave seismic tomography: uncertainty and resolution

Resolution of a tomography model is determined by seismic wavelength, which in turn is proportional to the seismic wave period and inversely proportional to frequency. Generally, the higher the frequency, the higher the model resolution, and regional body-wave tomography typically utilizes seismic waves with a frequency of 0.1–10 Hz (e.g. Sipkin and Jordan, 1975; Inoue *et al*. 1990; Grand, 1994; Su *et al*., 1994; Masters *et al*. 1996; Trampert and Woodhouse 1996). Recent global travel time P-wave tomography models (e.g. Spakman *et al*. 1993; Zhou, 1996; Bijwaard *et al*., 1998) can image the seismic velocity structure of particular regions of the upper mantle with lateral resolution as detailed as that in regional tomographic studies (50–100 km) allowing us to distinguish even localized anomalies such as slabs in the upper mantle of the present subduction zones (e.g. van der Hilst *et al*., 1997; Grand, 2002) and lower mantle slabs associated with ancient subduction zones (e.g. van der Voo *et al*., 1999b; Fukao *et al*., 2001). However, lateral resolution of teleseismic body-wave tomography based on direct arrivals is significantly non-uniform and is limited by ray path coverage which is good only in tectonically active regions and areas with dense distribution of seismometers (direct arrivals are assumed to be sensitive mainly to the upper mantle structure in a narrow zone beneath sources and receivers). To overcome this problem, teleseismic body-waves multiply reflected from the surface and turned in the upper mantle have been used in some regional studies (e.g. Grand and Helmberger, 1985).

Most teleseismic phases arrive at the receiver along near-vertical ray paths, in particular phases from the core which are widely used in body-wave tomography studies (Figs. 3.75, 3.76). The near-vertical propagation in the upper mantle puts strong limitations on vertical resolution which at present does not exceed 50–100 km. One way to improve the vertical resolution is to also use travel times of waves from local earthquakes observed at local

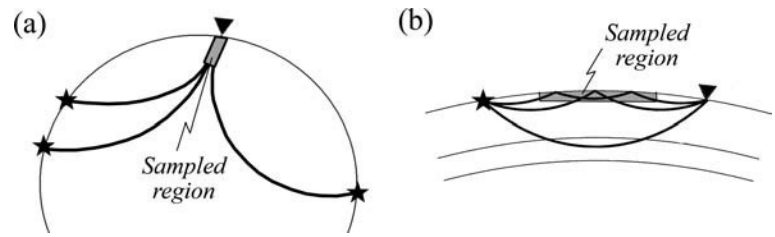

Fig. 3.75 Sketch showing ray paths in body-wave (a) and surface-wave (b) tomography. Gray shading – region sampled by seismic waves. Due to near-vertical propagation of body-waves, they provide low vertical resolution. In contrast, surface waves smear lateral velocity structure.

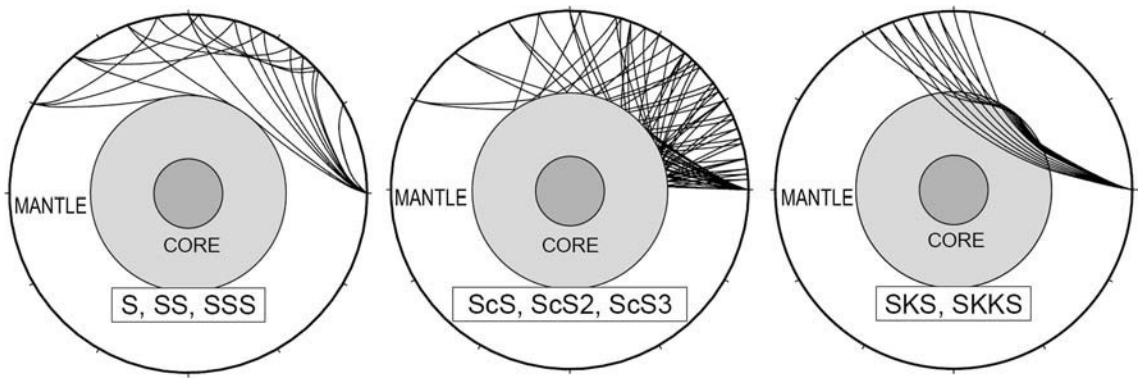

Fig. 3.76 Geometric ray paths for the shear wave phases (i.e. body-wave phases that propagate through the mantle with shear wave speed). These phases (i) propagate through the lower mantle (S) or diffract along the core–mantle boundary, (ii) reflect once (SS), twice (SSS), or three times (SSSS) off the Earth's surface, (iii) reflect once (ScS), twice (ScS2), or three times (ScS3) off the core–mantle boundary, or (iv) propagate as compressional waves through the core (SKS and SKKS) (from Ritsema and and van Heijst, 2000b).

stations, as these waves tend to travel sub-horizontally in the upper mantle. However, this approach is limited by local seismicity and also by the tendency of earthquakes to occur only along distinct fault zones.

Another approach is used in body-wave tomographic models of S. Grand (e.g. Grand, 1994, 2002; Grand *et al*., 1997), where all velocity anomalies are put ad hoc into the upper 200 km. The approach is validated by the spectrum of mantle velocity anomalies as revealed by both body-wave and surface-wave global whole mantle tomography: velocity perturbations with amplitude exceeding 2% are restricted to the shallow mantle and the core–mantle boundary, while the spectrum of middle-mantle anomalies is "white" (e.g. Ritsema *et al*., 2004).

Computations of the spatial resolution of body-wave tomography based on several traveltime phases have demonstrated the following (Vasco *et al*., 2003):

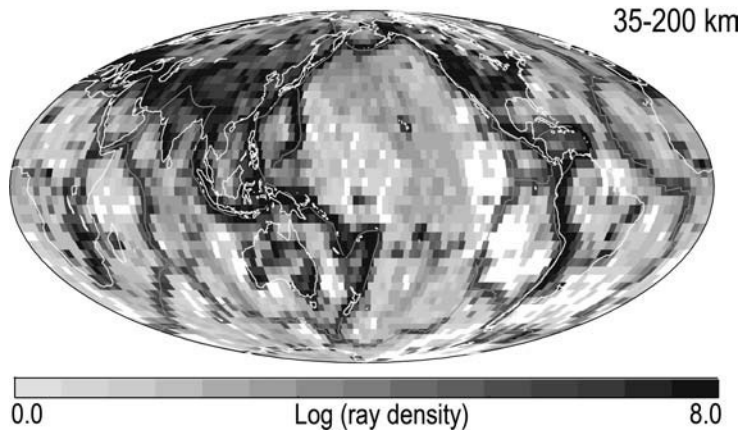

Fig. 3.77 Ray path sampling by compressional waves in the upper mantle. The logarithmic scale shows the number of rays intersecting each $3° \times 3°$ cell (unsampled blocks are shown in white) (from Vasco *et al.*, 2003).

- The errors associated with different phases differ significantly and core phases can lead to greater errors than first arriving P phases. As a result, inclusion of various phases into the inversion does not guarantee an improvement in model resolution.
- Model parameter resolution is correlated with ray density which is controlled by distribution of seismic events and seismic stations. This leads to highly variable resolution of tomographic images.
- The best resolved cells lie beneath the southern parts of Eurasia and North America, and a narrow zone of subduction zones encircling the Pacific Ocean (Fig. 3.77). Localized high velocity anomalies interpreted as slabs often coincide with narrow zones of high resolution in the mantle along event-station corridors and are a consequence of ray density–model resolution correlation.
- The mantle structure is moderately resolved beneath mid-ocean ridges and in the northern parts of Eurasia and North America. The worst resolved cells include the Pacific, Atlantic, and Indian ocean basins, the Arctic, Siberia, and most of the southern hemisphere except for Australia, southern Africa, and the Andes. In poorly constrained cells, the errors can exceed several percent.
- Mantle anisotropy affects ray density–model resolution correlation, in particular beneath the central Pacific: cells with a high ray density may still be poorly resolved.
- Existing crustal models allow for calculation of local velocity perturbations due to heterogeneities in crustal thickness and average crustal velocities. Although such corrections are of particular importance in surface-wave modeling (see below in this section), teleseismic frequency-dependent site effects (as compared to frequency-independent station corrections commonly used to correct for site effects) may have a significant effect on teleseismic P-wave amplitudes with the major contribution of amplitude losses in the sedimentary layer (Zhou *et al*., 2003).
- Depth "leakage" due to smoothing in tomographic inversions reduces vertical resolution of the models (see also next section).

Surface-wave tomography: uncertainty and resolution

Dispersion, vertical resolution, and depth leakage

The advent of surface-wave tomography methods (Toksöz and Anderson, 1966; Cara, 1979; Woodhouse and Dziewonski, 1984; Nolet, 1990; Kennett, 1995; Trampert and Woodhouse, 1995, 1996) provided some of the best constraints on the structure of the Earth's upper mantle (e.g. Zhang and Tanimoto, 1993; Zielhuis and Nolet, 1994; Laske and Masters, 1996; Ekström *et al*., 1997; van der Lee and Nolet, 1997a; Shapiro and Ritzwoller, 2002; Ritsema *et al*., 2004; Debayle *et al*., 2005; Panning and Romanowicz, 2006; Kustowski *et al*., 2008a). Surface waves are commonly the strongest arrivals recorded at teleseismic distances. Seismic surface waves that propagate through the upper mantle include Rayleigh waves and Love waves. The latter are essentially horizontally polarized shear waves (SH waves) and their sensitivity to compressional velocities is exactly zero (Fig. 3.27).

The amplitudes of surface waves generally decrease exponentially with the depth of the source. Simple rules-of-thumb state that for fundamental modes, the depth best resolved with phase velocity is *c*. 0.4 times the wavelength of Rayleigh waves and *c*. 0.25 times the wavelength of Love waves (Love waves are particularly sensitive to the velocity structure in the upper 40 km of the Earth). Because of the frequency dependence of surface wave velocities (Fig. 3.78), their waveforms are strongly dispersed. As a result, surface waves, Rayleigh waves in particular, are sensitive to seismic velocity structure in the upper mantle over a relatively broad depth range. Backus–Gilbert averaging kernels (Backus and Gilbert, 1968) for Rayleigh waves illustrate three important features of surface wave tomography:

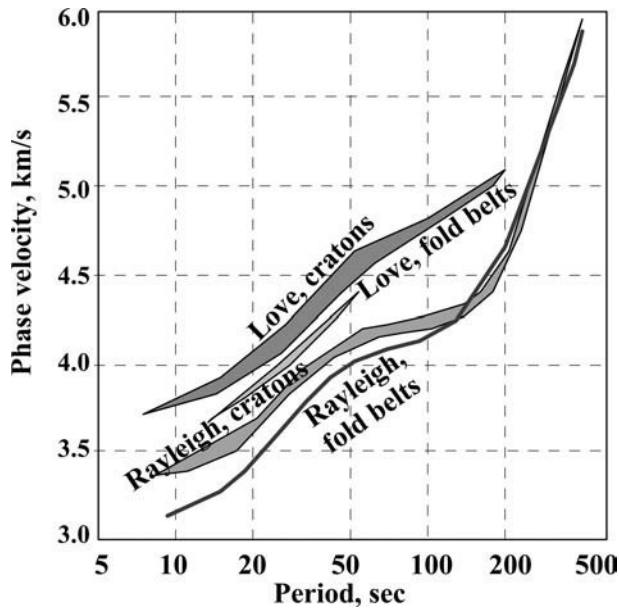

Fig. 3.78 An example of frequency-dependent phase velocity data for Rayleigh waves and Love waves from the cratonic regions and Proterozoic fold belts (after Lebedev *et al*., 2008).

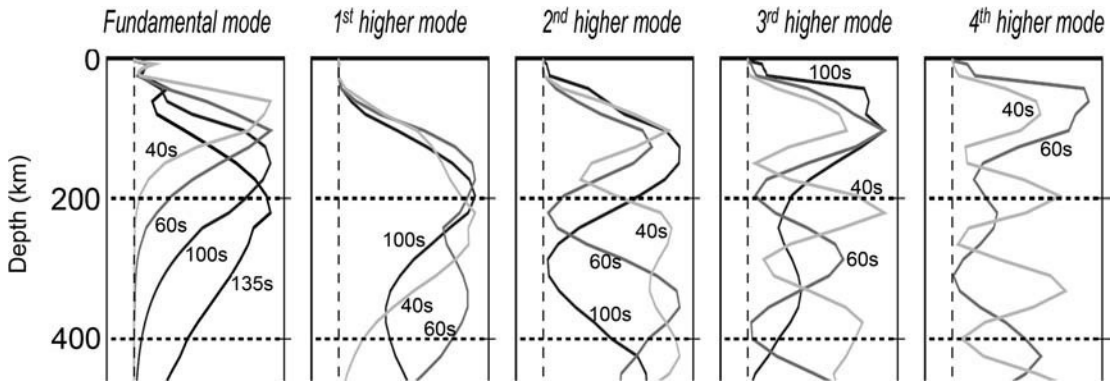

Fig. 3.79 Sensitivity kernels that relate phase velocities of the fundamental and the 1st, 2nd, 3rd, and 4th overtone Rayleigh waves to shear velocity in the PREM model (after Ritsema *et al*., 2004). They illustrate that Rayleigh waves are sensitive to seismic velocity structure in the upper mantle over a relatively broad depth range. Numbers near the curves – seismic wave period in sec. Fundamental mode at periods of 40 sec or less samples only the upper 200 km; higher modes allow for sampling of deeper mantle. Long-period Rayleigh waves sample deeper layers in the upper mantle and propagate faster than shorter period Rayleigh waves because mantle structure at greater depth has higher wave speeds.

- The depth of wave penetration is very different for different modes (Fig. 3.79). Fundamental mode samples only the upper layers of the mantle. The higher the mode, the deeper the Rayleigh waves penetrate. Although the upper 300 km of the Earth are best sampled by surface waves, higher-mode surface-wave dispersion allows for constraining shear velocity variations down to at least 1000 km depth (Ritsema *et al*., 2004).
- The depth of penetration depends on wave period. Long-period Rayleigh waves sample deeper layers in the upper mantle. They also propagate faster than shorter period Rayleigh waves because mantle structure at greater depth has higher wave speeds.
- Sensitivity kernels illustrate effective "depth resolution" and lateral resolution of Rayleigh wave tomography models (Fig. 3.79). To achieve the best vertical resolution, sensitivity kernels should be close to the delta-function. In reality, in particular for fundamental mode models, depth resolution is low and depends on wave period.

The last point is of particular importance for meaningful interpretation and comparison of surface-wave tomography models, especially fundamental mode models, but is often forgotten. Backus–Gilbert averaging kernels illustrate that fundamental modes of surface waves with period less than 40 sec do not resolve mantle structure below a *c*. 200 km depth. For this reason, Rayleigh waves with periods of 60–80 sec are widely used in tomography studies of the lithosphere–asthenosphere boundary. However, models based on 60 sec and 100 sec fundamental mode Rayleigh waves integrate velocity structure over the top *c*. 200 km and the top *c*. 400 km of the mantle, respectively (Fig. 3.79). For surface-wave models that are constrained not only by fundamental modes, vertical resolution in the uppermost 200 km of the mantle is of the order of 30–50 km. This means that in the uppermost mantle seismic velocity variations within a depth range of 30–50 km are

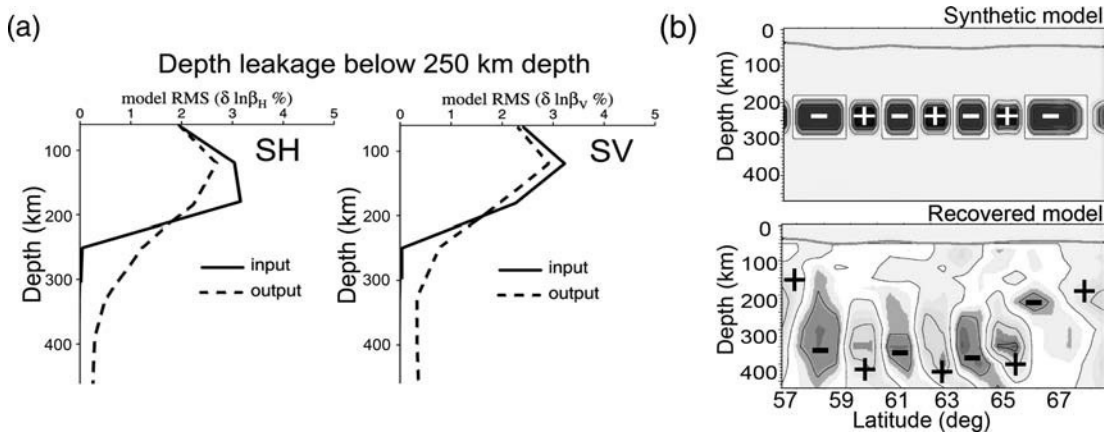

Fig. 3.80 Depth leakage in tomographic models. (a) RMS depth profiles of the input (solid lines) and output (dashed lines) SH and SV shear velocity models calculated for a global surface-wave tomographic model (Zhou *et al.*, 2006). The velocity anomaly in the input model was truncated below 250 km depth. However, in the output model some velocity anomaly persists down to the transition zone. Depth leakage (i.e. depth smoothing) is inevitable in tomographic inversions due to limited path coverage and random noise in synthetic data. (b) Synthetic test for body-wave tomography (after Eken *et al.*, 2008). Top: synthetic model which includes relative negative and positive *Vs* anomalies (±3%) at depths of 180–300 km. Bottom: recovered synthetic model. Pluses and minuses indicate the sign of the recovered anomalies. The amplitude of the recovered anomalies is significantly weaker than that of the anomalies in the synthetic model.

indistinguishable and the depth extent of mid-ocean ridges (~200 km) and of the cratons (~250 km) cannot be better resolved than ~50 km (Ritsema *et al*., 2004). The worst resolution is for the depth range *c*. 300–400 km, the depth to which the deepest roots of the cratonic lithosphere (or tectosphere) may extend (Jordan, 1975a).

Smoothing used in tomographic inversions leads to another limitation on vertical resolution of tomographic models: depth leakage, i.e. velocity anomalies that in the real Earth terminate at a certain depth in the upper mantle, "leak" down in tomographic inversions, and produce a tail of weak anomalies extending well below the bottom of the real anomaly (Fig. 3.80). Such depth smoothing (leakage) is inevitable because of limited data coverage and noise in the data, and weak anomalies should be interpreted with great caution (Zhou *et al*., 2006).

Ray path coverage and lateral resolution

In the horizontal direction, the amplitudes of surface waves decay as the square root of the distance the wave has traveled from the source. Thus they decay more slowly with distance than do body waves and can orbit the Earth several times along great circle paths. An uneven distribution of seismic sources (since most earthquakes occur at plate boundaries) and receivers (most of which are located on land) results in incomplete data coverage of the mantle by surface waves. As for teleseismic body-wave tomography, this puts additional limitations on the effective resolution of surface-wave tomography, although surface waves provide more uniform

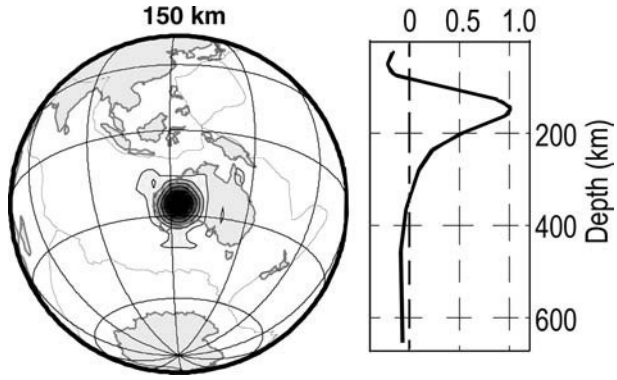

Fig. 3.81 Backus–Gilbert resolution kernels for a point beneath Australia, depth 150 km (left) and the radial dependence of the kernel (on the right) for the tomography model S20RTS which is a degree 20 shear velocity model based on fundamental and higher-mode Rayleigh wave dispersion, teleseismic body-wave travel times, and normal-mode splitting data (after Ritsema *et al*., 2004). The resolution kernels illustrate lateral (left) and vertical (right) averaging in the final tomography model.

data coverage than body waves. As a result of uneven ray path coverage, the resolution of any tomographic model is heterogeneous and high resolution is geographically restricted.

The minimum lateral resolution of a tomography model is proportional to the wavelength $\lambda = V_s T_o$ and is at least *c*. 400 km (here V_s is the average seismic speed in the mantle and T_o is the period). However, the real lateral resolution is much poorer since surface waves orbit several times around the Earth before they are recorded at a seismic station and average the Earth structure along their path (Fig. 3.75). For example, at 150 km depth beneath Australia lateral resolution of the S20RTS surface-wave model (which is a degree 20 shear velocity model based on fundamental and higher-mode Rayleigh wave dispersion, teleseismic body-wave travel times, and normal-mode splitting data, Ritsema *et al*., 1999) is almost half of the continent (~1000 km) (Fig. 3.81). The diameter of the resolution kernel indicates the size of the area over which the velocity anomaly at a given location is averaged.

An uneven ray path coverage may create additional problems in interpretation of regional velocity perturbations in tomographic models as further illustrated by an example from Australia. Because of poor ray path coverage in western Australia, tomography models based on the SKIPPY seismic data could not reliably resolve the upper mantle structure under the western part of the continent (van der Hilst *et al*., 1994). Since in Australia the Archean cratons are located exactly in a poorly resolved domain (Fig. 3.82), some regional tomographic models have been interpreted as evidence for, contrary to globally observed patterns, thinner lithosphere beneath the Archean cratons than beneath the Proterozoic parts of the continent (e.g. Simons *et al*., 1999). Relatively thin lithosphere (~200 km) beneath the Archean cratons of Australia is apparently an artifact of poor model resolution (Fig. 3.83) as evidenced by recent regional tomographic models with an improved ray path coverage for the western domain (B. Kennett, personal communication).

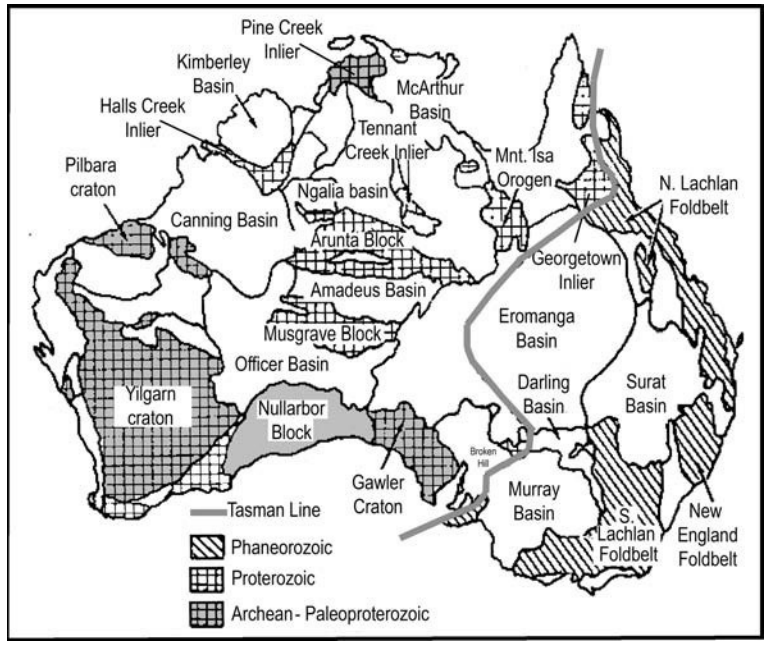

Fig. 3.82 Tectonic map of Australia (based on Goodwin, 1996). The Tasman line marks the transition from the Precambrian western-central part of the continent to the Phanerozoic eastern part of the continent. Western Australia includes two Archean cratons: Yilgarn and Pilbara; central Australia is formed by Mesoproterozoic–Neoproterozoic orogenic belts. Large inner parts of the continent are covered by a thick sedimentary cover and their detailed geology is poorly known.

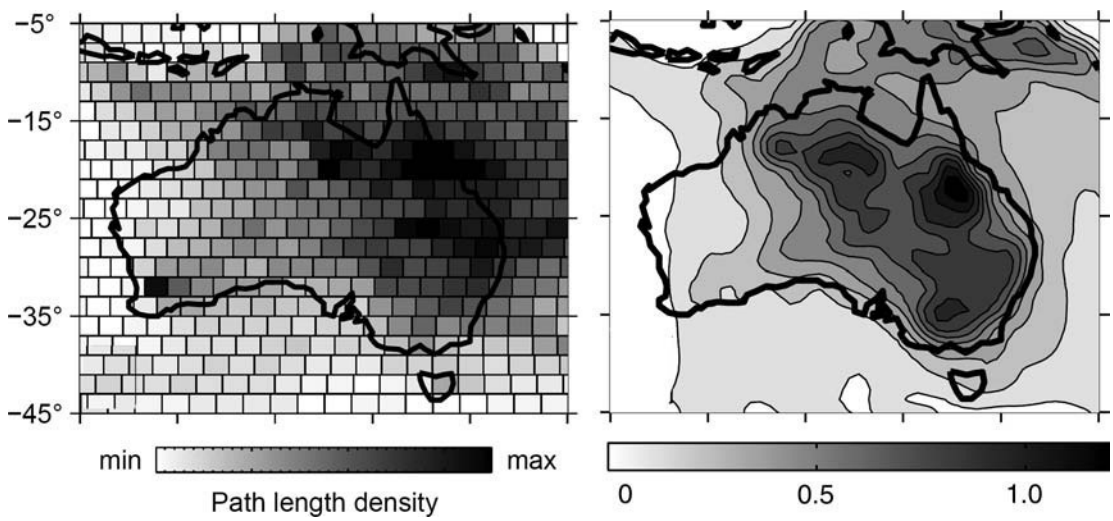

Fig. 3.83 Ray path coverage for Australia based on SKIPPY data (left) and the corresponding resolution test for isotropic surface-wave model (right, darker shades refer to higher resolution) (from Simons *et al*., 2002). Except for western Australia, the tomography model gives a fair representation of the upper mantle shear-velocity structure under Australia.

Crustal corrections

The 21.4 km-thick globally averaged crust incorporated in PREM differs significantly in thickness from both the oceanic and the continental crust. However, propagation of surface waves in the upper mantle is significantly affected by the laterally variable properties of the Earth's crust, and tomographic inversion can erroneously propagate crustal structure down into the mantle. To compensate for this effect, a crustal correction is applied to seismic data before inverting for the mantle structure. Crustal corrections require independent knowledge of the crustal structure since global-scale and regional-scale tomographic models cannot resolve this. Surface waves are sensitive to *V*p and *V*s seismic velocities and density, and thus crustal models should include all of these parameters.

One of the early crustal models used in tomographic modeling was the model of global variations in crustal thickness of Soller *et al*. (1982) complemented by estimated average seismic velocities and densities for oceans and continents (Smith, 1989). A different crustal model was provided by the 3SMAC global tomographic model (Nataf and Richard, 1996). Global crustal models of the next generation are CRUST 5.1 and CRUST 2.0 (Mooney *et al*., 1998; Bassin *et al*., 2000). As compared to earlier crustal models, they are based on an extensive set of seismic reflection/refraction data available at that time for continents and oceans, complemented by high-resolution data on thickness of sedimentary cover (e.g. Laske and Masters, 1997). These models are parameterized on 5 deg x 5 deg and 2 deg x 2 deg grids, respectively, and include average values of thickness, density, *V*p and *V*s velocities for seven crustal layers; cells with no seismic data are filled with statistical averages for a crust of the same type (tectonic setting and age) (see also Section 3.3.1 and Figs. 3.38 and 3.39).

The effect of crustal structure on the phase velocities of surface waves has been analyzed in detail by Mooney *et al*. (1998), Boschi and Ekstrom (2002) and Ritsema *et al*. (2004) for the CRUST 5.1 model and by Bassin *et al*. (2000) for the CRUST 2.0 model. Additional discussions can be found in Laske and Masters (1997) and the effect of ice is discussed by Ritzwoller *et al*. (2001). The following summary is based on the results of these studies.

The effect of crustal heterogeneity is different for fundamental and higher-mode surface waves:

- For fundamental mode Rayleigh waves and the highest overtones, the crustal effect on velocity perturbations in the model is of critical importance because phase velocity variations caused by crustal heterogeneity and derived from the seismic data have similar amplitudes (Fig. 3.84).
- For the first and second Rayleigh overtones, the effect of crustal corrections is small as compared to the observed seismic data. Although these overtones provide constraints on mantle structure that are largely independent of the crust, they average the entire upper mantle and have low sensitivity to the lithospheric structure (Fig. 3.79).

The effect of crustal heterogeneity on velocity perturbations in the model depends on the period of surface waves:

Long-period surface waves:

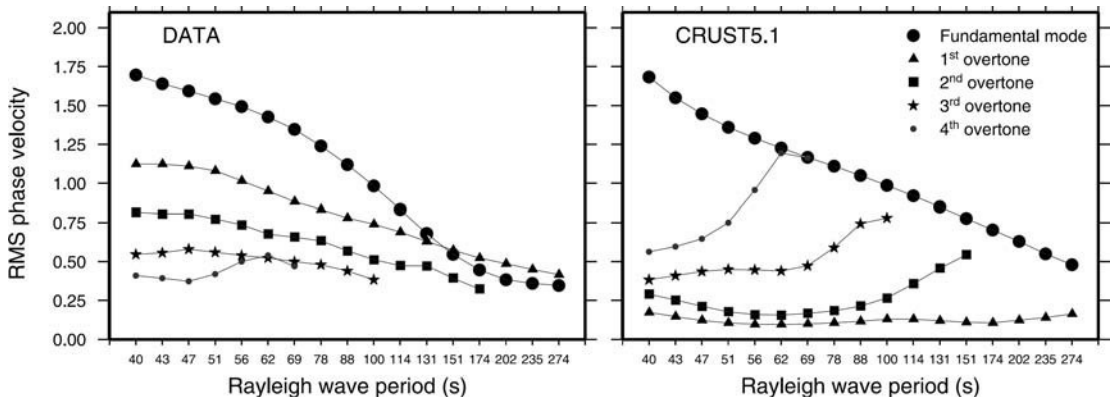

Fig. 3.84 Root-mean-square (RMS) phase velocity perturbation with respect to PREM (in %) of the Rayleigh wave phase velocity fundamental-mode and overtones in the data (left) and produced by crustal correction (for the CRUST 5.1 model, Mooney *et al*., 1998) due to thickness and velocity variations in the crust (right) (from Ritsema *et al*., 2004). For the fundamental-mode Rayleigh wave and the highest overtones, the RMS of the phase velocity distribution caused by variations in the crustal structure and the RMS derived from the data have similar amplitudes; for these modes the crustal effect on velocity perturbations in the model is of a critical importance. For the first and second Rayleigh overtones, the RMS of the crustal corrections is small compared to the observed RMS; this means that these overtones provide constraints on mantle structure that are largely independent of the crust. However, these overtones average the entire upper mantle and have low sensitivity to the lithospheric structure (Fig. 3.79).

- Variations in crustal structure have little effect on lateral variations in phase velocities.
- Crustal corrections, however, increase the variance of observed phase velocities in the mantle since seismic signals from the crust and from the upper mantle are often anti-correlated. For example, the peak-to-peak amplitude of 167 s Rayleigh waves increases by a factor of 1.3 after the crustal correction is applied.
- For Rayleigh waves at a period of 150 s the crustal contribution to phase velocity variations can be as large as 50% of the total signal and with sign opposite to that of the mantle contribution.

Short-period surface waves:

- Phase velocity variations caused by crustal heterogeneities are very strong. If crustal correction is applied, the peak-to-peak amplitude of phase velocity anomalies for 40 s Rayleigh waves is twice as large as for 167 s Rayleigh waves.
- Crustal corrections to Rayleigh waves significantly redistribute phase velocity anomalies and in many cases make them more localized.
- Rayleigh waves are sensitive to Vp velocity heterogeneity in the crust, in particular in the near-surface layers, and the presence of large sedimentary basins may have a significant effect on phase velocities. For example, the analysis performed for Rayleigh waves at 35 s indicates that underestimation of sedimentary thickness by 1 km produces a +1% erroneous increase in phase velocities, while a 3 km overestimation of sediment thickness in large parts on the continents has the opposite effect and produces a velocity error of

c. +2.5% (the consequences of different crustal models on tomographic results can be assessed by comparing Figs. 3.39 and 3.40 for Eurasia).

- Similarly, the presence of a thick ice sheet such as in Antarctica and Greenland, strongly affects surface wave velocities at short and intermediate periods: because of the very low density of ice at short periods the ice reduces the velocities similar to a sedimentary basin, and its presence on top of the crust also reduces the surface-wave velocities at intermediate periods.
- Since the sensitivity of Love waves is greatest in the upper 40 km of the Earth, these waves mainly sample the crust and are highly sensitive to variations in crustal structure. Note that Love waves are affected only by variations in *V*s and density and are insensitive to *V*p variations. As a result, they sample the crust and the mantle in different ways than Rayleigh waves at the same period. The effect of crustal correction on Love waves is twice as large as for Rayleigh waves at the same period. Strong dependence of very short wavelength Love waves on crustal structure can be used to refine crustal models in regions with poor coverage by seismic refraction data (Ekström *et al*., 1997).

Note that CRUST 5.1 and CRUST 2.0 models average crustal structure over large areas (*c*. 550 km x 550 km and 200 km x 200 km, respectively). Use of even these advanced models for crustal correction can lead to significant artifacts at tectonic boundaries that separate crustal types with significantly different thickness, velocity, and density structure. This effect may be particularly important at the continent–ocean transition or at the transition from the Precambrian to Phanerozoic crust with significantly different average crustal structure (e.g. Fig. 3.41). Because of its higher lateral resolution the CRUST 2.0 model should provide a better correction for crustal heterogeneity.

Absolute versus relative velocities

As discussed earlier, a simple comparison between different tomographic models is hindered by differences in:

- data sets used to constrain them,
- parameterizations and regularization schemes,
- crustal models used for crustal corrections.

Most of the tomographic models work not with real velocities but with velocity perturbation with respect to some reference velocity model (for details see the overview by Kennett, 2006). Use of different reference models, when the results are presented as velocity perturbation with respect to them, but not as absolute velocities, further complicates comparison between different tomographic results.

The most commonly used reference models are *iaspei* (or *ak135*) and PREM. The latter is dominated by the oceanic velocity structure (as oceans comprise *c*. 70% of the Earth) and thus has the step at 220 km depth not required by the continental seismic data. As a result, all tomographic models that use PREM as a reference model inherit the velocity drop at 220 km depth (e.g. Su *et al*., 1994). Tuning of the reference model in tomographic models for the continents to a "zero-level" model smooths the step but does not exclude it entirely (Fig. 3.86). This leads to

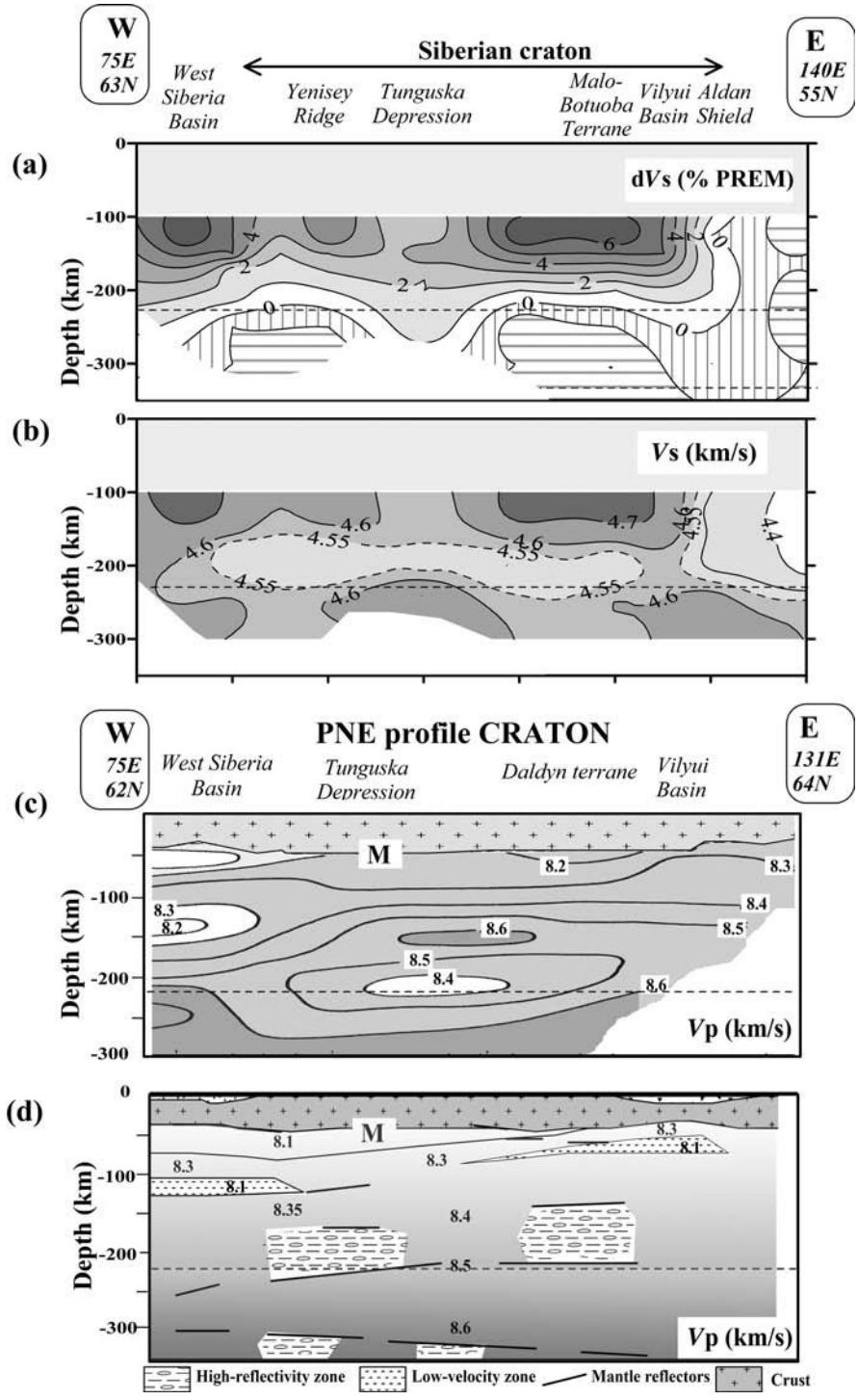

Fig. 3.85 Velocity structure of the upper mantle beneath Siberia. (a) Relative *Vs* velocity perturbations with respect to PREM based on Rayleigh wave tomography (results of Priestley and Debayle, 2003); (b) the same velocity model recalculated to absolute velocities; (c) and (d) *Vp* velocity structure along the part of the long-range PNE profile CRATON that crosses similar tectonic

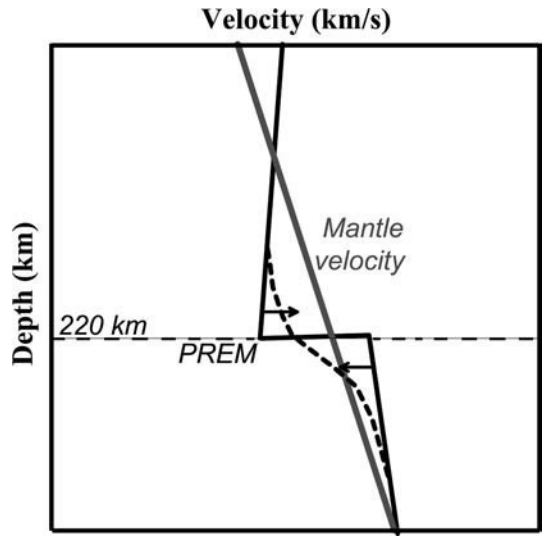

Fig. 3.86 Sketch illustrating that using PREM as a reference model in tomographic inversions for continental regions may lead to erroneous interpretations of the thickness of the seismic lithosphere. Inversion tends to 'smooth' the step at 220 km depth, which is not required for the continental mantle, by increasing velocities above and decreasing velocities below 220 km depth (dashed line), thus artificially enhancing the velocity gradient across the 220 km depth.

artificially perturbed seismic velocities in a *c*. ±70 km thick corridor above and below 220 km depth (at *c*. 150–300 km depth). Since seismic velocities beneath many stable continental regions still show positive velocity anomalies below a 300 km depth, a velocity decrease around 220 km depth and a strong velocity gradient zone commonly observed at *c*. 220 km depth beneath stable continents may be an artifact of using PREM in inversion.

Unfortunately, 220 km is also the depth where the deepest kimberlite magmas are generated and from which deep mantle xenoliths are brought to the surface. As xenolith data seem to indicate lithospheric thickness in cratons to be 200–220 km (perhaps only because greater depths are not sampled by kimberlite magmatism, see detailed discussion in Chapter 5), it is not surprising that many seismologists are tempted to interpret a sharp change in relative velocities at the same depth as the base of the seismic lithosphere. However, a high velocity gradient zone may not even exist if the absolute velocities are considered.

A dramatic effect of the reference model on tectonic interpretations is illustrated by Fig. 3.85 (see Fig. 3.68 for the location map). A tomographic model for Siberia was

Caption for figure 3.85 (cont.)
structures to the tomographic model (based on results of (c) Burmakov *et al*. (1987) and (d) Pavlenkova *et al*., 1996). Apparent location of the base of seismic lithosphere at *c*. 200 km depth as suggested by a sharp change in the sign of relative *Vs* velocity perturbations in (a) is inherited from a velocity step at 220 km depth (marked by dashed lines) in PREM and is also not supported by the absolute *Vs* velocities which show only a moderate velocity decrease at around 200 km depth (b) or by *Vp* velocities along the subparallel CRATON profile (c, d). See Fig. 3.68 for the location map. A reduced-velocity zone at a depth of 150–200 km is observed along the PNE profiles beneath many terranes of Siberia (Fig. 3.70).

calculated from fundamental and higher mode *S*V Rayleigh waves as relative perturbations with respect to PREM (Priestley and Debayle, 2003). As a result, the final model inherited a velocity discontinuity at around 220 km depth. A sharp change in the sign of relative *V*s velocity perturbations at *c*. 200 km depth was interpreted by the authors as the base of the seismic lithosphere beneath the Siberian craton. However, absolute velocities show only a small decrease (by 0.05 km/s) in seismic velocities at *c*. 170–220 km depth with higher velocities below 220 km. Although this reduced-velocity zone may be an artifact associated with PREM, similar low-velocity zones at a depth of 150–200 km are observed along PNE profiles beneath many terranes of Siberia (Fig. 3.70). The *V*p velocities along the long-range PNE profile CRATON that crosses the Siberian craton further north through the same tectonic structures show some lower velocity anomaly only beneath the Tunguska Basin (Fig. 3.85c), while other interpretations along the same profile demonstrate a gradual increase in *V*p with depth down to the transition zone (Pavlenkova *et al*., 1996; Nielsen *et al*., 1999).

3.6.2 Elastic tomography models of the upper mantle

Global patterns

Teleseismic tomography images calculated by different research groups over the past 25 years provide a coherent qualitative portrait of the 3D velocity structure of the upper (and lower) mantle. Recent S-velocity tomographic models are well correlated at the long wavelengths (spherical harmonics < degree 12), and P- and S-velocity variations in the upper mantle are well correlated also (e.g. Ritzwoller and Lavely, 1995; Ritsema and van Heijst, 2002). Since the heterogeneity spectrum of the Earth is distinctly "red" (i.e. dominated by large-wavelength components (Su and Dziewonski, 1991)), the large-scale velocity anomalies are easier to recover and they are the most reliable in tomographic modeling. Furthermore, Dziewonski (2003) argues that

> the observed anomalies in seismic data result from integration of perturbation in structure either along the ray path, for travel times, or volume for splitting of low order normal modes. Perturbation is a smoothing operation and, assuming constant amplitude, the effect of the component of the structure with a wavelength λ_1 compared to that of λ_2 is equal to the ratio λ_1/λ_2. Thus long-wavelength components of the structure are much easier to recover than short-wavelength ones.

Significant discrepancies in the amplitudes and in the radial distributions of velocity anomalies, in particular in the uppermost mantle, result, in part, from incomplete crustal corrections, unaccounted variations in topography of first-order seismic discontinuities in the mantle, and from incorrect assumptions on the relations between *V*p and *V*s heterogeneity.

The most important robust result of global tomography is the observation of a strong correlation of velocity structure of the upper 200–300 km with surface tectonics observed in all tomographic models (Fig. 3.87). Strong (~15%) velocity heterogeneity in the upper mantle (down to *c*. 300 km depth) is related to plate tectonics and the ocean–continent variation (Nataf and Ricard, 1996). The ocean–continent variation is the first-order feature revealed by all types of seismic data. In the upper 200 km, P-velocity heterogeneity in body-wave tomography models is well correlated with major surface tectonics elements such as

cratons and subduction zones, where peak anomalies exceeding 2% are observed (Vasco *et al*., 2003). Low-velocity anomalies associated with back arc basins can be traced down to 200–400 km depth, while some cratons are seen as high-velocity anomalies (although of a smaller lateral extent) down to 400 km depth.

Similarly, surface-wave tomography indicates the existence of a strong correlation between surface tectonics and the patterns of velocity heterogeneity in the upper mantle: fast regions (with positive velocity anomalies with respect to PREM) are observed beneath the cratons, while slow regions are observed beneath the oceans. Except for tectonically active regions such as western USA, regional continental models have high shear velocities throughout the entire upper mantle (higher than 4.5–4.6 km/s) and, in a good agreement with PREM, flat-gradient velocity profiles between 200 km and 410 km depth (Fig. 3.88). Linear belts of high mantle velocities clearly correlate with major continent–continent and continent–ocean collisional zones (e.g. the Andes, the Himalayas–Tibet, the Altaids of Central Asia, and Java–Sumatra) and are associated with subducting slabs. Tectonically active regions, although not so well resolved due to their smaller size, show slow velocities in the upper mantle. Similarly, the oceanic upper mantle has slow velocities, in particular at shallow depth along mid-ocean ridges (Fig. 3.87).

In the cratonic regions high upper mantle velocities may persist down to 200–300 km depth (Fig. 3.89). As discussed earlier, the apparent termination of high-velocity anomalies at these depths can be a systematic artifact due to:

(1) use of PREM in tomographic inversions for the continents (Fig. 3.86);
(2) use of fundamental modes that (for periods <40 sec) cannot resolve upper mantle deeper than ~200 km (Fig. 3.79);
(3) a general decrease in resolution of tomographic models at 300–400 km depth.

Global observations of the velocity structure of the upper mantle are supported by recent high-resolution continent-scale and regional tomographic models. Seismic velocity structure of the continents and oceans is discussed in more detail below. First, an overview of continent-scale and ocean-scale patterns is provided, followed by the characteristic velocity structures for various continental and oceanic tectonic settings.

Continents

A detailed description of regional studies is outside the scope of this book which aims to discuss general patterns in lithospheric structure related to the tectonic evolution of the Earth. A brief (and inevitably incomplete due to the huge number of regional publications) overview of continent-scale tomographic models is presented below. The limitations on vertical, lateral, and amplitude resolution of tomographic models are discussed in detail in the previous section.

North America and Greenland

Since the early tomographic models (Grand and Helmberger, 1984), it has been recognized that the velocity structure of the upper mantle in North America is well correlated with

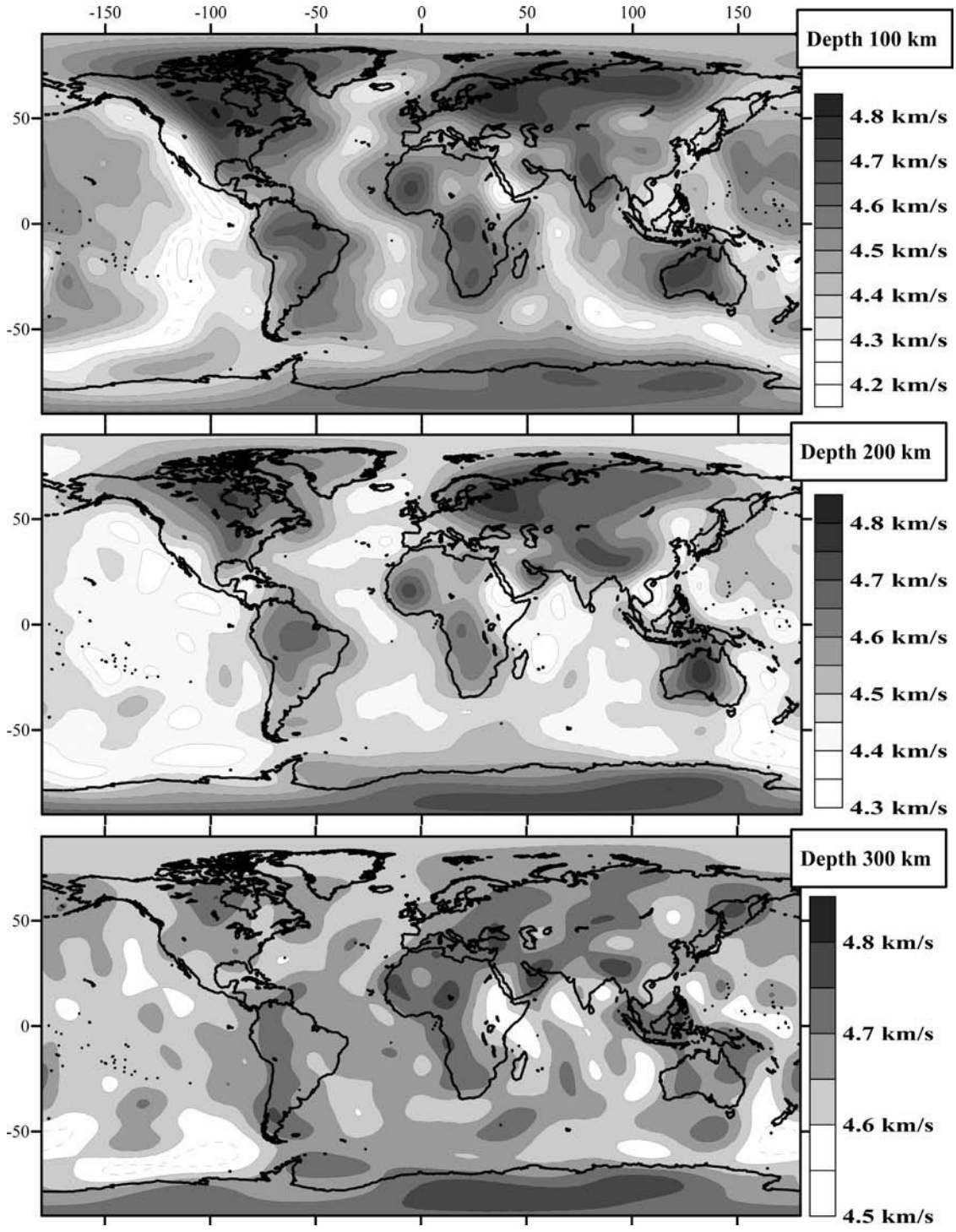

Fig. 3.87 Shear-wave velocity structure of the upper mantle at 100 km, 200 km, and 300 km depth based on the global S362ANI tomography model of Kustowski *et al*. (2008). In this model, radial anisotropy is confined to the uppermost mantle (that is it becomes very small below a depth of 250 km and disappears at 410 km). Including anisotropy in the uppermost mantle significantly improves the fit of the surface-wave data. The inversion is based on a new spherically symmetric reference model REF.

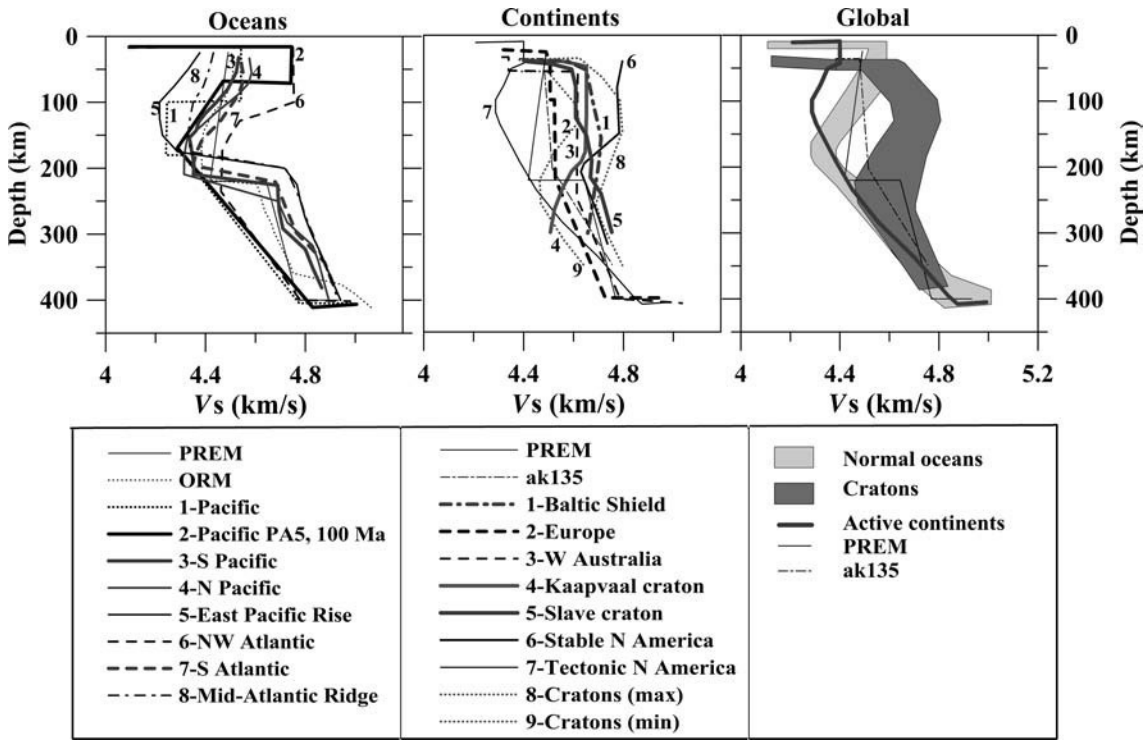

Fig. 3.88 Mean isotropic shear velocity profiles for regional and global oceanic (left) and continental (middle) tomographic models. Regional models commonly provide a better fit to observed seismograms from these regions than the existing global tomographic models. Right panel: typical shear velocity profiles for normal oceans, cratons, and active continents. Reference models are shown as a comparison: global model *PREM* (Dziewonski and Anderson, 1981), global continental model *ak135* (Kennett *et al*., 1995), and global reference models for normal oceans (ORM) and continents (CRM) based on S20RTS model (Ritsema *et al*., 2004). References for regional models: Grand (1994, 1997); Lerner-Lam and Jordan (1987); Kennett *et al*. (1994); Gaherty *et al*. (1999); Simmons *et al*. (2002), Pedersen *et al*. (2009), Lebedev *et al*. (2009). Compare with Fig. 3.101a.

surface geology (e.g. Grand, 1994; Humphreys and Dueker, 1994; van der Lee and Nolet, 1997a; Nettles and Dziewonski, 2008):

(1) In the Archean–Paleoproterozoic provinces of the Canadian Shield, the strongest shear-velocity anomaly is observed in the upper 200 km of the mantle with a weaker velocity anomaly extending down to *c*. 300 km depth (Fig. 3.90).
(2) A recent high-resolution seismic tomography model indicates the presence of two distinct lithospheric domains in the Canadian Shield with the boundary at approximately 86–87° W (the Wabigoon-Wawa/Quetico boundary) (Frederiksen *et al*., 2007). To the west of this boundary, the lithospheric mantle has high velocities, while to the east the average shear-velocity anomaly is *c*. 2.5% weaker (relative to *iasp91*).

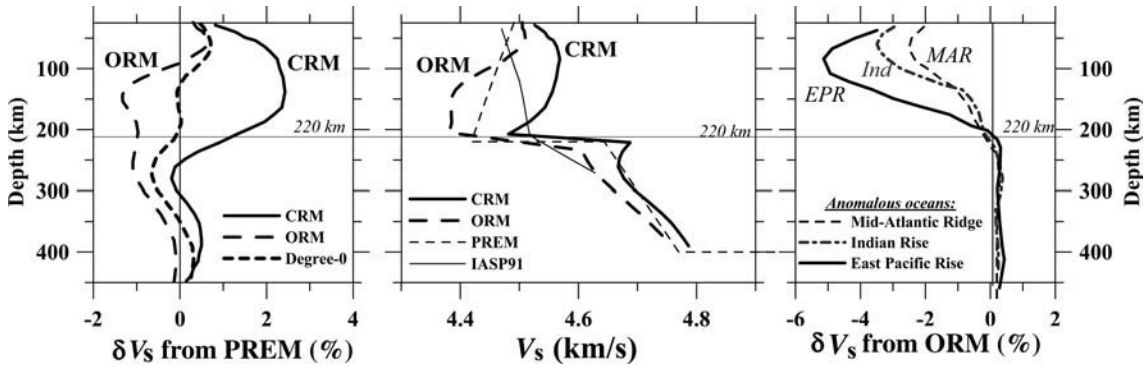

Fig. 3.89 Depth profiles of average shear velocity anomalies in the upper mantle based on the S20RTS global tomographic model of Ritsema *et al*. (2004). Left: average seismic velocity profiles with respect to PREM beneath continents (the Continental Reference Model, CRM) and beneath those oceanic regions where water depth is 5500–6500 m and lithosphere is 40–80 My old (the Oceanic Reference Model, ORM; for these ocean regions, cooling plate models explain the bathymetry and the surface heat flow well); dashed line labeled "Degree–0" – average anomaly of the entire S20RTS model (Ritsema *et al*., 2004). Middle: the same reference models converted to absolute velocities; global models PREM and *iasp91* are shown for comparison. CRM and ORM inherit the LVZ at around 220 km depth when converted to absolute velocities. Right: Depth profiles of average S20RTS shear velocity heterogeneity in the upper mantle of anomalous oceanic structures (the East Pacific Rise, Indian Rise, and the Mid-Atlantic Ridge) with respect to ORM (after Ritsema *et al*., 2004). Below 220 km depth and down to the transition zone, both oceanic and continental velocity profiles based on the S20RTS model have systematically higher values (by 0.1–0.2 km/s) than global models.

(3) At present, tomographic models of the Archean Slave craton are largely restricted to models based on the POLARIS seismic array in the central part of the craton. They indicate that high shear velocities in the upper mantle persist down to at least a 300 km depth (Pedersen *et al*., 2009).
(4) In the terranes of Mesoproterozoic age in south-central North America (Fig. 3.66), a positive velocity anomaly in the upper mantle is more shallow than beneath the Archean–Paleoproterozoic terranes and terminates at around 200–250 km depth.
(5) Western North America, as other tectonically active continental regions, is, in general, characterized by slow upper mantle velocities which already start at *c*. 50–70 km depth and have a minimum at *c*. 100–120 km depth (Figs. 3.88, 3.90b).

However, recent high-resolution regional tomographic models for northwestern USA image a very complex mosaic of velocity anomalies in the upper mantle related to post-Laramide tectono-magmatic events and the tectonic evolution of the Cascadia Subduction Zone (e.g. Roth *et al*., 2008). The major features of the upper mantle P-wave velocity structure are well-resolved fast velocities associated with the Juan de Fuca–Gorda slab (which is traced down to at least 500 km), beneath the Idaho batholith and beneath Nevada where a slab-like

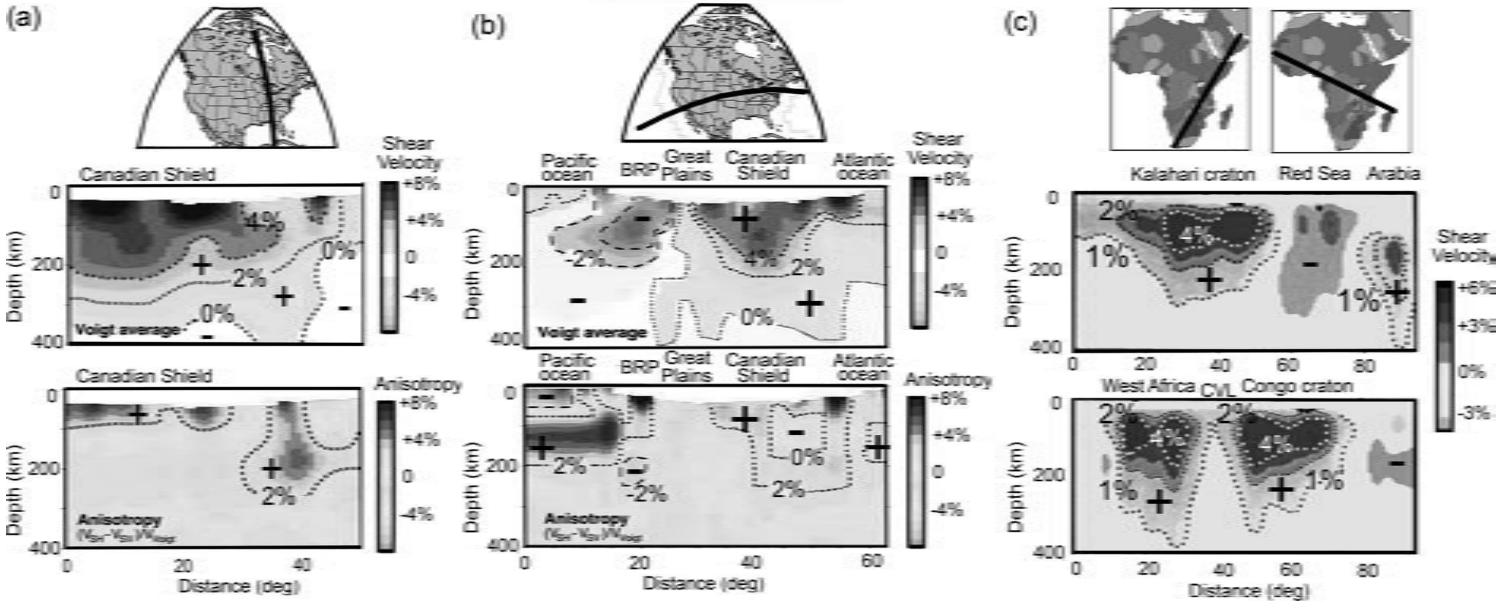

Fig. 3.90 Shear velocity perturbations in the upper mantle of (a, b) North America (based on Nettles and Dziewonski, 2008) and (c) Africa (based on Ritsema and van Heijst, 2000a). (a, b) Top – locations of two profiles: (a) N–S from the Hudson Bay to the Gulf of Mexico and (b) W–E from the Pacific to the Atlantic Ocean across North America. Middle – Voigt average shear-wave velocity along the profiles, plotted with respect to the global average at each depth. Bottom – anisotropy along the profiles (no average has been removed). Dotted lines outline contours of 0%, +2%, and +4% velocity anomalies; dashed lines – contours of negative anomalies. BRP = Basin and Range Province. (c) Top – locations of two profiles: SE–NW from the Cape Fold belt to the Persian Gulf and NE–SW from West Africa to Madagascar. Middle and bottom – shear wave velocity perturbations along the profiles, plotted with respect to the PREM model at each depth. Dotted lines outline contours of +1%, +2%, and +4% velocity anomalies. CVL = Cameroon Volcanic Line.

eastward-dipping feature of increased P-wave velocities is observed down to at least 300 km depth (and perhaps as deep as 700 km). Slow upper mantle velocities are observed beneath the Yellowstone–Snake River plain, the north-central Oregon, and along the Pacific coast. Several tomographic studies have imaged fast linear velocity anomalies below a 200–300 km depth that are sub-parallel to the Pacific coast and extend down to *c*. 1500 km depth beneath the western-central North American continent. They are interpreted as fragments of the Farallon plate, a huge oceanic plate that has subducted beneath the American plates during the Mesozoic and Cenozoic eras (van der Lee and Nolet, 1997b; Bunge and Grand, 2000).

For Greenland, the number of regional-scale tomographic models is so far very limited and restricted to the GLATIS project (Darbyshire *et al*., 2004). The analysis of *fundamental-mode* Rayleigh wave phase velocity dispersion curves (over the period range 25–160 s) suggests that in the "lithosphere" the shear wave velocity is 4–12% above global reference models (for resolution kernels, see Fig. 3.79). The thickness of the lithosphere is estimated to be *c*. 100 km along the southeast coast of Greenland increasing to *c*. 180 km beneath central-southwestern Greenland where the highest velocities are reported. A body-wave tomographic model (e.g. Grand, 2002) indicates that the region of high shear velocities (2% above PREM) may extend down to *c*. 300 km.

South America

Until recently, regional tomographic models of South America suffered from insufficient ray coverage, and the upper mantle velocity structure beneath most of the stable part of the continent to date remained largely unconstrained (Fig. 3.91). Recent tomographic models provide reliable images for the upper 100–200 km of the mantle, but their resolution is still limited due to the poorly known crustal structure of the continent. The best known is the velocity structure of the upper mantle beneath the Andes (both for compressional and for shear waves) which has been resolved in great detail by numerous studies. They indicate a complex short-wavelength pattern of fast and slow velocities which suggests that lateral variations in composition, melting, and water content play an important role in velocity variations in the mantle wedge.

The major large-scale features of the South American upper mantle revealed by recent tomographic studies include:

(1) slow subhorizontal shear-velocity anomalies in the upper mantle down to *c*. 150 km depth beneath the Andes associated with flat subducting slab;
(2) Eastward-dipping slow-velocity anomaly in the mantle continues beneath the Chaco Basin and extends as far east as the Paraná Basin where it is imaged at a 200–300 km depth; low velocities down to *c*. 200 km beneath the Chaco and the Pantanal Basins can be associated with the subducting slab;
(3) high *V*s velocities beneath the Paraná and the Parnaiba Basins down to 100–150 km depth and perhaps as deep as 250 km (Lebedev *et al*., 2009);
(4) fast-velocity anomaly down to *c*. 200 km depth beneath the Archean Amazonian craton as consistently imaged by different tomographic models; some regional tomographic

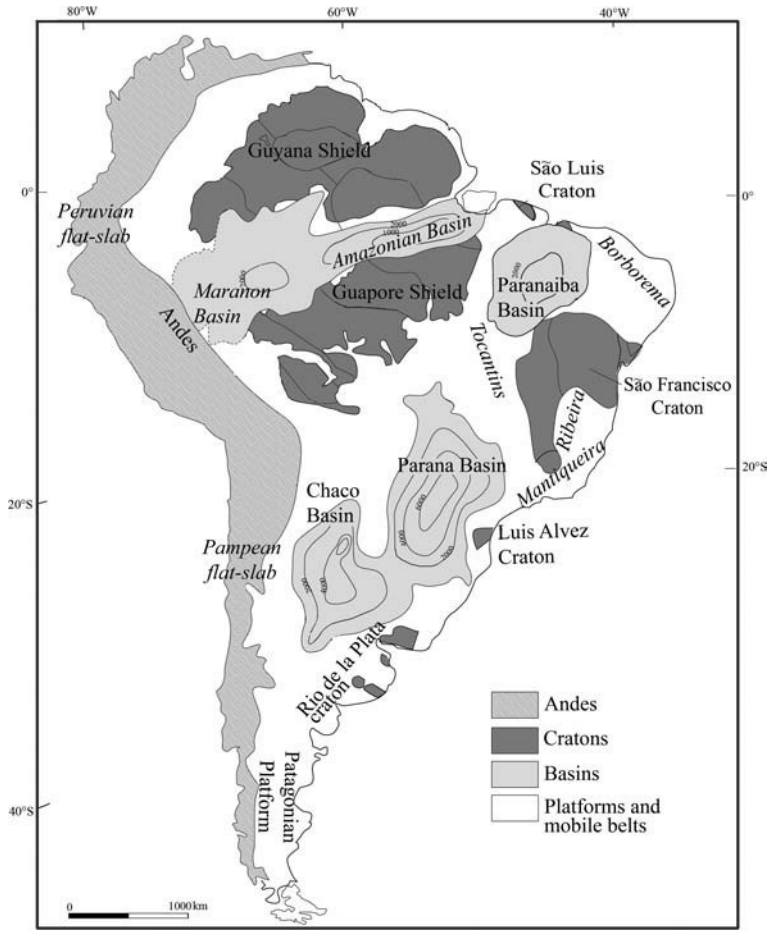

Fig. 3.91 Major tectonic provinces of South America (based on Heintz *et al.*, 2005).

studies image a reduced-velocity anomaly beneath the Amazon Basin (a paleorift?) which cuts the oldest part of the continent into two subcratons (the Guayana and the Guapore Shields);

(5) high-velocity region in the upper mantle (down to 150–200 km depth) beneath the Archean Saō Francisco craton.

Most tomographic results for South America are based on fundamental mode surface waves (e.g. Feng *et al*., 2007) and thus cannot reliably resolve the upper mantle structure below 200 km depth (Fig. 3.79).

Europe

Tomographic models for Eurasia, one of the best studied continents, are numerous, both on the continent-scale and at regional scales (e.g. Panza *et al*., 1980; Spakman, 1991; Zielhuis and Nolet, 1994; Villaseñor *et al*., 2001; Piromallo and Morelli, 2003; Kustowski *et al*.,

2008b). The major large-scale patterns are as follows (for details and references see Artemieva *et al*., 2006).

High-velocity compressional and shear-velocity anomalies are imaged in the upper 200–250 km beneath the cratonic regions, with the strongest anomalies beneath south-central Finland in the Baltic Shield where they extend down to at least 250 km. Below this depth, most published tomography models lose resolution since they are based on fundamental-mode surface waves. Tomographic models based on body waves and higher-mode surface waves display fast shear-velocity anomalies (Vs > 4.7 km/s) down to at least 300 km depth. High-resolution tomographic shear-velocity models of the Baltic Shield based on the SVEKALAPKO seismic tomography experiment image a surprisingly complex upper mantle structure with large velocity and anisotropy variations at relatively small lateral and vertical scales. While a certain correlation is recognized between shallow upper mantle anomalies and surface geology, deeper anomalies are difficult to correlate with tectonics.

For the East European (Russian) Platform which lacks seismic events, high resolution regional tomographic images are limited mostly to the southern and western parts, where ray path coverage is better. There, fast Vs- and Vp- velocities are observed down to *c*. 150 km depth with smaller-scale anomalies extending down to at least 250 km. Recent analysis based on broad-band surface wave dispersion indicates that the high-velocity "lid" of the platform can be 250–300 km thick (Lebedev *et al*., 2009). The fastest upper mantle velocities (Vs > 4.7 km/s at 250–320 km depth) are reported for the Archean Volga–Uralia province in the eastern part of the platform and for the Archean Ukrainian Shield–Vitebsk block in the western part of the East European craton (Fig. 3.69). Surprisingly, the velocity structure of the upper mantle beneath the huge Paleozoic Dnieper–Donets rift in the southern part of the platform does not differ from the surroundings, probably due to lack of lateral resolution. A strong positive-velocity anomaly is found beneath the Caspian basin at 100 km depth.

The western edge of the East European craton is marked by a remarkably sharp change in the upper mantle velocity structure at the transition from the cratonic to Phanerozoic crust of western and central Europe (the Trans-European suture zone, the major tectonic boundary in Europe). While in cratonic Europe fast velocities extend down to *c*. 200 km, they typically terminate at *c*. 70–100 km depth in most of Phanerozoic Europe. The maximum velocity contrast across the cratonic margin is between the Pannonian Basin and the East European Platform (12% at 80 km depth) (Zielhuis and Nolet, 1994). A zone of low shear velocity at 300–400 km depth beneath the cratonic margin has been interpreted as a relic from the paleosubduction zone (Nolet and Zielhuis, 1994).

The recent seismic tomography experiment (TOR) across the Trans-European suture zone (TESZ), from the stable lithosphere of the Baltic Shield to the Phanerozoic lithosphere of western Europe, has demonstrated a contrasting upper mantle seismic structure between lithospheric terranes of different ages. The interpretation of the lithospheric base, constrained by a transition from positive to negative velocity anomalies with respect to the reference model, suggests that over the lateral distance of 200–250 km the lithospheric thickness decreases step-wise from *c*. 220 km beneath the Baltic Shield to *c*. 50 km beneath Phanerozoic Europe (Fig. 3.92). Since the thermal regime of the lithosphere along the TOR

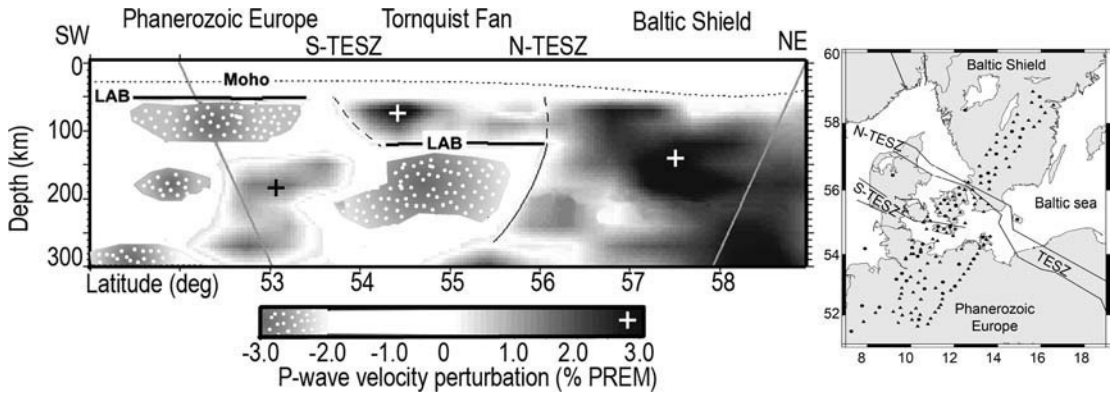

Fig. 3.92 P-wave tomography model across the margin of the Baltic Shield (after Arlitt, 1999). LAB = Lithosphere–asthenosphere boundary; TESZ = Trans-European Suture Zone which marks the transition from the East European craton to Phanerozoic Europe; it appears as two major trans-lithospheric sutures in the Danish area, where the TESZ splits into two branches bounding the Tornquist Fan.

profile is approximately the same on the cratonic and on the Phanerozoic sides, the observed sharp change in velocity anomalies in the upper mantle is likely to be of a compositional origin (Artemieva *et al*., 2006). In this case, the transition from positive to negative velocity anomalies seen in TOR tomography should be interpreted as the base of the *chemical* lithosphere. Such an explanation has petrological grounds: iron-depleted cratonic lithosphere should have higher seismic velocities than the fertile Phanerozoic lithosphere of western Europe and the Proterozoic lithosphere of the Tornquist Fan (the area located between two split branches on the TESZ in the north, Fig. 3.92) which has been subject to wide spread Paleozoic magmatism and thus could have been metasomatised by basaltic melts.

The velocity structure of the upper mantle of the tectonically young structures of Europe is highly heterogeneous at small scales. Low-velocity anomalies at *c*. 70 km depth are imaged in the upper mantle beneath the Pannonian Basin and some parts of the French Massif Central. Seismic tomography images a mosaic of high- and low-velocity bodies in the upper mantle of southern Europe and the Mediterranean (e.g. Bijwaard *et al*., 1998; Piromallo and Morelli, 2003). High-velocity anomalies are commonly interpreted as images of subducting slabs pushed into the mantle by complex tectonic stresses associated with the collision of the European and African plates.

High-resolution regional tomography across the Alpine orogen has revealed several high-velocity bodies in the upper mantle that have been interpreted as subducting slabs. One of them dips southeastwards beneath the Adriatic microplate in the western and central Alps and is interpreted as subducted European lower lithosphere. Another dips northeastwards in the eastern Alps and is interpreted as Adriatic lower lithosphere subducting beneath the European plate (Fig. 3.93, compare with Fig. 3.62). Similarly, a near-vertical localized high-velocity body is imaged in the upper mantle beneath the Vrancea zone in the Carpathians. Tectonic interpretations of its origin remain controversial. Since the velocity anomaly

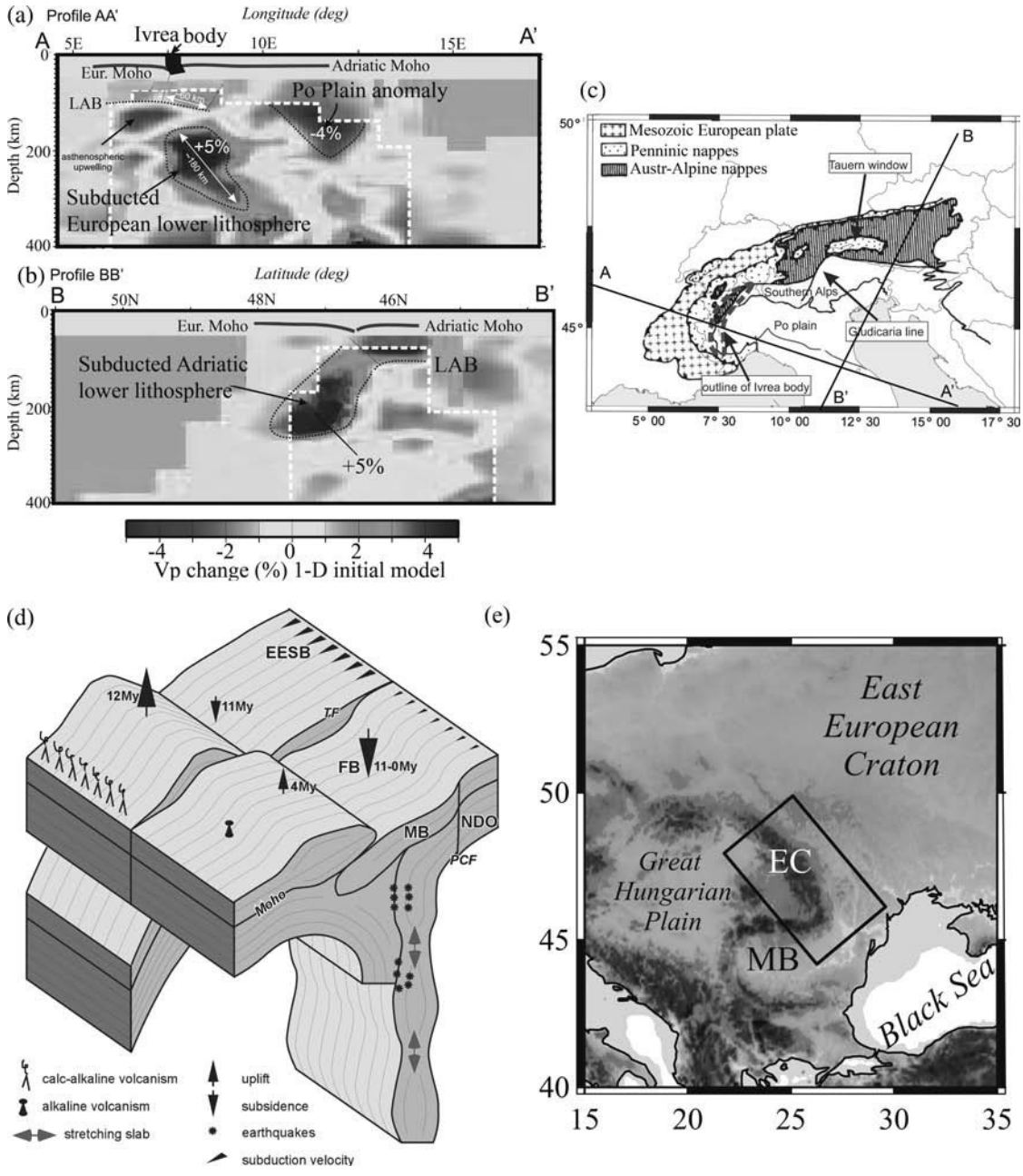

Fig. 3.93 (a)–(c): Upper mantle structure beneath the Alpine orogen from high-resolution teleseismic P-wave tomography (based on Lippitsch *et al*., 2003). Regions with high resolution are outlined by white dashed lines. (c) Tectonic map of the Alps with the location of the profiles across the western and eastern Alps. (d): 3D cartoon of the subduction pattern in the East Carpathians (the Vrancea zone) (from Cloetingh *et al*., 2005). (e) Shaded topography of the region; the box shows the area illustrated in (d). EC – East Carpathians; EESB – East-European/Scythian block; MB – Moesian block; NDO – North Dobrogea orogen; TF – Trotus Fault; PCF – Peceneaga-Camena Fault.

correlates with the zone of high seismicity, most interpretations invoke the presence of a subducting slab or a delaminated lithosphere fragment in the upper mantle of the region (Section 9.3 and Fig. 9.25).

Siberia and Kazakhstan

Tomographic models for the Paleozoic West Siberian Basin (which contains buried terranes of Archean ages) and for the largely Archean–Paleoproterozoic Siberian craton (the southeastern parts of which were rifted in the Paleozoic) remain controversial, in part due to significant differences in the crustal models used in tomographic inversions (in particular the CRUST5.1 model significantly, >5 km, underestimates the crustal thickness in some parts of the Siberian Platform). Fundamental-mode surface-wave tomography models image fast shear velocities down to at least 200–250 km depth beneath the Siberian craton (Villaseñor *et al*., 2001), with some of them displaying fast upper mantle velocities (2% higher than in the *iaspei* reference model) down to *c*. 250–300 km depth, below which they lose resolution (Shapiro and Ritzwoller, 2002). However, a body-wave model (Grand, 2002) displays fast *V*s velocities (+2+4% with respect to *ak135*) beneath all of the Siberian Platform at 175–250 km depth and beneath major kimberlite fields at 250–325 km depth. At 325–400 km depth the Siberian Platform has near-zero velocity anomalies, while the Volga–Uralia province of the East European craton displays +1+2% *V*s anomalies even at these depths.

The West Siberian Basin (considered by Sengör *et al*. (1993) to be part of the Paleozoic Altaids orogen) was assembled in the Paleozoic as a result of progressive convergence between the Siberian and the North China cratons. It has a very complex tectonic structure which includes fragments of ancient (Archean or Paleoproterozoic) massifs, Meso-Neoproterozoic oceanic complexes, and island arcs. Similarly to the Siberian craton, fast velocities in the upper mantle of the basin persist down to *c*. 200 km; however at 150 km depth shear velocity beneath the basin is *c*. 0.2 km/s slower than beneath the Siberian craton. The Kazakh Shield to the south from the West Siberian Basin apparently may have fast upper mantle velocities (above the *ak135* reference model) down to the transition zone, however the deflection from the reference model is significant only in the upper 200 km (Lebedev *et al*., 2009).

Tomographic models of the Baikal Rift zone at the southern margin of the Siberian craton are controversial. Most tomographic models, in general, do not display slow velocities in the upper mantle beneath the rift zone and interpret it as a "passive rift", the geodynamic origin of which is in one way or another related to convective (or asthenospheric) flow at the edge of the Siberian craton (Petit *et al*., 1998; Achauer and Masson, 2002; Lebedev *et al*., 2006; Artemieva, 2009; Thybo and Nielsen, 2009). An exception is one teleseismic P-wave tomography model that displays a localized low-velocity anomaly beneath the rift axis at depths 50–200 km interpreted as the signature of a mantle plume (Zhao *et al*., 2006). A low-velocity anomaly to the southwest from the rift zone is imaged in all tomographic models. High-velocity anomalies in the lower mantle west of Lake Baikal seen in P-wave tomographic models are interpreted as remnants of slabs subducted in the Jurassic when the Mongol–Okhotsk and Kular–Nera oceans closed between the Siberian craton and the Mongolia–North China block (van der Voo *et al*., 1999a).

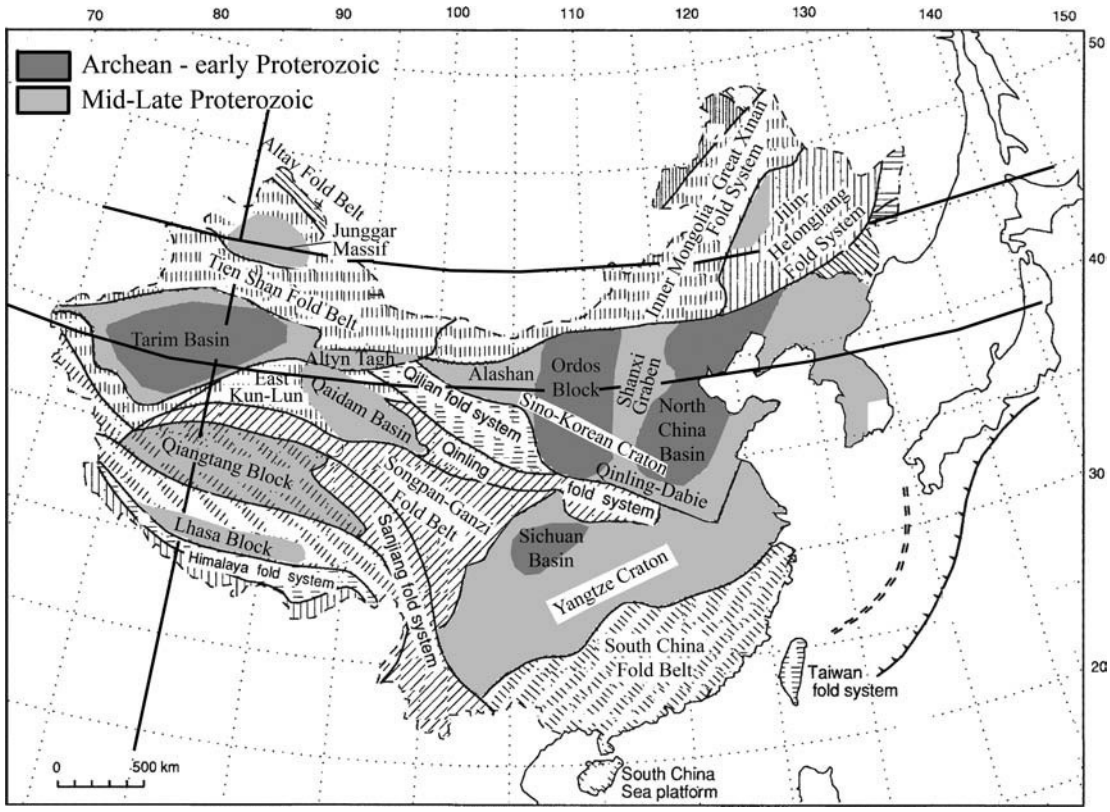

Fig. 3.94 Tectonic map of China and adjacent regions (based on Goodwin, 1996; Ren *et al*., 1981). Two-dimensional profiles along bold lines are shown in Fig. 3.95.

China, Mongolia, and India

Several existing high-resolution tomographic models of China (Fig. 3.94) image a highly heterogeneous structure for the upper mantle that is well correlated with surface tectonics. A tomographic model based on group velocity dispersions of fundamental Rayleigh waves (Huang *et al*., 2003) images the following upper mantle shear-velocity anomalies (see the previous section for a discussion on the resolution) (Fig. 3.95):

(1) fast shear velocities in the upper mantle down to 150–200 km depth beneath the cratonic central-northern India;
(2) a thin high-velocity "lid" (lithospheric keel) beneath the North China craton that terminates at *c*. 100–120 km depth (compare with Fig. 2.20); a localized (*c*. 500 km across) high-velocity block extending down to 200–250 km depth beneath the Archean Ordos block of the North China craton is, however, imaged in a regional P-velocity tomography model (Tian *et al*., 2009);

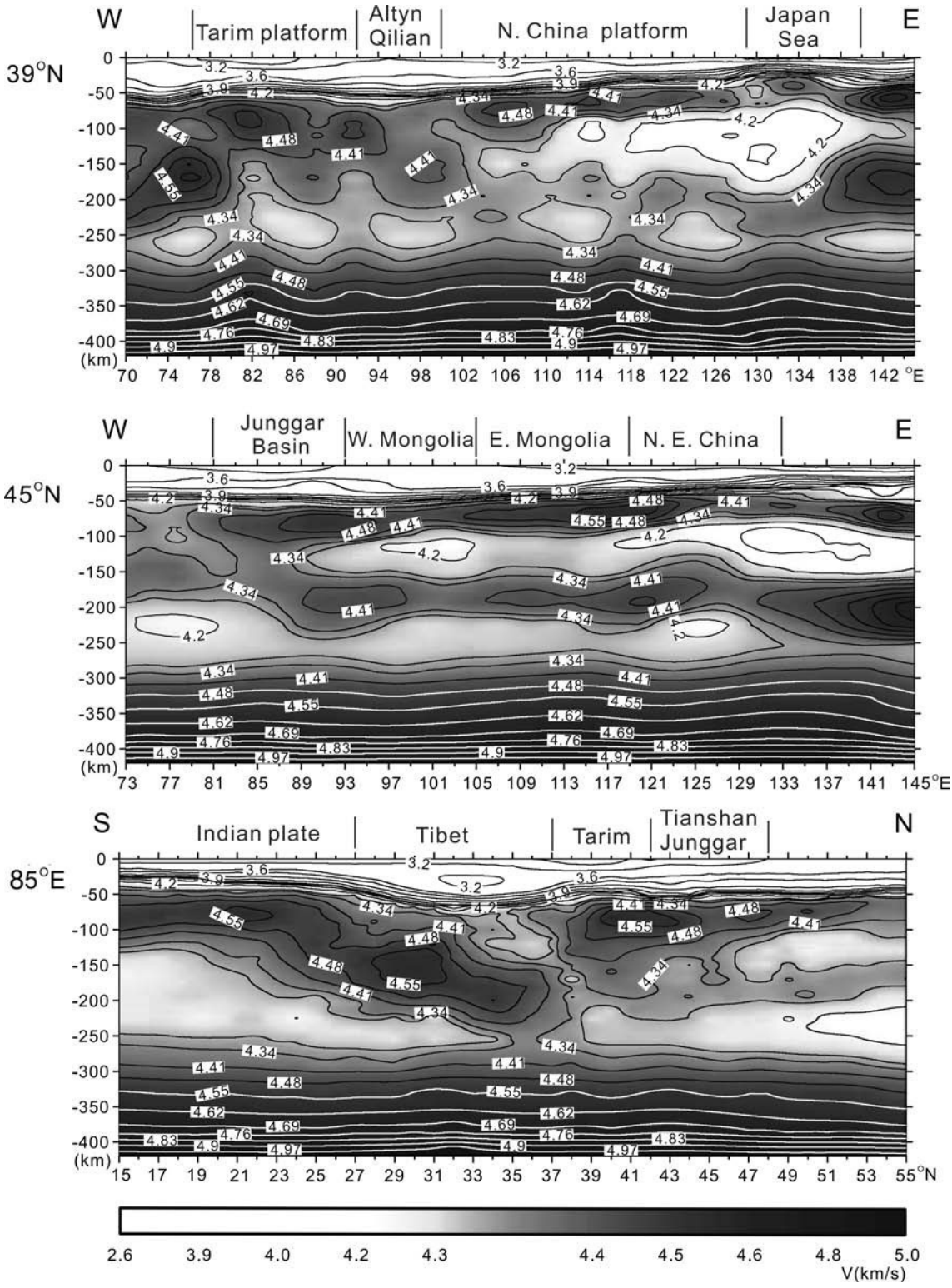

Fig. 3.95 Shear-velocity in the upper mantle of China constrained by surface wave tomography (from Huang *et al.*, 2003). See Fig. 3.94 for profiles location (bold lines).

(3) high-shear velocities down to *c*. 200 km depth beneath the Yangtze craton (Lebedev *et al*., 2009), the Tarim Basin, and the Jungar Basin; a strong high-velocity shear-velocity anomaly beneath the Sichuan Basin at 150–250 km depth is also imaged in other regional tomographic models (Lebedev and Nolet, 2003);
(4) a low-velocity anomaly extending from 50–70 km depth down to *c*. 300 km depth beneath Inner Mongolia;
(5) beneath southern Mongolia, a low-velocity anomaly at 100–150 km depth which is underlain by a zone of fast velocities at 150–200 km depth;
(6) low upper mantle velocities in coastal areas and in the continental shelves of China and Indochina;
(7) a northwards-dipping high-velocity zone that resembles a subducting plate and reaches a 200 km depth is imaged beneath the Tibetan Plateau up to the Kunlun Mountains in the north; the tomographic models do not support the presence of any low-velocity anomalies beneath Tibet that may indicate an uplift of hot asthenospheric material or delamination of the lower lithosphere (Griot *et al*., 1998).

Australia

The velocity structure of the Australian upper mantle has been the subject of several tomographic studies (Simons *et al*., 1999, 2002; Kennett, 2003; Fishwick *et al*., 2005; Pedersen *et al*., 2009). Tomographic models based on SKIPPY data have had problems resolving the structure of western Australia, where the oldest Archean cratons are located (Fig. 3.83). Furthermore, since these cratons are close to the continent–ocean transition with a sharp contrast in velocity structure (Fig. 3.82), damping used in tomographic inversion will result in an underestimate of the true velocity variations (Kennett, 2006). With this limitation in mind, tomographic models that show a thin (down to *c*. 175–250 km depth) high-velocity lid (lithospheric keels) beneath the Archean Pilbara and Yilgarn cratons in western Australia as compared to thick (down to *c*. 250–300 km depth) high-velocity lid beneath the Proterozoic Central Australia should be interpreted with caution (Simons *et al*., 1999). The conclusion based on such tomographic models that no general relationship exists between seismic signature and lithospheric age (not supported by data from any other stable continental region) could be questioned.

The major features of the upper mantle velocity structure of the Australian continent are the following (Simons *et al*., 2002; Kennett, 2003; Fishwick *et al*., 2005; Pedersen *et al*., 2009):

(1) the high-velocity lid beneath the Archean cratons of Western Australia extends, at least, down to *c*. 200–250 km depth. Small-scale velocity variations in the upper mantle of the cratons correlate with terrane boundaries. A recent comparison of shear-velocity structure beneath four Archean cratons indicates that, at depths between 50 km and 170 km, the lithosphere of the Yilgarn craton has significantly faster shear velocities (by *c*. 0.08–0.15 km/s) than the lithospheres of the Kaapvaal, the Slave craton, and the Baltic Shield;
(2) the transition from the cratonic lithosphere in western and northern Australia to Phanerozoic upper mantle in eastern Australia is marked by a velocity contrast down

to *c*. 200 km depth; the eastern margin of the high-velocity region in the upper mantle coincides with the Tasman Line which marks the eastern limit of outcrops of the Proterozoic basement; at 200–260 km depth a high-velocity region beneath the northern part of Australia extend eastwards beyond the Tasman Line;

(3) a fast wave-speed anomaly continues down to at least 250 km depth beneath the North Australian Craton, suggesting that the Archaean lithosphere may extend underneath areas with Proterozoic crust. High upper mantle velocities down to *c*. 200 km depth are observed northwards from Australia beneath the Indian Ocean and Papua New Guinea and may indicate an off-shore extension of the North Australia craton;

(4) beneath Proterozoic Central Australia a region of low seismic velocities is observed at *c*. 75 km depth in the uppermost mantle. Below, down to 200–250 km depth, the upper mantle has fast shear velocities typical of cratonic lithosphere;

(5) in eastern Australia the region of high upper mantle velocities terminates at *c*. 100 km depth and is underlain by a slow mantle with a velocity minimum at *c*. 150 km depth.

Africa

Continent-scale tomographic models are not available for Africa. Knowledge on upper mantle velocity structure is based either on regional tomographic studies available for southern Africa (e.g. SASE, the Southern Africa Seismic Experiment (Carlson *et al*. 1996 and several papers published in *Geophys. Res. Lett*., 2001, v. 28)), for the Tanzanian craton (Weeraratne *et al*., 2003), for the Kenya Rift (KRISP, Kenya Rift International Seismic Project, Prodehl *et al*., 1997), and for the Ethiopian Plateau–Afar region (EAGLE), or on high-resolution global wavespeed models that provide information on the upper mantle structure of other tectonic provinces of Africa, including the West African craton, the Congo craton, and the East Saharan craton (Fig. 3.96). In particular, high-resolution multi-mode global surface wave tomography model S20RTS (Ritsema *et al*., 2004) shows fast mantle (with +4% velocity with respect to PREM) extending to at least 200 km depth beneath the cratons of Africa (Fig. 3.90). In West Africa the depth extent of the fast anomaly (seismic lithosphere) may be significantly deeper than beneath the cratons of central and southern Africa.

Regional surface-wave tomographic studies of the Tanzanian craton and the adjacent segments of the East African Rift indicate that upper mantle beneath the craton is faster than the global average down to a depth of 150 ± 20 km (Fig. 3.97). Below this depth, shear velocity rapidly decreases from *c*. 4.65 km/s at 140 km depth to 4.20 ± 0.05 km/s at depths of 200–250 km, where it has a minimum. At the depth interval between 200 km and 400 km, shear velocities beneath the Tanzanian craton are slower than beneath the adjacent branches of the East African Rift. This significant drop in shear velocities can be attributed to high mantle temperatures and possible presence of melts (Weeraratne *et al*., 2003). The same surface-wave tomographic model displays a sharp minimum in upper mantle shear velocities (3.7–4.0 km/s) at a depth of 120–170 km beneath the East African Rift. Tomographic models of the Kenya Rift, developed as a result of the KRISP broadband seismic experiment, also display a cylindrical low-velocity (–0.5–1.5%) anomaly below the rift extending to about 150 km depth with steep, near-vertical boundaries

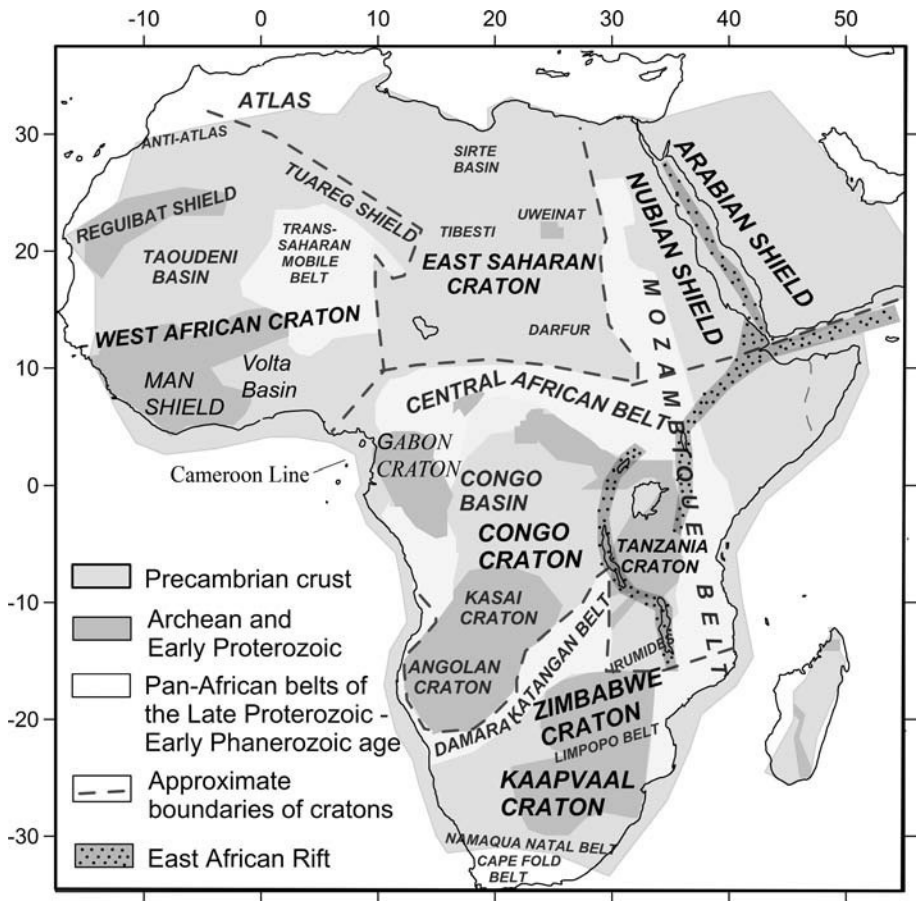

Fig. 3.96 Tectonic map of Africa.

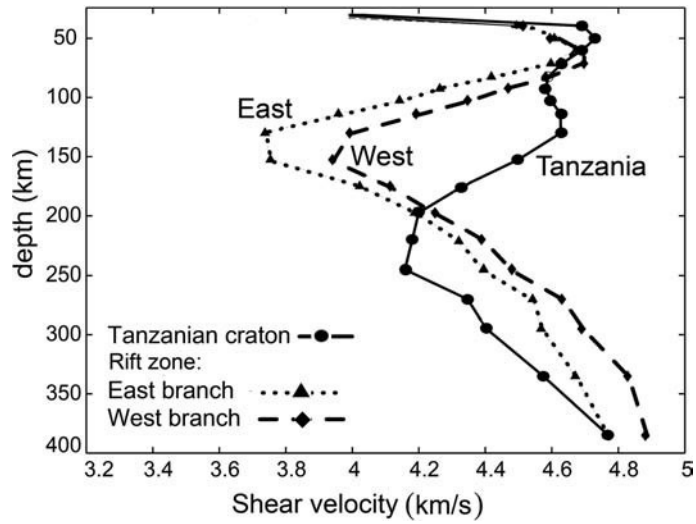

Fig. 3.97 Shear-velocity structure of the upper mantle beneath the Tanzanian craton and the eastern and western branches of the East African Rift from Rayleigh wave tomography (based on Weeraratne *et al*., 2003).

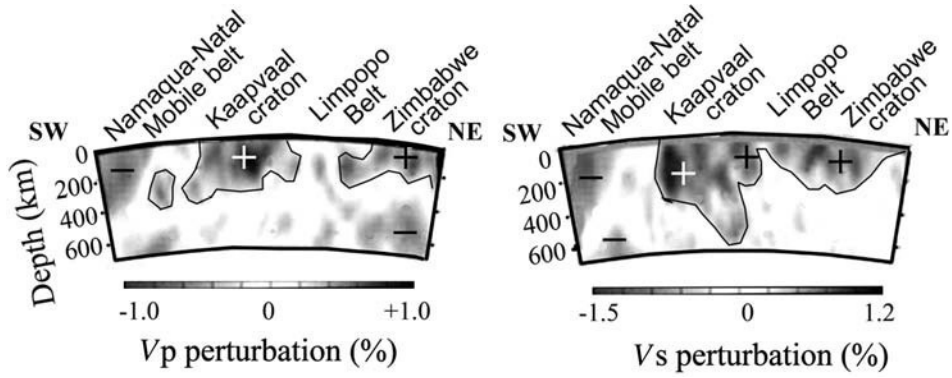

Fig. 3.98 *Vp* and *Vs* velocity structure of the upper mantle beneath South Africa from body-wave tomography (based on James *et al*., 2001). The profile goes from approximately 20E, 35S to 30E, 20S. Plus and minus signs indicate the sign of velocity perturbations (for an unspecified reference model). The resolution of the S-velocity model is weaker due to fewer observations and greater uncertainties in relative time delays.

located under the rift border faults (e.g. Achauer and Masson, 2002). Recent models suggest that a low wave-speed anomaly along much of the East African rift (observed in the upper mantle of Kenya, Tanzania, and Ethiopia) may be dipping westwards below depths of ~150–200 km.

Regional high-resolution tomographic studies of southern Africa provide a wealth of data on the upper mantle velocity structure beneath the Kalahari craton. However, up-to-date seismic interpretations are highly controversial, in particular on the depth extent of the high-velocity lid (seismic lithosphere or tectosphere) and on regional seismic anisotropy. The upper mantle of southern Africa cratons is one of the best sampled by mantle-derived xenoliths from more than 1000 kimberlite pipes (see Chapter 5). However, despite several attempts to correlate velocity anomalies in the upper mantle with petrological data and diamond occurrences, no convincing conclusions have been made.

Recently body-wave tomography has imaged high velocity upper mantle beneath southern Africa down to 300–400 km depth. In particular, a one-dimensional model for P-wave velocities displays a high-velocity anomaly (*c*. 3% higher than global averages) down to 300 km depth (Zhao *et al*., 1999). The results for the linear travel-time inversion for P- and S-waves support this finding (Fig. 3.98). Although the resolution of the S-wave model is weaker, both models display similar patterns: high-velocity mantle anomalies coincide with the tectonic boundaries of the Archean Kaapvaal and Zimbabwe cratons and extend down to at least a 300 km depth, while the upper mantle Proterozoic Namaqua–Natal mobile belt and the Archean Limpopo belt (disrupted by the Bushveld complex emplaced at *c*. 2.05 Ga) has significantly lower velocities (James *et al*., 2001). *V*p and *V*s seismic velocities beneath the Bushveld (although loosely constrained) are, respectively, ~0.5% and ~0.8% lower than beneath the craton; and the mantle zone of reduced velocities associated with the Bushveld extends from beneath the intrusion itself well to the west into Botswana.

The low mantle velocities beneath the Bushveld complex may be interpreted as indicating chemical modification of the mantle during a Proterozoic magmatic event (James *et al*., 2001). This hypothesis is consistent with Re–Os results which indicate Proterozoic resetting of the age of mantle nodules from the Bushveld region (Carlson *et al*., 2000).

In contrast to body-wave studies, a recent multi-mode teleseismic surface wave tomographic model displays a high-velocity anomaly beneath the cratonic region of southern Africa only down to 175 ± 25 km depth (Priestley *et al*., 2006). The authors argue that because of the technique employed in the inversion, the final velocity structure is weakly dependent on the reference model (smoothed PREM) and thus should not inherit a step at *c*. 220 km depth. Unfortunately, according to the presented checkerboard resolution test, the model cannot reliably resolve the upper mantle velocity structure at 250 km depth and exhibits a strong vertical and lateral smearing already at 150 km depth. Another tomographic study based on *fundamental-mode* Rayleigh and Love waves (with limited resolution below *c*. 200 km depth) supports the conclusion that mantle beneath the Kaapvaal craton is characterized by high seismic velocities in the upper 200 km with no evidence for a substantial LVZ down to this depth (Freybourger *et al*., 2001). In a recent study (Pedersen *et al*., 2009), a pronounced decrease in shear velocity (from *c*. 4.65–4.70 km/s at 200 km depth to *c*. 4.50 km/s at 300 km depth) was resolved beneath the Kaapvaal craton, while such a velocity decrease below 200–250 km depth has not been recognized in the same study beneath the Slave, Yilgarn, and South-Central Finland cratons. Since the latter study is based on phase velocities of *fundamental-mode* Rayleigh waves, these conclusions are speculative.

Antarctica

Tomographic modeling of Antarctica is challenging due to the unknown crustal structure and the presence of a thick ice cap. Regional models are hampered by the limited number of stations and seismic events on the continent (Kobayashi and Zhao, 2004; Morelli and Danesi, 2004; Kuge and Fukao, 2005). Recent surface wave tomographic inversions for the Antarctic region display high upper mantle velocities in the cratonic East Antarctica at periods of 90–150 s, suggesting a very thick seismic lithosphere of East Antarctica underneath the Dronning Maud Land, Enderby Land, Gamburtsev Mountains, and Wilkes Land. In contrast, mantle velocities in tectonically young West Antarctica are low at all periods between 20 s and 150 s, suggesting on-going tectonic activity in the West Antarctic Rift System. In the Ross Embayment low seismic velocities are imaged down to 250 km. The transition from fast to slow upper mantle correlates with the Transantarctic Mountains.

Oceans

For the "normal" oceans, the bathymetry follows the square root of age pattern (Schroeder, 1984) and the cooling half-space model provides a good approximation for the thickness of the thermal boundary layer (lithosphere) (see Chapter 4). The amplitude of velocity

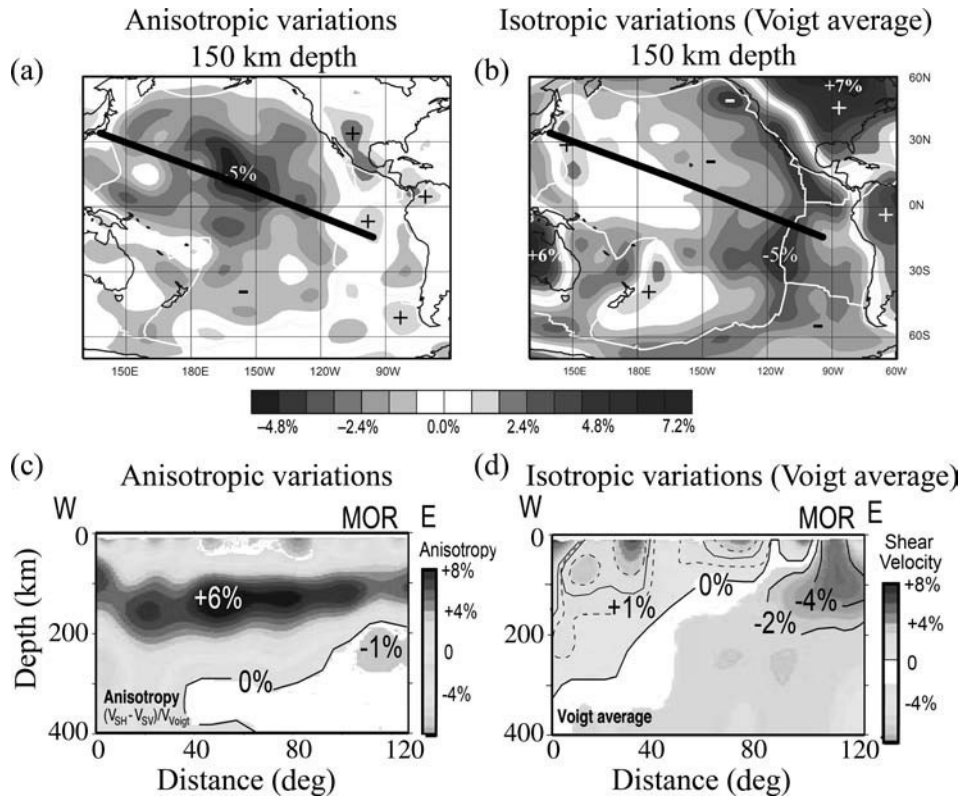

Fig. 3.99 Shear-wave velocity variations beneath the Pacific Plate. (a) Difference between the SV and SH velocities at 150 km depth; (b) the Voigt averaged isotropic variation in S-wave velocity at 150 km depth. The isotropic (thermal) S-wave variations in general correlate with the age of the ocean floor (the Pacific Superswell is a clear exception); anisotropic velocity variations are as large as isotropic variations. (c) Shear velocity anisotropy along the profiles shown in (a, b). (d) The Voigt average shear-wave velocity along the profile, plotted with respect to the global average at each depth. Note a strong negative anomaly beneath the mid-ocean ridge (MOR) and a gradual deepening of a zero-velocity anomaly with ocean floor age. (a) and (b) based on Ekström and Dziewonski (1998); (c) and (d) based on Nettles and Dziewonski (2008).

perturbations in the normal oceanic upper mantle is age dependent: the strongest low-velocity anomalies are clearly resolved along mid-ocean ridges (near-zero age), in particular at 100 km depth (Figs. 3.87; 3.99; 3.100cd; 3.125). In general, low shear velocities beneath mid-ocean ridges are restricted to the upper 200 km of the mantle. In old (>80 Ma) oceans, shear velocities in the upper mantle become similar so that the difference between velocity anomalies in 80 Ma and 140 Ma old oceans becomes statistically insignificant (Fig. 3.100c).

Tomographic models for normal oceans have a high-velocity lid in the upper 80–100 km, particularly pronounced beneath the Pacific Ocean and south-west Atlantic Ocean (Fig. 3.88). This high-velocity lid is absent in anomalous ocean regions such as the East Pacific Rise, the Indian Rise, and the Mid-Atlantic Ridge. At *c.* 100–200 km depth, the oceanic upper mantle

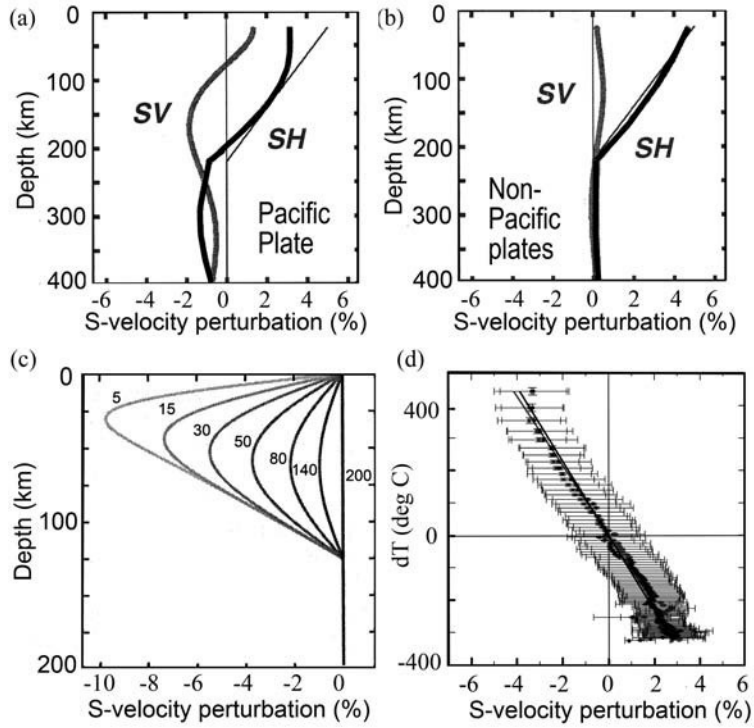

Fig. 3.100 (a–b) Average profiles of S velocity perturbations in the Pacific plate for different age of plate (based on Ekström and Dziewonski, 1998). The profiles are referenced to the oldest profile. (c–d) Correlation between seismic and thermal structure of oceanic upper mantle. (c): The predicted evolution of S velocity with depth as a function of ocean age. The profile is referenced to a profile for 200 Ma age. Numbers on the curves: ocean floor age in Ma (from Ekström and Dziewonski, 1997). (d) Comparison of seismic shear velocity and temperature anomalies in the oceanic lithosphere (based on Forte, 2007). Seismic shear velocity anomalies are based on tomography models SAW24 (Megnin and Romanowicz, 2000) and TX2002 (Grand, 2002). The age-dependent temperature variations in the oceanic lithosphere are based on a cooling half-space model with thermal parameters as for the GDH1 plate model (Stein and Stein, 1992). Both shear-velocity and temperature anomalies are vertically averaged in the depth interval 0–100 km and are spatially averaged into 2 Ma age bins, and are shown with respect to the global oceanic mean value.

has a distinct LVZ with $V_S \sim 4.3$–4.4 km/s. The strongest negative V_S anomalies with respect to global or oceanic reference models are observed at 100–200 km depth beneath the East Pacific Rise (Fig. 3.89c), while the anomalies beneath the Mid-Atlantic Ridge are significantly weaker, and the mantle beneath the Indian Rise has intermediate velocity anomalies (Ritsema and Allen, 2003). In the Pacific Ocean the upper mantle is on average 1% slower with respect to PREM down to at least 400 km depth (Ekström and Dziewonski, 1998). In contrast to a flat-gradient region below 220 km depth in the PREM model, a high gradient zone is observed between 200 km and 410 km depth in the oceanic mantle (Fig. 3.88a,c).

Surface-wave tomographic models require that age-dependent variations in oceanic upper mantle extend down to at least 200 km depth, while the cooling half-space model predicts lithosphere thickness of less than 100 km (Fig. 3.100c). For example, at 150 km depth

SH-velocity anomalies in the mantle below the Pacific Ocean vary from −4% at the East Pacific Rise to +3% in the Western Pacific (Dziewonski, 2003). Decomposition of the shear-wave velocity model into isotropic (Voigt average) and anisotropic parts helps us to understand the age dependence of mantle velocity structure below the base of the thermal boundary layer. For the Pacific Ocean, the isotropic part of velocity perturbations becomes more consistent with the cooling half-space model (below 175 km depth no age-dependent differences are observed for isotropic shear velocities, Fig. 3.99d), except for anomalous ocean between the East Pacific Rise and the Pacific "Superswell" which has low shear velocities at 150 km depth. The anisotropic part of the model has the peak of the anomaly at 100–200 km depth and a rapid decrease in anomalies at 200–250 km depth (Figs. 3.90b, 3.99c). Thus the greater depth extent of the SH anomalies than would be required by lithospheric cooling can be interpreted as a change in polarization anisotropy with age (see discussion in Section 3.6.4).

Synopsis for some tectonic settings

Stable continents

Global and regional tomography models provide strong support for the tectosphere hypothesis and the existence of thick lithospheric roots beneath the Precambrian cratons with high seismic velocities. High velocities can be due to low temperatures and/or petrologically distinct composition (FeO-poor, olivine-rich, and garnet-poor). Fast velocity anomalies beneath the ancient parts of all of the continents are clearly seen in all tomographic models down to at least 200–250 km depth (Fig. 3.87). In most of the cratons, fast velocities persist down to *c*. 300 km depth (below this depth many tomographic models lose resolution), with peak seismic velocities at *c*. 100–200 km depth (Fig. 3.88). Lebedev *et al*. (2008) report isotropic-average Vs velocities in the range 4.58–4.94 km/s at depths between the Moho and ~250 km beneath the Archean Baltic Shield, East European (Russian) Platform, Guyana Shield, Parana Basin, Congo Craton, and the Archean Western Australia; beneath the Proterozoic mobile belts of Kazakhstan and China (Yangtze craton) Vs velocities range from 4.49 to 4.75 km/s (for a comparison, at depths 40–200 km the reference, continental average Vs velocity in the *ak135* model is 4.5 km/s).

There are, however, significant differences in the velocity structure of the upper mantle of different cratons, even when constrained by the same data set and the same inversion, and when xenoliths suggest similar geotherms. Recent surface-wave tomography based on analysis of dispersion curves for four Archean cratons (Kaapvaal (South Africa), Slave (north-central Canada), Yilgarn (western Australia), and Baltic Shield (central Finland)) indicate significantly different velocities in the lithospheric mantle (Pedersen *et al*., 2009). The highest velocities (0.08–0.12 km/s above Kaapvaal velocities) were determined in the Yilgarn lithosphere with half of that velocity anomaly determined for the Baltic Shield. This implies that seismic velocity models for the upper mantle do not necessarily support a simple relationship between crustal age and upper mantle composition.

Polet and Anderson (1995) have analyzed the shear-velocity structure of the cratonic upper mantle constrained by body-wave and surface-wave global tomographic models. Their analysis (still statistically valid despite significant progress in tomographic studies over the past

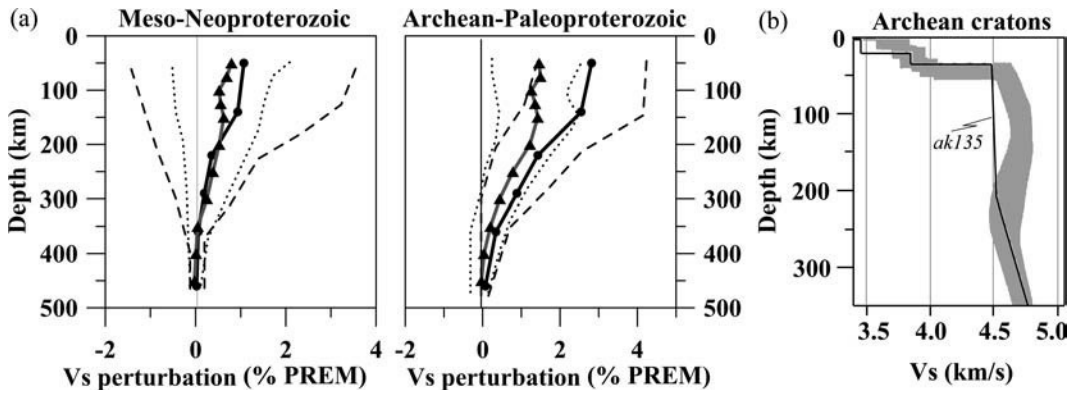

Fig. 3.101 (a) Depth extent of shear-velocity perturbations (with respect to PREM) in the continental upper mantle for cratons of two ages (based on the analysis of Polet and Anderson, 1995). Shear velocities are derived from global tomography models based on body waves (Grand, 1997) (shown by black lines and circles, standard deviation indicating the 66% confidence level is outlined by dashed lines) and on surface waves (Zhang and Tanimoto, 1993) (shown by gray lines and triangles, standard deviation is outlined by dotted lines). (b) Summary profile of isotropic-average shear-wave velocity (gray shading) beneath the cratons of the Baltic Shield, East European Platform, Guyana Shield, Parana Basin, Congo Craton, and Yilgarn–Pilbara cratons (after Lebedev *et al*., 2008). Solid line – global continental reference model *ak135* (Kenneth *et al*., 1994). Compare with Fig. 3.88.

years) is based on numerical cross-correlations for two age groups (Archean–Paleoproterozoic cratons with ages greater than 1.7 Ga and Mesoproterozoic–Neoproterozoic cratons with ages between 0.8 Ga and 1.7 Ga). It is performed on a 1 deg x 1 deg spatial grid which is significantly finer than the lateral resolution of the surface-wave model used in the analysis (constrained on a 5 deg x 5 deg spatial grid). The major conclusions of the analysis are the following (Fig. 3.101):

- High velocity anomalies are restricted to the oldest parts of the continents.
- The Archean–Paleoproterozoic cratons have fast *V*s velocities down to *c*. 500 km, although not statistically significant below *c*. 250 km depth.
- For the Mesoproterozoic–Neoproterozoic regions, the velocity anomalies are not statistically significant at any depth (even in the shallow mantle).
- Cratons of the same age have a different velocity structure of the upper mantle.
- Beneath the West African craton, the Canadian Shield, and the cratonic part of Europe significant high-velocity anomalies are observed down to 300–450 km depth.
- At depths between 100 and 250 km, the strongest high-velocity anomalies are observed beneath the Canadian, Baltic, Siberian, Australian, and the West African cratons, but not beneath southern Africa.
- In the Archean–Paleoproterozoic cratons of South America, Central Africa, India, and China, high velocity anomalies are relatively shallow (down to 150–250 km depth). The Neoproterozoic Arabian Shield has low seismic velocities (atypical for other shields) in the upper mantle.

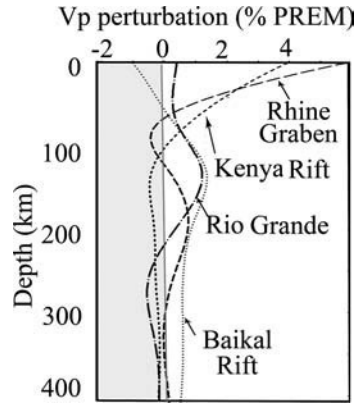

Fig. 3.102 Compressional velocity versus depth in the upper mantle of four continental rifts (based on Achauer and Masson, 2002). P-velocity deviations from PREM are estimated from S-velocity perturbations.

Continental rifts

The tectonic evolution of rifts is governed by complex regional and far-field stresses produced by plate motion and by the rheological strength of the lithosphere, so that continental rifts tend to follow the pre-existing zones of rheological and tectonic weakness. A comparative analysis of absolute upper mantle velocities derived from recent global 3D surface-wave tomography of four Cenozoic continental rifts (the Kenya, Baikal, and Rio Grande rifts, and the Rhine Graben) indicates that the mantle structure beneath the rifts differs substantially down to depths of ~300 km (Fig. 3.102). While the Kenya and Rio Grande rifts may be considered as active rifts where large mantle upwellings control their tectonic evolution, the southern Rhine Graben and the Baikal Rift zone are more likely to be passive rifts (Achauer and Masson, 2002): at depths between 50 km and 300 km the upper mantle beneath the latter two rifts is faster than a global reference model. Long-offset seismic refraction and teleseismic studies of the East African Rift and the Rio Grande Rift provide compelling evidence for hot mantle down to a depth of at least 100–200 km, and support the hypothesis of their deep mantle origin (Braile *et al*., 1995; Baldridge *et al*., 1995). In contrast, recent tomographic models show fast-velocity anomalies beneath the Baikal Rift zone at depths of 100–500 km and thus support the conclusion of its passive origin. Similarly, paleorifts within stable continents such as the Proterozoic Mid-Continent Rift in North America, the Paleozoic Dnieper–Donets Rift in southern Russia, the Paleozoic Oslo Graben in Baltica, and the Paleozoic Viluy Rift in the eastern part of the Siberian craton do not display low-velocity anomalies in the upper mantle with respect to global averages, implying that the present thermal regime of the mantle may not differ significantly from the surrounding (adjacent) cratonic mantle.

Past and present subduction zones

Tomographic images only provide a snapshot of present-day mantle velocity anomalies, and any "temporal interpretations" of them, e.g. in terms of images of subducting slabs or plumes, should be made with caution. Elongated high-velocity anomalies in the upper and lower mantle seen in

tomographic models are often interpreted as evidence for past and present subduction processes. Together with data on regional seismicity, the presence of subducting slabs in the upper mantle beneath most of the presently active zones of continent–continent and continent–ocean collisions is imaged by global and regional tomographic models. This includes the flat-subducting slab beneath the Andes along the Pacific coast of South America, subduction of the Indo-Australian plate beneath the Himalayas and Tibet, and numerous subduction zones imaged in the upper mantle of the Mediterranean and Asia Minor, the origins of which are related to the plate collision between Africa and Europe and the closure of the Paleo–Tethys Ocean. Low-velocity anomalies in the Trans-Pacific mantle can be explained by temperature anomalies of 200–300 K associated with subducted slabs (Fukao *et al*., 2004).

Ancient subduction zones, many of which presently located far from the continental margins, have been imaged by tomographic studies beneath several continents. A pronounced high-velocity anomaly clearly seen in a regional surface-wave tomographic model at a distance of ~2000 km from the present Pacific margin has been interpreted as the fragments of the subducted Farallon slab beneath North America (van der Lee and Nolet, 1997b). A linear shear-wave anomaly along the western margin of the East European craton is interpreted as the signature of a paleosubduction along the cratonic margin with an increased fluid content in the upper mantle (Nolet and Zielhuis 1994). High-velocity P-wave anomalies in the lower mantle beneath Siberia, west of Lake Baikal, are interpreted as Jurassic lithospheric slabs associated with the closure of a paleoocean (van der Voo *et al*., 1999a). One should remember, as noted above, that in some tomographic inversions localized high-velocity anomalies can be a consequence of ray density – model resolution correlation (Vasco *et al*., 2003).

High-resolution P-wave and S-wave tomography studies of presently active subduction zones indicate that while most of the subducted slabs are deflected near the 660 km discontinuity, some fast seismic velocity anomalies that may relate to subducting slabs reach into the lower mantle (van der Hilst *et al*., 1997; Bijwaard *et al*., 1998; Fukao *et al*., 2001) (Fig. 3.103). This result has an important bearing on models of mantle convection (whole-mantle, layered, or hybrid) and provides indirect support for the hypothesis of episodic catastrophic overturns in mantle associated with sinking of the slabs to a compositionally heterogeneous layer at 1700–2300 km depth (van der Hilst and Karason, 1999) or to the core–mantle boundary (Chapter 9).

Mantle plumes and hotspots

Hotspots, the areas that have experienced long-term volcanism, exist both at intraplate settings (like Hawaii, Yellowstone, and Afar) and on mid-ocean ridge axes (like Iceland and Azores). Different authors recognize different numbers of hotspots; a widely accepted compilation lists 37 (Sleep, 1990). Mantle plumes are a generally accepted hypothesis for their formation (Morgan, 1972) as well as a petrologically based estimate that they are associated with a 200–250 °C access temperature in the mantle (Sleep,1990).

The very existence of mantle plumes and their number, if they exist, is a subject for hot debate (e.g. see http://www.mantleplumes.org; Morelli *et al*., 2004). This paragraph overviews the competing opinions in the most general way, without any attempt to discriminate between them. Five criteria have been proposed by Courtillot *et al*. (2003) as specific for plumes:

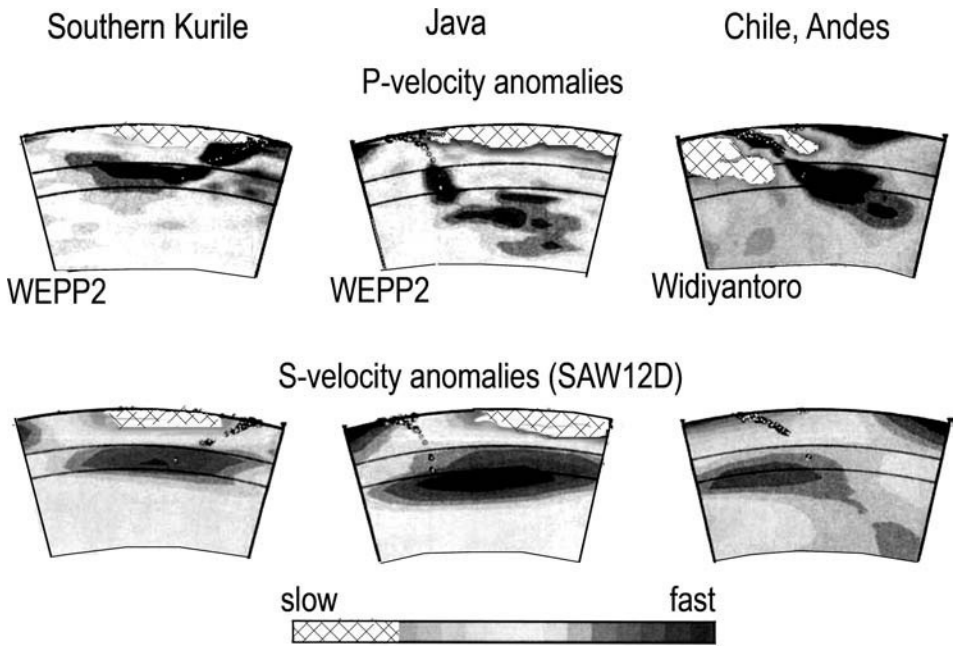

Fig. 3.103 Vertical cross-sections across the mantle of subduction zones beneath the Southern Kuriles, Java, and Chile (based on Fukao *et al.*, 2001). P-velocity models (WEPP2 of Obayashi *et al.*, 1997 and Widiyantoro, 1997) show velocity perturbations relative to the spherical average of the final aspherical model; S-velocity model (SAW12D of Li and Romanowicz, 1996) shows velocity perturbations relative to PREM. Thin lines show the locations of 410 km and 660 km discontinuities.

(1) hotspot track (volcanic chain),
(2) large igneous province at one of the ends,
(3) high buoyancy flux,
(4) high $^{3}He/^{4}He$ ratio, and
(5) low seismic velocities down to a 500 km depth in the mantle.

These "plume criteria" have been expanded to twelve to include the parameters that characterize the seismic structure of the entire mantle (i.e. the presence of low-velocity anomalies at several depths in the upper and lower mantle) and its thermal state (Anderson, 2005). Global analysis of proposed mantle plumes indicates that many of them exhibit equally many of the characteristics of both a "plume" and of a "plate tectonics" model.

Seismic tomography provides some of the most important arguments for the on-going debate on the existence of mantle plumes (Nataf, 2000; Sleep, 2006). However, since seismic velocity anomalies provide only a snapshot of present-day mantle structure, their extrapolations in time are uncertain (and may even be misleading). In particular, a new insight into the debate on the existence and temporal evolution of mantle plumes is provided by laboratory modeling of thermo-chemical convection. Simulations of plume generation, evolution, and death indicate that in a dying plume negative compositional buoyancy becomes uncompensated by positive thermal buoyancy. This causes downward material flow along a still hotter-than-normal "plume channel" so that

> *dying plumes start disappearing from the bottom up, sometimes even before reaching the upper boundary, . . . they finally fade away by thermal diffusion. This sequence of events shows that time-dependence is a key-factor when interpreting present-day tomographic images of mantle upwellings. In particular, it could be erroneous to identify the depth of a present-day slow seismic anomaly with the depth of its origin, or to interpret the absence of a long tail as the absence of a plume*" (Davaille and Vatteville, 2005).

The global multi-mode surface-wave tomographic model RTS20S indicates large shear-velocity variations in the upper mantle beneath different hotspots (Ritsema and Allen, 2003): beneath 9 out of 37 hotspots (including the Afar, Hawaii, and Iceland hotspots) the upper mantle is 1% slower than the Oceanic Reference Model (ORM) (Fig. 3.89); beneath 14 hotspots that are located on or near mid-ocean ridges (including Tristan, Azores, and Galapagos) low velocity anomalies are observed only in the upper 200 km of the mantle; 15 hotspots (including Reunion and Yellowstone) do not display a low shear-wave velocity anomaly anywhere in the upper mantle.

Seismic evidence for the existence of a mantle plume beneath Iceland remains controversial. Body-wave tomographic models display a low-velocity anomaly below Iceland that persists below the transition zone and thus argue in favor of a narrow whole mantle plume (Bijwaard and Spakman, 1999; Morelli *et al*. 2004). Regional surface-wave tomography models image a significant low-velocity anomaly around Iceland with a diameter of *c*. 1000 km extending down to a depth of at least 600 km (e.g. Ritsema and Allen, 2003). The observed amplitude (*c*. 5–10%) of the S- and P-wave velocity anomaly in the shallow mantle can be explained by a temperature anomaly of *c*. 50–100 °C with less than 1% of melt and perhaps as little as <0.1% (Foulger *et al*., 2005 and references therein). In contrast with tomographic models, receiver function analysis of seismic data from Iceland (Vinnik *et al.*, 2005) indicates that a low-velocity zone is restricted to the shallow mantle only (with the velocity minimum centered at a depth of 100 km) and that the transition zone has a normal thickness; a weak depression of the 410 km discontinuity can be explained by a *c*. 50 °C thermal anomaly in the mantle and does not support the presence of a plume beneath Iceland.

In contrast to Iceland, the presence of a mantle plume beneath the Hawaiian hotspot, as supported by geophysical and geochemical data, is generally accepted. Joint interpretation of global seismic tomography and semi-global electromagnetic tomography for the depth range 350–850 km in the mantle shows consistently high temperature anomalies (200–300 °C) in the mantle transition region beneath Hawaii (Fukao *et al*., 2004).

3.6.3 Origin of seismic velocity anomalies in the upper mantle

The major mechanisms responsible for seismic velocity anomalies in the upper mantle are temperature variations, compositional variations, presence of melts and fluids, and anisotropy. Other parameters such as grain size variations may also contribute to seismic velocity perturbations. The effect of upper mantle anisotropy is addressed in detail in the next section, while Section 3.1 provides background information on the effect of temperature and compositional variations on seismic velocities in the mantle. Since interpretation of

seismic velocity variations is impossible without discussing compositional effects, the cross-references between this section and Chapter 6, where the upper mantle composition is addressed in detail, were difficult to avoid (readers unfamiliar with the topic may find it useful to first read Section 6.1).

Correlations with the thermal regime

Velocity variations in the upper mantle are strongly correlated with surface tectonics and tectono-thermal ages; surface heat flow and thermal state of the continental and of the oceanic upper mantle also depend on tectono-thermal ages (see Chapter 4). This leads to the logical conclusion, supported by laboratory data on a strong temperature dependence of seismic velocities, that a significant part of seismic velocity variations in the mantle can be attributed to temperature variations. This conclusion is further supported by a strong correlation between seismic shear velocity and temperature anomalies in the oceanic lithosphere (Fig. 3.100d), except for regions with a strong seismic velocity anisotropy in the upper mantle (e.g. Fig. 3.99c). These observations provide a basis for estimation of mantle temperatures from seismic velocity models (this approach is discussed in detail in Chapter 5). Importantly, the effect of lateral temperature variations on velocities is strong in the uppermost mantle, where lateral temperature variations are the strongest, but decreases with depth whilst the lithospheric geotherm approaches the mantle adiabat. However, at near-solidus temperatures other processes become important in reducing seismic velocities.

A significant (up to several percent) drop in seismic velocities occurs at near-solidus temperatures before any melting in the mantle starts (Fig. 3.3), while the presence of even small amounts of melt leads to a dramatic drop in seismic velocities (Fig. 3.13). Near-solidus temperatures and partial melting are widely used to explain low-velocity anomalies in the upper mantle of tectonically active regions where high mantle temperatures may be expected, such as below the continental rift zones and regions of high lithosphere extension. Similarly, melting beneath the mid-ocean ridges is the major mechanism responsible for low mantle velocities at oceanic spreading centers.

Correlation between the upper mantle velocity structure and the thickness of (depth to) the transition zone provides further support to the hypothesis that many of the velocity variations in the upper mantle are of thermal origin, since both velocity anomalies in the upper mantle and the thickness of the mantle transition zone show a significant difference between the oceanic and the continental mantle (Fig. 3.57). However, this correlation holds only for large-scale tectonic structures. Furthermore, the thickness of the transition zone poorly correlates with the crustal ages of the continents and thus mechanisms other than thermal should be invoked to explain seismic velocity anomalies in the subcontinental mantle.

Effect of water

A significant amount of water is present in the upper mantle as solid solution in major minerals, rather than in hydrous phases. Experimental studies show that, under upper mantle conditions, up to 0.1 wt% of water can be dissolved in mantle olivine (Bai and Kohlstedt,

1992; Kohlstedt *et al*., 1995). A particularly large amount of water is expected in the mantle wedge above subducting oceanic lithosphere (Fig. 7.19). The presence of even a small amount of water or fluids in mantle rocks significantly (by a few percent) reduces seismic velocities. This fact has allowed for interpretation of a strong low-velocity shear-wave velocity anomaly at 300–500 km depth along the western boundary of the East European Platform by water injection into the mantle during Paleozoic subduction associated with the closure of the Tornquist Ocean (Nolet and Zuilhuis, 1994).

Based on mineral physics observations, Karato (1995) analyzed the possible effects of water on seismic wave velocities in the upper mantle. He examined three mechanisms:

(1) the direct effect of water through the change in bond strength,
(2) an indirect effect due to enhanced anelastic relaxation caused by the presence of water, and
(3) indirect effects due to the possible change in preferred orientation of olivine leading to changes in seismic anisotropy.

The analysis by Karato indicates that, for a reasonable range of water content in the upper mantle, the first mechanism yields negligibly small effects on seismic velocities. However, the two indirect effects, which involve the motion of crystalline defects, can be significant in reducing seismic velocities. The effect of anisotropy is considered in the section to follow. Here it is worth mentioning that the effect of water on creep in olivine is anisotropic: large for [001] but small for [100], and thus deformation of olivine under high water fugacities may result in a change of the dominant slip systems.

Enhanced anelastic relaxation may reduce the seismic wave velocities by a few percent. Under dry conditions, anelasticity Q reduces seismic wave velocities and the amplitude of the effect depends on temperature (eq. 3.8). The presence of water will produce a change in Q which will result in a significant change in seismic wave velocities (Fig. 5.17). The effect of water on enhanced anelastic relaxation is particularly strong for low Q values (~50) under dry pre-conditions. For $\alpha = 0.1$–0.3 and Q between 50 and 100, seismic velocity reduces by 1–6% (eq. 3.8, 3.11). Since water solubility increases with pressure, the effect of water on the reduction of seismic velocities should be stronger at greater depth within the upper mantle.

Effect of grain size

Another candidate is a change in grain size with depth, since grain size in the upper mantle is controlled by competing stress-dependent processes of dynamic recrystallization and grain growth. It is intriguing that in the cratonic mantle of the Kaapvaal craton a change in grain size occurs at *c*. 140–150 km depth (Fig. 3.104), the depth where a significant change in mantle composition is documented by petrological studies of mantle-derived xenoliths from different cratonic settings worldwide (Gaul *et al*., 2000). However, this depth is far too shallow to correspond to the base of the seismic lithosphere, since high-velocity anomalies beneath the Kaapvaal are observed down to 250–300 km depth (Fig. 3.98). Numerous studies of mantle-derived peridotites from cratonic settings indicate that iron depletion decreases with depth (Figs. 3.104a, 6.15b). Group I kimberlites from the Kaapvaal mantle erupted at ~90 Ma indicate fertile mantle composition at depths below 150–180 km. If this picture is representative of the Kaapvaal mantle, then high seismic velocities in the depth

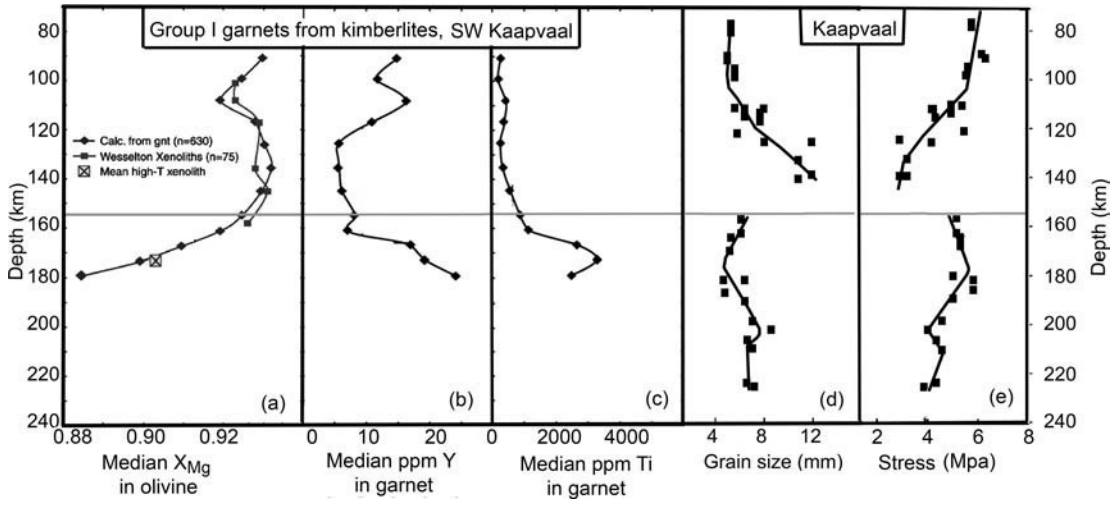

Fig. 3.104 (a–c) Variations in composition with depth in group I garnets from kimberlites of SW Kaapvaal (based on O'Reilly and Griffin, 2006); (d) olivine grain size variations in xenoliths from Kaapvaal (best fit to data of Mercier, 1980, Fig. 3.9). Note a synchronous change in composition and grain size at a depth of 150–160 km (marked by a thin line). The change in composition is related to metasomatism of the lower lithosphere by small-scale asthenospheric melts, while the discontinuity in olivine grain size is explained by a change in the recrystallization mechanism, from subgrain rotation at shallow depths to grain boundary migration below 150 km. Since recrystallization processes are stress dependent, grain size variations with depth allow for calculating deviatoric stresses in the lithosphere (e) (based on Mercier, 1980). Grain size deformation has been calibrated by olivine aggregates, and the results may not be entirely representative of the upper mantle.

range 150–250 km are unrelated to iron depletion and should have a primarily thermal origin. In contrast, older kimberlites suggest significant depletion of the Kaapvaal upper mantle down to 200–220 km depth (Fig. 6.15a).

Compositional anomalies

Compositional heterogeneity is another strong candidate for velocity variations in the upper mantle. While high temperatures, fluids, and partial melts are successful in explaining low-velocity anomalies, changes in composition may be important in explaining some high-velocity anomalies. Griffin *et al*. (1998a) argue that compositional anomalies can account for at least 50% of the seismic velocity anomalies observed in tomographic models for the continents, while Deen *et al*. (2006) reduce this value to ~25%, suggesting that temperature variations account for ~75% of seismic velocity variations in the upper mantle worldwide. Artemieva *et al*. (2004) argue that in 50% of continents, half of the amplitude of velocity anomalies in the lithospheric mantle cannot be explained by temperature variations alone.

The presence of compositional variations in the upper mantle is supported by geochemical data. Fundamental differences in composition of the subcontinental and suboceanic

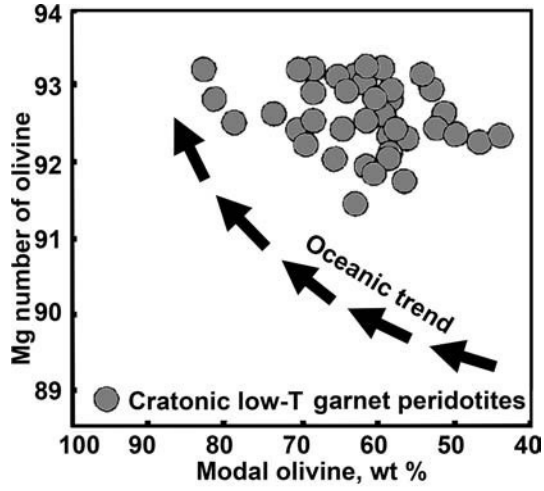

Fig. 3.105 A plot of Mg number versus modal proportion of olivine for various tectonic settings (redrawn from Boyd, 1989). Mg number is 100 Mg/(Mg + Fe) of olivine for ophiolite and abyssal peridotites and a bulk value for compositional models. Oceanic trend – a trend line joining the compositions of residues and model sources that include residues of oceanic volcanism together with model compositions for fertile, parental, upper-mantle peridotite. Cratonic low-T garnet peridotites are coarse, low-temperature, garnet peridotite xenoliths from the kimberlites of the Kaapvaal craton, southern Africa. See Fig. 6.8 and related discussion.

mantles have been recognized from analyses of the major-element compositions of oceanic peridotites and mantle-derived xenoliths from different tectonic settings (Fig. 3.105 and Chapter 6). This conclusion is supported by geophysical analysis based on gravity and seismic data that shows that the ocean–continent difference in seismic tomography is not purely thermal in origin and internally stabilized continent–ocean chemical differences are present in the upper mantle (Forte *et al*., 1995).

On the continents, compositional variations in lithospheric mantle (primarily in iron-content) are well correlated with the age of the overlying crust (Fig. 6.11 and Chapter 6). This correlation is interpreted as a secular, irreversible trend from highly depleted (due to loss of iron during melt extraction) Archean continental lithospheric mantle to fertile Phanerozoic continental and suboceanic mantle. It forms the basis for geophysical interpretations, most of which consider iron depletion as the only source of compositional velocity and density anomalies in the upper mantle.

For example, joint inversions of a large set of geodynamic data related to mantle convection, including global tomography models, have been used for mapping depth variations in iron content in the subcontinental upper mantle (Forte and Perry, 2000). The results suggest, in general agreement with petrological data, that iron depletion is restricted to the upper 200–300 km. Depending on modeling assumptions, the depletion anomaly either has the peak at *c*. 150 km depth, or gradually decreases in amplitude from the Moho down to the transition zone (Fig. 3.106).

Regional geophysical studies support the presence of significant compositional differences in the continental upper mantle, particularly between the cratonic and Phanerozoic

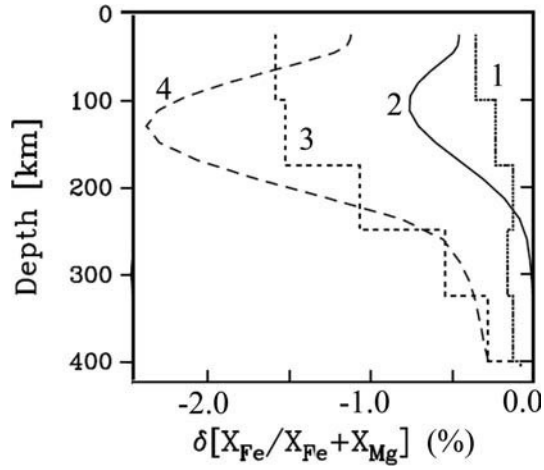

Fig. 3.106 Iron depletion anomalies in the subcratonic upper mantle (from Forte and Perry, 2000; compare with Fig. 3.19). The calculations are based on the assumption that perturbations in iron and garnet content in the tectosphere are correlated as a result of basalt depletion. Curves 1 and 2: the internally consistent estimate of iron depletion in the tectosphere based on $\partial \ln\rho/\partial \ln V_s$ scaling factor and calculated for two tomographic models. Since the approach is invalid when partial melting or thermally induced *V*s attenuation are present in the thermal mantle, independent mineral physics estimates of average $\partial \ln\rho/\partial \ln V_s = 4$ in the upper mantle (Karato, 1993) are used to calculate curves 3 and 4. Tomographic models used in geodynamic calculations: curves 1 and 3 – Grand *et al*., 1997; curves 2 and 4 – Ekström and Dziewonski, 1998.

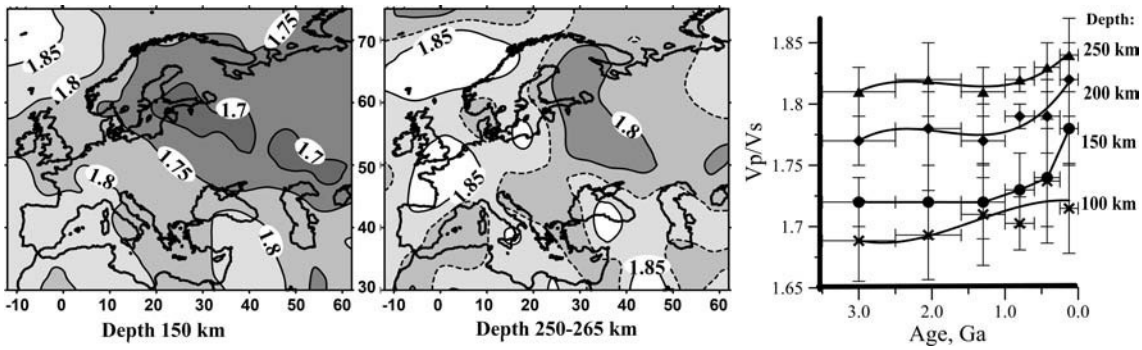

Fig. 3.107 *V*p/*V*s variations in the upper mantle of Europe at depths of 150 km and 250–265 km (smoothed by Gaussian filtering), based on the tomography models of Bijwaard and Spakman (2000), Piromallo and Morelli (2003), Shapiro and Ritzwoller (2002). The *V*p/*V*s ratio is more sensitive to compositional than thermal anomalies in the upper mantle. Note a sharp expression of the cratonic margin at depth 150 km. Right-hand plot shows variations of the *V*p/*V*s ratio at four depths as a function of the tectono-thermal age of the lithosphere of Europe (based on Artemieva, 2007).

mantle. For example, the *V*p/*V*s ratio, which is more sensitive to chemical than to temperature variations, displays a sharp change across Europe that correlates remarkably well with the Trans-European suture zone that marks the western margin of the East European Craton (Fig. 3.107). It is tempting to attribute the change in the *V*p/*V*s ratio across the cratonic margin to changes in mantle Mg# (Fig. 3.22).

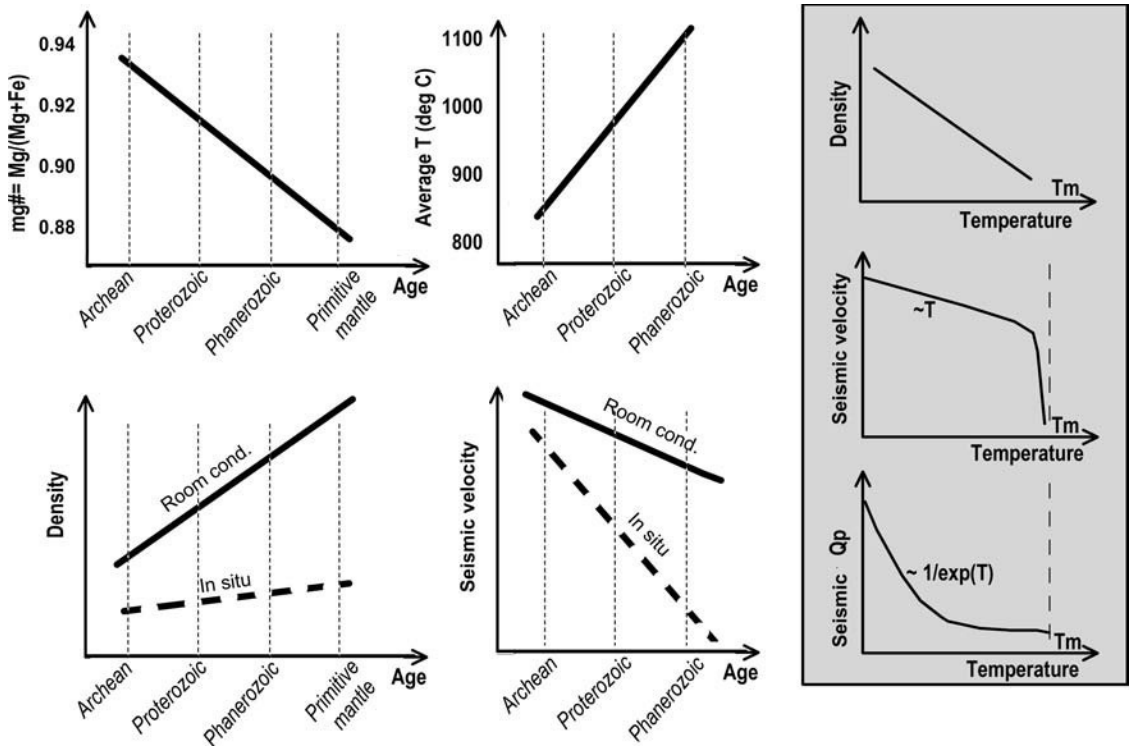

Fig. 3.108 Sketch illustrating secular variations in iron content (expressed by Mg#), density, and seismic velocity in mantle rocks as indicated by laboratory measurements (at room conditions) on mantle-derived xenolith peridotites and typical average temperatures in the lithospheric mantle of different tectonic provinces. Gray insert shows the effect of temperatures on density, seismic velocities, and inverse seismic attenuation. Dashed lines for densities and seismic velocities refer to *in situ* conditions in the mantle, where high temperatures cause density and velocity to decrease. Systematic age-dependent variations in lithospheric temperatures from hot tectonically young provinces to old and cold cratonic lithosphere mask variations in *in situ* densities (providing the basis for the isopycnic (i.e. equal density) hypothesis of Jordan (1978)), but enhance variations in *in situ* seismic velocities (thus providing "grounds" for interpretation of seismic "blue-versus-red" velocity perturbations in terms of "cold-versus-hot" mantle).

Large-scale compositional heterogeneity of the upper mantle should be reflected in seismic tomography and gravity models. However, compositional and temperature effects are difficult to separate due to strong lateral and vertical temperature variations in the upper mantle (see Chapter 4) and the strong effect of temperature variations on physical properties of mantle rocks (Section 3.1). In the subcontinental upper mantle both iron depletion and mantle temperatures (at the same depth within the lithospheric mantle) systematically decrease with age (Figs. 3.108, 4.33, 6.11, 6.15). High upper mantle temperatures produce a density decrease in Phanerozoic regions due to thermal expansion, thus reducing *in situ* density contrast between the low-dense depleted cratonic and young, iron-rich, fertile and heavy lithospheric mantle. The existence of such a thermally balanced *in situ* density equilibrium between depleted and fertile lithospheric mantle (the isopycnic, or equal-

density hypothesis) was proposed by Jordan (1978, 1988) based on the analysis of geophysical (including gravimetric and geothermic) data (see discussion in Chapter 6). It explains the absence of significant geoid anomalies in the cratons. A global analysis of gravity data, corrected for temperature-induced density variations in the upper mantle, indicates a strong contrast in composition between the oceanic and continental upper mantle, and shows that a strong compositional heterogeneity exists within subcontinental mantle even for regions of the same age (Kaban *et al*., 2003; Fig. 6.32).

In contrast with density, temperature increase causes reduction in seismic velocity; as a result a difference in mantle temperatures between the Archean and Phanerozoic regions enhances the seismic velocity contrast between depleted and fertile mantles thus supporting a common interpretation of seismic velocity anomalies in terms of "cold" versus "hot" regions (Fig. 3.108). Although variations in the volumic fraction of olivine and in the iron content certainly have an effect on seismic velocities and densities, it is not so strong as the effect of variations in mantle temperature (Karato and Karki, 2001). An analysis of the effects of temperature and iron content on seismic velocities (Deschamps *et al*., 2002) shows that a 1% velocity anomaly can be produced by an iron anomaly (i.e. the volumic fraction of iron Fe/[Fe+Mg]) of 4% or by a temperature anomaly of 50–100 °C (which is about the accuracy of thermal constraints at any lithospheric depth) (Fig. 6.14a).

In contrast with this prediction, a recent geophysical analysis has indicated the presence of strong non-thermal velocity variations in the upper mantle of the continents if the effect of temperature variations is removed (Artemieva, 2009). The results are constrained by shear-wave tomographic velocity models for the upper mantle that were corrected for lateral temperature variations (Figs. 3.109 and 6.35a). On all continents, the surface transition from the cratonic to the Phanerozoic lithosphere is marked by a sharp decrease in non-thermal seismic velocity anomalies in the lithospheric mantle, which is correlated with a sharp change in the non-thermal part of mantle gravity anomalies (i.e. increase in mantle density) (Kaban *et al*., 2003). Lateral, non-thermal in origin, variations in seismic velocity and density structure may be attributed, in part, to a change in olivine content at the transition from the cratonic to non-cratonic lithospheric mantle, although a significant part of these variations may be caused by other compositional and non-compositional effects.

Interpretations of seismic velocity anomalies in the cratonic lithospheric mantle in terms of iron depletion are challenged by recent laboratory measurements and theoretical calculations for chemical and mineralogical compositions of natural peridotites (Kopylova *et al*., 2004; Matsukage *et al*., 2005). These indicate that seismic velocities in the continental lithosphere are characterized by two parameters, Mg# and Opx# (volume fraction of orthopyroxene) (Figs. 3.21, 3.24). While compressional and shear seismic velocities increase almost linearly with increasing Mg#, addition of low-velocity orthopyroxene decreases seismic velocities. Maximum velocity anomalies produced by variations in Opx# (−1.8% and −2.3% for Vs and Vp, respectively) are larger than Vs and Vp anomalies caused by iron depletion (+1.1% and +1.0%, respectively). Matsukage *et al*. (2005) argue that variations in orthopyroxene content can be the main cause of seismic velocity variations at garnet stability field (depths between 70 to 190 km). Thus, at present the conclusions of laboratory and theoretical studies on the effects of compositional variations in the subcontinental lithospheric mantle remain incomplete.

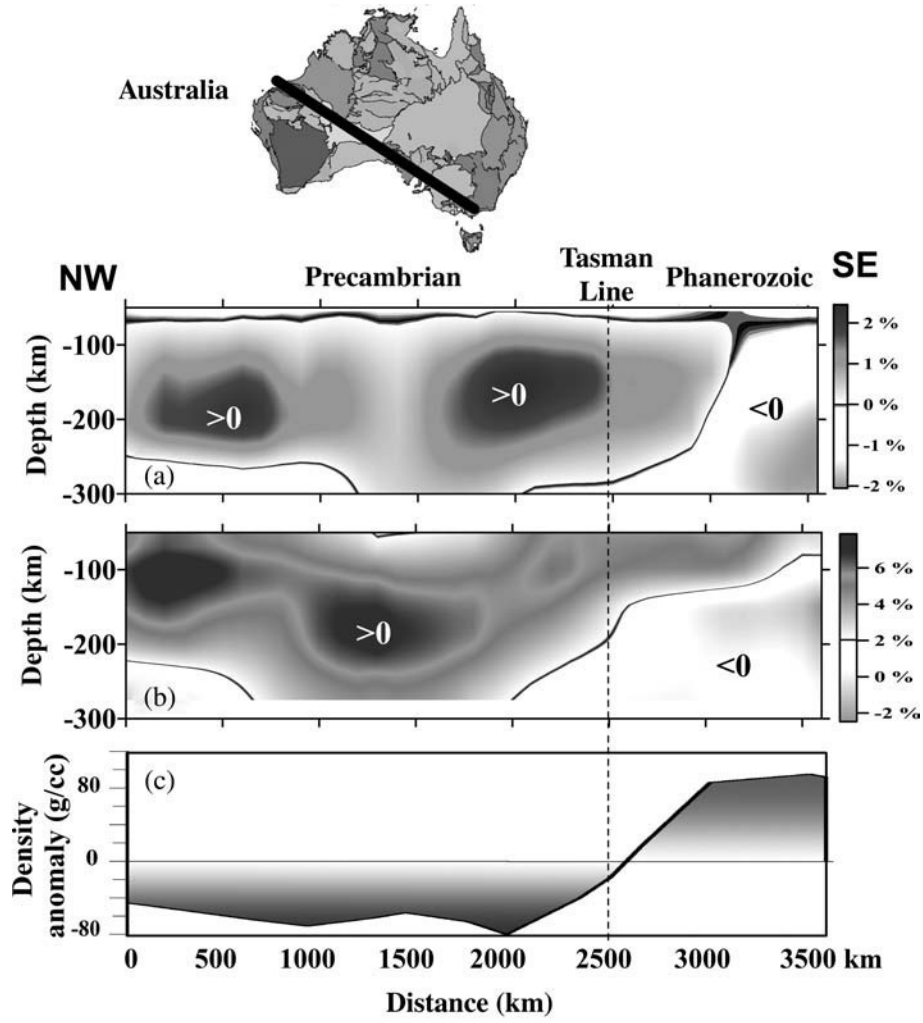

Fig. 3.109 Profile across Australia showing compositional heterogeneity in the upper mantle (based on Artemieva, 2009). (a–b): *Vs* seismic velocities corrected for lateral and vertical temperature variations based on (a) surface-wave model (Shapiro and Ritzwoller, 2002) and (b) body-wave tomographic model (Grand, 2002). (c) Density variations in the upper mantle of Australia constrained by temperature-corrected gravity anomalies (Kaban *et al*., 2003). The depth distribution of these anomalies is unconstrained and the values reflect density anomalies integrated over the entire lithosphere.

Density-to-shear-wave velocity scaling factor

Owing to strong temperature-dependence, seismic velocity anomalies alone are insufficient to distinguish chemical variations in the mantle. An independent set of data, such as density anomalies, is needed to separate the compositional and thermal effects on seismic wave speeds and to infer chemical variations in the mantle. A relative density-to-shear-wave velocity

scaling factor $\zeta = \partial \ln\rho / \partial \ln V_s$ has been proposed to discriminate between thermal and chemical heterogeneity (see eq. 3.13 and Section 3.1.8). It provides a crude diagnostic of the thermal versus compositional origin of density and seismic velocity anomalies in the mantle. For purely thermal anomalies, when temperature variations produce density and velocity variations of the same sign, $\zeta > 0$. Unlike temperature variations, the effect of chemical variations is more complicated since compositional changes may have a different effect on the scaling factor and both cases, $\zeta > 0$ or $\zeta < 0$, are possible depending on composition. For example, two end-member upper mantle compositions have opposite signs of synthetic ζ values (positive for olivine–garnet but negative for olivine–diopside mineralogies) since an increase in the volume fraction of diopside leads to an increase in both density and velocity, whereas an increase in the volume fraction of garnet produces a density increase, but smaller velocities (Deschamps *et al*., 2001). Tables 3.1 and 3.2 summarize information on the effects of various factors on mantle density and seismic velocities.

On the whole, for the real upper mantle the values of ζ are not well known and remain controversial (Fig. 3.110). Joint inversions of gravity and tomographic models for the whole mantle commonly use low-degree spherical harmonics which are sensitive to the structure of the deep mantle. The reported ζ values range from $-0.3 < \zeta < 0.3$ with the change of the sign at *c*. 300 km depth for inversions for degrees $l = 2$–8 of spherical harmonics ζ (Forte *et al*., 1994). Inversions for $l = 11 - 16$ based on global tomographic model S16RLBM (Trampert and Woodhouse, 1995) and on the EGM96 geoid model (Lemoine *et al*. 1998) predict $-0.05 < \zeta < 0.05$ for the upper 400 km (Deschamps *et al*., 2001). The results of the latter inversion suggest that in the subcontinental upper mantle the sign of ζ changes from positive to negative at *c*. 200 km depth, while beneath the oceans $\zeta < 0$ at between the depths of *c*. 120 km and 220–240 km (Fig. 3.110b). The negative sign of the scaling factor in the lower parts of the subcontinental lithosphere (deeper than 200 km), where temperatures approach mantle adiabat and thus the thermal effect on velocity variations decreases, indicates the important role of chemical anomalies on seismic velocities and mantle density. Compositional anomalies with intermediate length scale are expected to be present in the uppermost part of the subcontinental mantle, where the shapes of depth variations of ζ and relative *V*s anomalies are significantly different (Deschamps *et al*., 2001).

The results of Deschamps *et al*. (2001) are in contrast, both for continents and oceans, with similar studies performed by other groups. Kaban and Schwintzer (2001) use the isotropic part of shear-wave tomography model S20 (Ekstrom and Dziewonski, 1998) and the EGM96 spherical harmonic expansion of the gravitational geopotential (Lemoine *et al*. 1998) to derive mean gravity values for $1° \times 1°$ blocks. They further correct gravity data for the effect of crustal density heterogeneity using the CRUST 5.1 model (Mooney *et al*., 1998) and calculate the density-to-shear velocity scaling factor from the thus derived "crust-free" gravity model, performing the inversion for the whole mantle (for spherical harmonic degrees $l = 3 - 20$). Their analysis indicates the presence of compositional layering in the oceanic upper mantle with a transition between the two layers at 70 km depth (although lateral temperature variations produce most of the density variations in the oceanic upper mantle). Above a 75 km depth and below a 225 km depth, the velocity-to-density scaling factor is close to predictions based on mineral physics analysis and is consistent with the composition of dry partially depleted peridotite (Fig. 3.110d). The oceanic layer between a

Table 3.1 Non-thermal effects on variations of upper mantle density and *Vs* seismic velocity

Parameter	Affected depth	$\delta\rho$	δVs	Reference
Iron content increase	CLM	+1.4%(for $X_{Fe} = +4\%$)	– 1.0% (for $X_{Fe} = +4\%$)	D02, L03
Garnet content increase	CLM	> 0	> 0	D02
Substitution of pyrore-rich garnet by grossular garnet	CLM	< 0, Weak effect	> 0	D02
Clinopyroxene content increase	CLM	< 0	− 0.4 % (for $X_{di} = +6\%$)	NZ94
Orthopyroxene content increase	CLM (70 to 190 km depth)	No effect	Up to +1.8%	M05
Fluids	CLM	Indirectly, through the effect on solidus	Indirectly, through the effect on anelastic relaxation – 1 to − 6%	T81
Anelasticity at high homologous temperature $T/T\mathrm{m} > 0.95$	The lower part of the TBL	No effect		S89
Melts	Chiefly the lower part of the TBL	< 0	− 10% for ~ 5% melt (strongly depends on melt geometry)	MK79
Anisotropy	CLM	No effect	Either sign	BIM98

(Source: Artemieva, 2009).

Comments: CLM = continental lithospheric mantle. Where absolute values are unavailable, only the sign of δVs and δp variation is given. Positive values (>0) indicate a velocity or density increase, while negative values (<0) refer to a decrease in the corresponding parameter.

References: BIM98 – Ben Ismail and Mainprice, 1998; D02 – Deschamps *et al*., 2002; L03 – Lee, 2003; MK79 – Murase and Kushiro, 1979; M05 – Matsukage *et al*., 2005; NZ94 – Nolet and Zielhuis, 1994; S89 – Sato *et al*., 1989; T81 – Tozer, 1981.

Table 3.2 Factors affecting Density and velocity anomalies in the upper mantle of different tectonic provinces

Tectonic setting	Major factors affecting ρ and Vs	$\delta\rho/\rho_o$ (%)*	$\delta V s/V_o$ (%)*
Archean cratonic mantle	• Low Fe (Fo = 93)	− 1.8%	+ 1.3%
Proterozoic cratonic mantle	• Intermediate Fo = 92	− 0.6 –1.2%	+ 0.4%
Phanerozoic or metasomatised Fe-enriched cratonic mantle (Fo = 90)	• In the case of high garnet content • In the case of high diopside content	> 0 < 0	> 0 − 0.4%
Orogens	• Metamorphism (in a 20 km thick layer) • Fluids • Melts?	+ 1.0% (overall effect for 80 km thick mantle) No effect < 0	No effect < 0 − 10% for ~5% melt
Active (plume-related) continental regions	• Melts • Subsolidus T	< 0 No effect	− 10% for ~5% melt − 6% (in a 10 km thick basal layer)
Subducted Precambrian slab (made of 40 km thick crust + 110 km thick low-Fe (Fo92) mantle)	• Composition of crust and mantle • Metamorphism (in a 20 km thick layer) • Fluids	− 6.2 % (overall effect) + 0.4% (overall effect) No effect	< 0 (crust), + 1% (mantle) No effect < 0
Subducted Phanerozoic slab (made of 40 km thick crust + 80 km thick harzburgite mantle (high ol, low gnt, no cpx))	• Composition of crust and mantle • Metamorphism (in a 20 km thick layer) • Fluids	− 6.7 % (overall effect) + 0.4% (overall effect) No effect	< 0 (crust), No effect (mantle) No effect < 0

(Source: Artemieva, 2009).

* Relative density and velocity anomalies are given at SPT (room conditions, thermal effect excluded) with respect to "normal" (Fo90) stable continental lithosphere (such as is typical of Paleozoic platforms).

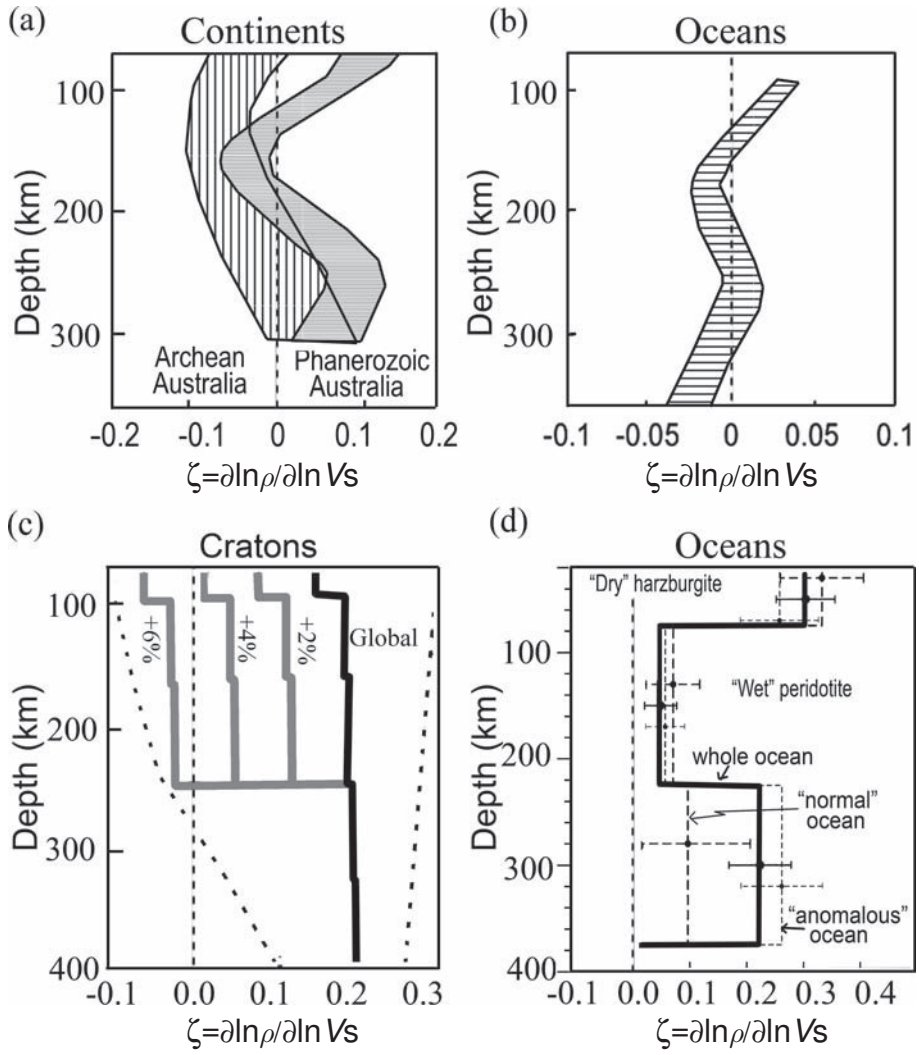

Fig. 3.110 A relative density-to-shear-wave velocity scaling factor ζ in the subcontinental and suboceanic upper mantle (eq. 3.13) based on different inversions for the whole mantle. Negative values of the scaling factor indicate the presence of compositional variations, whereas positive values may be caused either by temperature or by chemical variations. Note different horizontal scales. (a) ζ calculated for the Archean and Phanerozoic regions of Australia for the SKIPPY-based isotropic surface-wave tomography model AUS-04VS (results of van Gerven *et al*., 2004); (b) ζ calculated in a joint inversion of the global tomographic model S16RLBM and the EGM96 geoid model (results of Deschamps *et al*., 2001). Shaded areas in (a–b) indicate both the mean values and the error bars estimated by introducing randomly generated errors in the seismic model. (c) Optimal global 1D scaling based on simultaneous inversion of shear-wave travel-time data and convection-related geodynamic constraints. Solid gray lines – profiles corrected for velocity perturbations of dVs = 2%, 4%, 6% within the cratonic roots; dotted lines – range of 3D variations of the scaling factor (results of Simmons *et al*., 2009). (d) Scaling factor for oceanic mantle calculated from the isotropic part of shear-wave tomography model S20 and global gravity based on the EGM96 geoid model and corrected for the effect of crustal density heterogeneity (results of Kaban and Schwintzer (2001)).

70 km and 225 km depth has a significantly lower density/velocity ratio and may have the composition of wet fertile peridotite.

Simmons *et al*. (2009) simultaneously inverted shear-wave travel-time data and a set of geodynamic convection-related constraints consisting of the global free-air gravity field, tectonic plate divergences, dynamic surface topography, and the excess ellipticity of the core–mantle boundary, represented by surface spherical harmonic functions up to degree 16. The temperature-dependence of the relative density-to-shear-wave velocity scaling factor $\zeta = \partial \ln \rho / \partial \ln V_s$ in the upper mantle is significant due to the temperature-dependence of seismic attenuation. The inversion provides an optimum 1D thermal profile of ζ that is generally compatible with all considered data except for the cratonic regions where dynamic topography produced by density anomalies in shallow mantle is expected (Fig. 3.110c). The results, based on calculation of the relative magnitudes of the thermal and compositional (non-thermal) contributions to mantle density anomalies, indicate that within the non-cratonic mantle thermal effects dominate shear-wave and density heterogeneity. However, within the cratonic mantle, strong negative correction factors to ζ are required due to the significant compositional buoyancy of cratonic roots. Similar results have been obtained in a recent regional inversion for central Australia (van Gerven *et al*., 2004). This study reports $\zeta < 0$ at 75–150 km depths and near-zero ζ values down to *c*. 300 km depth which are interpreted as indicating strong compositional heterogeneity of the upper part of the cratonic upper mantle (Fig. 3.110a).

3.6.4 Seismic anisotropy in the upper mantle

The following paragraph largely follows an excellent review of seismic anisotropy studies of the upper mantle published by Savage (1999). It has been updated to include major results from the past decade. A discussion of crustal anisotropy (the major mechanisms for which are anisotropic rock fabric, alignments of cracks and fractures within the crust, and alternate layers of fast and slow material) is omitted here; a review can be found in Crampin (1977). Since the total measured anisotropy results from a combination of crustal and mantle components, which may have different orientations (e.g. Christensen *et al*., 2001), the effect of crustal anisotropy must be separated out in studies of mantle anisotropy.

Types of anisotropy

Theoretical studies of the propagation of elastic waves in anisotropic media were started by Christoffel (1877) and were further developed by Lord Kelvin (1904), Love (1944) and Musgrave (1959). Experimental studies of seismic anisotropy began largely in the early 1960s with the works of Birch (1961), simultaneously with field observations of seismic anisotropy in the uppermost mantle of the oceans (e.g., Hess, 1964; Francis, 1969).

Three major types of anisotropy include intrinsic, azimuthal, and polarization anisotropy.

- *Intrinsic anisotropy* refers to the material itself and is defined by the difference between the maximum and minimum velocities in a medium (Birch, 1961).
- *Azimuthal anisotropy* is the variation of wavespeed for a certain type of wave as a function of the azimuth of the propagation direction (Figs. 3.28, 3.111) and in early studies it was constrained by *P*n velocity variations based on refraction data (e.g., Hess, 1964).

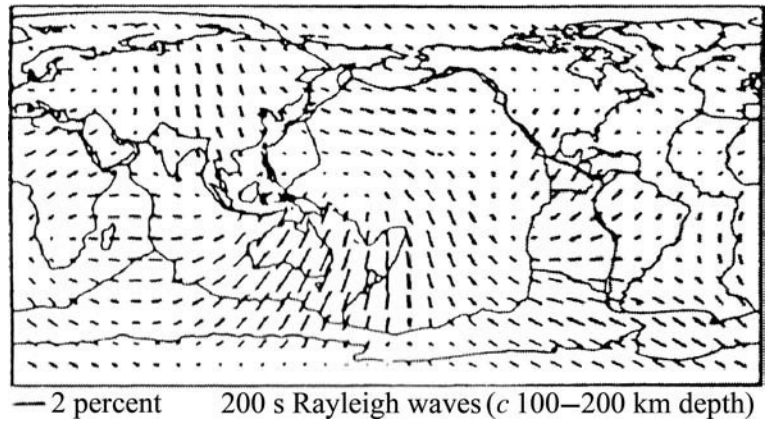

Fig. 3.111 Azimuthal anisotropy of Rayleigh waves of 200 s period. Lines show the propagation direction of the fast waves (after Tanimoto and Anderson, 1984).

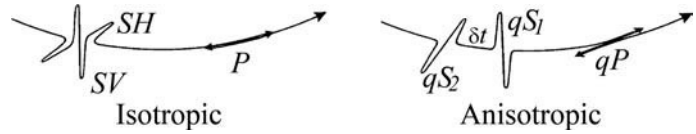

Fig. 3.112 Sketch of isotropic and anisotropic wave propagation (redrawn from Savage, 1999). In the isotropic case, the P-wave has linear particle motion in the propagation direction and the S-wave has a particle motion perpendicular to propagation; two S-wave components are arbitrarily defined as oriented horizontally (SH) and vertically (SV). In the anisotropic case, linear particle motion in a quasi-P wave is not quite parallel to the propagation direction, while two quasi-S waves (qS_1 and qS_2) with polarizations parallel and perpendicular to the fast direction for the propagation direction are separated by time δt.

- *Polarization anisotropy* is the variation of wavespeed of phases with different polarization that travel along the same direction; it is less sensitive to heterogeneous isotropic structure than azimuthal anisotropy. Examples of polarization anisotropy include:
  (1) Love and Rayleigh surface waves (Fig. 3.27) since horizontally polarized Love waves travel faster than vertically polarized Rayleigh waves (e.g., Anderson, 1961);
  (2) SH (fast) and SV (slow) phases of body waves (e.g., Shearer, 1991);
  (3) Shear-wave splitting (e.g. of body waves) that has the same physical meaning as optical birefringence (e.g. Crampin, 1977) (Fig. 3.112).

Laboratory measurements of anisotropy on mantle-derived samples indicate that most of them have either orthorhombic or hexagonal symmetry (Fig. 3.14). For horizontal alignment of the *a*-axis and near-vertical incidence angle, the anisotropy patterns produced by these symmetry systems do not differ significantly. Elastic anisotropy in the mantle is commonly attributed to the preferred orientation of olivine crystals which results from deformation. Large-strain deformation aligns the olivine [100] axes along the flow direction or parallel to the direction of extension. For horizontal flow it leads to $V_{SH} > V_{SV}$ and for vertical flow to

$V_{SH} < V_{SV}$. These interpretations, commonly accepted in most seismic studies, have been challenged by recent laboratory experiments on deformation of olivine aggregates (see Section 3.1.5). In particular, in the case of partial melting such as in the mantle wedge, the [001] olivine axes may align along the shear direction with its [100] axes oriented normal to the macroscopic flow direction (Fig. 3.15c).

Origin of mantle anisotropy

Tectonic processes that produce deformation of mantle rocks and are thought to be responsible for mantle anisotropy include the following.

(1) *Fluid-filled cracks deformed by local stress*. This mechanism produces fast polarizations aligned parallel to the maximum compressional stress and is likely to be the major cause of anisotropy beneath oceanic spreading centers where the fast axis of anisotropy is parallel to the spreading direction (Vinnik *et al*., 1989; Blackman and Kendall, 1997; Wolfe and Silver, 1998), continental rift zones (Sandvol *et al*., 1992; Vinnik *et al*., 1992), and the East Pacific Rise (Forsyth, 1975; Forsyth *et al*., 1998).

(2) *Lithosphere deformation by strain*. In the case of collisional events caused by uniaxial compression, *b* is the axis of symmetry (the slow direction) and it is parallel to the direction of shortening; fast polarization is parallel to the strike of the mountain belts, e.g. due to "escape" tectonics (Christensen and Crosson, 1968; Milev and Vinnik, 1991; Silver, 1996; Meissner *et al*., 2002).

(3) *Frozen-in anisotropy.* In many regions anisotropy in the crust, in the shallow and in the deep lithosphere reflects different tectonic episodes and preserves frozen-in anisotropy from past tectonic events (i.e. deformation at temperatures above 900 °C followed by cooling, so that temperature never rose again to the critical value of *c*. 900 °C). In the continents the crust and the lithospheric mantle may experience coherent deformation through geologic history. In such a case, fast polarization in the mantle should correlate with crustal tectonics (Silver and Chan, 1988, 1991; Vinnik *et al*., 1992; Silver, 1996). Anisotropy at deeper, hotter depths may be different and caused by recent deformations. Similarly, in the Pacific Ocean shallow (<100 km) frozen-in anisotropy is related to fossil spreading whereas deeper mantle anisotropy is related to the present-day flow direction (Nishimura and Forsyth, 1988; Montagner and Tanimoto, 1991).

(4) *Large-scale asthenospheric flow.* Asthenospheric flow produces the preferred orientation of olivine and mantle anisotropy (Vinnik *et al*., 1992). In the case where flow occurs by simple shear, fast polarization tends to be aligned with the flow direction (within 30° of the direction of flow for large strain and at about 45° for small strain). Examples of this are the Pacific and the Indio-Australian plates (Montagner, 1994). However, anisotropy in the North Atlantic is inconsistent either with the fossil seafloor spreading direction or with present-day plate motion (Montagner and Tanimoto, 1991). Asthenospheric flow plays an important role in producing azimuthal anisotropy (Vinnik *et al*., 1992).

(5) *Relative motion of lithospheric plates and convective mantle*. Similarly to asthenospheric flow, fast polarization tends to be parallel to the direction of relative plate motion

(spreading direction) (Ribe, 1989). In subduction zones slabs may channel asthenospheric flow parallel to the slab dip and the anisotropy axis is expected to be parallel to the direction of subduction. In some regions (e.g. the North Atlantic) plate motion may be decoupled from convective flow deeper in the mantle (Bjarnason *et al*., 1996).

(6) *Small-scale asthenospheric flow.* It may be important in some tectonic settings. Corner flow at mid-ocean ridges may produce horizontal stretching lineation and the horizontal foliation plane (Hess, 1964; Silver, 1996). In some cases, due to small-scale flow, fast polarizations may be non-related to surface tectonics (Makeyeva *et al*., 1992).

(7) *Temperature difference* in mantle convective cells (Montagner and Guillot, 2002).

Body-wave studies

Preamble

Body-wave studies of seismic anisotropy have the same limitations regarding vertical resolution as body-wave tomography: while shear-wave splitting provides lateral resolution as good as <50 km, the depth extent of the observed anisotropy cannot be reliably constrained by seismic data. The most popular body-wave studies are SKS and similar phases. They begin propagation as S-waves, convert to P-waves at the liquid outer core, and are then converted back to S-waves when they exit from the core. The advantage of these phases is based on the fact that any splitting from the source side of the path is destroyed during their propagation in the outer core and any anisotropy produced at the source side is lost. The polarization of the S-wave when it enters the mantle is known (because it is generated by a P-wave traveling in the core, the emerging wave has SV polarization) and is independent of the earthquake focal mechanism, while S-wave splitting occurs on the path between the core–mantle boundary and the receiver. Near-vertical S-wave propagation in the upper mantle provides high lateral resolution (within the first Fresnel zone).

Two parameters characterize shear-wave splitting (Fig. 3.112): polarization of the first (fast) shear wave and a time delay between the two quasi-S-waves. The latter depends on the wavespeed difference between them and on the path length in anisotropic medium. However, for most symmetry systems both fast polarization direction and time delay depend on the back azimuth and incidence angle. The simplest interpretation of shear-wave splitting assumes transverse anisotropy with a horizontal symmetry axis. Most of the reported values of time delays range between 1.0 s and 2.0 s. If shear-wave splitting is distributed over a 400 km thick layer, minimum values for average anisotropy of 1.0 s and 2.0 s are 1.1% and 2.2%, respectively; in the case of a 250 km thick layer these values are 1.8% and 3.6%. Laboratory measurements of mantle xenoliths that came from a 40–170 km depth indicate comparable values of shear-wave splitting anisotropy, between 3.5% and 7% (Mainprice and Silver, 1993; Kern, 1993).

Frozen versus asthenospheric anisotropy

The observation of shear-wave splitting on broadband seismic waveforms has led to two competing models for anisotropy within the upper mantle (Fig. 3.113). According to one group of authors, anisotropy is primarily within the asthenosphere as indicated by agreement

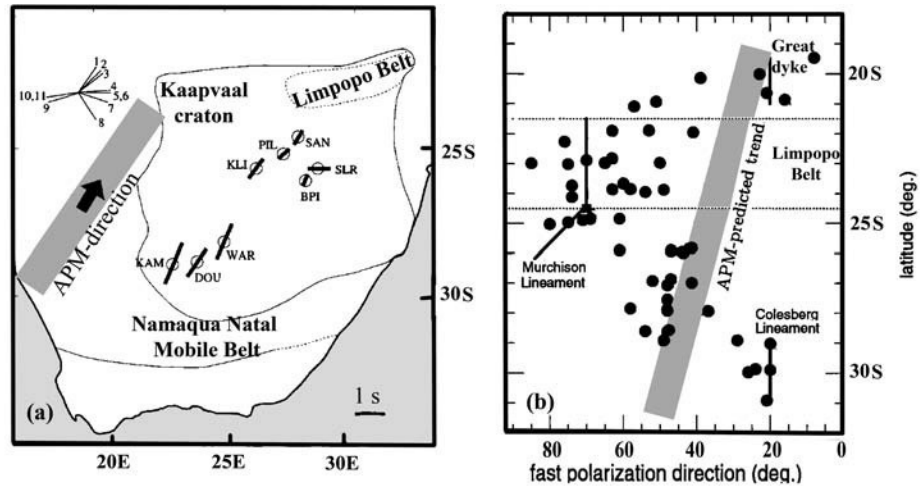

Fig. 3.113 Two alternative views on the origin of seismic anisotropy beneath southern Africa based on shear-wave splitting analyses of SKS and similar phases (a – after Vinnik *et al*., 1995; b – based on Silver *et al*., 2001). (a) The direction of polarization of the fast split wave at different stations is shown by straight lines, the lengths of which are proportional to the time lag of the slow wave (see scale bar in the lower right corner). The upper left corner shows azimuths of the recorded events. The direction of the Absolute Plate Motion (APM) since the end of the Jurassic is shown by gray shading with an arrow. The results for all stations (except SLR) indicate that the direction of mantle flow beneath southern Africa is close to the APM and suggest that mantle anisotropy is related chiefly to shearing of the sublithospheric mantle at depths between 150 km and 400 km by the plate above. (b) Direction of fast shear-wave polarization in the mantle plotted versus station latitude. The crustal component of shear-wave splitting has been isolated in the analysis. Fast polarization directions predicted for the present-day APM model for the African plate (shown by gray shading) are in sharp contrast to the data. The anisotropy pattern seems to be better correlated with geological features.

between present-day plate motion directions and the orientation of the fast axis of wave-speed (Vinnik *et al*., 1995, 1998). Such correlations are found in several continental regions (South Africa, North America) and in most oceanic regions at 100–200 km depth (e.g., Montagner, 1994; Vinnik *et al*., 1999; Lévêque *et al*., 1998; Bokelmann, 2002). Although the depth distribution of anisotropy is unknown, some indirect assessments can be made from mantle temperatures since olivine mobility below *c*. 1000 °C is low. Beneath the South African craton this temperature is reached at *c*. 150 km depth and it has been proposed that the deep part of the continental root (between 150 km and 400 km) can experience deformation associated with plate motion and mantle flow. This hypothesis is supported by the distribution of olivine grain-sizes and deviatoric stress in the lithosphere beneath the Kaapvaal craton (Fig. 3.104). An estimated lateral displacement of the deep portion of the root at 400 km depth with respect to a 150 km depth is a few hundred kilometers as compared to a *c*. 3000 km shift of the lithospheric plate since the Jurassic (Vinnik *et al*., 1995). In cratonic North America, where a large-scale coherent SKS anisotropy is present, while large-scale azimuthal anisotropy is absent in long-range seismic refraction data for the upper 100 km of the mantle, shear-wave splitting seems to be generated below a

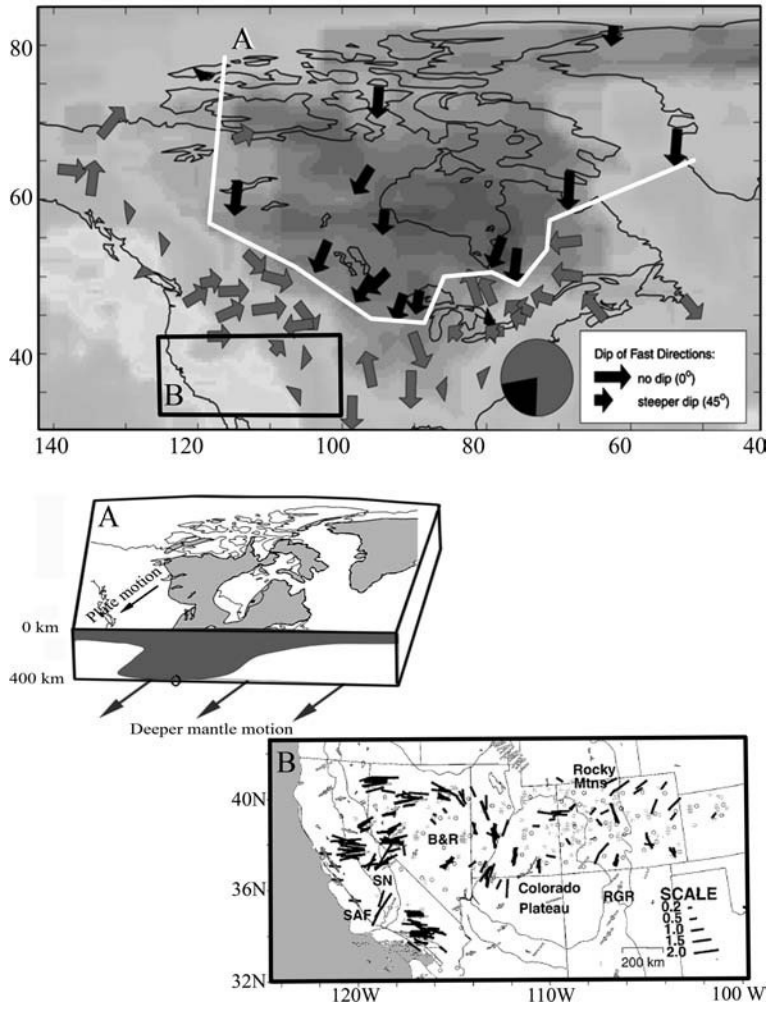

Fig. 3.114 Seismic anisotropy in North America (after Bokelmann, 2002). Orientation of fast axes for stations in North America are shown by arrows (black for azimuths between 180° and 260°). Shaded background – vertically integrated travel-time residuals in the upper mantle in the S-wave tomographic model (Grand, 1994). Insert A: proposed interpretation of anisotropy origin beneath the cratonic part of North America (schematically outlined by a white line in the map) caused by simple shear due to the relative motion of thick cratonic root over deeper mantle (after Bokelmann, 2002). Insert B: Shear-wave splitting measurements in western USA plotted at 220 km depth projection of the ray. Bars are oriented parallel to the fast polarization direction, their length is proportional to the delay time (after Savage, 1999).

100 km depth. Thus it is likely to be caused by present-day flow in the mantle rather than reflect past tectonic processes (Vinnik *et al*., 1992; Bokelmann, 2002) (Fig. 3.114).

The other competing point of view on the origin of mantle anisotropy is that anisotropy originates primarily within the lithosphere ("frozen-in anisotropy") as indicated by the agreement between the geometry of surface tectonics (continental accretion) and the

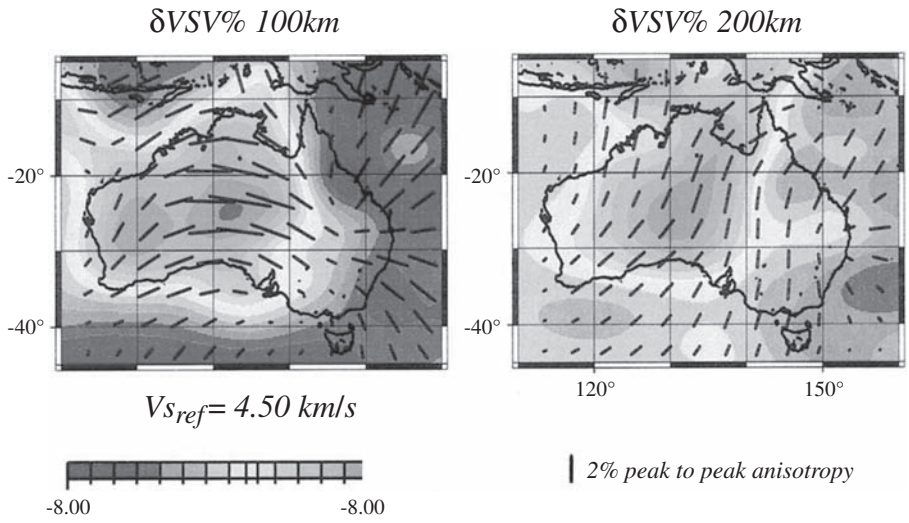

Fig. 3.115 SV wave heterogeneities and azimuthal anisotropy (from Debayle and Kennett, 2000). Gray shading shows velocity anomalies and bars show azimuthal anisotropy (the length indicates the strength of anisotropy).

orientation of the fast axis in North America and South Africa (Silver and Chan, 1988, 1991; Silver *et al*., 2001). This means that mantle deformation can have been preserved in the lithosphere structure since the Precambrian, implying coherent deformation history for the crust and the lithospheric mantle. Similarly to continents, anisotropy in the suboceanic mantle can also be frozen-in and associated with the spreading direction (e.g. Nishimura and Forsyth, 1989).

These two points of view need not be incompatible since seismic observations are best modeled by a combination of lithospheric and asthenospheric anisotropy (Vinnik *et al*., 1992). Differences in the depth distribution of radial and azimuthal surface-wave anisotropies provide strong support for this conclusion (Lévêque *et al*., 1998). In particular, below the Australian continent the drastic change in the direction of anisotropy occurs at a depth of 150–200 km, while a positive velocity anomaly is clearly seen down to ~300 km depth. Observation of polarization anisotropy down to at least 200 km beneath the Australian continent supports a two-layered anisotropic pattern as constrained by the azimuthal anisotropy of SV waves. In the upper layer down to *c*. 150 km depth, anisotropy has roughly a sublongitudinal pattern which does not correspond to the present plate motion; it is interpreted as a frozen-in anisotropy related to past deformation. In the lower layer, below *c*. 150 km depth anisotropy has a sublatitudinal pattern that may reflect present deformation due to plate motion (Debayle and Kennett, 2000) (Fig. 3.115).

Similarly, stratified anisotropy in the upper mantle has been reported recently beneath the North American craton (Deschamps *et al*., 2008). SKS splitting and long-period teleseismic waveform analysis indicate stratification of the lithospheric mantle in North America with transition between the two layers at *c*. 150 km depth (Yuan and Romanowicz, 2010). Other studies propose that the source of shear-wave splitting beneath the North American craton is deeper than 200 km (Li *et al*., 2003a). A recent study for North America suggests the presence of two anisotropy layers with different orientations of the fast

axis in the upper mantle of the craton: at shallow depth (80–200 km) the fast axis is oriented roughly north–south, while deeper (200–400 km), the fast axis is subparallel to the absolute plate motion (Marone and Romanowicz, 2007).

Stratified anisotropy was long ago reported for the Pacific Ocean (Nishimura and Forsyth, 1988; Montagner and Tanimoto, 1991): while the shallow (<100 km) upper mantle anisotropy of the Pacific Ocean is related to fossil spreading, mantle anisotropy below a 100 km depth is related to the present-day flow direction.

Global patterns

On the global scale, studies of azimuthal anisotropy display the following patterns.

- In the regions of the present plate convergence, the fast direction of anisotropy is usually parallel to the plate boundary suggesting similar stress orientation in the crust and the upper mantle (Christensen and Crosson, 1968; Milev and Vinnik, 1991; Silver, 1996). For example, studies of azimuthal anisotropy in Tibet indicate similar directions for shear-wave splitting and crustal strain and suggest a coherent deformation of the entire lithospheric plate. However, SKS anisotropy in mountain regions around Tibet shows a very complicated pattern.
- In many strike-slip regions the fast direction of anisotropy is parallel to the strike-slip motion. The results from the San Andreas Fault are controversial, probably due to the presence of several anisotropic layers (Vinnik *et al*., 1989, 1992).
- Other tectonically active regions such as western North America display a very complex anisotropy pattern which is apparently not well related to surface tectonics but may be controlled by flow deeper in the mantle (e.g. Fig. 3.114).
- In some continental rifts and oceanic spreading centers (the Baikal Rift, the Red Sea, the southern Mid-Atlantic Ridge, the East Pacific Rise, Iceland) the fast direction of anisotropy (and inferred mantle flow) is often parallel to the direction of extension in the crust (Sandvol *et al*., 1992; Vinnik *et al*., 1992; Forsyth *et al*., 1998). In other rifts and spreading centers (the Rio Grande Rift, the East African Rift, and the East Pacific Rise according to several studies) the fast direction is parallel or subparallel to the tectonic structure, suggesting either olivine alignment in ridge-parallel flow or anisotropy produced by fluid-filled cracks (Gao *et al*., 1997).
- The anisotropy pattern in subduction zones is very complicated (see review by Savage, 1999). The mantle above and below the slabs has anisotropy between 0.5% and 2.0%, while anisotropy within the slab may reach 5%. Fast ScS polarizations perpendicular to the slab are observed in Japan and western South America. However, SKS data for stations above subduction zones often indicate fast polarizations parallel to the plate boundary (e.g. Shih *et al*., 1991).
- The anisotropy of oceanic mantle is fossil and was formed at the spreading ridge with the fast axis parallel to the spreading direction as indicated by seismic data and by ophiolite sequences. However, in the Pacific mantle anisotropy is two-layered with frozen-in anisotropy in the shallow layer (down to 100 km) related to the fossil spreading direction and parallel to the present day plate motion at greater depths (Montagner and Tanimoto, 1991). The pattern for the Atlantic Ocean is controversial (Bjarnason *et al*., 1996).

- Stable continents have a combination of frozen anisotropy in the lithospheric mantle and recently formed anisotropy in the asthenosphere and, globally, display a positive correlation between the directions of absolute plate motion and the fast direction of anisotropy (Vinnik *et al*., 1992; Bokelmann, 2002). However, there are exceptions and controversies. In the cratons of Australia and North America anisotropy is two-layered: the shallow layer preserves fossil anisotropy, but anisotropy in the deeper lithosphere (below 150 km) correlates with the present plate motion (Yuan and Romanowicz, 2010). Surface-wave studies (see next section) indicate that the upper mantle beneath the Baltic Shield may also have a two-layer anisotropy, but the direction of azimuthal anisotropy in the deep layer differs significantly from the present direction of absolute plate motion (Bruneton *et al*., 2004).

Surface-wave anisotropy

Preamble

Studies of polarization anisotropy of surface waves are based on comparisons between propagation of Love and Rayleigh waves. Rayleigh waves are produced as interference waves by the interaction of incident P and SV waves with the free surface and are mostly sensitive to SV velocity, whereas Love waves are produced by interference of reflections of SH waves generated at the free surface and trapped in a near-surface waveguide (e.g. Lay and Wallace, 1995). Therefore, separate inversions of Love waves and Rayleigh waves provide insight into the radial anisotropy of the upper mantle.

Simple symmetry systems are commonly used to interpret seismic anisotropy, in particular because fundamental modes are sensitive to a limited number of elastic constants (Montagner and Tanimoto, 1991). Most techniques can distinguish velocity anisotropy only in two orthogonal directions, e.g. vertical and horizontal, which is characterized by V_{SH}/V_{SV} (see Section 3.1.5 and Fig. 3.15). Radial anisotropy (hexagonal, or cylindrical, anisotropy with a vertical symmetry axis and phase velocity independent of the propagation azimuth) explains the polarization anisotropy of Love and Rayleigh waves and the differences between SH and SV arrivals (Anderson, 1961). This type of anisotropy with a vertical symmetry axis is best explained by horizontal shearing (flow).

Radial shear-wave anisotropy is present in the anisotropic version of the PREM model (Dziewonski and Anderson, 1981), where it is confined to the upper mantle down to 220 km depth with maximum anisotropy just below the Moho and its monotonic decrease with depth (Fig. 3.116). Other 1D reference models (such as *iasp91*, *ak135*) include similar anisotropy for P- and S-waves in the upper mantle with isotropic mantle beneath. Three-dimensional tomographic models calculated as a perturbation with respect to PREM display globally averaged anisotropy in the upper mantle that is similar to the reference model. However, tomographic inversions based on isotropic starting models without the 220 km discontinuity display an anisotropic pattern of shear velocities in the upper mantle that differs significantly from PREM (e.g. Nettles and Dziewonski, 2008).

A brief remark on comparison of body-wave and surface-wave anisotropy is appropriate (Montagner *et al*., 2000). In the simplest case of a horizontal fast symmetry axis, upper mantle anisotropy constrained by surface-wave dispersion curves and body-wave SKS data can be explained by the same three anisotropic parameters. Although it allows for direct comparison

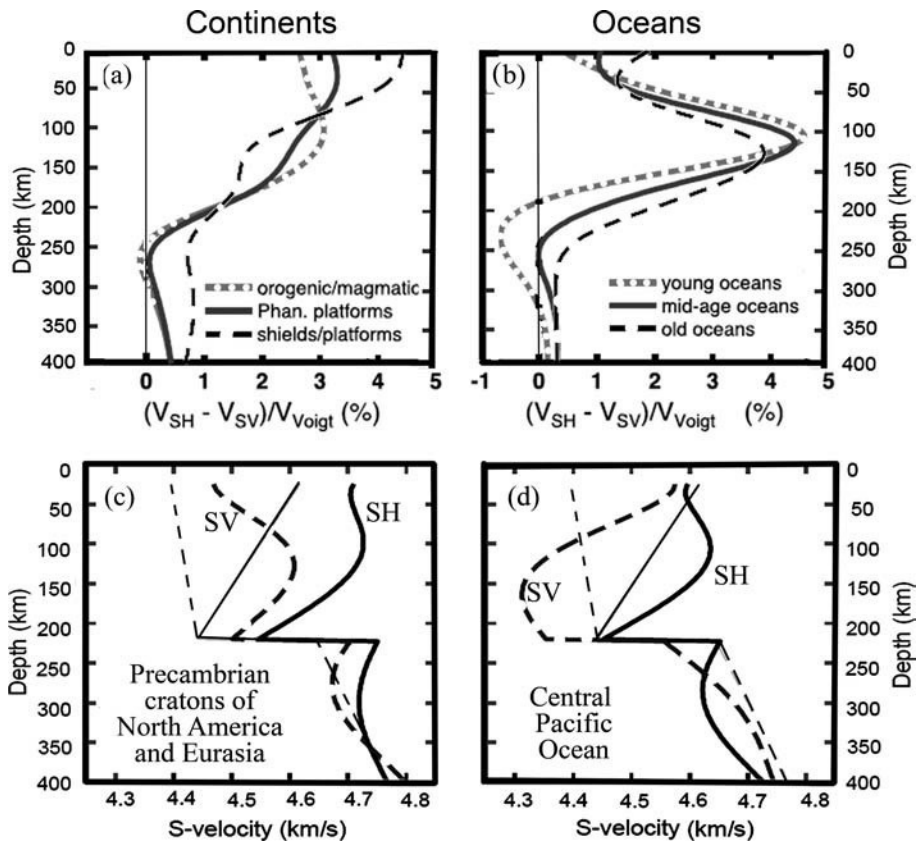

Fig. 3.116 Depth profiles showing average shear-velocity anisotropy in the upper mantle of continents and oceans constrained by surface-wave tomography (a and b – based on Nettles and Dziewonski, 2008; c and d – based on Ekström and Dziewonski, 1998). (a) and (b): Average anisotropy profiles calculated for the continental and oceanic regions (for tectonic regionalization of Jordan, 1981). (c) and (d): average velocity profiles of shear-wave velocities SH (solid lines) and SV (dashed lines) beneath the Precambrian cratons of North America and Eurasia and beneath the central part of the Pacific plate. In all other oceanic plates except the Pacific plate, the average SH and SV velocities in the upper mantle are close to that of the PREM model. Thin solid and dashed lines – SH and SV velocities in the anisotropic PREM model. The step in seismic SH and SV around 220 km depth is a consequence of the PREM reference model.

of the SKS delay time and surface-wave anisotropy tomography, large-scale comparison between the two approaches happens to be disappointing due to the limited areal coverage for both data types. In particular, surface-wave tomography is commonly used for studies of suboceanic mantle, while most SKS splitting data are available only for subcontinental mantle. However, good agreement between surface-wave and body-wave upper mantle anisotropy was found in tectonically active regions, such as the western United States and in Central Asia. Comparison of surface-wave tomography and body-wave SKS data is further complicated by different vertical and lateral resolutions of the two different data types. In a way, the two approaches are complementary since body-wave SKS data provides high lateral

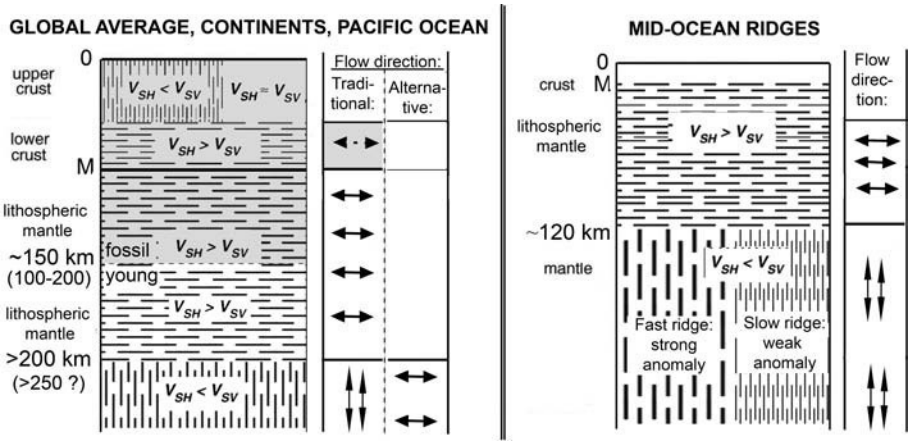

Fig. 3.117 Schematic summary of a typical depth distribution of anisotropy styles in the upper mantle. Left panel: the global average and anisotropy beneath stable continents and the Pacific Ocean. Right panel: anisotropy patterns beneath fast- and slow-spreading mid-ocean ridges.

resolution (but cannot determine the depth distribution of anisotropy), while surface-wave tomography provides constraints on the depth of anisotropy (with certain limitations, such as for example depth leakage associated with tomographic inversion, Fig. 3.80). The major results from surface-wave anisotropy studies of the upper mantle are summarized below.

Continents

Major results for shear-wave anisotropy in stable continents (Precambrian shields and platforms) include observations that polarization anisotropy extends down to at least 200 km depth. The depth extent of seismic anisotropy in the upper mantle is the subject of strong debate (e.g. Gung *et al*., 2003; Mainprice *et al*., 2005). It has some bearing on the controversy of whether mantle anisotropy is due primarily to strain at the base of the plate in the asthenosphere (Vinnik *et al*., 1995), or rather is due to remnant, orogenic events that have been frozen into the lithosphere (Silver and Chan, 1991).

Figures 3.116 and 3.117 summarize major results of surface-wave anisotropic tomography. Strong shear-wave anisotropy reported for the upper mantle down to 200–250 km depth is a robust feature revealed by all tomographic studies. Even at 250–350 km depth, surface-wave anisotropy is significantly stronger beneath the cratons than in any other regions (Fig. 3.116). Maximum anisotropy is observed in the shallow mantle and gradually decreases with depth. For shear waves horizontally propagating in this anisotropic upper mantle layer, horizontally polarized waves, SH, have faster velocities than vertically polarized waves, SV. Radial anisotropy with a vertical symmetry axis produced by horizontal shearing is a widely accepted model for these observations. Studies of mantle-xenoliths from different cratonic settings indicate that both in spinel-peridotites and garnet-peridotites deformation in olivine occurs by dislocation creep with dominant [100] slip down to a depth of at least 150 km.

Below 220–250 km the upper mantle becomes weakly anisotropic with a strong decrease in anisotropy with depth and with a change of seismic anisotropy pattern to $V_{SH} < V_{SV}$ (in particular

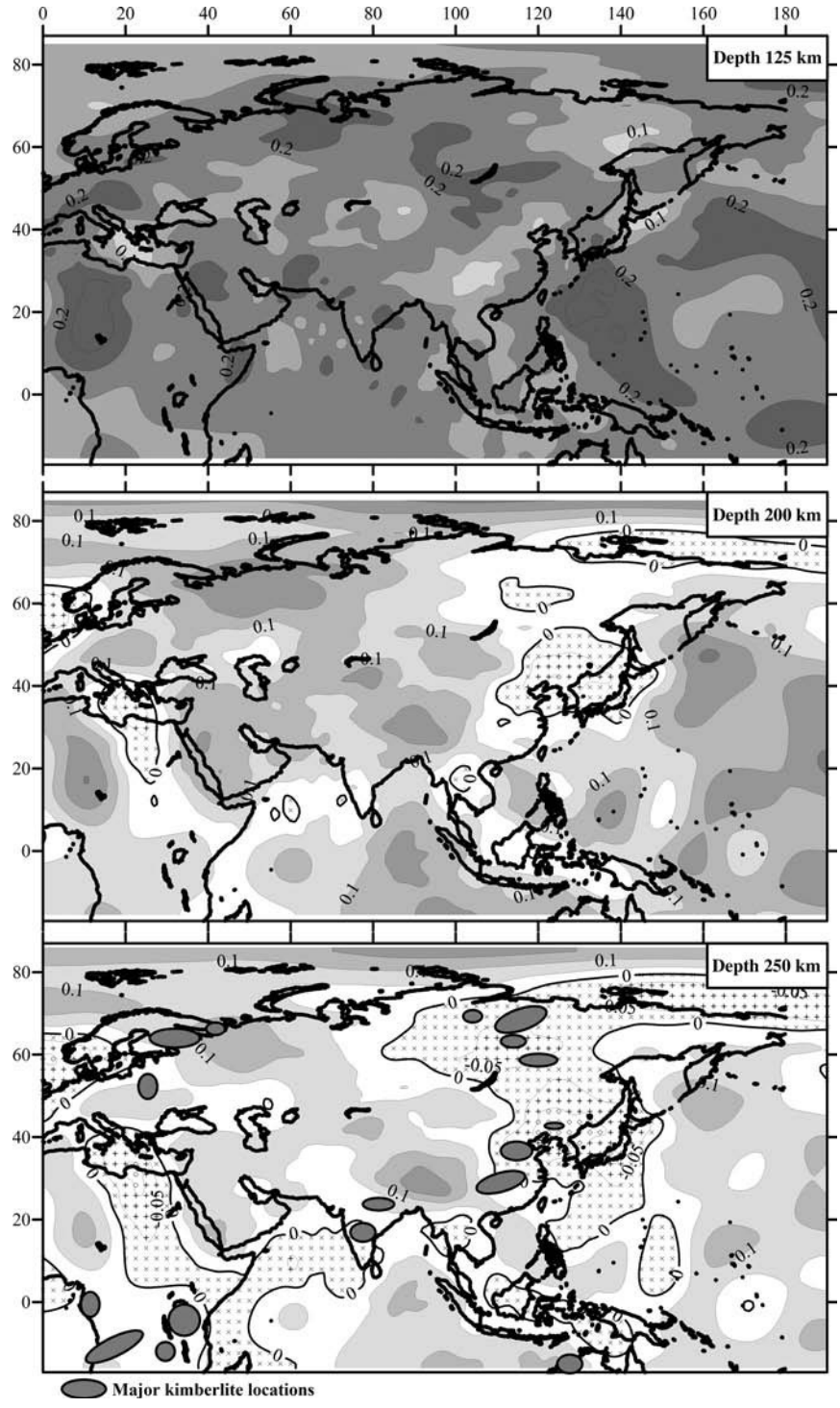

Fig. 3.118 The difference between the SH and SV velocity perturbations at 125 km, 200 km, and 250 km depth beneath Eurasia, northern Africa, and the western Pacific Ocean (based on the surface-wave tomography model of Kustowski *et al.*, 2008). Gray shading – regions where $V_{SH} > V_{SV}$; hatching – regions where $V_{SH} < V_{SV}$. Black shading on the lower map – locations of major kimberlite fields (based on the database of Faure, 2006).

beneath the Precambrian cratons and the Central Pacific Ocean). However, beneath the oceanic basins of the Pacific and Indian plates, anisotropy with $V_{SH} > V_{SV}$ may persist down to 250–300 km depth (Lévêque *et al*., 1998).

Global observations, that at *c*. 220–250 km depth the anisotropy sharply decreases and its pattern changes from $V_{SH} > V_{SV}$ to $V_{SH} < V_{SV}$, are commonly interpreted by a transition in deformation mechanism in mantle olivine from dislocation creep with dominant [100] slip to diffusion creep, and making the basis for interpretations of the origin of the Lehmann discontinuity (Fig. 3.44). Then 220–250 km depth would also correspond to the zone of mechanical decoupling between the lithosphere and the underlying mantle and can be interpreted as the base of the rheological lithosphere (Gung *et al*., 2003).

This point of view is challenged by two arguments.

(1) If the continental lithosphere were indeed confined to the upper mantle layer with $V_{SH} > V_{SV}$, the results of recent surface wave tomography would indicate a *c*. 200 km thick lithosphere beneath the major kimberlite fields of the Siberian craton (Fig. 3.118). In conflict with this conclusion, the deepest xenoliths from the lithospheric mantle beneath Siberia come from a 240-250 km depth (Griffin *et al*., 1996; Aschepkov *et al*., 2003).

(2) Recent synthetic calculations and simple-shear laboratory measurements examine deformation of olivine aggregates at high pressure (11.8 GPa) and high temperature (1380 °C) which correspond to a depth of 355 km in the mantle (Mainprice *et al*., 2005). The results indicate that dislocation creep is still possible under high P–T conditions, but with a different dominant slip: both [100] slip and [010] slip become normal to the shear plane, while [001] concentrates parallel to the shear plane and thus the [001] slip system becomes dominant. As a result, the fastest P-wave velocity is no longer parallel to the shear direction as is observed for the dominant [100] slip in the upper mantle above 220 km depth, but propagates at a high angle to the shear plane. If deformation of the upper mantle below 220 km depth still occurs by horizontal shearing, almost no azimuthal variation of P-wave velocity is expected and a vertically propagating P-wave is only slightly faster than a horizontally propagating P-wave. Similarly, the fastest shear waves are the waves polarized at a high angle to the shear plane and the largest delay times are expected for shear waves propagating at a high angle to the shear direction in the shear plane. If shear waves propagate in the shear plane, the fastest shear waves are polarized at a high angle to the shear plane. This implies that for horizontal shearing, $V_{SH} < V_{SV}$. The results also indicate that the transition from dislocation creep with the dominant [100] slip to dislocation creep with the dominant [001] slip results in a significant decrease in anisotropy to *c*. 0.9% and 1.9% for compressional and shear waves, respectively.

These results have important implications for the thickness of the rheologically strong upper mantle layer (the lithosphere):

- the upper mantle even below 220–250 km depth can be deformed by dislocation creep;
- the transition from strong to weak anisotropy at 220–250 km depth may not reflect the extent of mechanical coupling between the lithosphere and the asthenosphere, but may reflect a change in slip direction in dislocation creep;

- the upper parts of the upper mantle can be strongly coupled with the deeper mantle down to the transition zone.

In general agreement with SKS studies, shear-wave polarization anisotropy in the subcontinental upper mantle provides evidence for the existence of two (or perhaps, several) anisotropic layers with different orientations of the fast polarization axes. A surprisingly complex structure with considerable variations in radial and azimuthal anisotropy has been revealed by analysis of fundamental-mode Rayleigh and Love waves and P-waves under the SVEKALAPKO array in the Baltic Shield (e.g. Plomerová *et al*., 2005; Bruneton *et al*., 2004). Although azimuthal anisotropy down to *c*. 200–250 km depth is negligible, data on P-wave residuals indicate a complex anisotropy pattern in the area. The apparent absence of azimuthal anisotropy can result from different orientations of the olivine fast axis beneath the array. Significant azimuthal anisotropy appears below 200–250 km depth, but its direction (roughly 0–40°N) differs significantly from the present direction of absolute plate motion (55–62°N). A possible explanation of the discrepancy between the directions of the plate motion and anisotropy in the lower parts of the lithosphere is that it reflects fossil flow direction, while the short time elapsed since the change in the flow direction was not sufficient to change the olivine alignment in the case of simple shear (Kaminski, 2002).

Seismic anisotropy preserves information on multi-episodic tectonic activities in the subcontinental lithosphere, such as cratonic amalgamation and later tectonic deformations and rejuvenation. For example, a recent high-resolution seismic tomography and shear-wave splitting study of the Precambrian Canadian Shield revealed the presence of two distinct lithospheric domains with a boundary at approximately 86–87°W which corresponds to the tectonic boundary between the Wabigoon and Wawa/Quetico provinces (Frederiksen *et al*., 2007). Strong anisotropy in the lithospheric mantle is observed only to the west of this boundary, while to the east the average split times are half as long and the average velocity anomaly is smaller by 2.5%.

Regional tomographic studies in western Europe reveal the presence of paleosubduction zones in the European lithosphere associated with continental growth during the Paleozoic orogeny (Babuska *et al*., 1998). The lithosphere beneath the Armorican Massif in NW France consists of two seismologically distinct domains that have different seismic velocities and different anisotropy down to ~150 km depth. These lateral variations have been interpreted as resulting from collision-related subduction-type processes that predated the Variscan orogeny (Judenherc *et al*., 2002). In young orogens the largest difference between the SH and SV waves is observed in the upper 150 km with a maximum at *c*. 100–150 km depth (Fig. 3.116). However, since lateral resolution of teleseismic surface-wave tomographic models is low, tectonically young structures with small lateral dimensions are better resolved by body-wave SKS data.

Oceans

The oceanic upper mantle is highly anisotropic with the strongest SH–SV anisotropy at around 100–120 km depth (Fig. 3.116). The dependence of anisotropy on the age of the ocean floor is insignificant down to *c*. 150 km depth, below which the difference between SH and

SV velocities becomes age dependent with higher values for old oceans and $V_{SH} > V_{SV}$ in young oceans below 200 km depth. Below 300 km depth suboceanic upper mantle, in general, becomes isotropic. However, significant $V_{SH} < V_{SV}$ anomalies are observed beneath the Mid-Atlantic Ridge and the Red Sea down to at least 400 km depth (Zhou *et al*., 2006).

Unique upper mantle anisotropy is observed beneath the Pacific plate (Ekström and Dziewonski, 1998). In contrast to PREM and to other oceanic plates that display SH and SV close to PREM down to 400 km, the Pacific Ocean displays anomalous anisotropy in the upper mantle. Above the 220 km discontinuity it does not show a smooth decrease with depth: polarization anisotropy is small in the shallow mantle and increases with depth down to 150–180 km where maximum anisotropy is confined to a relatively narrow layer (Fig. 3.99). Significant anisotropy is also observed at 250–350 km depth.

The most anomalous mantle is beneath the Central Pacific plate around the East Pacific Rise, where strong anomalous (as compared to PREM) anisotropy extends from *c*. 50 km (where SH and SV velocities are very close) to 220 km depth. The maximum difference between SH and SV velocities (*c*. +5%) is in the upper mantle southwest of Hawaii. Large geographical variations in upper mantle anisotropy beneath the Pacific plate are not correlated with ocean floor age; however the isotropic part calculated from SH and SV velocities displays a clear correlation with age (except for very low velocities beneath the Pacific Superswell). A possible explanation for the unique anisotropy of the Pacific mantle includes strong olivine alignment by small-scale convection flow (Ekström and Dziewonski, 1998).

A recent finite-frequency surface-wave tomography study of global shear-wave velocity structure and radial anisotropy in the upper mantle with a high resolution of small-scale mantle heterogeneities reveals a peculiar pattern of anisotropy beneath the spreading centers (Zhou *et al*., 2006). Significant $V_{SH} < V_{SV}$ anomalies are observed beneath mid-ocean ridges at depths greater than 120 km with distinctly different patterns beneath slow- and fast-spreading ridges (Fig. 3.117). Polarization anisotropy beneath fast-spreading ridges is stronger, but rapidly decreases below 250 km depth, while beneath slow-spreading centers (the northern Mid-Atlantic Ridge, the Red Sea), weak anisotropy extends down to at least the top of the transition zone. This observation implies that the primary driving force of seafloor spreading may be different beneath fast- and slow-spreading ridges.

3.6.5 Lithosphere thickness from elastic tomography

Definitions and uncertainties

The base of the lithosphere is a diffuse boundary that stretches over a particular depth interval and thus any practical definition of its base is somewhat arbitrary (see also Section 3.3.2). The seismic lithosphere (or the lid) is defined as the layer above a rheologically weak zone caused by high temperatures and/or partial melting and in tomographic studies its base is defined as:

(1) the bottom of the seismic high-velocity region on the top of the mantle that generally overlies a low-velocity zone;
(2) a depth where the mantle anisotropy pattern changes from frozen-in anisotropy in the lithosphere to anisotropy in the asthenosphere caused by plate motion and mantle flow.

The first definition of the lithosphere as the lid above a LVZ is based on the common assumption that the LVZ corresponds to the asthenosphere where partial melting occurs. However, a LVZ can be solid state associated with mineralogy, and thus the top of a LVZ may not necessarily be associated with the lithosphere–asthenosphere boundary (see discussion for Fig. 3.130).

In practice, the first approach is used when the velocity structure of the upper mantle is known, so that the base of the lithosphere is defined either by the zone of high velocity gradient in the upper mantle or by the bottom of the layer with positive velocity anomalies that should correspond to the transition from a high-velocity lithosphere to LVZ. Use of velocity gradients in the mantle for defining the lithospheric base is hampered by a wide use of reference models in tomographic studies; in particular continental models based on PREM inherit a velocity gradient at around 220 km depth, not necessarily required by the data. Furthermore, absolute velocities may not always preserve a gradient zone in the upper mantle seen in relative velocity perturbations (e.g. Fig. 3.85).

The base of the lithosphere is not marked by a sharp change in temperature or in composition, and thus it is not marked by a sharp change in seismic velocities. Since the lithospheric base has a diffuse character with a transition zone where seismic velocities gradually decrease from lithospheric to asthenospheric values, the lithospheric thickness depends significantly on the amount of velocity perturbation chosen to define the lithospheric base. Commonly the base of the seismic lithosphere is determined as the bottom of the layer where positive velocity anomalies drop below +1% or +2% with respect to a reference model. The difference in lithospheric thickness estimates based on a +1% or a +2% velocity anomaly may be significant. For example, the tomographic cross-section for Africa (Fig. 3.90) illustrates that the lithosphere thickness beneath West Africa is *c*. 200 km if defined by a +2% velocity anomaly, but may extend down to *c*. 400 km depth if defined by a +1% velocity anomaly.

Further problems arise when comparing results of different studies, since there may be a significant difference between reference models, so that the same relative velocity perturbation corresponds to different absolute velocities. While PREM is a widely used reference model for global studies and for the oceanic regions, *ak135* or similar reference models (e.g. *iasp91*) are more suitable for studies of the continents.

Another problem is related to the amplitude of velocity perturbations (used to define the lithospheric base) which depends on the regularization used in tomographic inversion to stabilize the inverse problem (in particular, in poorly constrained regions) (see Section 3.2.3). In particular, damping permits rough models with large velocity perturbations, while roughness control (i.e. the absence of strong contrasts in adjacent blocks) results in models with smoothly varying heterogeneity. Combined with an arbitrary chosen (say, +1% or +2%) velocity perturbation defining the lithospheric base, ambiguity in lithosphere thickness determinations can hardly be assessed.

Depth resolution of tomographic models puts additional limitations on thickness constraints, and in many inversions the details of the velocity structure cannot reliably be resolved (Fig. 3.119). The near-vertical propagation of body waves in the upper mantle limits their vertical resolution obtained in tomographic studies to 50–100 km. Resolution of surface-wave tomographic models that use only fundamental modes rapidly decreases with

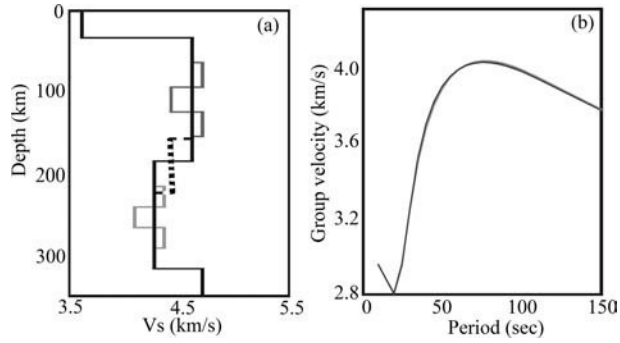

Fig. 3.119 Inversion tests for surface-wave tomography showing: (a) velocity profiles and (b) dispersion curves for tests of velocity variability with depth (gray lines) and of LAB discontinuity sharpness (dotted line). Note that neither velocity variations in the upper mantle nor variations in lithosphere thickness can be distinguished in dispersion curves from the initial velocity profile (black solid line in (a)) (after Pasyanos, 2009).

depth, and models based on Rayleigh waves at 40–60 s cannot resolve mantle structure below *c*. 200 km depth (Fig. 3.79). Furthermore, resolution kernels indicate that tomographic inversions provide velocity structure averaged over a significant depth interval in the upper mantle (Fig. 3.81). The worst resolved is the depth between 300 and 400 km. Depth leakage of velocity anomalies, an inevitable consequence of inversion, further complicates estimates of lithosphere thickness (Fig. 3.80).

Finally, uneven ray path coverage may further bias results of tomographic inversions (Fig. 3.83). This problem is particularly important at the transitions between structures with a high contrast in mantle velocities and lithospheric thickness (such as the ocean–continent transition).

Global patterns

With all of the uncertainties in defining the thickness of the seismic lithosphere, any reported absolute numbers should be treated with caution, while a comparative analysis of different tectonic regions is more helpful in recognizing robust global patterns. Figure 3.120 shows the thickness of seismic lithosphere defined by a +1% and +2% shear-wave velocity perturbations with respect to the reference models derived from a global body-wave tomography model (Grand, 1997, 2002) and a global surface-wave tomography model (Shapiro and Ritzwoller, 2002). Since the maps are smoothed by interpolation, the lithosphere thickness appears underestimated for deeply extending continental roots and overestimated for regions with thin lithosphere. In spite of different vertical and lateral resolution of the two tomographic models, they are consistent in depicting general patterns in lithosphere thickness variations.

In the oceanic regions seismic lithosphere is typically thinner than 100 km. According to surface-wave models, the lithospheric thickness shows a pronounced correlation with the age of the ocean floor and increases from near-zero values in spreading centers to *c*. 80 km in old oceans (Fig. 3.121). The pattern is not observed in body-wave models, perhaps due to lack of vertical resolution and geographical limitations.

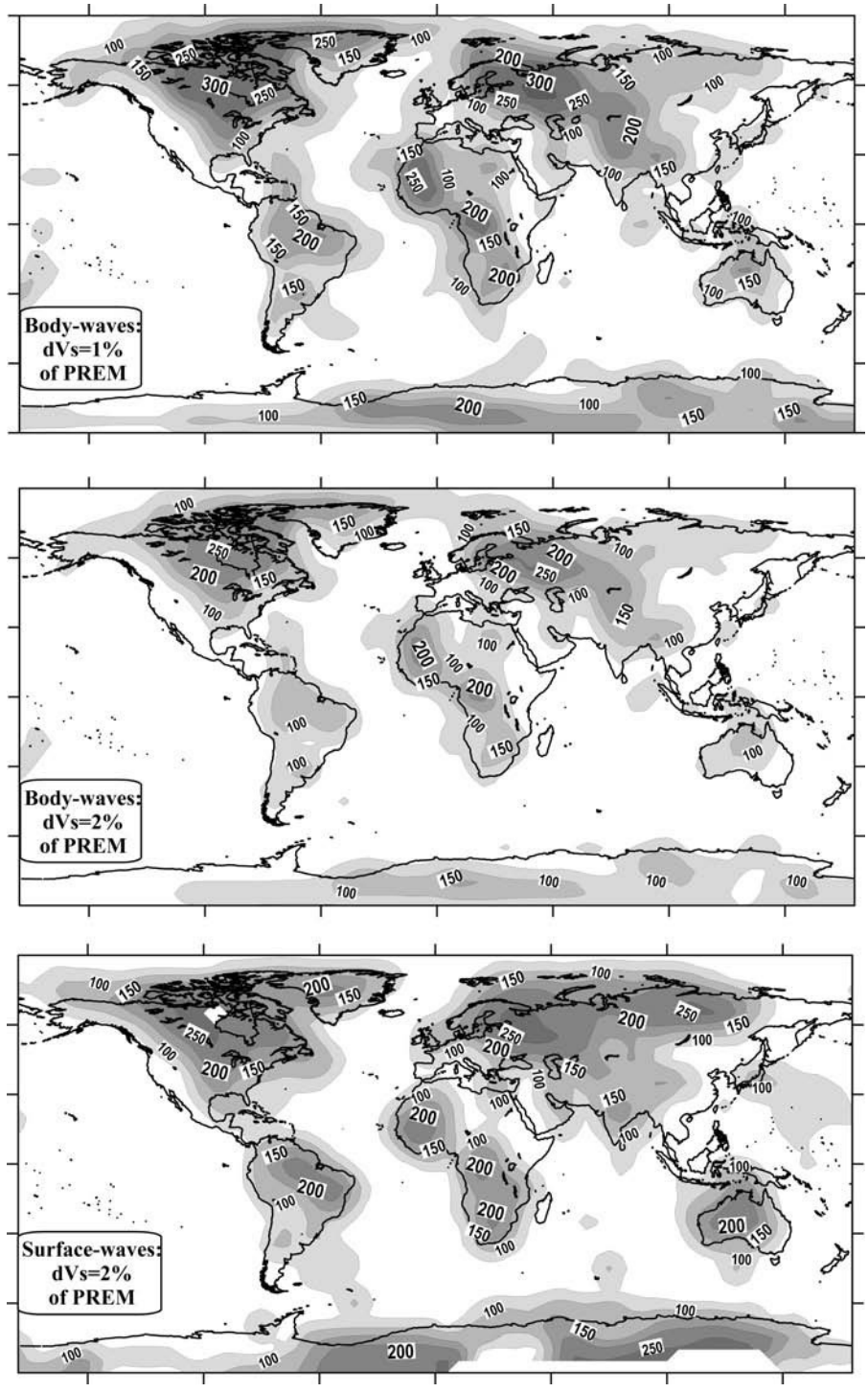

Fig. 3.120 Thickness of seismic lithosphere based on a global body-wave tomography model (Grand, 1997, 2002) and a global surface-wave tomography model (Shapiro and Ritzwoller, 2002). The base of the lithosphere is defined by a 1% (upper map) and 2% (middle and lower maps) shear-wave velocity perturbation with respect to the reference model (PREM for the upper and middle maps and *ak135* for the lower map). The maps are smoothed by a Gaussian filter. As a result, the thickness is underestimated for deeply extending continental roots and overestimated for regions with thin lithosphere. In most of the oceans, seismic lithosphere is thinner than 100 km. In stable continents, lithosphere thickness may exceed 300 km.

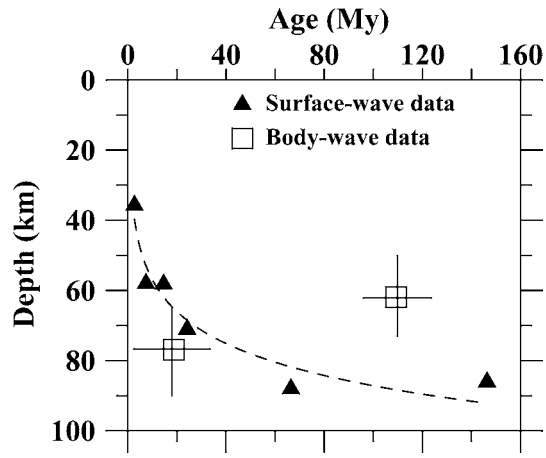

Fig. 3.121 Thickness of the oceanic lithosphere versus age of the ocean floor (data of Forsyth, 1975; Revenaugh and Jordan, 1991; Gaherty *et al*., 1996) (based on Karato, 2003b).

Below the continents, lithosphere thickness is correlated with surface tectonics and crustal ages (compare with Fig. 2.16). However because of significant variations in velocity structure in tectonic provinces of any age, the age dependence is much less pronounced than for the suboceanic lithosphere. In general, thick lithosphere is observed in old continents and thin lithosphere in tectonically young structures (except for zones of continent–continent or continent–ocean collision where subducting lithosphere slabs can be traced deep into the mantle). The deepest lithospheric roots are clearly associated with the cratons.

The depth extent of the cratons as constrained by tomographic models is a subject of ongoing debate (Fig. 3.122). An analysis by Polet and Anderson (1995) shows that the depth extent of continental lithospheric roots is strongly age dependent. If the lithospheric base is defined by a +1% *V*s anomaly, the Archean and Paleoproterozoic cratons typically have lithospheric roots that are 240–280 km thick, whereas the lithosphere beneath Meso-Neoproterozoic terranes is only about 150 km thick (for a +0.5% *V*s anomaly the lithosphere is about 60 km thicker). Furthermore, cratons of the same age have a different depth extent of the lithospheric roots. In particular, seismic tomography models indicate that Archean–Paleoproterozoic cratons that have undergone Phanerozoic reworking (e.g. the Sino-Korean craton) have lost deep lithospheric roots.

Depth variations in seismic anisotropy have been proposed to define the lithospheric thickness (Babuska *et al*., 1998). In this approach the lithosphere–asthenosphere boundary (LAB) is considered to be the transition from 'frozen-in' anisotropy in the lithosphere to mantle flow-related anisotropy in the asthenosphere. Since these two anisotropic zones may have different alignment of mantle olivine, the depth where a change in the direction of anisotropy occurs can be interpreted as the LAB. Based on this definition, the lithospheric thickness is estimated to be *c*. 350 km beneath the Superior province in the Canadian Shield and the Siberian craton, and *c*. 220–250 km beneath the Baltic Shield and the Hudson Bay in Canada. This approach is complicated by recent studies that indicate that many cratons may have (at least) a two-layer anisotropy with significantly different orientations of the fast axis.

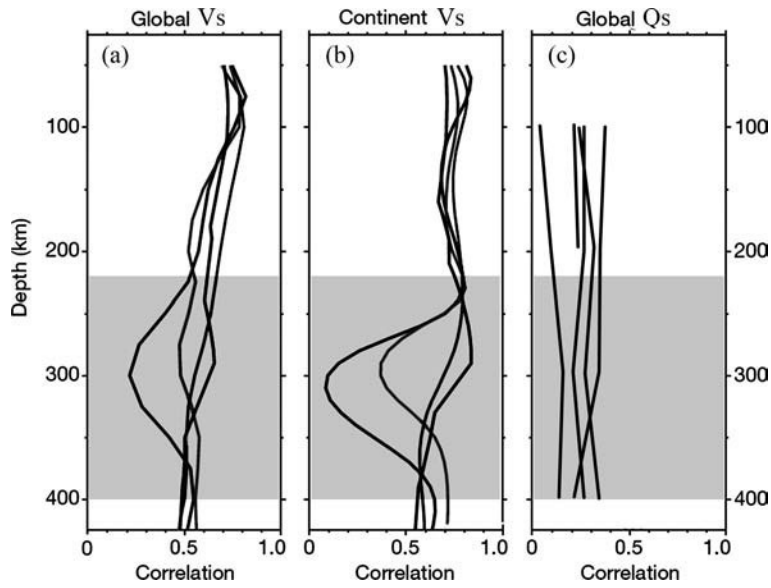

Fig. 3.122 Correlation coefficient as a function of depth between five global tomographic shear velocity (a and b) and shear attenuation (c) models (after Gung *et al*., 2003; Dalton *et al*., 2008). For S-velocity models correlation is computed between an SH model SAW24B16 and models S20A_SH9 (an SH model), SB4L186 (a hybrid model), S20A_SV9 and S20RTS7 (both are SV models) (a) over the whole globe and (b) over the continental areas only (defined as all areas of elevation >−500 m to include the shelves). Note that in the continental regions correlation between SH/hybrid models and SV models is strongly reduced below 250 km depth. For shear attenuation models correlation (c) is computed between model QRLW8 and models WS02, MQCOMB, SW02, QR19, and QRFSI12. Correlation between all global shear attenuation models is weak.

Surface-wave tomographic models are being widely used to assess depth variations in SV and SH waves (e.g. Gung *et al*., 2003). As discussed in the previous section, the depth extent of the cratonic roots as constrained by polarization anisotropy is strongly debated. Most tomographic models observe strong anisotropy only down to a 200–250 km depth and the change from $V_{SH} > V_{SV}$ to $V_{SH} < V_{SV}$ at the same depth. This change in anisotropy pattern is commonly interpreted as the transition from dislocation to diffusion creep. If this is correct, the upper part of the mantle becomes mechanically decoupled below this depth from the deeper mantle, and the depth of 200–250 km corresponds to the base of the lithosphere. As discussed in detail in Section 3.6.4, this conclusion is non-unique and is questioned by laboratory studies on olivine deformation at P–T conditions which correspond to a 300–350 km depth (Mainprice *et al*., 2005). Experimental results suggest that the change from $V_{SH} > V_{SV}$ to $V_{SH} < V_{SV}$ does not necessarily imply mechanical decoupling of the layers, which can remain coupled down to the transition zone. Thus, the question of whether the change in anisotropy at 200–250 depth beneath the continents may be interpreted as the lithospheric base, remains open.

3.6.6 Anelastic tomography

General remarks

Studies of seismic attenuation in the Earth's mantle began in the 1960s (Anderson and Archambeau, 1964; Ben-Menahem, 1965; Anderson *et al*., 1965); but global tomographic models of seismic attenuation have only been calculated recently (Romanowicz, 1994, 1995; Bhattacharyya *et al.*, 1996; Durek and Ekström, 1996; Reid *et al.*, 2001; Selby and Woodhouse, 2002; Dalton *et al*., 2008). A significant number of papers have focused on regional studies, in particular for the oceans. These papers as well as the review papers of Mitchell (1995) and Romanowicz and Durek (2000) provide a comprehensive overview of attenuation studies of the crust and the upper mantle.

Seismic waves attenuate with travelled distance faster than predicted by geometrical spreading of wave fronts. This energy loss is caused by anelastic processes (internal friction, or intrinsic attenuation). Anelasticity is generally quantified in seismology by the quality factors, Q_p and Q_s, for compressional and shear waves, respectively. The loss of seismic energy during wave propagation is quantified by the inverse quality factor, or internal friction. Scattering attenuation (caused by scattering off small-scale heterogeneities, focusing/defocusing, refraction and reflection) also reduces the amplitude of seismic waves, but does not change the integrated energy in the total wavefield.

Laboratory studies indicate that seismic attenuation is sensitive to seismic frequency, temperature, and grain size (see Section 3.1). The strong temperature dependence of attenuation (eq. 3.9–3.10) is of fundamental interest for geophysics since it provides higher sensitivity of anelastic tomography to elevated temperatures and melts than elastic tomography. Tomographic inversions based on surface waves provide values of seismic Q_s that can be converted into Q_p (Anderson *et al.*, 1965):

$$Q_p^{-1} = 4/3\, V_s^2/V_p^2 Q_s^{-1}. \tag{3.17}$$

For the upper mantle velocities and at near-solidus temperatures $Q_p = 2.25\ Q_s$. In shallow low-temperature mantle, however, thermo-elastic mechanisms of attenuation lead to $Q_p \sim Q_s$ (Frankel, 1982). In the globally spherical PREM model the radial average Q_s has a value of 600 at depths between 40 km and 80 km and of 80 between 80 km and 220 km depth.

Anelastic tomography suffers from the same limitations and uncertainties as elastic tomography (see Section 3.6.1). Additional uncertainties are caused by scattering attenuation, since commonly the effects of intrinsic and scattering attenuation are difficult to separate. On the whole, the amplitudes of surface wave attenuation depend on:

(1) the intrinsic attenuation along the ray path,
(2) elastic focusing/defocusing effects along the ray path (Selby and Woodhouse, 2002),
(3) uncertainties in the strength of excitation at the source,
(4) uncertainties in the response at the station (e.g. Dalton *et al*., 2008), and
(5) the damping used in the inversion.

Simultaneous inversion of amplitude data for models of attenuation and seismic velocities facilitates separation of focusing effects on amplitude anomalies and thus improves amplitude resolution of anelastic models. Similarly to elastic tomography, crustal corrections have a strong effect on the amplitude of attenuation, in particular in shallow mantle.

Correlations with surface tectonics

Global and regional models of attenuation in the crust and upper mantle differ significantly, in particular in amplitude (Fig. 3.122). However, a large span of calculated attenuation values (>2 orders of magnitude) allows for meaningful comparison of different models and recognition of global and regional trends despite large uncertainties in attenuation amplitudes.

Similarly to elastic tomography, upper mantle seismic attenuation exhibits a strong correlation with surface tectonics (Fig. 3.123). Stable continents have high Q values (low attenuation) down to at least around 150 km depth. Apparent exceptions include cratons of South Africa, South America, India, and China. However, attenuation anomalies beneath these cratons may not be resolved due to their small lateral sizes: lateral resolution of global tomographic models is limited by spherical harmonic representation; most of the models are constrained in degrees up to 8–12 which corresponds to *c*. 3000–5000 km and, at present, is lower than the lateral resolution of modern elastic tomography models. A recent attenuation model QRFSI12 constrained up to degree 12 by fundamental mode Rayleigh waves at periods between 50 and 250 s (Dalton *et al*., 2008) shows a similar pattern and displays low attenuation beneath the stable continental interiors of Europe, Siberia, North America, Greenland, Australia, west-central Africa, and Antarctica down to at least 200–250 km depth with a possible weaker continuation of high-Q anomalies down to 300–400 km depths. Since some smearing of the signal may occur below 200–250 km depth (e.g. Fig. 3.79), the model cannot resolve if the correlation between attenuation and surface tectonics is restricted to the upper 200–250 km (Fig. 3.124).

Low attenuation is found beneath Tibet–Himalayas, in particular at *c*. 100–150 km depth (Bhattacharyya *et al*., 1996). Phanerozoic platforms such as western Europe and West Siberia and tectonically active continents such as western North America have a higher upper mantle attenuation than cratonic upper mantle. A recent study of the coda of Lg waves in Eurasia (Mitchell *et al*., 2008) further supports the conclusion that upper mantle attenuation structure is strongly correlated with surface tectonics and that the Q value is proportional to the tectono-thermal age (i.e. the time since the most recent episode of major tectonic or orogenic activity).

The strongest attenuation is observed beneath young oceans that have high attenuation through the entire period range (Mitchell, 1995). "Normal" oceanic regions display a correlation between the age of the ocean floor and attenuation in the upper mantle. Strong attenuation anomalies are associated with the East Pacific Rise, Mid-Atlantic Ridge, and other ridge systems down to 150–200 km and perhaps deeper. For example, a regional shear-wave study displays high attenuation in the Pacific Ocean down to 100–150 km depth

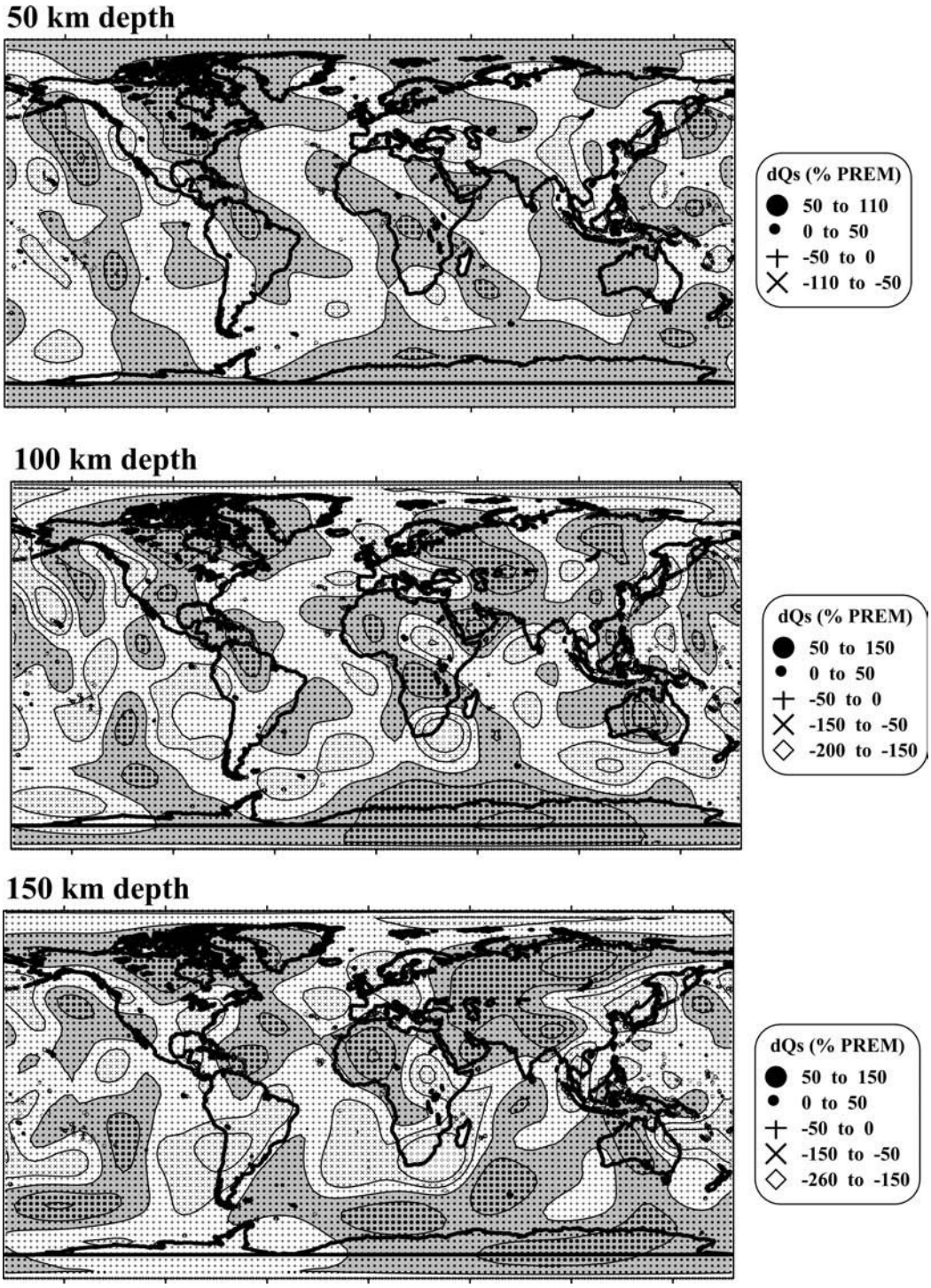

Fig. 3.123 Inverse shear attenuation in the upper mantle (as percent of the PREM value) (based on the tomography model of Billien *et al*., 2000). The anelastic tomography model is calculated from fundamental-mode Rayleigh waves at periods between 40 and 150 sec and includes both anelastic and scattering effects (the effect of focusing due to velocity heterogeneities has been accounted for). The model is represented by spherical harmonics up to degree 12. Gray shading – positive anomalies.

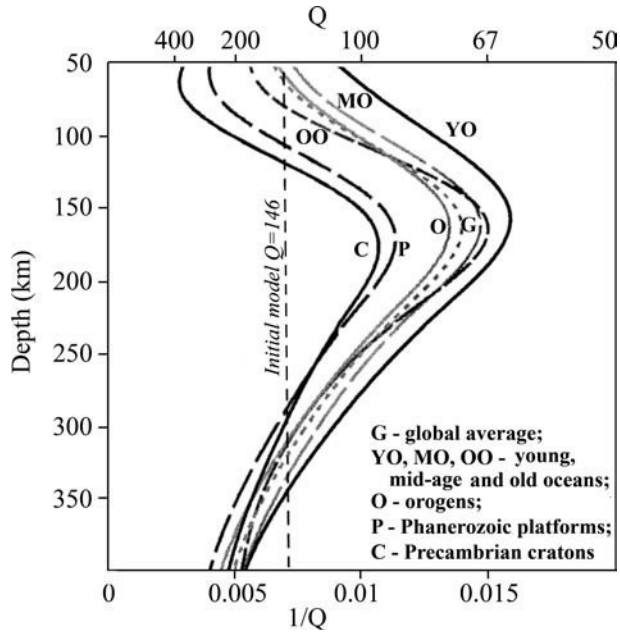

Fig. 3.124 Regionally averaged shear attenuation profiles for six tectonic provinces and the global average (short dashes) based on surface-wave global tomographic modeling (the reference model has constant $Qs = 146$ throughout the mantle) (based on Dalton *et al.,* 2008).

(Fig. 3.125). However, Q anomalies beneath the Pacific Ocean display a highly asymmetric pattern which becomes more pronounced at 300–450 km depth (Fig. 3.126). Joint interpretations of attenuation and shear velocity models for the Pacific Ocean indicate that melt may be present at 25–100 km depth beneath the MELT (the Mantle Electromagnetic and Tomography) seismic array (age of ocean floor *c*. 2 My) and at 40–100 km depth beneath the GLIMPSE area about 400 km away from the East Pacific Rise.

Correlations with temperature and surface heat flow

Strong, Arrhenius-type, exponential dependence of attenuation on temperature as indicated by laboratory measurements (e.g. Berckhemer *et al*., 1982; Kampfmann and Berckhemer, 1985; Sato *et al*., 1989; Gribb and Cooper, 1998; Jackson, 2002) implies that regions of high attenuation in the mantle should be correlated with high mantle temperatures. The temperature dependence of seismic attenuation has been used in a number of studies to calculate mantle geotherms from seismic attenuation (e.g., Kampfmann and Berckhemer, 1985; Sato *et al*., 1988; Sato and Sacks, 1989).

A global analysis indicates that in the upper 250 km, attenuation anomalies calculated from the amplitudes of low-frequency Rayleigh waves on a $10° \times 10°$ grid (the QR19 model) are, to some extent, correlated with surface heat flow (the correlation coefficient r is 0.20–0.35 with the correlation peak at $z \sim 200$ km). Deeper in the mantle (below the

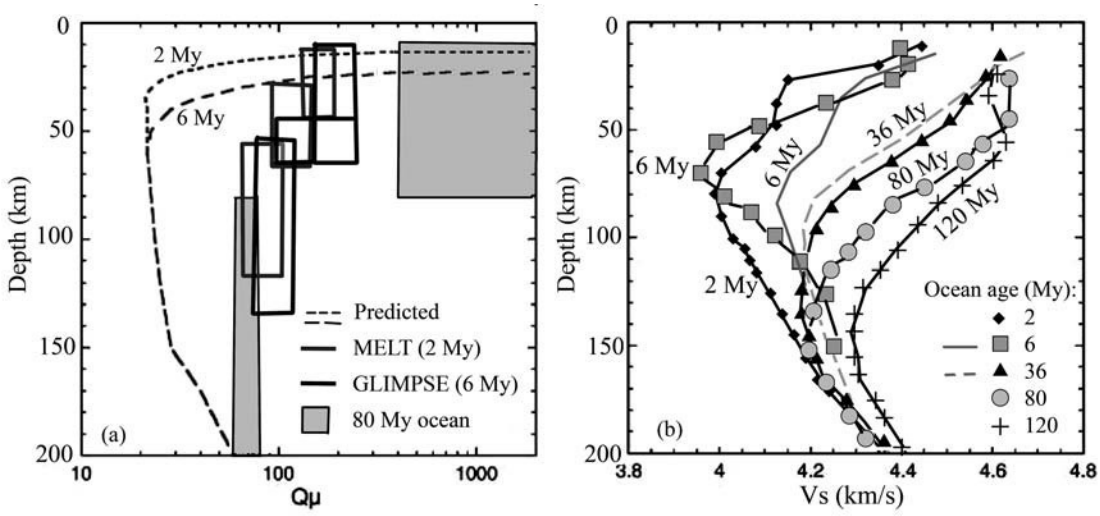

Fig. 3.125 Quality factor (a) and shear velocity (b) as a function of depth and age of seafloor in the Pacific Ocean (based on Yang *et al*., 2007). (a) Quality factor: empty boxes show range of acceptable quality factor based on MELT and GLIMPSE seismic arrays which have resolution down to 100 km and 150 km depth, respectively. Gray boxes – average oceanic values; dashed lines – theoretical predictions for a simple half-space cooling model based on the data of Faul and Jackson (2005). (b) SV component of shear velocities: different symbols refer to ocean floor with different ages (tomographic model of Nishimura and Forsyth, 1989). Gray lines – theoretical predictions for a simple half-space cooling model. The difference between observed and predicted values at 50–80 km depth beneath a young ocean is attributed to the presence of melts.

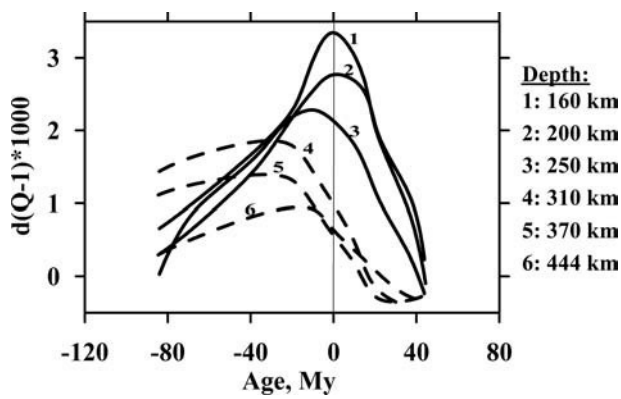

Fig. 3.126 Dependence of the *Q* anomaly (degree-6 model QR19) on seafloor age in the southern Pacific Ocean (based on Romanowicz, 1998) at six different depths: 160–250 km (solid lines) and 310–444 km (dashed lines). Note that the symmetry around the ridge is broken at any depth, and in particular in the deeper depth range.

transition zone) *Q*-anomalies are better correlated with hotspot distribution ($r \sim 0.35$–0.38) (Fig. 3.127). This conclusion is supported by global anelastic models which display low seismic attenuation in the upper mantle beneath stable continents where mantle temperatures are low (e.g. Romanowicz, 1994, 1995; Bhattacharyya *et al*., 1996). Regional seismic

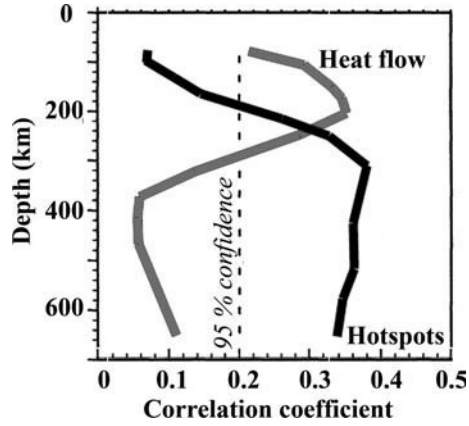

Fig. 3.127 Global correlations of shear attenuation model QR19 (up to degree 6 spherical harmonics) with surface heat flow and hotspot distribution (after Romanowicz, 1995).

studies of shear-wave attenuation also reveal a qualitative correlation between regional attenuation anomalies in the crust and upper mantle and tectonic provinces, thus supporting the idea of the thermal origin of most of the upper mantle Q_s anomalies (e.g., Canas and Mitchell, 1978; Durek and Ekström, 1996; Sarker and Abers, 1998, Selby and Woodhouse, 2002; Mitchell *et al*., 2008).

Note that relatively high global correlations are based mostly on high attenuation anomalies documented for oceanic regions such as mid-ocean ridges (Fig. 3.127). Although an essential part of attenuation anomalies in the oceanic upper mantle can be explained by temperature variations, seismic studies of the North Atlantic and western Pacific subduction zones (Nakanishi, 1978; Sheehan and Solomon, 1992; Tsumura *et al*., 2000) suggest that partial melting is important in producing high attenuation anomalies.

Statistical analysis shows that, globally on the continents, correlation between quality factor Q_s and upper mantle temperature is significantly weaker than one might expect from laboratory experiments (Fig. 3.128). Although a weak correlation between quality factor and temperature can, in part, result from different lateral and vertical resolutions of seismic and thermal models, non-thermal effects, such as compositional variations and the presence of fluids and melts, play an important role in producing attenuation anomalies in the upper mantle (Artemieva *et al*., 2004). Studies of the Lg coda wave attenuation for Eurasia confirm this conclusion: while most attenuation anomalies are apparently related to the tectonic history of the Eurasian crust, attenuation in Eurasia is most easily explained by fluid flow or by scattering from fluid-enhanced zones that may be associated with past subduction zones (Mitchell *et al*., 2008).

Correlations with seismic velocities

Correlation between seismic elastic and anelastic properties has been examined in a number of seismic and laboratory studies. Both global and regional anelastic tomography models for the oceans indicate that anomalies of seismic velocity and attenuation are correlated in the

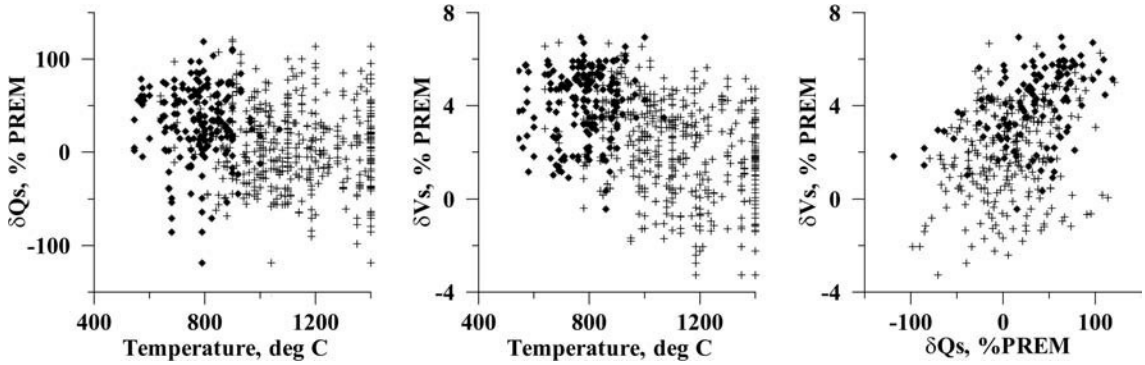

Fig. 3.128 Correlation between inverse shear attenuation, shear velocity, and temperature at 100 km depth beneath continents (from Artemieva *et al.*, 2004). Note that attenuation and velocity were constrained by the same tomographic inversion (Billien *et al.*, 2000). Crosses – all continents; dots – cratonic regions only.

upper mantle, at least qualitatively (Romanowicz, 1995; Romanowicz & Durek, 2000; Sheehan & Solomon, 1992; Roth *et al*, 2000; Tsumura *et al*, 2000; Dalton *et al*., 2008). A quantitative correlation is significantly hampered:

(1) by significantly different sensitivities of seismic attenuation and velocity to temperature (exponential and linear, respectively, Fig. 3.3), and
(2) by large uncertainties in amplitudes of attenuation anomalies resulting in a low global correlation (Fig. 3.128).

An attempt to quantitatively relate attenuation and velocity anomalies has been made for the Fiji–Tonga region (Roth *et al*., 2000). The assumption behind the study was that both anomalies have a similar thermal origin. Theoretical calculations aimed to match seismic observations indicate that, at depths greater than 100 km, velocity and attenuation anomalies are strongly correlated and can be fit by an exponential equation, while at shallower depths seismic data show a high degree of scattering (Fig. 3.129). Analyses of the correlation between attenuation and shear-wave velocity anomalies globally and for the continents further indicate that the strong correlation between Qs and Vs observed in the Fiji–Tonga subduction zone is more a regional phenomenon than a general rule (Roth *et al*., 2000). Comparison of seismic velocities and seismic attenuation with theoretical predictions based on laboratory measurements of the temperature sensitivity of attenuation and velocity (Faul and Jackson, 2005) indicate that temperature variations alone can only explain about half of the observed global variations in velocity and attenuation in the continental regions (Artemieva *et al*., 2004). Similar global analysis suggests that the observed velocity–attenuation relationship agrees with the predicted values (calculated from temperatures) in the upper 100–150 km of the oceanic regions, while beneath the cratonic regions seismic data deviate from theoretical predictions down to 250 km depth (recall limitations on resolution) that may represent the base of a chemical boundary layer (Dalton *et al*., 2008).

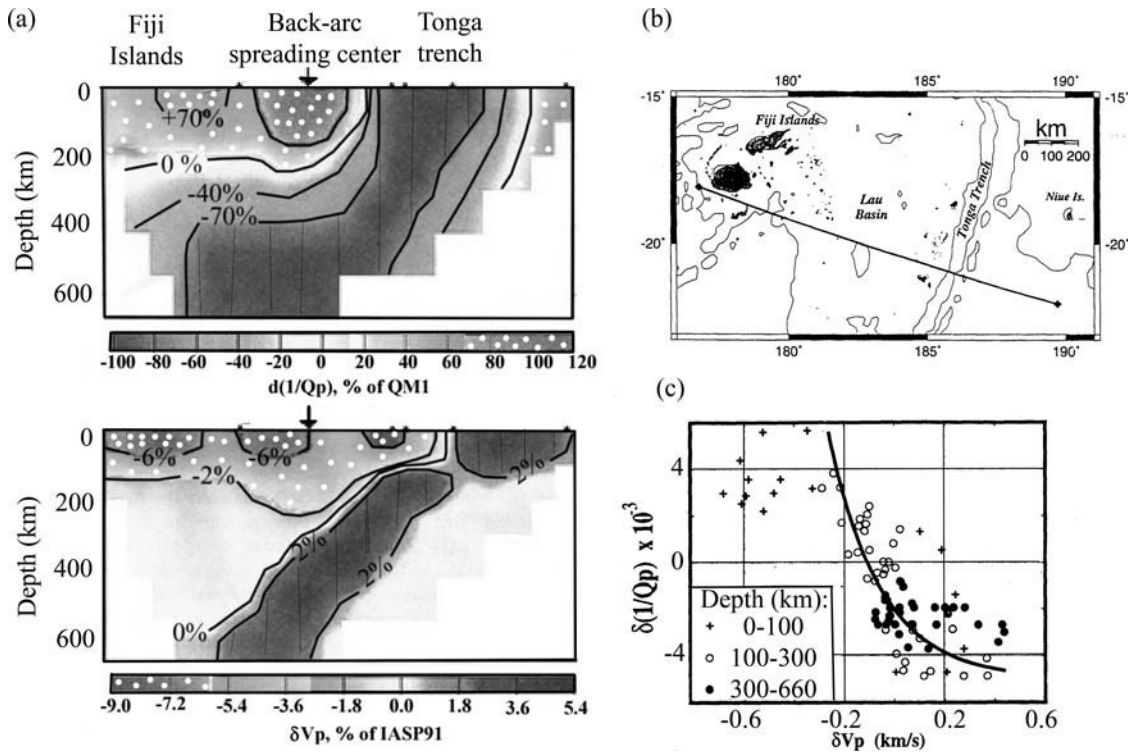

Fig. 3.129 Seismic structure through the Tonga–Fiji subduction zone (from Roth *et al.*, 2000). (a) 2D cross-sections of P-wave attenuation (upper) and velocity (lower) anomalies as percent difference between the tomographic and reference models. (b) Location of the profile; thin lines – bathymetry contours. (c) Correlation between attenuation and velocity anomalies at different depths. Solid line – the best exponential fit through all data.

3.7 Seismic lithosphere: summary

Factors affecting seismic velocities and attenuation

Seismic velocities and attenuation in the lithosphere are primarily controlled by temperature variations and the presence of (even small quantities of) melt or fluids (Section 3.1). Variations in pressure, composition, and grain size have further effects on both velocity and attenuation. Porosity may have a strong effect on seismic velocities in the shallow crust, while anisotropy is important through the entire lithosphere.

Temperature effects on velocities and attenuation are different and complicate a direct comparison of elastic and anelastic seismic tomography models, in particular at high temperatures: while velocities display a linear dependence on temperature, attenuation follows an exponential law (Fig. 3.3).

Seismic velocities and attenuation depend on frequency and thus laboratory studies performed at ultrasonic frequencies should not necessarily be applicable to data obtained at seismic frequencies (Section 3.1).

Resolution problems

Resolution of seismic studies has both theoretical and practical limitations. The size of the Fresnel zone (eq. 3.14) puts theoretical limits on the resolution of seismic methods based on transmitted waves (refraction seismology, travel time tomography, surface-wave dispersion analysis), so that higher frequency waves provide higher resolution. However, lower frequency waves penetrate deeper into the Earth. Practical limitations on resolution also depend on the method employed. In the receiver-function method there is an inevitable trade-off in resolving both the velocity structure and depths to seismic converters (Section 3.4.1; Fig. 3.49).

Surface-wave tomographic models have better vertical resolution, but poorer lateral resolution than teleseismic body-wave tomographic models (Section 3.6.1). However, surface-wave tomography based on fundamental modes commonly cannot resolve structure deeper than 200–300 km where it loses resolution (Fig. 3.79). Sensitivity kernels provide a measure for both lateral and vertical resolution of tomographic models (Fig. 3.81). In large-scale tomographic models, vertical resolution is not better than 50 km (i.e. results displayed for, for example, 150 km depth refer to the depth layer between 125 km and 175 km); moreover, any tomographic inversion inevitably results in depth leakage (Fig. 3.80).

The amplitudes of velocity anomalies depend on the regularization method used in tomographic modeling (Section 3.2.3), which results in a relatively low quantitative correlation between different models (Fig. 3.122). Crustal corrections (in particular corrections for the effects of sediments and ice) have an important effect on the amplitudes of both surface-wave and body-wave tomographic models (Section 3.6.1).

Reference models used in seismic inversion have a strong effect on seismic models. In particular, continental models based on PREM commonly inherit a velocity step at around 220 km depth, not necessarily required by the seismic data. A seismic model presented in absolute and in relative velocities may display significantly different qualitative features (Section 3.6.1).

Major results and global trends

In spite of certain limitations of seismic modeling, all seismic models display a strong correlation between seismic velocity and attenuation structure of the lithosphere and surface tectonics (i.e. lithospheric ages). Since crustal structure is highly heterogeneous even as short scales, this correlation is especially evident for the upper mantle (Sections 3.6.2, 3.6.3).

In many regions there is a clear correlation between the velocity and attenuation structure of the upper mantle and surface heat flow (Sections 3.6.2, 3.6.3). In particular, in normal oceans (i.e. oceans where the bathymetry can be explained by a cooling half-space model), seismic structure correlates with the ocean floor age. Beneath the continents, faster velocities and lower attenuation in the upper mantle are observed in the oldest regions with (commonly) low surface heat flow. The thickness of the mantle transition zone is also well correlated with surface tectonics (Section 3.4.2).

The unquestionable global correlation between seismic (both velocity and attenuation) and thermal structure of the upper mantle indicates that a significant part of seismic anomalies is produced by temperature variations. However, chemical variations in the upper mantle have a significant effect on the seismic structure of the mantle (Sections 3.4.2; 3.6.2).

Thickness of seismic lithosphere: results and uncertainties

The seismic lithosphere (the lid) is commonly defined as the high-velocity layer above the low-velocity zone (LVZ) in the upper mantle (Section 3.3.2). The LVZ is traditionally attributed to the top of the zone with partial melting, although other mechanisms such as high-temperature relaxation, a contrast in volatile content, or a drastic change in grain size are suggested by recent studies. All of these mechanisms imply that the base of the lid has a transitional character and extends over some tens of kilometers in depth.

Based on the definition of the seismic lid, the lithospheric base in a receiver-function (or converted waves) method is defined as a mantle interface with negative velocity contrast (Section 3.4.2). However, negative velocity gradients characteristic for the LVZ (i.e. velocity decreasing with increasing depth) can be explained without melting. A solid-state LVZ is possible when the seismic velocity increase due to compression is less than the velocity decrease due to heating. For example, theoretical calculations for a pyrolitic upper mantle show that, except for very young oceans (< 5 Ma), seismic observations in a 100 Ma Pacific Ocean can be quantitatively explained by a solid-state low-velocity zone (Fig. 3.130). The possibility of the existence of a solid-state low-velocity zone due to compositional variations in the upper mantle has been demonstrated by velocity–temperature inversions for the Kaapvaal craton (Kuskov *et al*., 2006) (Fig. 5.23).

Interpretations of the base of the seismic lithosphere based on seismic tomography velocity models are subject to large uncertainty:

- reference models may introduce artifact low-velocity anomalies, such as at around 220 km depth beneath the continents when PREM is used as the reference model; use of velocity perturbations relative to a reference model may produce similar artifacts;
- choice of a 2% (or any other) velocity perturbation with respect to a reference model as the lithospheric base is arbitrary and may result in significant differences in lithosphere thickness estimates (Fig. 3.120); significant differences in the amplitudes of velocity perturbations in different tomographic models further complicate the matter;
- significant smearing may occur at the boundaries between tectonic structures with significantly different lithospheric thickness (such as ocean–craton transition);
- body-wave tomographic models do not have strong control on the vertical distribution of seismic velocities, while surface-wave tomographic models either integrate velocity structure over a large depth interval (which weakens the depth resolution) or (in the case of fundamental modes) lose resolution below 200–300 km depth (Figs. 3.79, 3.81, 3.119); depth leakage further reduces depth resolution of tomographic inversions (Fig. 3.120).
- In case where the origin of the LVZ below the seismic lithosphere is associated with the presence of partial melt, the lithospheric base is likely to be a rheological boundary. A change in mantle rheology may lead to a change in the mechanism of mantle deformation from dislocation creep to diffusion creep and, as a result, to a change in mantle anisotropy

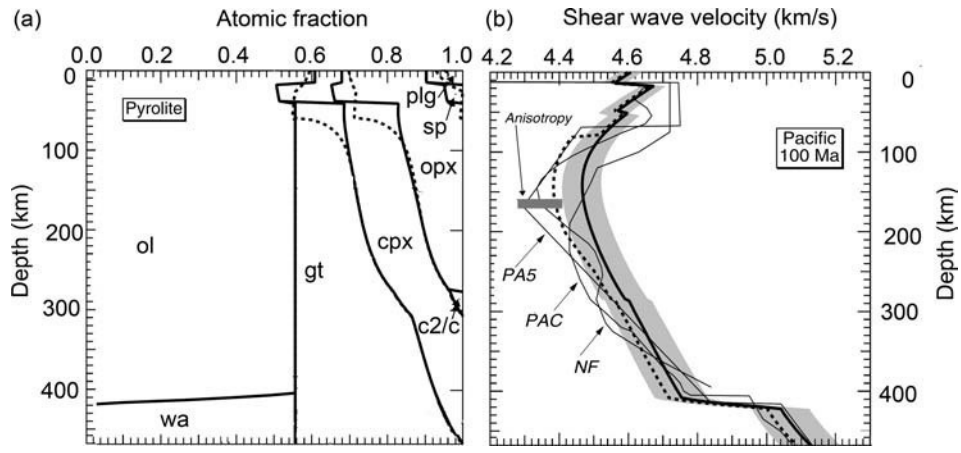

Fig. 3.130 Explanation of LVZ in the oceans by means of a solid-state low-velocity zone (after Stixrude and Lithgow-Bertelloni, 2005). (a) Phase proportions as atomic fraction computed along the 1600 K mantle adiabat (dashed) and along a geotherm for 100 Ma oceanic lithosphere (solid). (b) Shear-wave velocity calculated for pyrolite composition along the 100 Ma oceanic geotherm (bold line). Shading represents the uncertainty in the calculated velocity. The bold dashed line – velocity corrected for attenuation model QR19 for 100 Ma Pacific. Thin lines – seismological models for Pacific ocean. Gray bar – the approximate magnitude of SH–SV anisotropy. For younger lithospheric age the low velocity zone will shift to shallower depths and the value of the minimum velocity will decrease.

pattern. However, the change in the pattern of SV and SH velocities in the upper mantle may not necessarily indicate the transition from dislocation creep to diffusion creep in the mantle (Sections 3.1.5, 3.6.2).

In spite of significant controversy and ambiguity in interpretations of the base of the seismic lithosphere by different methods and research groups, the results obtained within each approach consistently indicate that the thickness of the lid increases with the age of the lithosphere both in the oceans (except for anomalous regions) and in the continents. In the oceans, the thickness of the seismic lithosphere increases from 30–60 km in young oceans to *c*. 80 km in oceans older than 80 Ma. However, in case of solid-state LVZ which is also in quantitative agreement with seismic observations from the Pacific Ocean (Fig. 3.130), lithospere of old oceans can be much thicker than 80 km.

In the continents, the thickness of the seismic lithosphere clearly correlates with lithospheric age. In Phanerozoic regions the base of the lid is typically at 50 to 100 km depth and deepens to more than 150 km in stable continents. In the collisional orogens, lithospheric slabs extend down to 150–250 km. Although the values of *c*. 200–220 km are often reported as thickness of seismic lithosphere beneath the Precambrian terranes, they do not provide compelling evidence that the tectosphere cannot extend down to the transition zone. Some high-resolution tomographic models indicate high mantle velocities and no LVZ down to a 300–400 km depth beneath the cratonic regions of West and Central Africa, Europe, Siberia, and Canada. More details on the upper mantle structure of different tectonic provinces are provided in Table 3.3.

Table 3.3 Summary of seismic structure of the mantle for some tectonic provinces

Tectonic structure	Summary of seismic structure of the mantle
Normal oceans	• Age-dependent thickness of the high-velocity lid: increases with age from mid-ocean ridges to *c*. 80–100 km in old oceans. Velocity structure of the upper mantle beneath oceans >80 Ma is similar. • LVZ with Vs ~ 4.3–4.4 km/s at 100–200 km depth. • High gradient in seismic velocity at 200–410 km depths. • Strong anisotropy down to 150–200 km depth with a peak at *c*. 100 km depth. Depth distribution shows only a weak dependence on age. • Decreased thickness of the mantle transition zone.
Pacific Ocean, East Pacific Rise	• Low Vs at 100–200 km depth (the strongest anomaly for the oceanic regions). • Strong anisotropy $V_{SH} > V_{SV}$ at depths between *c*. 100 km and 200 km. • Strong attenuation anomaly, in particular in the upper 250 km, with a pronounced a-symmetric pattern with respect to the spreading center.
Mid-ocean ridges (MOR)	• Strong low-velocity anomalies down to 150–200 km depth. • Strong anisotropy $V_{SH} > V_{SV}$ in the upper 120 km associated with mantle flow in the spreading zone. • $V_{SH} < V_{SV}$ below 120 km depth, strong anomalies beneath fast ridges, weak but deep anomalies beneath slow ridges. • Strong attenuation anomalies along MOR, at least down to 200–250 km.
Collisional structures	• Slab-like high-velocity anomalies in the upper mantle down to 150–250 km. • Beneath some collisional orogens (e.g. the Caucasus) subducting slabs in the upper mantle have not been reliably resolved. • Presence of paleo-slabs (the oldest – Archean in age) in the upper mantle of several cratonic regions as indicated by seismic reflection studies.
Cratons	• High seismic velocities down to 200–250 km depth as reported by all studies (with smaller values for some cratons, such as China and the Arabian Shield), possibly down to 300–400 km in some cratons. • Fastest and deepest high-velocity lids beneath the Archean–Paleoproterozoic cratons; in some interpretations down to the transition zone (in particular, the Canadian, Baltic, Siberian, and West African cratons). Velocities peak at *c*. 100–150 km depth (Vs ~ 4.6–4.8 km/s), below their amplitude decreases with depth and becomes uncertain at 300–400 km depth due to resolution problems. • Strong anisotropy in the upper mantle, in particular at shallow depths. • Two-layered anisotropy in the upper mantle of several cratons: frozen-in in the upper lithospheric layer and related to present-day plate motion in the lower (lithospheric or asthenospheric) layer. • Low attenuation in the upper mantle, down to at least 200–250 km. • Increased thickness of the mantle transition zone.
Phanerozoic platforms	• Seismic velocities close to global continental averages through the entire upper mantle. • Strong anisotropy in the shallow mantle. • Increased thickness of the mantle transition zone.
Rifts	• Velocity structure significantly different for rifts of the same age. • In East African Rift low Vp velocities down to *c*. 150 km depth (Vp ~ 7.7 km/s; Vs ~ 3.7–4.0 km/s). • In Baikal (and Rio Grande) rifts, no low-velocity anomaly in the upper mantle.

Table 3.3 (cont.)

Tectonic structure	Summary of seismic structure of the mantle
Young continents (except for orogens)	• Low seismic velocities from 50–100 km down to *c*. 200 km depth. • Strong anisotropy in the shallow mantle.

Data on the crustal structure are summarized in Section 3.3.1.